EVALUATION OF NUMERICAL LIMIT ANALYSES BY FINITE ELEMENTS AND LINEAR PROGRAMMING

by

BOONCHAI UKRITCHON

B.Eng. Civil Engineering, Chulalongkorn University, 1992

SUBMITTED TO THE DEPARTMENT OF CIVIL
AND ENVIRONMENTAL ENGINEERING
IN PARTIAL FULFILLMENT OF THE
REQUIREMENTS FOR THE DEGREE OF

MASTER OF SCIENCE IN CIVIL AND ENVIRONMENTAL ENGINEERING

at the

MASSACHUSETTS INSTITUTE OF TECHNOLOGY

February 1996

Signature of Author_____
Department of Civil and Environmental Engineering
October 27, 1995

Certified by_____
Professor Andrew J. Whittle
Thesis Supervisor

Accepted by_____
Professor Joseph M. Sussman
Chairman, Departmental Committee on Graduate Studies

EVALUATION OF NUMERICAL LIMIT ANALYSES BY FINITE ELEMENTS AND LINEAR PROGRAMMING

by

BOONCHAI UKRITCHON

Submitted to the Department of Civil and Environmental Engineering
on October 27, 1995 in partial fulfillment of the
requirements for the Degree of Master of Science
in Civil and Environmental Engineering

ABSTRACT

This thesis describes a numerical method for plane strain limit analysis and its application in computing the collapse load of footings on cohesive soil. The calculations of rigorous lower and upper bounds on the true collapse load are formulated and solved by a linear programming method with finite element discretization, as proposed in recent papers by Sloan (1988a) and Sloan and Kleeman (1994).

The analyses are validated through calculations of bearing capacity for vertical, concentric loading of footings on a deep clay layer, whose exact solutions are well known. These evaluations show how solution accuracy can be improved by: 1) selection of the size of the discretized domain; 2) yield surface linearization and 3) mesh discretization and refinement. The upper bound solution is much less sensitive to mesh arrangement than the lower bound solution. Further analyses for footings on non-homogenous clay layers are in excellent agreement (bounds within ± 3%) with exact solutions published by Booker and Davis (1973) based on the method of characteristics.

The numerical limit analyses are then applied in predictions of collapse for inclined, eccentric loading of footings on clay, for which there are no published exact solutions. These analyses required several modifications of the existing programs to generalize soil-footing interface properties and to select optimization functions. The results demonstrate different failure mechanisms associated with bearing capacity, separation between the footing and the underlying soil, interface sliding etc. For all analyses, collapse loads can be accurately predicted to within 4-5% and computational times required for each analysis are typically in the range of 30-45 minutes (DEC ALPHA 3000-300X workstation). The collapse loads are represented as a closed-convex surface failure envelope defined in terms of three statically equivalent loads and are well described using simple curve fitting techniques. Comparisons show that published empirical factors for inclined and eccentric loading contain comparatively large errors (up to 25%) and are generally conservative compared to the exact solutions. These studies confirm the capability and efficiency of numerical limit analyses for predicting complex collapse mechanisms.

Thesis Supervisor: Dr. **Andrew J. Whittle**
Title: Associate Professor of Civil and Environmental Engineering

Dedication

To my parents.

Acknowledgments

I would like to express my thanks and gratitude to the many people who provided professional expertise, guidance, and encouragement as well as to those who gave their personal support and friendship. In particular, I would like to thank:

Prof. Andrew Whittle, thesis supervisor, for his guidance and technical insights during all the research, and also for his meticulous review of this thesis. It has been a rewarding experience working with him.

Prof. Scott Sloan of the University of Newcastle, Australia for providing the numerical lower and upper bound programs for this research.

Prof. Charles Ladd for serving on my academic advisor and for his excellent teaching.

Lucy Jen for her time and patience in managing the gcube workstation system.

The following Thai students: Twarath Sutabutr, Trin Indra-Opas, and Manasa Muttamara for helping me in many areas, and for their great friendships.

Mary Elliff for making fresh coffee everyday for the geotech group and for her genuine concern on my analyses.

Other geotechnical staffs and students for providing a much lighter working atmosphere at MIT.

My parents and brothers who provided me with encouragement throughout this thesis.

Table of Contents

LIST OF TABLES

LIST OF FIGURES

1. Introduction

Collapse calculations are important in geotechnical engineering to ensure that all foundations and earthworks have adequate factors of safety against failure. All geotechnical design methods (e.g. Eurocode E7, 1993) include calculations of ultimate limit states. Examples of collapse calculations include prediction of the maximum load which can be applied to a foundation or the maximum height to which a slope can be excavated.

The available techniques for estimating the collapse loads include limit analyses, the method of characteristics, and limit equilibrium methods. These methods are all based on the theory of rigid-perfectly plastic material behavior. Limit analyses and the method of characteristics are based on powerful bound theorems (Drucker et al. 1952), but are difficult to apply for complex design problems involving non-homogeneous profiles, complex loading and geometries. In contrast, limit equilibrium methods can handle such complexities and hence, are widely used in geotechnical practice. Most of the stability charts, bearing capacity factors, and earth pressure coefficients have been produced by limit equilibrium methods. However, it is very difficult to assess the accuracy of limit equilibrium solutions due to approximations in the analyses.

The advent of large digital computers has increased tremendously the range of problems which can be solved using numerical methods such as the finite element method. This numerical technique has certain notable advantages: 1) it is able to simulate geometrically complex problems; and 2) can incorporate complicated constitutive stress-strain relations to model real soil behavior. Although collapse loads can be obtained numerically using finite element methods, these calculations are difficult to perform as they involve the incremental solution of a non-linear system of equations.

The above-mentioned difficulties of existing techniques for computing collapse loads have provided the motivation to develop more reliable and rigorous methods of stability analysis. One very promising technique is numerical limit analyses, which combine the advantages of numerical discretization, with the rigour of the bound theorems of classical plasticity theory. The technique was firstly proposed by Lysmer (1970), who

formulated numerical solutions for lower bound analyses using finite element discretization and linear programming. More recently, Sloan (1988a) and Sloan and Kleeman (1994) have formulated highly efficient numerical lower and upper bound limit analyses. The objective of this thesis is to apply and evaluate these numerical limit analyses in calculations of collapse for footings on clay with inclined and eccentric loading.

Chapter 2 presents a literature survey on the methods of stability analysis. The chapter also discusses the existing solutions for the stability of footings and shallow foundations in order to provide background information for subsequent chapters (4 and 5). There is also a short description of recent developments of numerical limit analyses using linear programming and finite element discretization.

Chapter 3 presents the formulation of the numerical lower bound and upper bound methods based on papers by Sloan (1988a) and Sloan and Kleeman (1994).

Chapter 4 presents results of numerical limit analyses for the undrained bearing capacity of footings on clay with vertical, concentric loading. Detailed calculations are performed to investigate factors affecting numerical accuracy of the solutions. Finally, the computed upper and lower bounds are compared with exact solutions published in the literature for footings on non-homogeneous clay layers, where the undrained shear strength increases linearly with depth (Davis and Booker, 1973).

Chapter 5 applies the numerical limit analyses to the undrained loading of a rough rigid footing on clay with inclined and eccentric loading. These problems have no exact theoretical solutions in the current literature. The research includes modifications of the programs which were necessary to incorporate the soil-footing interface. Results are presented for a wide range of eccentricity ratios, inclination angles, and shear strength profiles of the clay. Computed collapse loads are generalized to form a failure surface in terms of three statically equivalent forces, and the thesis proposes approximate functions for quantifying the failure conditions. The numerical analyses are also compared with published empirical and limit equilibrium solutions.

Chapter 6 summarizes the main results of the thesis and proposes further research on numerical limit analyses.

2. Literature Review

2.1 Introduction

In geotechnical engineering, there are two main classes of problem relating to the mechanical properties of soil: i) the prediction of deformations and stresses at working load levels and ii) assessment of ultimate loads required to cause instability or failure. Examples of the former include deformations caused by excavations, predictions of the stresses induced by surface loading of embankments, etc. In practice, stress analyses at working load levels are usually based on assumptions of linear, isotropic elastic (LIE) soil behavior (Poulos and Davis, 1974) while specialized techniques have evolved to handle non-linear soil properties in one-dimensional settlement calculations (Ladd and Foott, 1974; Mesri and Choi, 1985). In contrast, problems of bearing capacity, lateral earth pressure, and slope stability generally assume no (pre-failure) deformations and focus exclusively on the loading conditions which cause failure. There are three main classes of analyses available for rigid perfectly plastic (RPP) materials: 1) limit equilibrium; 2) slip-line analyses and 3) limit analyses. Most of the published data for bearing capacity and earth pressure are based on methods 2 and 3 (or empirical modifications thereof), and are limited to relatively simplified loading conditions, problem geometry, and subsurface stratigraphy (strength profiles). Limit equilibrium methods are most commonly used for slope stability problems and are widely favored in geotechnical practice as they can handle complex stratification and variations in strength properties.

In principle, powerful numerical techniques such as the non-linear finite element method can provide a unified analysis of deformation and stability problems by incorporating realistic constitutive models for the soil behavior (see Figure 2.1). However, in practice, it is difficult to perform numerically accurate non-linear finite element analyses, while the reliability of the predictions are largely dependent on the ability of the constitutive model to describe generalized stress-strain-strength properties of the soil (cf. Whittle 1987; Pestana, 1994). As a result, there is a continuing practical need for robust stability analyses based on assumptions of rigid perfectly plastic behavior[1].

[1] It should be noted that certain classes of problem involving progressive failure can only be handled with more comprehensive modeling of constitutive behavior etc.

This chapter reviews the methods for stability analysis in soils (Section 2.2) with particular emphasis on the lower and upper bound theorems used in limit analyses. Section 2.3 describes how these different types of analyses have been applied to predict the stability of shallow foundations and footings. Section 2.4 surveys the recent development of numerical methods for computing upper and lower bounds based on linear programming and finite element discretization. This section serves as an introduction to the subsequent Chapters, which describe the formulation of the numerical limit analyses (Chapter 3) and its applications for computing the stability of footings on clay (Chapters 4 and 5).

2.2 Methods of Stability Analysis in Geotechnical Engineering

2.2.1 Limit Equilibrium Method (LEM)

Limit equilibrium methods were firstly introduced into soil mechanics by Fellenius (1926) who considered the equilibrium of circular failure arcs for assessing short term (undrained) slope stability in clay. The technique has evolved significantly, especially for applications in slope stability where a large number of techniques have been proposed (Table 2.1). Fredlund and Krahn (1977) describe a generalized Limit Equilibrium Method which comprises the following steps:

1) Specify the spatial distribution of unit weights, pore water pressures and shear strength parameters of the underlying soil and rock stratum.
2) Assume a failure surface geometry[2] by subdividing the failed mass into a number of vertical slices and solving the static equilibrium equations (as shown in Table 2.1).
3) Solve the factor of safety for the specified failure surface. The factor of safety is defined as the ratio of the maximum available strength of the soil to the forces required for equilibrium.

[2] The failure surface is continuous and is usually constructed from segments which are of planar, circular or logspiral in shape. If the soil is purely cohesive, the failure surface is composed of planar and/or circular sections, whereas for frictional materials, the shapes of the failure surface are usually planar and logspiral.

4) Search for the critical failure surface with the lowest factor of safety.

In the first critical step, the selection of shear strength parameters depend on the type of analysis[1] and soil, while experience is also required to interpret strength parameters from laboratory and field test data. The undrained shear strength of clay depends on mode of shear, consolidation effective stress, etc; while drained shear strength parameters are usually required for free draining materials such as sands etc. The use of undrained strength means that the excess pore pressures have not had time to dissipate under an applied load, or that the critical mode of stability involves rapid mode of failure where there is no time for drainage of pore water. Thus, the in situ effective stress is treated as consolidation stress which controls the in situ undrained shear strength and stability. On the other hand, the use of drained strength implies that the excess pore pressures have sufficient time to dissipate during loading.

For the second step, the characteristic geometry of the failure surface is well defined when dealing with homogeneous slopes, but becomes very difficult to assess when the subsurface stratification is complex. For this case, the critical failure surface can be quite irregular and may be controlled by local features of the geology etc.

For the third step, the factor of safety corresponding to an assumed failure surface is obtained by the method of slices and solved by static equilibrium equations. In the method of slices, the assumed failure soil mass is divided into a number of slices. Figure 2.2a shows a typical slice with the forces which act on it. Static equations and unknowns are also summarized in Figure 2.2b. It can be shown that for a slope divided into n slices, there are in general (5n-2) unknowns while there are only (3n) equations of static equilibrium. Thus, the slope stability problem is statically indeterminate. In order to render the problem statically determinate, (2n-2) assumptions must be made. There are several classes of assumption which are commonly made:

1. Assumptions about the distribution of normal stress along the slip surface.
2. Assumptions about the positions of the line of thrust of the interslices forces.
3. Assumptions about the inclination of the interslices forces.

[1] Ladd (1991) describes three types of stability analyses: 1) total stress analysis (TSA); 2) effective stress analysis (ESA); and 3) undrained strength analysis (USA), which are recommended for stability calculations during staged construction on clays.

In all of the limit equilibrium methods of analysis (Table 2.1), the normal force P is assumed to act at the center of the base of each slice (provided that the width of each slice is small); hence, a statically determinate equilibrium problem requires only (n-2) additional assumptions. In many methods of analysis (e.g. Bishop; Spencer; Morgenstern and Price), an assumption is made about the inclination of the interslice forces. As this involves another (n-1) assumptions, the problem is now over-constrained. In this case, the analyses may be carried out either satisfying moment equilibrium or horizontal force equilibrium, which yield two different factors of safety F_m and F_f. Table 2.1 shows that differences in the assumptions concerning the interslice forces, and the interpretation of the safety factor (using overall force equilibrium, moment equilibrium or both equations) distinguish several different methods of slope stability analysis. For example, the Ordinary Method of Slices (or Swedish method, Fellenius, 1936) is the simplest of these methods as it is the only procedure which results in a linear factor of safety. To make the problem determinate, Fellenius assumes that the resultant of the interslice forces acting on any slice is parallel to its base. The factor of safety is obtained by satisfying moment equilibrium only. Figure 2.3 summarizes the analysis of ordinary method of slices or Swedish method.

Fredlund and Krahn (1977) have shown that the expression of factor of safety can be formulated in a general framework as shown in Figure 2.4. The vertical force equilibrium is used to calculate the normal force along the slip surface. The two factors of safety are computed separately, the first from moment equilibrium (F_m) and the second from horizontal force equilibrium (F_f). The factor of safety equations of each method (Table 2.1) differ (i) in the equation of statics satisfied explicitly for overall slope stability, and (ii) the assumptions used to make the problem determinate. Table 2.1 also summarizes these assumptions and the equilibrium equations used in each method.

A number of stability charts have been developed for slopes in homogeneous soil conditions. In practice, two stability charts are commonly used, Taylor (1948), and Bishop and Morgenstern (1960). Taylor (1948) used the ordinary method of slices to examine the undrained stability of an homogeneous slope in purely cohesive soils ($\phi = 0$) and introduced the stability number $N = c_u/\gamma H$, where c_u is the undrained shear strength, γ is the unit weight of soil and H is the height of slope. Taylor's stability chart is shown in

Figure 2.5. For a given height of vertical cut, the factor of safety against undrained failure is then, FS = c_u/c_{ureq}, where c_{ureq} is the undrained strength required for collapse in the stability chart and c_u is the actual strength of the clay.

Bishop and Morgenstern (1960) used Bishop's method of slices to examine the stability of slopes in soils using the effective stress analysis. Pore pressure was introduced as an independent variable using the pore pressure ratio r_u, which is defined as the ratio of pore pressure at a point of interest to the weight of overburden soil (i.e. $r_u = u/\gamma z$)[1]. Bishop and Morgenstern (1960) expressed the factor of safety as $F = m - nr_u$, where m and n are dimensionless parameters which depend on slope angle β, $c'/\gamma H$, ϕ' and the depth factor D. Figure 2.6 shows one of the charts prepared by Bishop and Morgenstern (1960).

The fourth step of the LEM involves searching for the critical failure surface (with the minimum factor of safety). This is often difficult to achieve, especially for complex failure mechanisms, as the search may correspond to a local minimum, rather the global minimum factor of safety. As a result, the critical failure surface and the collapse load obtained by LEM are highly dependent on the shape of the surface and the search procedure. It is often difficult to evaluate LEM analyses, as the inaccuracies in the method may be related to the selected shape of the failure surface and search procedures used. However, for some situations such as homogeneous cohesive soil, LEM gives similar solutions to upper bound limit analyses described below. Since LEM does not have a fundamental theoretical underpinning, it is very difficult to assess the accuracy and validity of the solutions.

2.2.2 Slip-Line Field Analyses

Slip-line field analyses were firstly used to study collapse loads by Kötter (1903) and Prandtl (1920). Thereafter, they were widely used for earth pressure and bearing capacity problems by Caquot and Kérisel (1949) and Sokolovskii (1965). Kötter (1903) was the first to derive the slip-line equations for strain problems, while Prandtl's (1920)

[1] In general, r_u varies throughout the slope. In practice, average values of r_u must be estimated from ground water measurements of other forms of conservative engineering judgment.

solution corresponds to the limit load on a homogeneous cohesive material[1]. Sokolovskii (1965) applied the slip-line method to study various stability problems for cohesive and frictional materials, and his studies represent the first main application in soil mechanics.

The original slip-line analyses can be summarized as follows. A stress field is constructed in the region near the applied load to satisfy the specified stress boundary conditions, equilibrium and yield criterion. This solution is referred to as *a partial plastic stress field*, and can be obtained by combining the equations of quasi-static equilibrium and yield criterion to generate a pair of hyperbolic partial differential equations. The solutions are represented by two set of lines whose directions at every point coincide with the directions of failure (often referred to as slip directions) which form a network of stress characteristics[2].

Further development of the slip line analyses followed the formalism of the theory of plasticity (Hill, 1950) and the rigorous limit theorems (Drucker et al, 1952). The original plastic equilibrium equations can be equated with lower bound solutions (see Section 2.2.3) provided that the partial plastic stress field is extended throughout the entire soil mass in statically admissible manner (i.e. satisfying equilibrium, yield, and traction boundary conditions). While upper bound solutions, kinematically admissible velocity fields are solved by combining compatibility equations, associated flow rule, and velocity boundary conditions. These equations produce a similar (dual) set of partial differential equations, which can be solved by methods of Sokolovskii to form a series of lines referred to as velocity characteristics.

A complete solution using the slip-line field theory includes both the stress and velocity characteristics, and is referred to as the method of characteristics or the method of associated fields (Atkinson, 1981). The method of characteristics satisfies all the conditions of equilibrium, compatibility and yield properties for the soil (with associated flow) and are thus exact solutions for rigid-perfectly plastic materials.

It is worth noting several important points in the slip-line field analysis. The partial plastic stress field obtained from the plastic equilibrium equation does not necessarily meet

---

[1] It should be noted that both Kötter (1903) and Prandtl (1920) were working on problems relating to a rigid punch loading on steel.

[2] Define from the Mohr circle.

all of requirements of the lower bound theorem of plasticity as there is no guarantee that the stress fields can be extended to the entire soil mass, satisfying the equilibrium, the yield criterion, and stress boundary conditions. Therefore, the partial plastic stress field is not necessary a true lower bound solution. On the other hand, the velocity field obtained from the method of characteristics satisfies all of the requirements of the upper bound solution and hence, is a rigorous upper bound solution.

The disadvantage of the slip-line field method is the difficulty in solving the stress and velocity characteristics. Graphical solutions can only be achieved for homogeneous soil (see Scott, 1963), while numerical methods have been applied to relatively simple soil profiles (e.g. Davis and Booker, 1973). In addition, it is difficult to extend the partial plastic stress field throughout the entire body in a statically admissible manner. This is because there is no any specific rule to apply. If only the partial plastic stress field is derived, the solution is not a true lower bound and hence, it is difficult to assess the accuracy of the solution. Another problem which frequently arises is that stress characteristics can be solved for some classes of problem, where the associated velocity characteristics cannot be found. For example, the effect of self-weight on the bearing capacity of a footing on a frictional soil (see Sokolovskii ,1965).

2.2.3 Limit Analysis Method

The limit theorems or bound theorems were developed in 1950's in conjunction with research on metal plasticity (Hill, 1950; Drucker et al. 1952). Applications of the limit theorems in soil mechanics were first published in Drucker and Prager (1952) and were surveyed by Chen (1975).

Limit analyses are based on two theorems: 1) the lower bound theorem, which states that any *statically admissible stress* field will provide a lower bound (or "safe") estimate of the true collapse; and 2) the upper bound theorem, which states that when the power dissipated by any *kinematically admissible velocity* field is equated with the power dissipated by the external loads, then the external loads are upper bounds (or "unsafe") on the true collapse load (cf. Drucker et al. 1952). A statically admissible stress field is one which satisfies the equilibrium equations, stress boundary conditions, and yield criterion

(the stress state must lie inside or on the yield surface at all points in the continuum). A kinematically admissible velocity field is one which satisfies strain and velocity compatibility equations, velocity boundary conditions, and the flow rule (of the soil at yield).

When combined, the two theorems provide a rigorous bound on the true collapse load. The following paragraph describe the main assumptions of the limit analyses.

2.2.3.1 The Yield Function and Flow Rule

The mechanical behavior of a rigid-perfectly plastic material is completely characterized by a convex yield function, $F(\sigma_{ij})$. Figure 2.7 shows a typical yield surface in a generalized stress space. Deformations (plastic flow) only occur when the stress state is at yield [i.e. $F(\sigma_{ij}) = 0$]. When the stress state lies inside the yield surface [$F(\sigma_{ij}) < 0$], the material remains rigid (no deformation). Stress states outside the yield surface [$F(\sigma_{ij}) > 0$] are not permitted within the framework of rigid-perfectly plastic behavior.

Plastic flow occurs when the stress state satisfies the yield criterion. The associated flow rule describes the direction and magnitudes of the plastic strain rates, $\dot{\varepsilon}_{ij}^{p}$ at yield. In perfect plasticity, the flow rule is *associated* with the gradient of the yield function at the current stress state as follows:

$$\dot{\varepsilon}_{ij}^{p} = \dot{\lambda}\frac{\partial F}{\partial \sigma_{ij}} \qquad \text{when} \quad F(\sigma_{ij}) = 0 \qquad (2.1a)$$

$$\dot{\varepsilon}_{ij}^{p} = 0 \qquad \text{when} \quad F(\sigma_{ij}) < 0 \qquad (2.1b)$$

where $\dot{\lambda}$ = a non-negative, plastic multiplier rate which controls the magnitude of the plastic strain rate

$\frac{\partial F}{\partial \sigma_{ij}}$ = the gradient of the yield surface which controls the direction (i.e. relative magnitudes) of the plastic strain rates

The expression in equation 2.1 means that for an associated flow rule of perfectly plastic material, when the stresses reach the yield criterion, the plastic strain rate will occur

and can be represented by a vector whose direction is outward normal to the yield surface at a stress point σ_{ij} such as point A in Figure 2.7.

Examples of yield criteria used in soil mechanics are Mohr-Coulomb, Tresca, and Von Mises, etc (Figure 2.8). The Mohr-Coulomb yield criterion is the most commonly used failure criterion in soil mechanics as it correctly accounts for changes in the shear strength as a function of the effective confining stress. On the other hand, the Tresca and Von Mises yield criteria can be applied to undrained shearing of saturated soils, where the shear resistance is controlled by the current water content of the clay, and is not affected by changes in a total confining pressure. Figures 2.8a, b and c shows perspective views of the three isotropic failure criteria in principal stress space while Figure 2.8d compares them in the π-plane projection.

The Mohr-Coulomb yield criterion can be written in τ-σ_n space as:

$$F(\tau, \sigma_n) = \tau - \sigma_n \tan\phi - c = 0 \qquad (2.2)$$

or in terms of the major and minor principal stresses:

$$F(\sigma_1,\sigma_3) = \sigma_1 (1-\sin\phi) - \sigma_3 (1+ \sin\phi) -2c\cos\phi = 0 \qquad (2.3)$$

where σ_1, σ_3 = the major and minor principal stresses[1]

τ, σ_n = shear stress and normal stress acting on a plane considered

c, ϕ = cohesion intercept and friction angle (material properties)

The associated flow rule can then be derived from equations 2.1a and 2.3:

$$\dot{\varepsilon}_1^p = -\dot{\varepsilon}_3^p \frac{1-\sin\phi}{1+\sin\phi} = -\dot{\varepsilon}_3^p \tan^2(\pi/4 - \phi/2) \qquad (2.4)$$

Equation 2.4 implies that any plastic deformation of the Mohr-Coulomb material must be accompanied by an increase in volume if $\phi \neq 0$. This property is known as dilatancy.

The Tresca yield criterion is a specific form of the Mohr-Coulomb criterion corresponding to $\phi = 0$:

$$F(\sigma_1,\sigma_3) = 0.5(\sigma_1 - \sigma_3) - c = 0 \qquad (2.5)$$

[1] Note: For soil mechanics, σ_n, σ_1, and σ_3 are effective stresses.

Thus, the associated flow rule corresponding to Tresca criterion is obtained by substituting $\phi = 0$ in equation 2.4.

$$\dot{\varepsilon}_1^p + \dot{\varepsilon}_3^p = 0 \qquad (2.6)$$

The associated flow rule of Tresca criterion implies that plastic deformation occurs with no change in volume (incompressibility condition).

Finally, in contrast to both Mohr-Coulomb and Tresca yield criteria, the Von Mises yield criterion is defined in terms of the three principal stresses:

$$F(\sigma_1, \sigma_2, \sigma_3) = (\sigma_1 - \sigma_2)^2 + (\sigma_2 - \sigma_3)^2 + (\sigma_3 - \sigma_1)^2 - 6k^2 = 0 \qquad (2.7)$$

where k = the yield stress of material in pure shear state[1]

The associated flow rule of the Von-Mises criterion also causes plastic flow with no change in volume:

$$\dot{\varepsilon}_1^p = 2\dot{\lambda}(\sigma_3 - \sigma_2);\ \dot{\varepsilon}_2^p = 2\dot{\lambda}(\sigma_1 - \sigma_3);\ \dot{\varepsilon}_3^p = 2\dot{\lambda}(\sigma_2 - \sigma_1) \qquad (2.8)$$

Thus, summing these principal plastic strain rates gives rise to:

$$\dot{\varepsilon}_1^p + \dot{\varepsilon}_2^p + \dot{\varepsilon}_3^p = 0 \qquad (2.9)$$

2.2.3.2 Virtual Work Assumption

The limit theorems assume that at the onset of collapse, changes in geometry of the body are very small and can be neglected (thereafter, deformations have no defined limit). At collapse, equilibrium equations are solved for the original undeformed dimensions. The assumption of no appreciable change in geometry enables the virtual work equation to be applied.

The principle of virtual work is composed of two separate and unrelated sets: the equilibrium set and the compatible set (Figure 2.9). The equilibrium set consists of states of external forces and internal stress which are in equilibrium, whereas the compatible set consists of states of displacement and strain which are compatible to each other. The

[1] The parameter k (Von Mises) can be related to the parameter c (Tresca) as: $k = 2c/\sqrt{3}$, where c is measure in a triaxial mode of shearing.

principal of virtual work states that if the system is in equilibrium, the work done by the external forces and displacement is equal to the work done by internal stresses and strains.

$$\int_A T_i u_i^* dA + \int_V F_i u_i^* dV = \int_V \sigma_{ij} \dot{\varepsilon}_{ij}^* dV \qquad (2.10)$$

where

T_i, F_i = external forces on the surface, and the body forces acting at all points within the continuum, respectively

σ_{ij} = a set of internal stresses which are in equilibrium with the external forces (T_i, F_i)

u_i^* = a set of 'trial' displacement rates (velocities) at all points in the continuum

$\dot{\varepsilon}_{ij}^*$ = a set of virtual strain rates compatible with the virtual displacement rate, u_i^*

V, A = volume and surface area of the body, respectively

The asterisk (*) signifies that the equilibrium (external forces and internal stresses relation) and the virtual deformation rates (compatible deformations and strains) are not necessary related to each other, and may be completely independent. The left hand side of the virtual work equation expresses the work done by the external forces, whereas the right side expresses the internal power dissipation due to the internal stresses and strains.

Referring to Figure 2.9, a valid equilibrium set (T_i, F_i , σ_{ij}) must satisfy the following equilibrium equations:

At surface points: $$T_i = \sigma_{ij} n_j \qquad (2.11)$$

At interior points[1]: $$\frac{\partial \sigma_{ij}}{\partial X_{ij}} + F_i = 0 \qquad (2.12)$$

$$\sigma_{ij} = \sigma_{ji} \qquad (2.13)$$

where n_j = the outward unit normal vector to a surface element

[1] Note: Quasi-static assumption in equilibrium equation

A valid compatible set $(u_i^*, \dot{\varepsilon}_{ij}^*)$ must also satisfy the following strain and displacement rate compatibility equation:

$$2\dot{\varepsilon}_{ij}^* = \frac{\partial u_i^*}{\partial x_j} + \frac{\partial u_j^*}{\partial x_i} \qquad (2.14)$$

2.2.3.3 The Upper Bound Theorem

The upper bound theorem states that when the rate of internal work dissipated by a kinematically admissible velocity field, u_i^* is equated to the rate at which the external forces do work, then the external forces (T_i, F_i) are upper bounds on the true collapse load.

A kinematically admissible velocity field is one which satisfies the following:

(i) strain and velocity compatibility equations (equation 2.14)

(ii) the velocity (rate of displacement) boundary conditions

(iii) the associated flow rule (equation 2.1)

The upper bound theorem ignores the equilibrium conditions, stress boundary conditions, and yield criterion (defined in terms of stresses). The proof of the upper bound theorem will be given in Appendix A.

In order to demonstrate upper bound calculations, the method will be used to evaluate the critical height of a vertical cut in cohesive soil as shown in Figure 2.10a. The unit weight of soil is γ. The critical height is defined here as the height at which the unsupported vertical cut will collapse due to its own weight. To establish an upper bound solution, we must assume a mechanism by which failure is likely to occur. For undrained loading of clay, the rigid block mechanism is kinematically admissible and is useful for collapse calculations. One such mechanism is also shown in Figure 2.10b. Here a wedge of soil is underlain by a single straight slip plane making an angle 45° with the vertical. Failure takes places as a rigid block sliding under the action of gravitational forces, and is resisted by shearing forces on the slip plane. Figure 2.10c shows the relative velocity diagram (hodograph) for such a failure mechanism. It is assumed that the wedge moves

with a displacement rate $\delta\dot{w}$ parallel to the slip plane. The rate of work done by the gravitational forces is the vertical component of the velocity multiplied by the weight of the soil wedge:

$$\tfrac{1}{2}\,\gamma H^2\,\delta\dot{w}/\sqrt{2}$$

while the rate of energy dissipated along the discontinuity surface is:

$$c_u\,H\sqrt{2}\,\delta\dot{w}$$

where c_u is the undrained shear strength of the clay layer.

Hence, equating the rate of external work to the rate of internal energy dissipation, an upper bound for the height of the vertical cut at collapse is given by:

$$H_u = 4c_u/\gamma$$

2.2.3.4 The Lower Bound Theorem

The lower bound theorem states that if a statically admissible stress field can be found throughout the system, then the loads, T_i, F_i will be lower bounds on the true collapse load.

A statically admissible stress field is one which satisfies the following:

(i) equilibrium equations (equations 2.12 and 2.13)

(ii) stress boundary conditions (equation 2.11)

(iii) does not violate the yield criterion [$F(\sigma_{ij}) \le 0$] at any point within the system

The lower bound theorem ignores all kinematic conditions (compatibility equations, velocity boundary conditions, and flow rule). The proof of the lower bound theorem will be given in Appendix B.

In order to demonstrate lower bound calculations, the method will be used to evaluate the critical height of vertical cut in cohesive soil as shown in Figure 2.11a. To establish a lower bound solution, a stress field must be which satisfies the conditions that the external loads are in equilibrium with the internal stresses, i.e.

$$\frac{\partial\sigma_x}{\partial x}+\frac{\partial\tau_{xy}}{\partial y}=0 \qquad (2.15)$$

$$\frac{\partial\sigma_y}{\partial y}+\frac{\partial\tau_{xy}}{\partial x}=\gamma$$

The stress field shown in Figure 2.11a automatically satisfies the equilibrium conditions of equation 2.15 and also satisfies the stress boundary conditions on the vertical and horizontal planes. Mohr's circles of stress for the element A and B in Figure 2.13a are shown in Figure 2.13b. The Mohr's circle A does not cross the Tresca failure envelope when

$$\gamma H_l = 2c_u$$

and hence

$$H_l = 2c_u/\gamma$$

Note that the Mohr's circle B is smaller than circle A and does not violate the failure criterion. This shows that the stresses are obtained in statically admissible procedure everywhere throughout the soil; thus, the obtained H_l is a lower bound on the actual height of the cut at collapse.

Therefore, from the upper bound and lower bound calculations, the true height, H_c, of the vertical cut in purely cohesive clay at collapse can be bracketed as:

$$2c_u/\gamma \leq H_c \leq 4c_u/\gamma$$

Thus, the average of the upper and lower bound solutions is $H = 3c_u/\gamma$ and hence the bounds differ from the average by 33%, which represents a large error for a practiced calculation, and requires refinement (primarily of the lower bound solution). This can be achieved by proposed more realistic statically admissible stress fields as discussed in detail by Heyman (1973), who gives an upper bound $H_u = 3.83c_u/\gamma$ and a lower bound $H_l = 2.83c_u/\gamma$.

2.2.4 Displacement Based Finite Element Analysis

Collapse loads can also be computed using the displacement based finite element method. These analyses model the complete load history and include the pre-yield elastic deformations of the soil. To obtain collapse loads by finite element analysis, the procedure is carried out using a step-by-step, incremental load-displacement analysis.

2.2.4.1 Incremental Procedure

The basic approach in an incremental step-by-step solution is to assume that the solution at the beginning of the increment is known. Thus, the solution for the next displacement increment can be obtained by solving the incremental equilibrium equations for each incremental load as:

$$[\,K\,]\{dU\} = \{dR\} \qquad (2.16)$$

where {dU}, {dR} = the vectors of displacement increment and load increment of the discretized body, respectively. The matrix [K] is the sum of the total geometrical stiffness and total material stiffness matrices and corresponds to the tangent stiffness of the current configuration of the body. The incremental displacement vector {dU} can be approximated using this tangential stiffness. For each successive step in the load path, the soil must satisfy the requirements of continuum mechanics namely the stress equilibrium equations, the kinematic compatibility equations and the non-linear constitutive relations (stress-strain-strength). Having evaluated an approximation to the displacement vectors corresponding to the applied load increment, then solution can proceed to the next increment of the calculation. However, the displacement increments do not generally satisfy the equilibrium of the discretized body at the next configuration due to material non-linearity[1]. As a result, various interactive procedures have been developed and applied to finite element analysis. The choice of a particular procedure depends on the loading condition, the accuracy required for the analysis, the constitutive relations etc.

Figure 2.12 shows the simplest incrementation procedure known as first order Euler integration method in which the tangent stiffness [K] at the beginning of an increment is directly utilized to obtain a linear approximation for the incremental response. As shown in Figure 2.12a, we suppose that the solution at Point A is known at the beginning and we want to determine incremental displacement {dU} associated with applied incremental load {dR}. We project along a tangent at Point A to obtain an approximate solution denoted by point B. However, because of the assumption in equation 2.16 which is always approximate equilibrium conditions, we can expect that after a number of increments, the approximate solution diverges from the true load path,

[1] Problems of geometric non-linearity are not considered here.

as shown in Figure 2.12b. It is possible that a solution may be subject to very significant errors and may indeed be unstable, depending on the size of the load step used. Although this kind of analytical error can be reduced by keeping the incremental load (or displacement) small, the number of increments will be correspondingly greater, causing an increase in computational time. Therefore, in practice it is frequently necessary to iterate until the non-linear equilibrium equations are satisfied[1] .

2.2.4.2 Iterative Solution Techniques

Due to the assumption of a constant stiffness within a load step, the displacement increments will, in general, be in error If left uncorrected, such errors will accumulate and solution will diverge from the correct load path. One solution is to adopt an iterative procedure which ensures that the solution is sufficiently accurate at each successive step. All iterative techniques are based on a piecewise linear method in which the stiffness is assumed constant and an iterative procedure is pursued until equilibrium is satisfied. A correction load vector corresponding to the unbalanced force vector (obtained from the external load vectors and the stress state) at the previous iterative step, is applied to approximate the displacement increment at the next iterative step. This procedure can be repeated until the correction load vector reaches an acceptable tolerance.

Bathe (1982) describes several iterative solution techniques including the full Newton-Raphson and modified Newton-Raphson, shown in Figure 2.13. For the Newton-Raphson method, the tangent stiffness matrix is recalculated at each time during an iteration as shown in Figure 2.13a. On the other hand, for the modified Newton-Raphson method, the stiffness matrix evaluated at the previous step is used throughout the iteration as show in Figure 2.13b. Thus, the number of iterations increases with the non-linearity of the system. It can be seen that even though Newton-Raphson method requires smaller iterations than the modified version, convergence of the solution is not guaranteed if the tangent stiffness becomes weak. In general, it is difficult to assess the number of iterations required to achieve a given tolerance (load path accuracy).

---

[1] There are higher order incremental schemes, which compute the error for a give step size and automatically adjust the step size to prevent progressive deterioration of the solution (e.g. Abbo and Sloan, 1994).

Convergence of the iterative solution is generally measured using either a displacement criterion or a residual force criterion. The first method compares the norms of two consecutive displacement solutions. Convergence is satisfied when the difference between two norms is less than some specified tolerance:

$$\frac{\left|\{U\}_{i+1}^{n+1}\right| - \left|\{U\}_{i}^{n+1}\right|}{\left|\{U\}_{i}^{n+1}\right|} \leq \text{Tol} \qquad (2.17)$$

where $\{U\}$ = displacement vector

the subscript i = the iteration number

the superscript n+1 = the incremental step

Norm of a vector $\{A\} = |\{A\}| = (\{A\}^T\{A\})^{1/2}$

Alternatively, the second method compares the norm of the residual (unbalanced) force vector to the norm of the total external load vector:

$$\frac{\left|\{R\}^{n+1}\right| - \left|\{R_I\}_{i+1}^{n+1}\right|}{\left|\{R\}^{n+1}\right|} \leq \text{Tol} \qquad (2.18)$$

where $\{R\}^{n+1}$ = the total external load vector = $\{R_B\}^{n+1} + \{R_S\}^{n+1}$

$\{R_B\}$ = the body force vector

$\{R_S\}$ = the surface force vector

$\{R_I\}$ = the resisting forces obtained by integration of the element stresses

Nayak and Zienkiewicz (1972) have suggested that the tolerance for these criteria should be on the order of 10^{-4} to 10^{-5}. This tolerance seems rather restrictive for geotechnical materials because of their non-linear properties.

Theoretically, the finite element analysis can give the complete results of stability calculations, namely stress-strain distribution, displacement, etc. However, in geotechnical practice, it is not easy to apply non-linear numerical analysis because of its complexity as described earlier. Moreover, the finite element analysis depends on idealization, or discretization of a problem so that an approximate solution to the governing differential equations is obtained. The accuracy of this solution relies upon the assumptions made

during the discretization of a problem and the numerical techniques used to obtain the solution. Some common sources of errors arise from:

1) constitutive relations,

2) element selection and mesh refinement.

The analysis also requires a generalized soil model (constitutive relations) in order to achieve reliable solutions. However, the measured behavior of real soil is very complex and includes properties such as anisotropic and rate dependent shear strength, strain softening, etc. Moreover, many of the existing soil models assume that the limiting (critical state) shear strength is only mobilized at large shear strains and hence, numerical analyses must include geometric non-linearities to capture this type of behavior. Numerical errors also occur due to the linearization and integration of the non-linear stress-strain relations when performing incremental or iterative schemes described earlier.

Displacement based finite element analyses approximate the continuum deformation field with specified interpolation functions (which describe displacement variations within an element). In order to achieve reliable predictions of collapse loads, the interpolation functions must be able to capture the deformation modes associated with incompressible or dilating soil (volume increase with shearing). Inaccuracies often occur in predictions of collapse loads due to the excessive number of kinematic constraints imposed on the incremental displacement fields as collapse is approached (e.g. Nagtegaal et al., 1974; Sloan and Randolph, 1982). Sloan and Randolph (1982) demonstrated that this problem can be solved by using higher order interpolation functions[1] which provide sufficient degrees of freedom to overcome incompressiblity constraints. In addition, they showed that analyses using standard types of (isoparametric) elements yields unreliable prediction of collapse loads, especially for undrained axisymmetric problems.

[1] For undrained analyses of collapse, they recommend cubic strain interpolation functions which are generated 15-noded triangular elements.

2.3 The Stability of Footings and Shallow Foundations

2.3.1 Terzaghi Bearing Capacity Theory

In 1920, Prandtl published results of his study regarding the penetration of hard bodies, such as metal punches into a softer material. Terzaghi (1943) extended the plastic failure theory of Prandtl (1920) to evaluate the bearing capacity of soils for shallow strip footings. The assumptions used in Terzaghi's bearing capacity are as follows:

1. A shallow foundation is defined as shallow when the depth of embedment, D_f is less than, or equal to its width, B.
2. The soils above the base of foundation acts as a uniform surcharge with no shear resistance.
3. Soil below the base level is a rigid-perfectly plastic material, which satisfies the Mohr-Coulomb yield criterion.
4. Solutions are obtained for a plane strain (strip footing) geometry.
5. Empirical correction factors are introduced to address the effects of foundation shape, pre-failure compressibility, inclination angles, etc.

Figure 2.14 shows the failure mechanism assumed by Terzaghi (1943) for determining the ultimate bearing capacity of a smooth flexible footing (uniform bearing pressure). The failure is composed of three zones: I) an Rankine active zone, ABJ (σ_1 vertical); II) two radial shear zones, AJE and BJD (rotations of principal stress directions); and III) two Rankine passive zones, GEA and BDF (with σ_1 horizontal). The curves JD and JE are arcs of a logarithmic spiral.

Based on this type of failure mechanism, Terzaghi evaluated the bearing capacity using an approximate method of superimposition:

$$q_{ult} = cN_c + qN_q + \tfrac{1}{2}\gamma BN_\gamma \qquad (2.19)$$

where N_c, N_q, N_γ are bearing capacity factors which are functions of the friction angle ϕ' and represent the effects of soil cohesion c, surcharge, q, and soil unit weight, γ, respectively. Terzaghi (1943) obtained the exact solutions of N_c, N_q for a weightless soil ($\gamma = 0$):

$$N_q = \exp[\pi \tan\phi'] \tan^2(45 + \phi'/2) \qquad (2.20)$$

$$N_c = (N_q - 1)\cot\phi' \qquad (2.21)$$

Approximate solutions[1] for N_γ have been proposed by several investigators including Hill (1950), Sokolovskii (1965), Caquot and Kérsiel (1948), Terzaghi (1943), and Prandtl (1920) (Table 2.2 summarizes result for smooth and rough bases). The most commonly used values of N_γ are those reported by Caquot and Kérsiel (1948) for a smooth base:

$$N_\gamma = 2(N_q + 1)\tan\phi' \qquad (2.22)$$

Figure 2.15 summarizes the three bearing capacity factors presented in equations 2.20, 2.21 and 2.22.

Equation 2.19 is applicable for general problems of drained bearing capacity (effective stress analysis). The undrained bearing capacity of a purely cohesive soil (total stress analysis, $\phi = 0$) is given by:

$$q_{ult} = c_u N_c + q \qquad (2.23)$$

Note that for $\phi = 0$, $N_q = 1$ and $N_c = 2 + \pi = 5.141$, are the standard results for a smooth foundation on a homogeneous cohesive clay layer.

In practice, there are many uncertainties in applying equations 2.19-2.23 to predict drained bearing capacity of sands including: 1) uncertainties in the analytical solution for N_γ (note: for $\phi = 0$, $N_\gamma = 0$); 2) the importance of non-linearities in the measured peak friction angles of sands at low stress levels (cf. Pestana, 1994); and 3) the compressibility of sand (cf. Vesic, 1975). Furthermore, bearing capacity is rarely the dominant design criterion for shallow foundations on sands, while the short term (undrained) bearing capacity of clays is often critical in the design of foundations.

[1] Note: $N_\gamma = 0$ for $\phi' = 0$.

2.3.2 Parameters Affecting Bearing Capacity

2.3.2.1 Effects of Embedment and Foundation Shapes

The theoretical basis for bearing capacity are slip-line analyses which apply only to plane strain footing geometry. For other foundation shapes such as circular or rectangular bases, there are no analytical solutions available. Similarly, by neglecting the shear resistance of the overburden soils, there are no exact solutions which account for the effects of embedment depth. Geotechnical practice uses semi-empirical correction factors to account for foundation shape and embedment depth.

The modified Terzaghi's bearing capacity formula is then written:

$$q_{ult} = cN_cD_cS_c + qN_qD_qS_q + \tfrac{1}{2}\gamma BN_\gamma D_\gamma S_\gamma \qquad (2.24)$$

where D_c, D_q and D_γ are depth factors and S_c, S_q and S_γ are shape factors listed in Table 2.3 and are based on recommendations by DeBeer (1967) and Hansen (1970), respectively.

2.3.2.2 Effect of Inclined and Eccentric Loads

To calculate the bearing capacity of shallow foundation with eccentric loading, Meyerhof (1953) proposed the concept of effective width based on experimental studies. Figure 2.16 shows the concept of the effective area for a footing of length, L, and width, B, subjected to an eccentric, vertical load, Q_u. The load eccentricities are e_L and e_b with respect to the length and width, respectively. The effective width concept assumes that the vertical load Q_u acts over the apparent width, $B' = (B - 2e_b)$ and the apparent length, $L' = (L - 2e_L)$. Thus, the collapse load can be approximated as $q_{ult}(B'.L')$.

When the footing is subjected to an inclined load, the problem is rather more complicated because of the presence of the horizontal component of the applied load. Failure can occur either by sliding of the footing along its base or by the general shear failure of the underlying soil. The bearing capacity of inclined loads can be obtained by introducing inclination factors, which take into account for the direction of load application inclined at a certain angle to the vertical. In practice, inclination factors are simply applied to each term of the bearing capacity equation:

$$q_{ult} = cN_cD_cS_c\tilde{i}_c + qN_qD_qS_qIq + \tfrac{1}{2}\gamma BN_\gamma D_\gamma S_\gamma I_\gamma \qquad (2.25)$$

where I_c, and I_q and I_γ are inclination factors

Hansen (1961) applied the method of stress characteristics to study a footing on weightless soil loaded with an inclined and concentric load as shown in Figure 2.17. The footing has a flexible rough base which indicates that the contact normal stress is uniform. In his analyses, Hansen assumes that the soil-footing interfaces obeys the Mohr-Coulomb criterion with the same properties as the underlying soil.

For undrained loading ($\phi = 0$), Vesic (1975) and Hansen's (1961) give:

$$I_c = 1/(\cos\alpha + 2\sin\alpha) \qquad (2.26)$$

$$I_q = 1$$

where α = inclination angle of the applied load to the vertical

In contrast, Meyerhof (1953) proposed empirical inclination factors:

$$I_c = I_q = (1 - \alpha°/90°)^2 \qquad (2.27)$$

More recently, Saran and Agarwal (1991) have solved the bearing capacity of a strip footing with an inclined and eccentric load, using a limit equilibrium method shown in Figure 2.18. They assume the following:

1. The base of the footing is rough.
2. The shear resistance of soil above the base of foundation is neglected and replaced by uniform surcharge.
3. Referring to Figure 2.18, the failure of the left side (direction of horizontal load direction) is fully mobilized, while the failure on the right is partially mobilized.
4. The footing can lose contact with the soil at large load eccentricity. Saran and Agarwal (1991) provided several expressions for the width of the contact area as a function of the eccentricity ratios.
5. The method of superposition still holds, which implies that three components of bearing capacity, (cohesion, self-weight, surcharge) can be evaluated separately.

Due to the complexity of the problem, the bearing capacity factor can not be derived in closed-form, but is solved numerically trial-and-error, with solutions shown in Figure 2.19.

2.3.2.3 Effect of Layer Thickness (on undrained bearing capacity)

The standard (Terzaghi, 1943) bearing capacity solutions apply for a deep clay layer (half-space). Shield (1955) used limit analyses to study the capacity of a smooth, rigid punch on the surface of thin layer of cohesive material (Tresca yield) resting on the rough rigid base. The square and circular punch were considered in his analyses. For thinner layer, Shield obtained the mathematical expressions for the upper and lower bound solutions for the bearing capacity factor, N_c as a function of the width-thickness ratio B/(2H), where B is the width of the footing and H is the thickness of the clay. Table 2.4 summarizes the expressions of bearing capacity for the square and circular punch while Figure 2.20 compares the analytical bounds. For both cases, the bearing capacity of thin clay layers increases significantly with the width-thickness ratio. Within the range of practical interest [B/(2H) = 10-80], N_c increase almost linearly with B/(2H). For a large value of B/(2H), the bounds for square punch differs from their mean about 10-15%, while those for circular punch are very small (less than 5%). Hence, the bounds are reasonably accurate for all practical cases of interest.

2.3.2.4 Effect of Strength Gradient on Undrained Bearing Capacity

Davis and Booker (1973) used numerical analyses to solve stress and velocity characteristics for undrained collapse of surface footings (with smooth and rough bases) on clay layer with non-homogeneous strength profiles (Figure 2.21). Their analyses consider two types of strength profile : i) undrained shear strength increases linearly with depth, and ii) a clay crust overlying layer whose strength increases linearly with depth. Davis and Booker (1973) have found both stress and velocity characteristics of these problems, thus their solutions are exact. Figure 2.21 summarizes the bearing capacity factors for these two cases.

2.3.2.5 Effect of Anisotropy on Undrained Bearing Capacity

Davis and Christian (1971) investigated the effect of anisotropic strength properties on the undrained bearing capacity using an anisotropic yield criterion, proposed by Hill (1950). Exact solutions for this problem (obtained from stress and velocity characteristics) can be represented as a simple modification of the bearing capacity:

$$q = \frac{1}{2} [\, c_u(0°) + c_u(90°) \,] N'_c + q N_q \qquad (2.28)$$

where $c_u(0°)$ = undrained shear strength for triaxial compression

$c_u(90°)$ = undrained shear strength for triaxial extension

N'_c = modified bearing capacity factor defined in terms of $c_u(0°)$, $c_u(90°)$ and $c_u(45°)$ in Figure 2.22.

Note that when parameters a and b are equal, N'_c becomes the conventional Terzaghi's bearing capacity factor(i.e. $N_c = 5.141$)

2.3.3 Survey of Analysis Methods Used for Footings and Foundations on Clays

The application of limit analyses to undrained loading of footing on clay are restricted to simple problems such as the effect of layer thickness of clay (Shield, 1955).

The method of characteristics has been used to investigate complicated problems of undrained loading on clay, including the effects of 1) strength non-homogeneity (Davis and Booker, 1973); 2) anisotropic strength (Davis and Christian, 1971); and 3) inclined loads (Hansen, 1961). In addition, Sokolovskii (1965) applied this method to obtain solutions for both cohesive and frictional soils for footing problems. All of the above analyses were solved for plane strain conditions. Houlsby and Wroth (1982) have used the method of characteristics to calculate the bearing capacity for axially symmetric footings and penetrometers. Their studies are relevant to interpreting the shear strength at the Liquid Limit test using the fall cone method. Cox et al. (1961) and Cox (1962) have also studied the axial symmetric problem of a smooth circular punch. Little work on foundation problems of axial symmetry has been reported.

The limit equilibrium method (LEM) has also been applied to estimate the bearing capacity of plane strain footings under inclined and eccentric loads by Saran and Agarwal (1991). Janbu (1985) used LEM methods to compute the collapse of footings under

inclined concentric load as shown in Figure 2.24a (the analyses assume $\gamma = 0$). The applied horizontal and vertical loads are assumed to be uniformly distributed over the width of the foundation, which implies that the solutions correspond to the case of flexible base. Figure 2.23b show Janbu's bearing capacity factor, N_c, plotted as a function of base roughness ratio, $r = H/Bc_u$, where H is the applied horizontal force, B is the width of the footing, and c_u is the undrained shear strength of the clay. Thus, the vertical collapse pressure, $q_v = [c_uNc + p]$, where p is the overburden pressure at the base of the foundation. Notice that to use Janbu's chart, the applied horizontal load must be known, which is a typical situation for offshore structure where the applied horizontal load is evaluated from wave action or wind loads.

Garber and Baker (1977) have proposed a variational method for assessing the stability problem, and evaluating Terzaghi's bearing capacity factors. The assumptions used in their analyses are similar to those used in Terzaghi's bearing capacity calculation. Plane strain conditions are considered and the effect of the soil above the foundation level is represented by a uniformly distributed surcharge. The variational method is similar in concept to the Limit Equilibrium Method (LEM) with unknowns corresponding to the location of the failure surface and the normal stress distribution along the failure surface. Their analyses consider only continuous functions for the failure surface and normal stress. The applied load from a footing is expressed as a function of the normal stress using one of three equilibrium equations. The bearing capacity problem is formulated by finding the smallest value of the applied load which permits the normal stress along the failure surface to satisfy the conditions of LEM (i.e. three equations of equilibrium, and the Mohr-Coulomb failure criterion). The formulation leads to a variational problem of the isoparametric type, which is solved using the method of Lagrange multipliers. Their solutions of bearing capacity factors match those obtained by Terzaghi (1943). Note that the variational method still suffers the same problem as LEM in which the resulting solutions contain errors of unknown magnitude.

Griffiths (1982) has applied non-linear, elasto-plastic finite element analyses to evaluate Terzaghi's bearing capacity equation for plane strain footings on cohesive, frictional soil (Mohr-Coulomb failure criterion) with a non-associated flow rule (zero

dilation at failure). These analyses also consider both smooth and rough bases. The results show that the bearing capacity factors N_c and N_q obtained from finite element analyses are in good agreement with those proposed by Terzaghi (1943), while the N_γ term corresponds with solutions of Hill (1950) and, Hansen and Christiensen (1969) at small friction angles ($\phi < 25°$; Table 2.2). Large differences occur between the finite element and published solutions of N_γ for $\phi > 25°$. The results confirm that Terzaghi's assumption is conservative due non-linearity in the N_γ term.

2.4 Numerical Solution of Limit Analyses By Linear Programming

2.4.1 Motivation

Limit analysis is a powerful method for analyzing stability problems in soil mechanics as the lower and upper bound theorems provide a rigorous bound on the exact collapse load. However, the conventional analytical techniques used to solve limit theorems (methods of characteristics) are very difficult to apply for complex geometries, soil profiles (non-homogeneities) and loading conditions. Furthermore, crude upper and lower bound loads may not provide adequate resolution of the collapse load (cf. section 2.2). For example, it is often difficult to construct statically admissible stress fields, which give a lower bound close to the true collapse load. Moreover, there is no rational method for refining statically admissible stress fields in order to improve the accuracy of the lower bound calculation. Finally, many published solutions are referred to as 'lower bounds' although they do not satisfy the complete requirements of the lower bound theorem.

For homogeneous soils, it is often much easier to obtain relatively accurate upper bound solutions which are close to the true collapse load[1] except in cases where the soil dilates ($\psi > 0$; see Figure 2.1)[2] at failure. Conventional analyses which assume rigid block mechanisms do not represent correctly the volume changes of these dilating materials and hence, do not satisfy fully the requirements of the upper bound theorem.

[1] When dealing with complex stratigraphy etc, it is also difficult to find kinematically admissible failure mechanism.

[2] For undrained analysis of clay $\psi = 0$ and there is no plastic volume change.

Since the application of the conventional analytical limit analysis is limited to simple problems, a more robust numerical method for computing the lower and upper bounds is highly desirable.

2.4.2 Numerical Lower Bound Formulation by Finite Element and Linear Programming

The numerical lower bound formulation was first proposed by Lysmer (1970) for plane strain problems. His approach uses the concept of finite element discretization and linear programming. In this procedure, the soil mass is discretized into 3-noded triangular elements whose nodal variables are unknown stresses. The stresses are assumed to vary linearly within element, while stress discontinuities are permitted to occur at the interface between adjacent triangles. The statically admissible stress field is defined by the constraints of equilibrium equations, stress boundary conditions, and the yield criterion. Each non-linear yield criterion is approximated by a set of linear constraints on the stresses which lie inside the parent yield surface, thus ensuring that the solutions are a strict lower bound[1]. This leads to an expression for the collapse load which is maximized and subjected to a set of linear constraints on the stresses. The lower bound load is solved by optimization, using techniques of linear programming. Other investigators have worked on similar algorithms (Anderheggen and Knopfel ,1972; Pastor, 1976; Bottero et al., 1980). However, the major disadvantage of these formulations is the linearization of the yield criterion which generates a large system of linear equations, and requires excessive computational times, especially if the traditional simplex or revised simplex algorithms are used (Sloan, 1988a). Therefore, the scope of the early investigations were limited to small problems. Lysmer (1970) attempted to improve the efficiency of his solutions by employing an iterative technique which used a small subset of the total number of yield constraints. Although this approach reduced the computational time significantly, it was only conditionally stable and not sufficiently robust for general applications.

More recently, efficient methods for solving numerical lower bounds by finite elements and linear programming have been developed (Bottero et al, 1980; Sloan, 1988a and 1988b; and Assadi and Sloan, 1990). The key concept of these analyses is the

[1] Sloan (1988a) uses the method of Lysmer (1970) to linearize the yield function.

introduction of an active set algorithm (Sloan, 1988b) to solve the linear programming problem where the constraint matrix is sparse. Sloan (1988b) has shown that the active set algorithm is ideally suited to the numerical lower bound formulation and can solve a large-scale linear programming problem very efficiently. A second problem associated with numerical lower bound solutions occurs when dealing with statically admissible conditions for an infinite-half space. Assadi and Sloan (1990) have solved this problem by adopting the concept of infinite elements originally proposed by Pastor (1978), and hence obtain rigorous lower bound solutions for general problems.

2.4.3 Numerical Upper Bound Formulation by Finite Element and Linear Programming

Numerical upper bound formulations finite elements and linear programming were also proposed by Anderheggen and Knopfel (1972) and Bottero et al.(1980). The former was primarily concerned with limit analyses for plates, whereas the latter formulation was generalized to include velocity discontinuities for plane strain problems. In the formulation of Bottero et al (1980), the soil mass is discretized into 3-noded triangular elements whose nodal variables are the unknown velocities. The velocities are assumed to vary linearly within element. Each element is associated with a specified number of unknown plastic multiplier rates ($\dot{\lambda}$; equation 2.1). Velocity discontinuities are permitted along pre-specified interfaces of adjacent triangles. Plastic deformation can occur within the triangular element and at the velocity discontinuities. Kinematically admissible velocity fields are defined by the constraints of compatibility equations, flow rule of yield criterion and velocity boundary conditions. The non-linear yield criterion (Von Mises, Tresca or Mohr-Coulomb) is linearized using a polygonal approximation (Sloan, 1989), which circumscribes the exact yield surface so that the solutions are a strict upper bound. The finite element formulation of the upper bound theorem leads to a linear programming problem whose objective function is the minimization of the collapse load and is expressed in terms of the unknown velocities and plastic multipliers. Bottero et al.(1980) obtained upper bound loads using the revised simplex algorithm.

One of the major disadvantages of this formulation is that the revised simplex algorithm required significant amounts of computational time. This problem was overcome

by Sloan (1988b, 1989) who adopted the same basic formulation as Bottero et al (1980), but solved the linear programming problem using the active set algorithm.

The second problem encountered by Bottero et al (1980) and Sloan (1989) is caused by the incompressibility condition of perfectly plastic deformation. The discretization using linear triangular elements must be arranged such that 4 triangles form a quadrilateral, with the central nodes lying at its centroid[1] .

Furthermore, the analyses only handled a limited number of velocity discontinuities with pre-specified directions of shearing. Sloan and Kleeman (1994) have recently developed a more general numerical upper bound formulation (also using linear triangular discretization) which permits velocity discontinuities along all edges between adjacent triangular elements, while the direction of shearing is solved automatically during the optimization process. Sloan and Kleeman (1994) have shown that this new formulation provides good estimates of the true collapse load even with a relatively coarse grid, and is much less sensitive to the mesh arrangement than the earlier prototype formulation (Sloan, 1989).

Recently, another type of numerical upper bound approach has been formulated by Chuang (1992). The soil mass is discretized into rigid triangular and rectangular elements with plastic deformation occurring along contact edges of adjacent elements. The kinematic formulation leads to a linear programming problem which is a primal problem. Chuang (1992) is able to show through the duality theorem of linear programming that the dual problem of the primal formulation for these conditions corresponds to the limit equilibrium method. Therefore, his solutions are more accurate than those obtained from conventional limit equilibrium calculations. However, his method is limited by the assumption of rigid elements, which indicates that velocity fields obtained are not kinematic admissible for frictional materials which dilate at failure.

[1] Yu et al. (1994) have shown that this constraint can be removed using higher order (quadratic) interpolation of the nodal point velocities.

2.4.4 Previous Applications of Numerical Limit Analyses

The numerical limit analysis technique has been applied successfully to assess a number of stability problems in soil mechanics for which no analytical solutions exist, including undrained stability of shallow square tunnels (Assadi and Sloan, 1990), undrained stability of shallow circular tunnels (Sloan and Assadi, 1993), undrained stability of a trapdoor (Sloan et al, 1990), and the bearing capacity factor due to self-weight, N_γ of a cohesionless soil (Yu and Sloan, 1993).

Figure 2.24 shows the undrained stability charts for shallow square tunnels in a homogeneous clay (Assadi and Sloan, 1990). The stability factor is represented by $(\sigma_s - \sigma_t)/c_u$, where σ_s is the surcharge at the surface, σ_t is the internal pressure in a tunnel, and c_u is the undrained shear strength of clay. The stability factor is plotted against the embedment depth-width ratio H/B. Figure 2.25 summarizes the results of similar studies for a circular tunnel in clay layer whose undrained shear strength increases linearly with depth. In this case, the stability factor is given as $(\sigma_s - \sigma_t)/c_{u0}$, where c_{u0} is the undrained shear strength of clay at the ground surface. All of the results correspond to active type failure, where the surcharge at the surface causes the soil to fail (at a specified internal pressure). For all analyses, the collapse loads can be accurately predicted within ±8-12% which is considered very reasonable for practical engineering calculations.

Figure 2.26 shows the bearing capacity factor N_γ for a smooth strip footing plotted as a function of friction angle with the ordinate plotted on a logarithmic scale. The plot compares: 1) the solutions obtained from the numerical limit analyses (Yu and Sloan, 1993); 2) Sokolovskii's partial stress field solutions; 3) Booker's upper bound solutions; and 4) Chen's upper bound solutions (Hill mechanism). All of the solutions indicate that the value of $\ln(N_\gamma)$ increases almost linearly with friction angle. The numerical upper bound solutions represent a significant improvement on solutions obtained by Sokolovskii and Chen. The bounds from numerical limit analyses typically differ by about 20%. Booker's upper bound solutions together with the numerical lower bound solutions enable to bracket the exact value for N_γ to within about 5%.

Several authors have applied numerical limit analyses to reinforced earth walls (Sawicki, 1983, 1988; de Buhan et al., 1989; de Buhan and Siad, 1989; Yu and Sloan, 1994b, Abdi et al., 1994) based on homogenization assumptions which treat the reinforced soil mass as an equivalent homogeneous, anisotropic material. Figure 2.27 shows the numerical upper and lower bound solutions for the bearing capacity of a strip footing on weightless cohesionless reinforced soil (Yu and Sloan, 1994b). These results are plotted as normalized bearing capacity, q/σ_0 against the soil friction angle ϕ, where q = the collapse pressure, $\sigma_0 = (d/h)\sigma_{yield}$, d = the thickness of the reinforcement, h = the spacing of the reinforcement, and σ_{yield} = the tensile yield strength of the reinforcement. Plotted in the same figure are: 1) the upper bound solutions obtained by de Buhan et al., who used a rigid body mechanism to find the collapse load; and 2) the exact solution obtained by Sawicki (1988). The results show the numerical upper bound solutions give more accurate estimates of the true collapse load than those obtained by de Buhan et al. It can be seen that the exact solution lies between the numerical lower and upper bound predictions, and can be accurately predicted by their mean to within 10% (while the numerical upper bound solution is much closer to the exact solution than the lower bound).

Method	Circular	Non-circular	Overall Moment Equilibrium	Overall Force Equilibrium	Assumptions about interslice forces
Infinite slope		*		*	Parallel to slope
Wedge analysis		*		*	Define inclination
$\phi_u = 0$	*		*		
Ordinary	*		*		Resultant parallel to base of each slice
Bishop	*	(*)	*		Horizontal
Janbu simplified	(*)	*		*	Horizontal
Lowe and Karafiath	*	(*)		*	Define inclination
Spencer	*	(*)	*	*	Constant inclination
Morgenstern and Price	*	*	*	*	$X/E = \lambda . f(x)$
Janbu rigorous	*	*	*	*	Define thrust line
Frelund and Krahn GLE	*	*	*	*	$X/E = \lambda . f(x)$

Note E and X are horizontal and vertical components of interslice forces respectively.

Table 2.1 Methods of stability analysis

N_γ Friction angle, ϕ'	Smooth Footing				Rough Footing		
	A	B	C	D	A	E	F
20	1.6	2.7	3.2	5.7	2.9	4.8	6.2
25	3.5	5.9	6.9	11.1	7.0	9.8	13.0
30	7.5	12.7	15.3	22.8	15.0	20.0	27.7
35	18.0	28.6	35.2	50.0	35.0	43.0	61.5
40	42.0	71.6	86.5	119.9	85.0	98.0	145.3

Sources:

A. Hansen and Christiensen (1969)

B. Hill (1950)

C. Sokolovski (1965)

D. Caquot and Kerisel (1949)

E. Terzaghi (1943)

F. Prandtl (1920)

Table 2.2 Values of bearing capacity factor N_γ, reported by different authors

Shape of the Base	Shape factors		
	S_c	S_q	S_γ
Strip	1.00	1.00	1.00
Rectangle	$1 + (B/L)(N_q/N_c)$	$1 + (B/L)\tan\phi'$	$1 - 0.4(B/L)$
Circle and Square	$1 + (N_q/N_c)$	$1 + \tan\phi'$	0.60

Note: B and L are width and length of foundation

a) Shape factors for shallow foundations (after Debeer, 1970)

Embedment ratio D/B	Depth factors		
	D_c	D_q	D_γ
$D/B \leq 1$	$1 + 0.4(D/B)$	$1 + 2\tan\phi'(1-\sin\phi')^2(D/B)$	1.00
$D/B > 1$	$1 + 0.4\tan^{-1}(D/B)$	$1 + 2\tan\phi'(1-\sin\phi')^2\tan^{-1}(D/B)$	1.00

Note: D is depth of embedment of foundation

b) Depth factors (after Hansen, 1970)

Table 2.3 Shape factors and depth factors for bearing capacity calculations

Foundation shapes	Limit analyses	Bearing capacity coefficient, N_c
Square	upper bound	$N_c = 5.07 + 0.384(B/2H)$
	lower bound	$N_c = 3.42 + 0.667(B/2H) + [\ 1.82(2H/B) - 0.26(2H/B)^2\ ]$
Circular	upper bound	$N_c = 4.83 + 0.667(B/2H)$
	lower bound	$N_c = 3.42 + 0.667(B/2H) + [\ 3.05(2H/B) - 0.44(2H/B)^2\ ]$

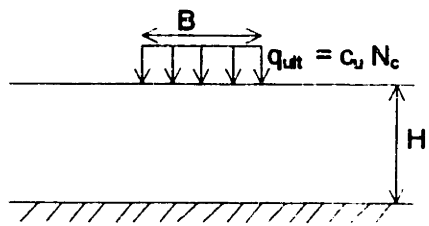

Table 2.4 Bearing capacity factor, N_c for limited thickness of clay (after Shield, 1955)

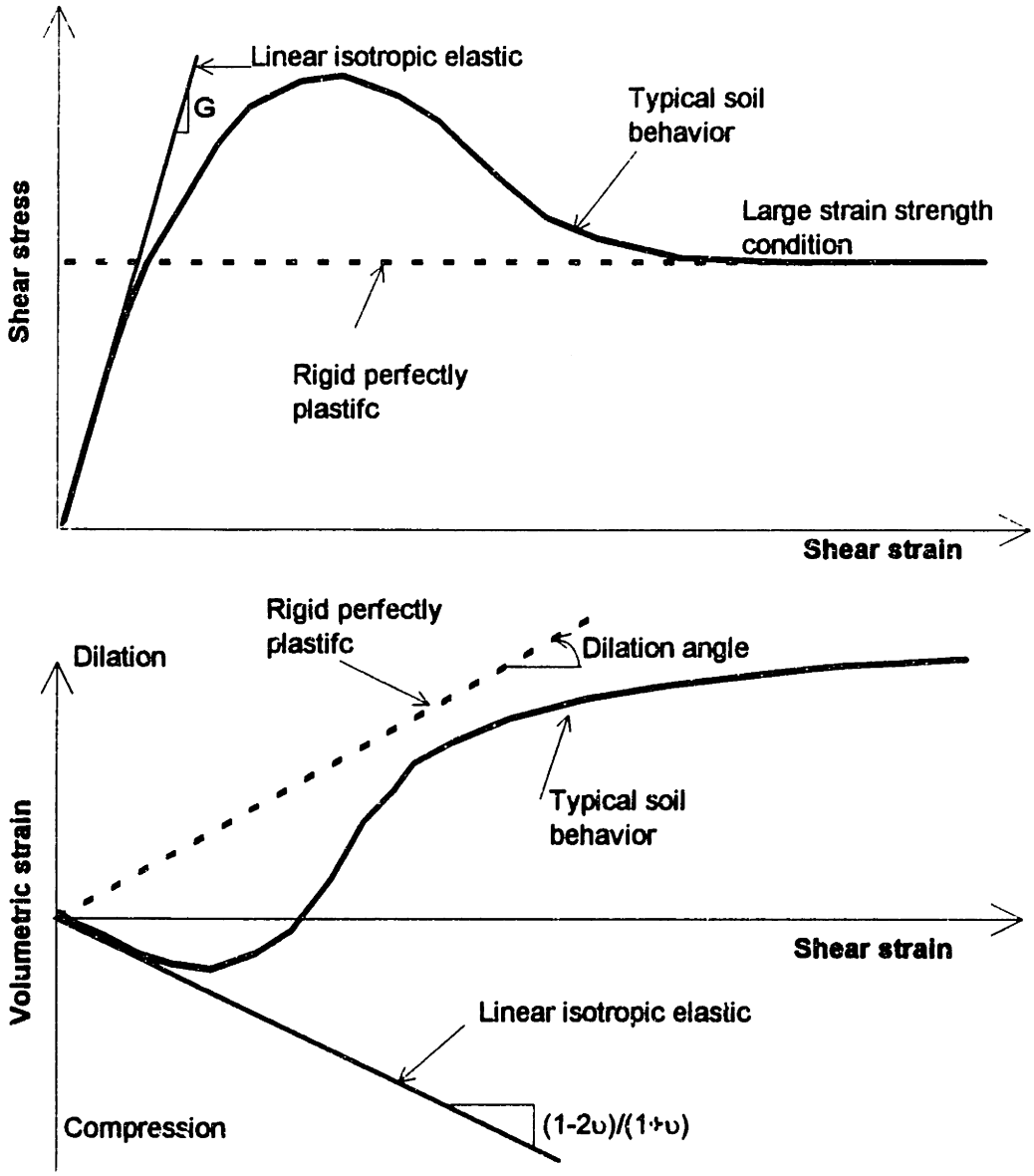

Fig. 2.1 Stress-strain and volumetric properties of soils

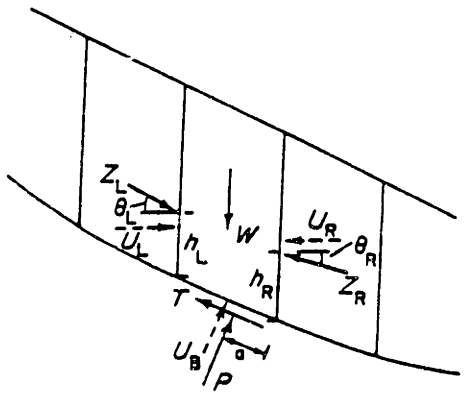

a) Forces on a typical slice

For slope divided into n slices

Equations available: total $3n$ (vertical, horizontal, and moment equilibrium)

Unknowns:	1	Safety factor F used to relate shear forces T to normal forces P
	n	Normal total forces P on base of slice (pore-water forces U_B are known)
	n	Positions a of forces P
	$n-1$	Interslice total forces Z (pore-water forces U_L, U_R are known)
	$n-1$	Inclinations θ of interslice forces
	$n-1$	Heights h of interslice forces
total	$5n-2$	

Thus $2n-2$ assumptions are required for the problem to be statically determinate.

Common assumptions:	n	Position of P taken as centre of slice
	$n-1$	Inclinations θ of interslice forces *or* heights h of line of thrust
total	$2n-1$	This implies that the problem is overspecified.

b) Equations and unknowns

Fig. 2.2 Summary of forces, equations and unknowns in method of slices (after Fredlund and Krahn, 1977)

ORDINARY METHOD OF SLICES

Failure is assumed to occur by rotation of a block of soil on a cylindrical slip surface centred on O. By examining moment equilibrium about O an expression for the factor of safety is obtained. It is assumed that the resultant of the interslice forces on each slice is parallel to its base.

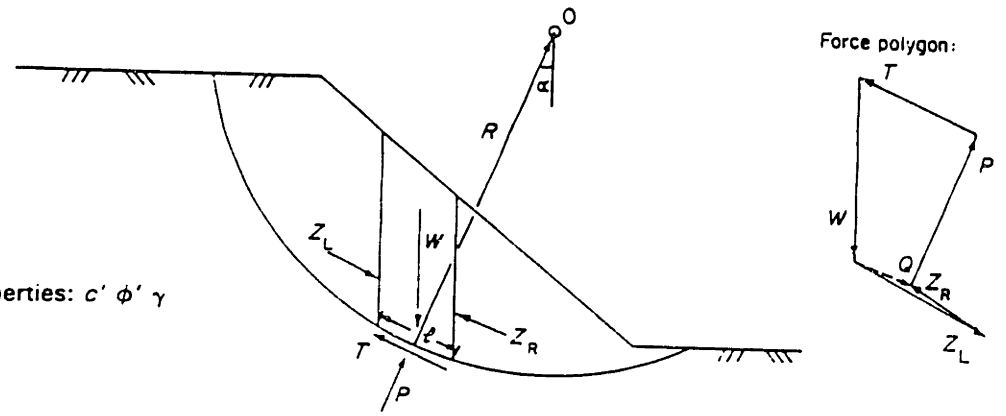

Soil properties: c' ϕ' γ

For slice shown: at base – total normal stress σ, shear stress τ, pore pressure u

Failure criterion: $s = c' + (\sigma - u)\tan\phi'$

Mobilized shear strength $\tau = s/F$ where F is factor of safety

Now $P = \sigma l$ $T = \tau l$ so $T = \frac{l}{F}(c'l + (P - ul)\tan\phi')$ (1)

Assume that the resultant of the interslice forces Q is parallel to base of slice.

Resolving normal to base of slice $P = W\cos\alpha$ (2)

Overall MOMENT Equilibrium about O: $\Sigma\, WR\sin\alpha = \Sigma\, TR$ (3)
(note that interslice forces are internal and their net moment is zero).

$$\text{so } \Sigma\, W\sin\alpha = \Sigma\, \frac{l}{F}(c'l + (P - ul)\tan\phi')$$

$$\text{hence } F_m = \frac{\Sigma(c'l + (P - ul)\tan\phi')}{\Sigma\, W\sin\alpha} \quad (4)$$

$$\text{substitute for } P\text{: } F_m = \frac{\Sigma(c'l + (W\cos\alpha - ul)\tan\phi')}{\Sigma W\sin\alpha} \quad (5)$$

This equation does not contain F on the right-hand side and so is easily solved by hand calculation. However the false assumption about the interslice forces results in errors which may be as large as 60% (Whitman and Bailey, 1967).

Fig. 2.3 Ordinary method of slices or Swedish method of analysis (after Fellenius, 1926, 1936)

GENERAL METHOD OF SLICES

Failure is assumed to occur by sliding of a block of soil on a non-circular (or circular) slip surface. By examining overall moment equilibrium about an assumed centre of rotation or overall force equilibrium, two expressions are obtained for factor of safety. An assumption must be made about the interslice forces.

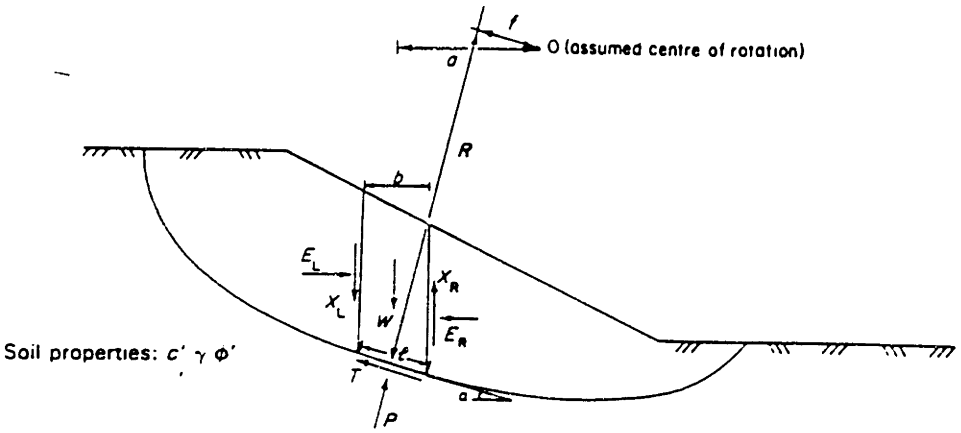

For slice shown: at base – total normal stress σ, shear stress τ, pore pressure u

Failure criterion: $s = c' + (\sigma - u)\tan\phi'$

Mobilized shear strength $\tau = s/F$ where F is factor of safety

Now $P = \sigma l \quad T = \tau l \quad$ so $T = \frac{1}{F}(c'l + (P - ul)\tan\phi')$ (1)

Resolve vertically: $P\cos\alpha + T\sin\alpha = W - (X_R - X_L)$ (2)

Rearranging and substituting for T gives

$$P = [W - (X_R - X_L) - \frac{1}{F}(c'l\sin\alpha - ul\tan\phi'\sin\alpha)]/m_\alpha \quad (3)$$

where $m_\alpha = \cos\alpha(1 + \tan\alpha \frac{\tan\phi'}{F})$

Resolve horizontally: $T\cos\alpha - P\sin\alpha + E_R - E_L = 0$

Rearranging and substituting for T gives

$$E_R - E_L = P\sin\alpha - \frac{1}{F}[c'l + (P - ul)\tan\phi']\cos\alpha \quad (4)$$

Overall MOMENT equilibrium (about O) : $\Sigma Wd = \Sigma TR + \Sigma Pf$ (5)

Rearranging and substituting for T gives

$$F_m = \frac{\Sigma[c'l + (P - ul)\tan\phi']R}{\Sigma(Wd - Pf)} \quad (6)$$

For circular slip surfaces $f = 0 \quad d = R\sin\alpha \quad R =$ constant

$$\text{so } F_m = \frac{\Sigma[c'l + (P - ul)\tan\phi']}{\Sigma W\sin\alpha} \quad (6a)$$

Fig. 2.4 continued on next page

Fig. 2.4 General method of slices (after Fredlund and Krahn, 1977)

continued

Overall FORCE equilibrium

In the absence of surface loading $\Sigma(E_R - E_L) = 0$ (7a)

$\Sigma(X_R - X_L) = 0$ (7b)

so from (4) $\Sigma(E_R - E_L) = \Sigma P \sin\alpha - \Sigma \frac{1}{F_f} (c'l + (P - ul) \tan\phi') \cos\alpha = 0$ (8)

$$\text{so } F_f = \frac{\Sigma (c'l + (P - ul) \tan\phi') \cos\alpha}{\Sigma P \sin\alpha} \quad (9)$$

In order to solve for F_m and F_f, P must be evaluated, and this requires evaluation of X_R, P_L the interslice shear forces. As the problem is indeterminate an assumption must be made. Some common assumptions are:

$X_R - X_L = 0$ Bishop (1955)

$\frac{X}{E}$ = constant Spencer (1967)

$\frac{X}{E} = \lambda f(x)$ Morgenstern and Price (1965)

In general $F_m = F_f$ and Bishop (1955) showed that F_m is much less sensitive to the assumption about interslice forces than F_f.

Fig. 2.4 General method of slices (after Fredlund and Krahn, 1977)

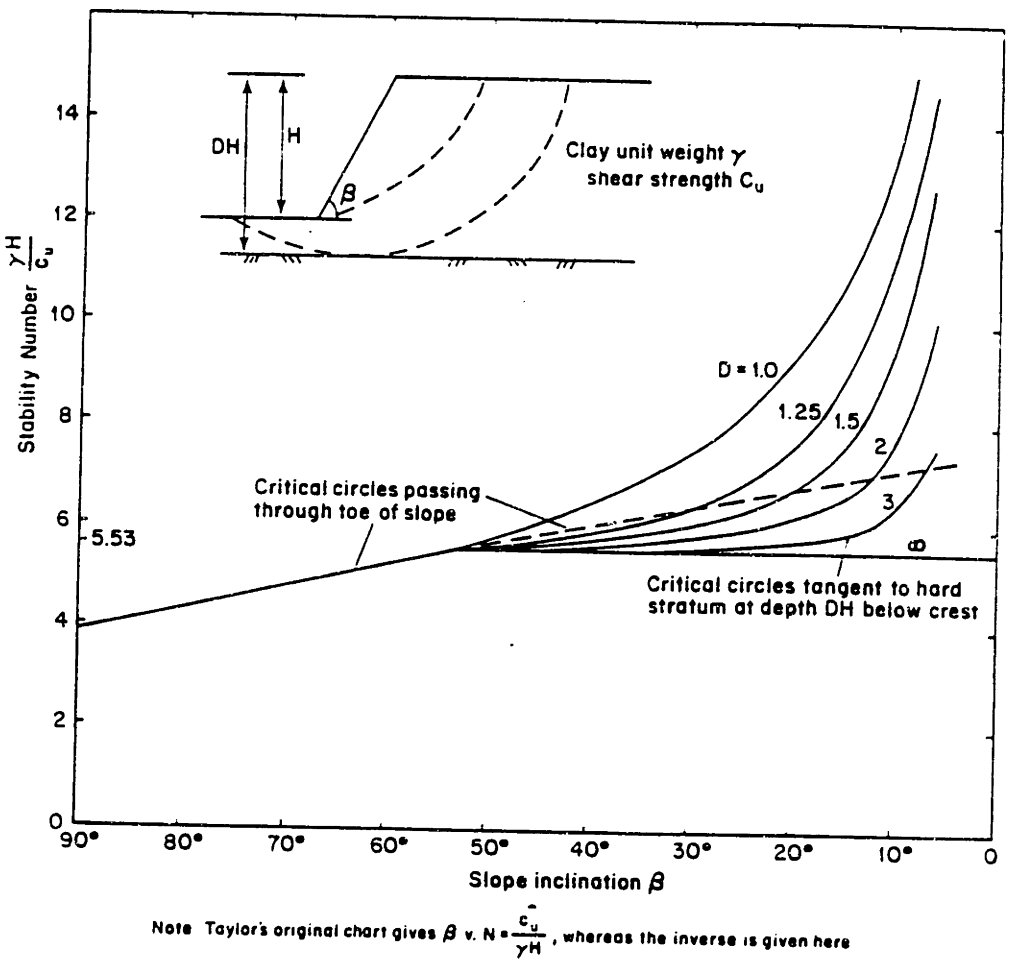

Fig. 2.5 Stability chart of Taylor (1948)

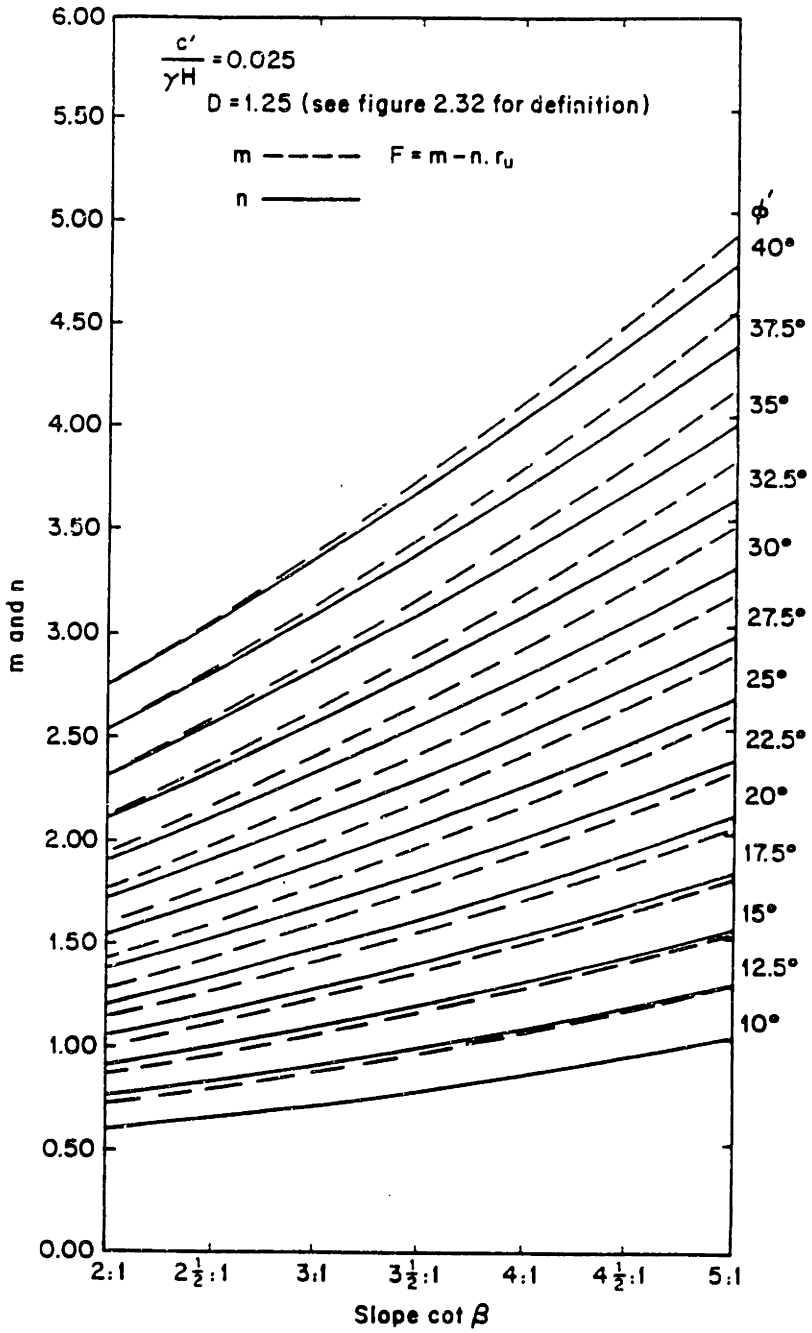

Fig. 2.6 Stability chart of Bishop and Morgenstern (1960)

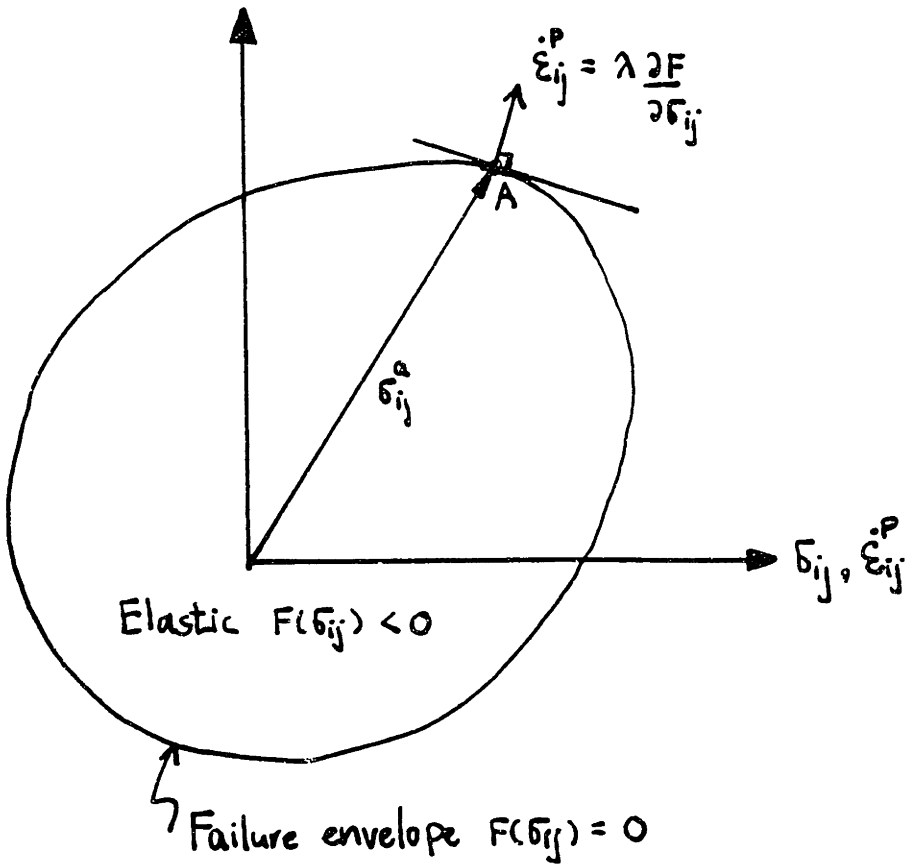

Fig. 2.7 Typical yield surface and concept of associated flow rule

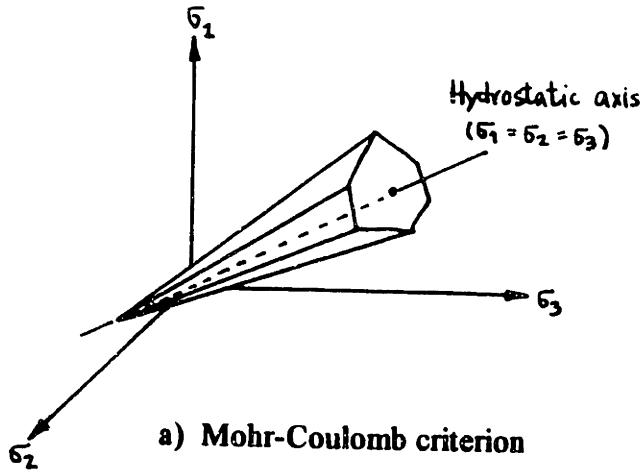

a) Mohr-Coulomb criterion

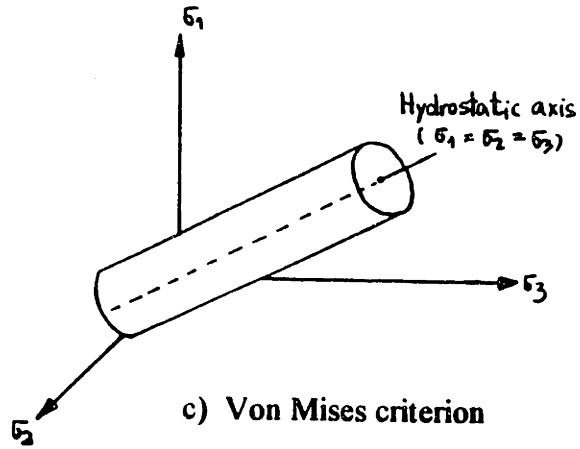

c) Von Mises criterion

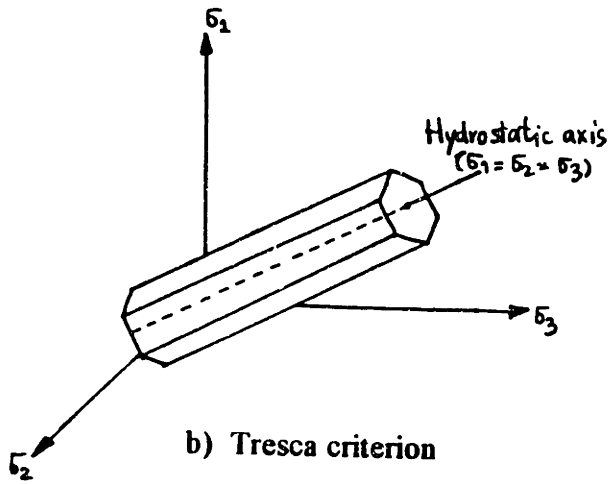

b) Tresca criterion

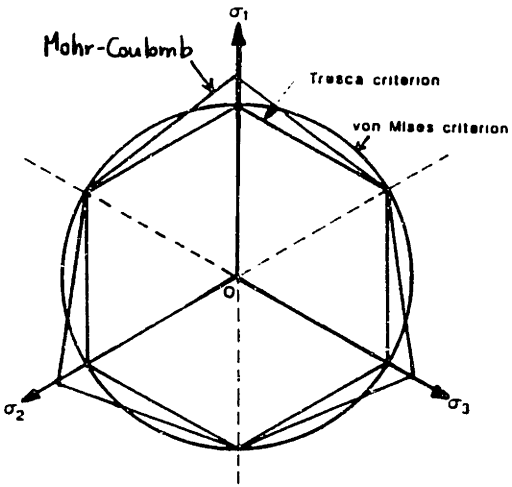

d) Section of yield surface by the π-plane

Fig. 2.8 Typical yield criterion in soil mechanics

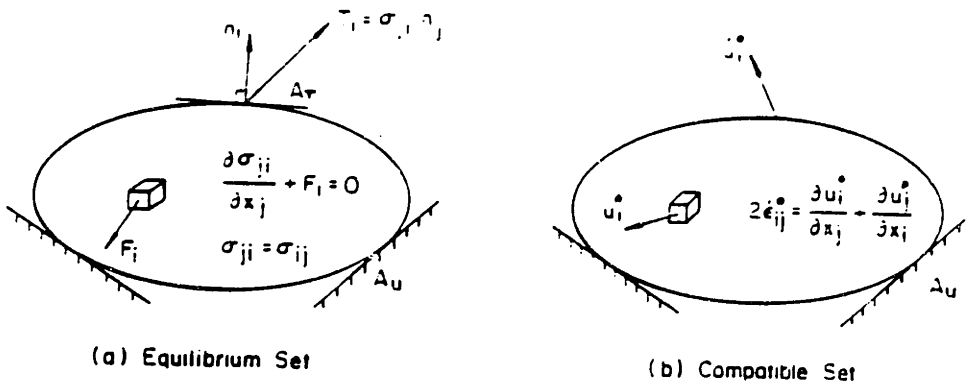

(a) Equilibrium Set (b) Compatible Set

Fig. 2.9 Two independent sets in the equation of virtual work (After Chen, 1975)

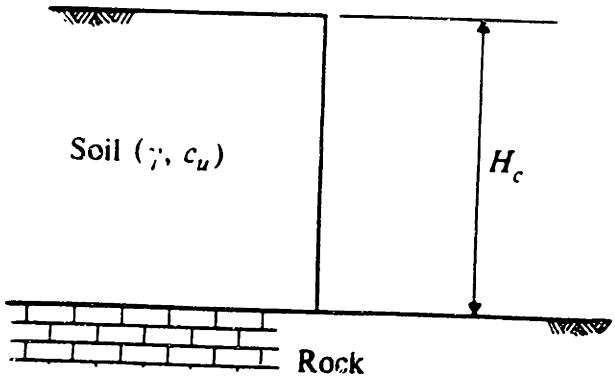

a) Geometry

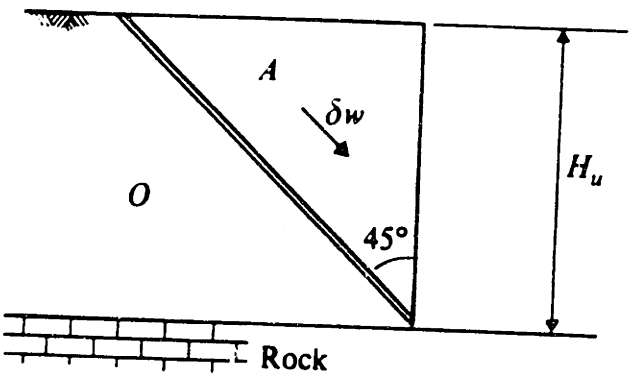

b) Assumed rigid block failure

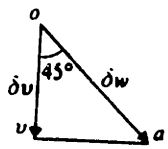

c) Velocity diagram (Hodograph)

Fig. 2.10 Upper bound calculation for a vertical cut slope for undrained loading (After Atkinson, 1981)

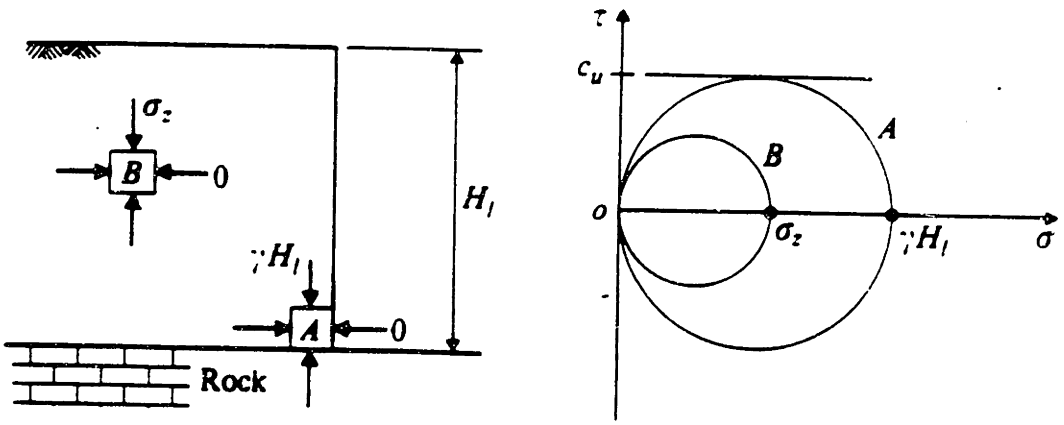

a) Geometry and Stress field

b) Mohr's Diagram

Fig. 2.11 Lower bound calculation for a vertical cut slope for undrained loading (After Atkinson, 1981)

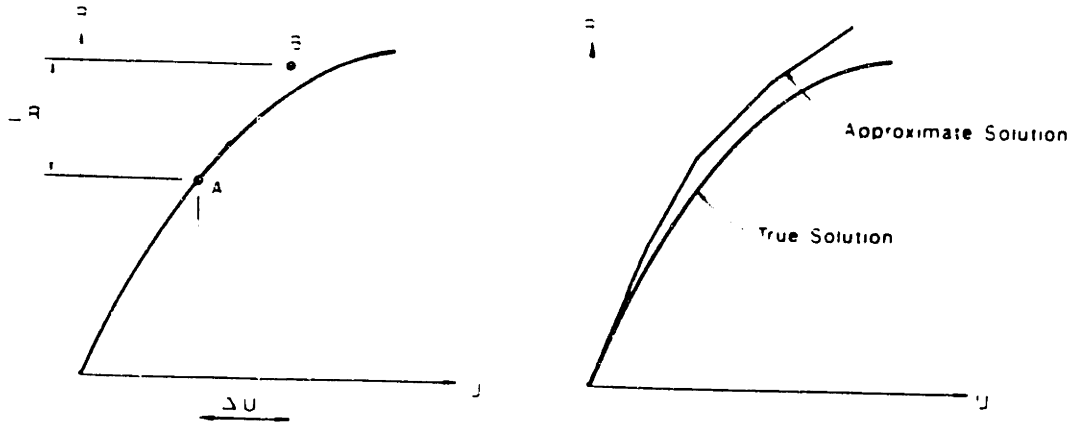

a) One Euler increment

b) Error build-up associated with Euler integration

Fig. 2.12 Euler integration scheme

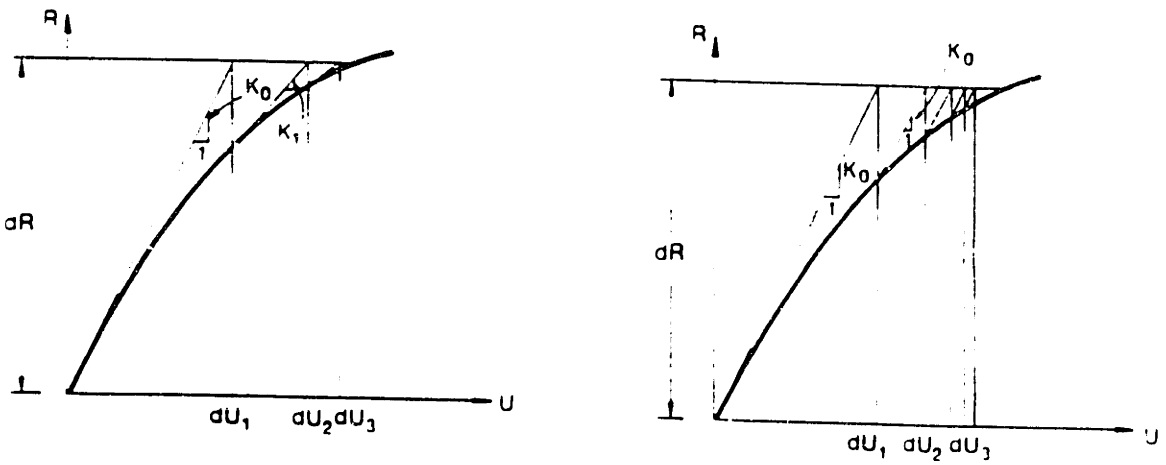

a) Newton-Raphson method

b) Modified Newton-Raphson method

Fig. 2.13 Iterative method of Newton-Raphson and modified Newton-Raphson

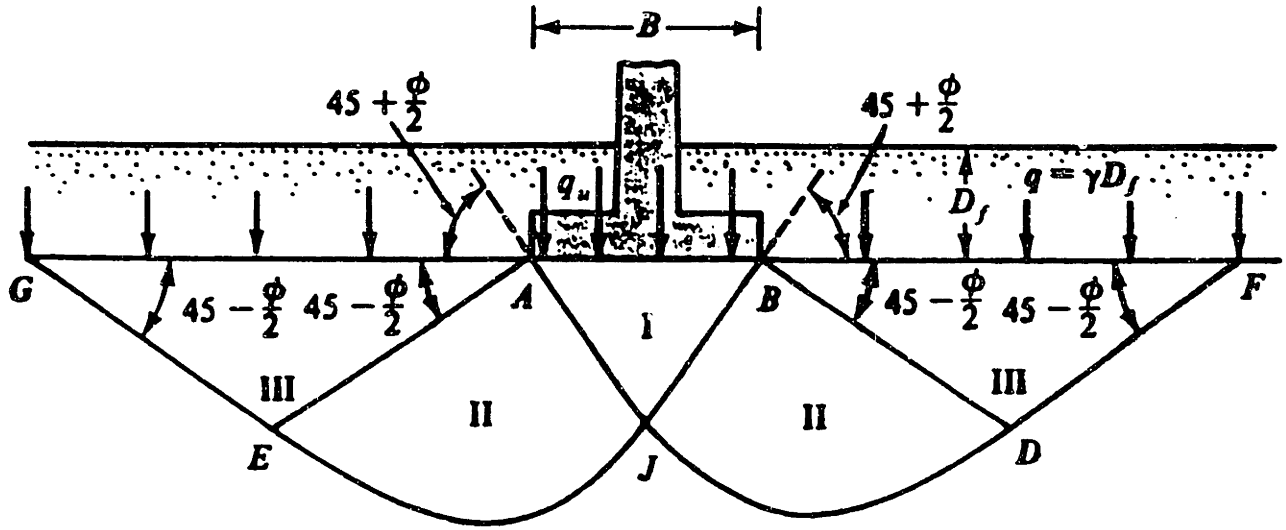

Fig. 2.14 Ultimate bearing capacity calculation according to Terzaghi (1943)

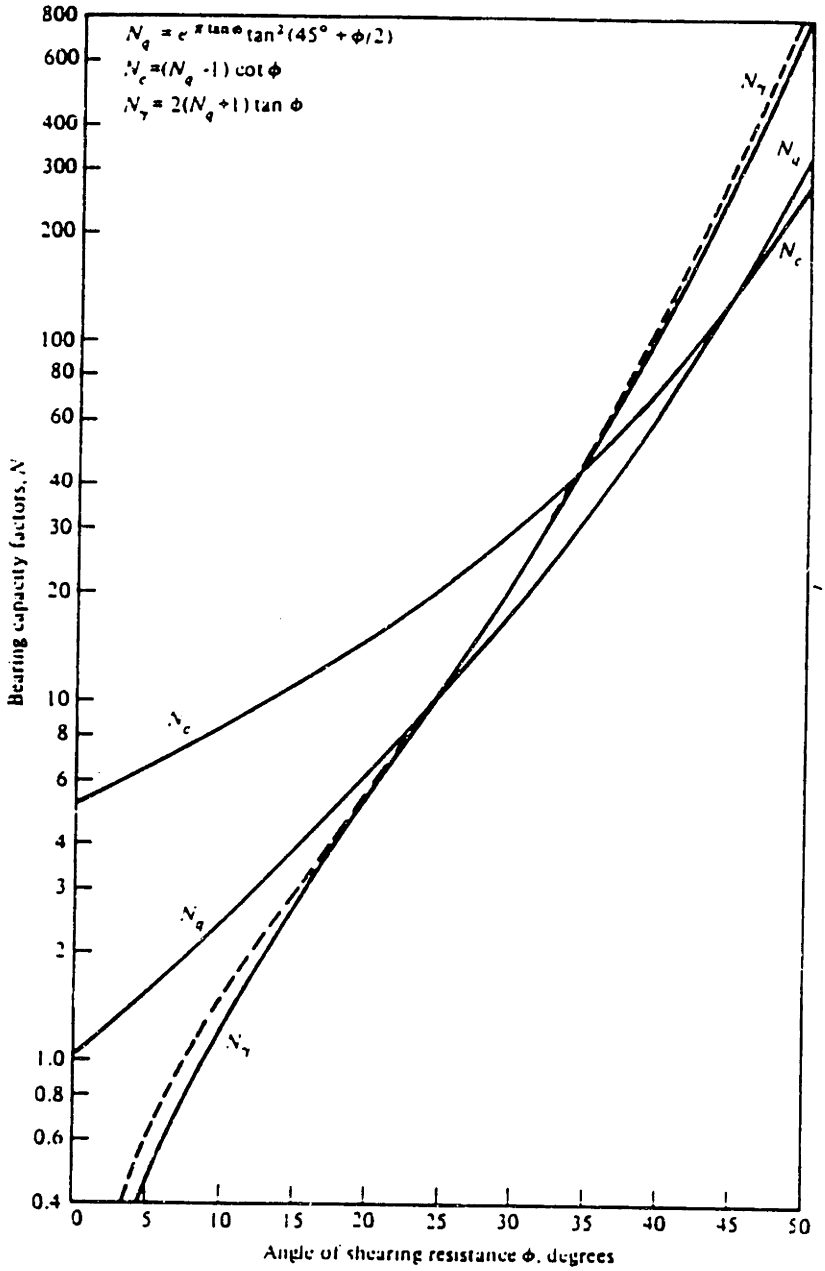

Fig. 2.15 Bearing capacity factors, N_c, N_q and N_γ

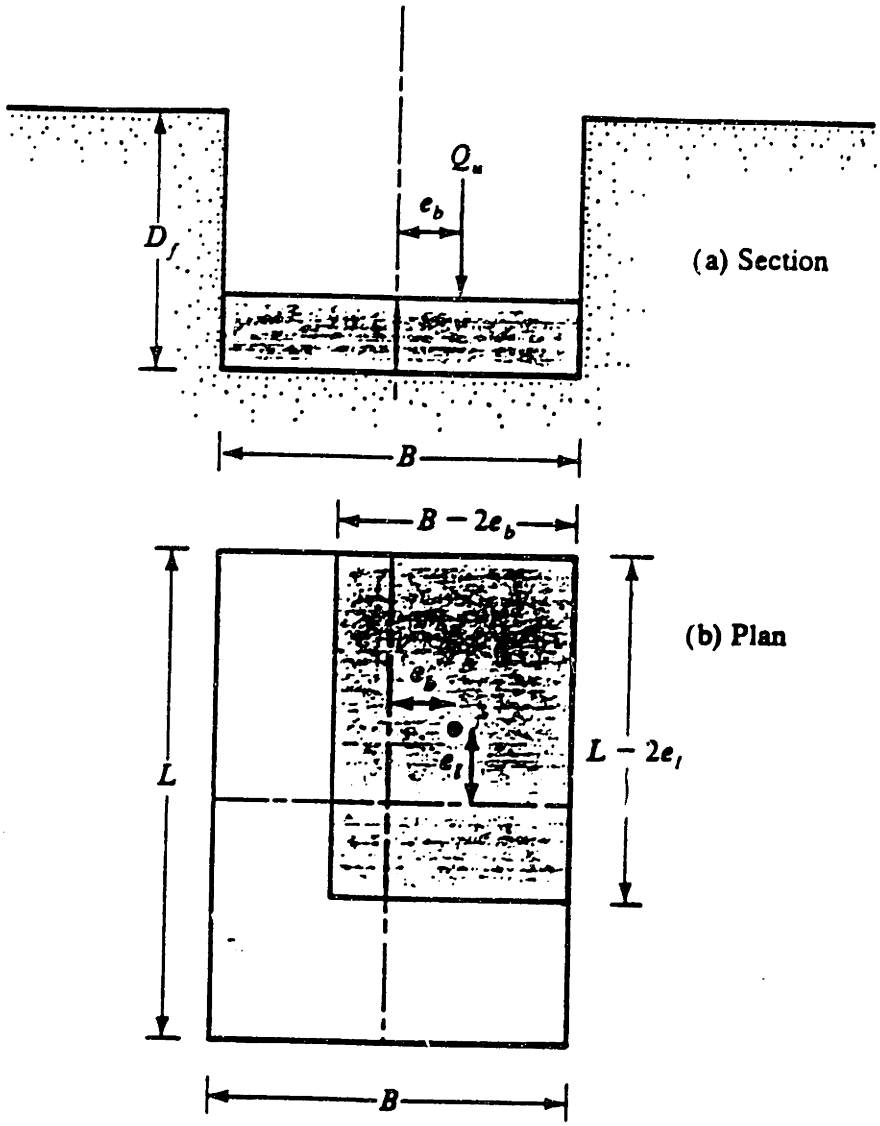

Fig. 2.16 Effective area concept according to Meyerhof (1953)

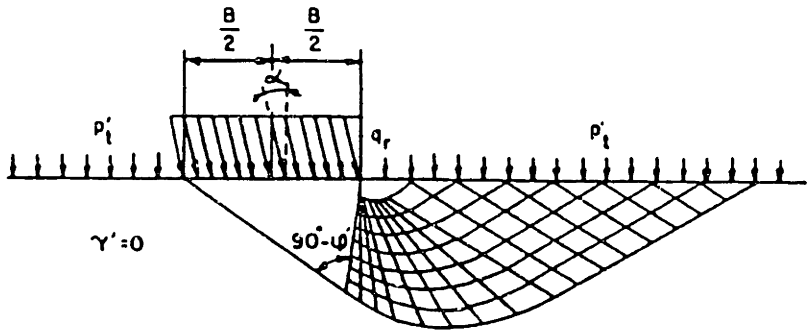

Fig. 2.17 Stress characteristics of a footing subjected to an inclined centric load, according to Hansen (1961)

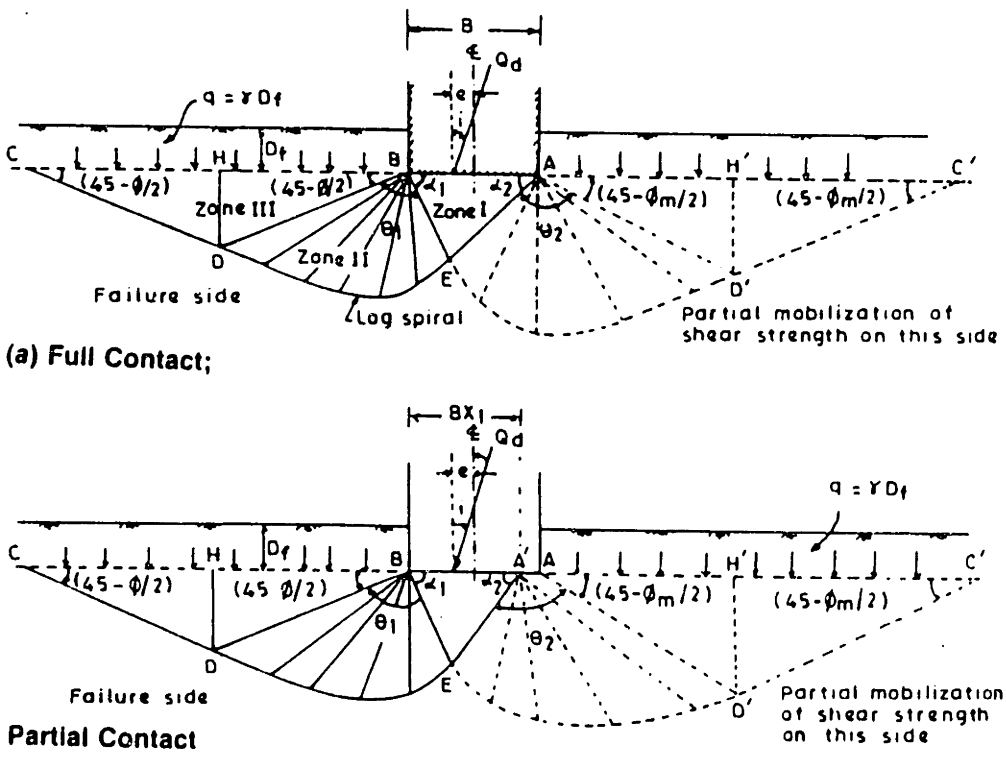

Fig. 2.18 Analyses of an inclined and eccentric load according to Saran and Agarwal (1991)

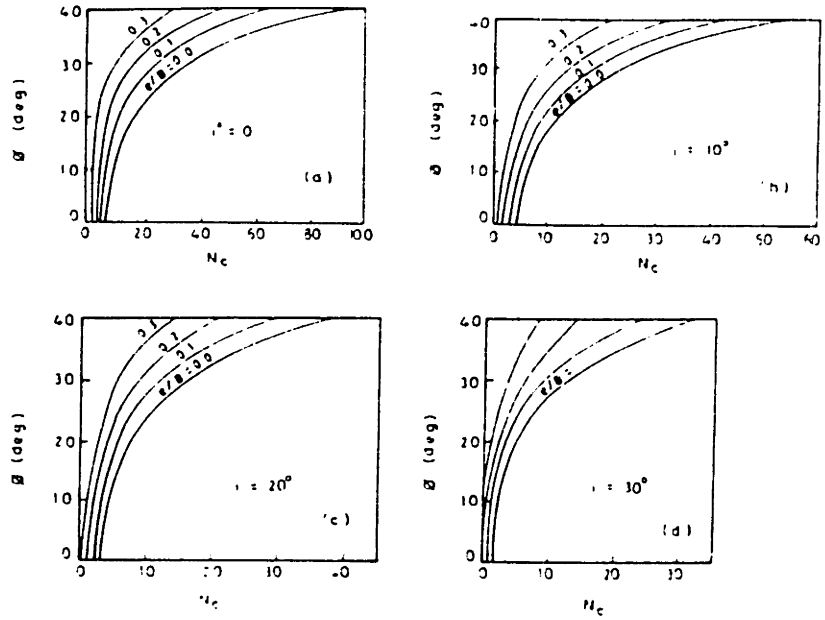

a) N_c versus ϕ

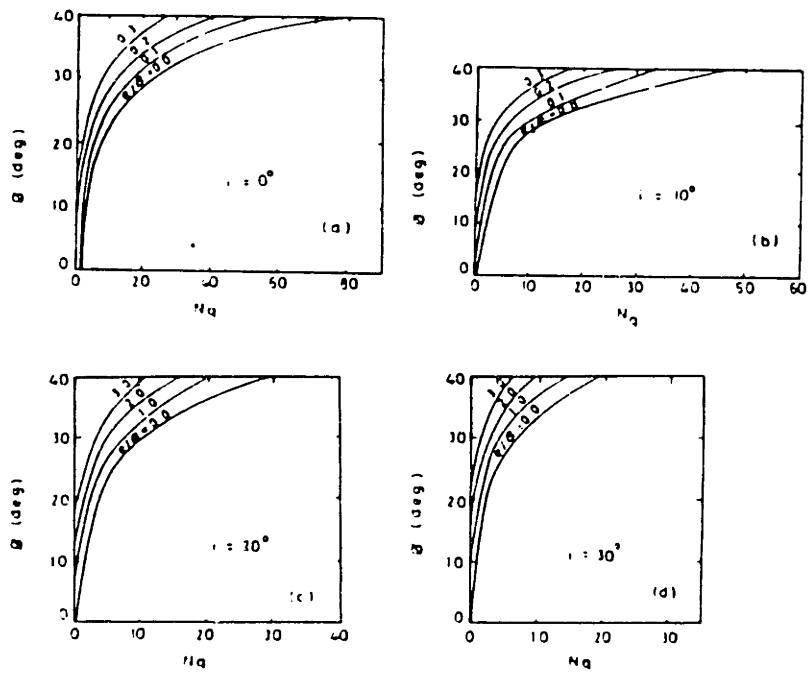

b) N_q versus ϕ

Fig. 2.19 Bearing capacity factors, N_c and N_q for an inclined and eccentric load, according to Saran and Agarwal (1991)

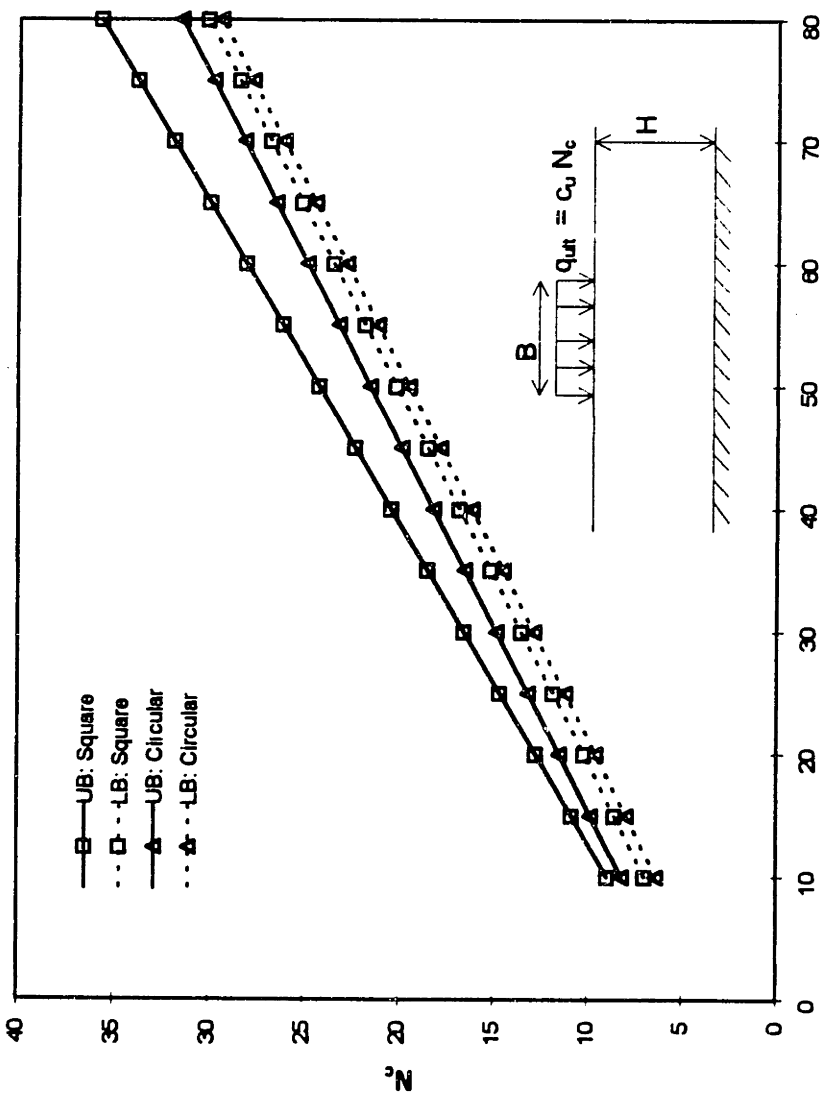

Fig. 2.20 Bearing capacity of a smooth rigid punch on thin layer of cohesive soil (after Shield, 1955)

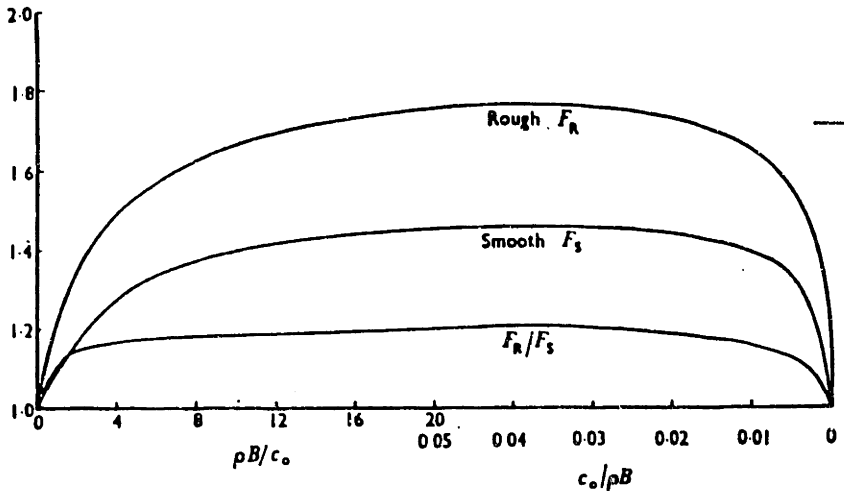

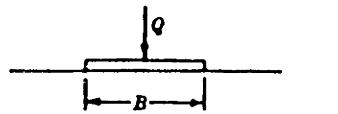

$$Q/B = F\left[(2+\pi)\,c_o + \rho B/4\right]$$

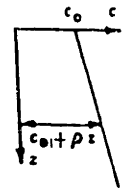

a) Linear increase in strength with depth

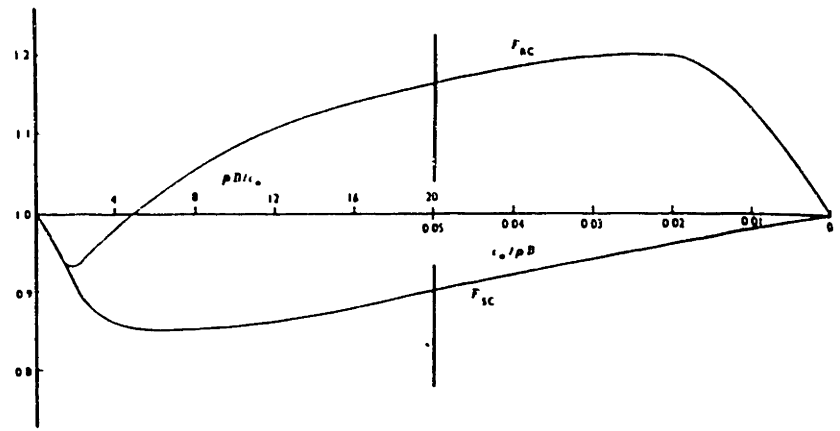

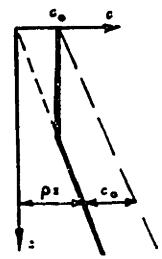

b) Clay with a crust layer

Fig. 2.21 Bearing capacity factors for strength inhomogenity
(After Davis and Booker, 1973)

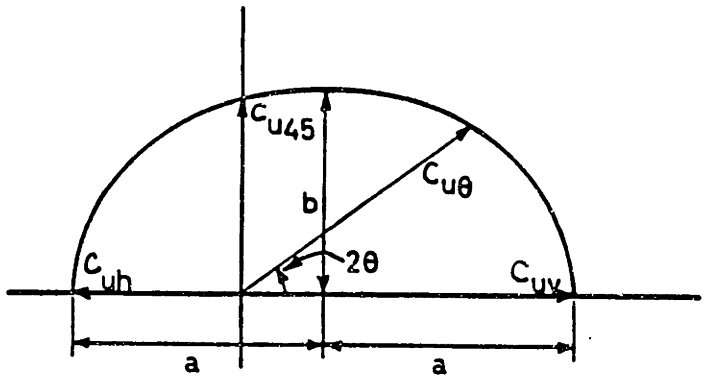

a) Anisotropic failure envelope

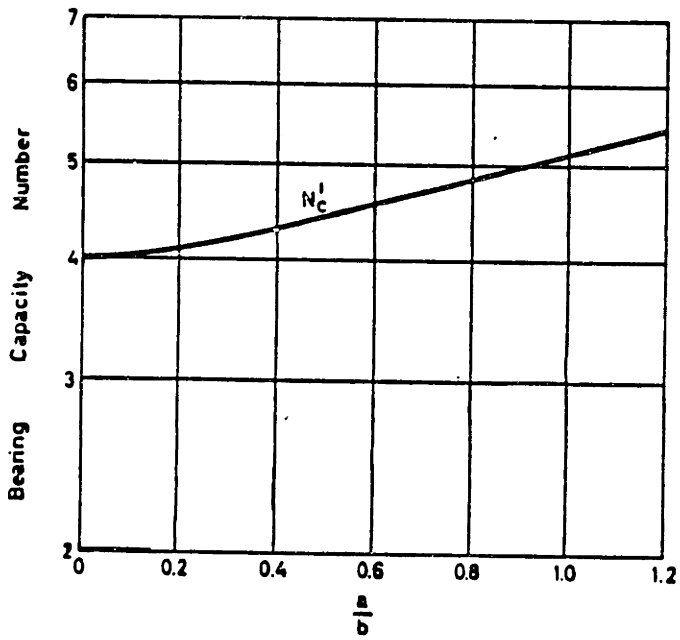

b) Bearing capacity, N'_c

Fig. 2.22 Bearing capacity of anisotropic cohesive soil (after Davis and Christian 1971)

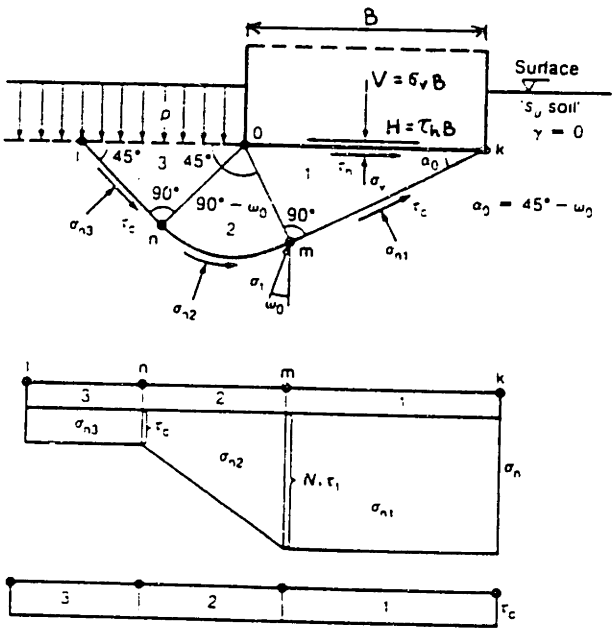

a) Failure wedges and stresses fields

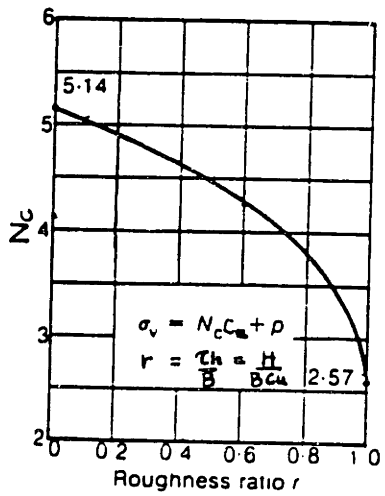

b) Bearing capacity factor, N_c

Fig. 2.23 Analyses of an inclined and eccentric load according to Janbu (1985)

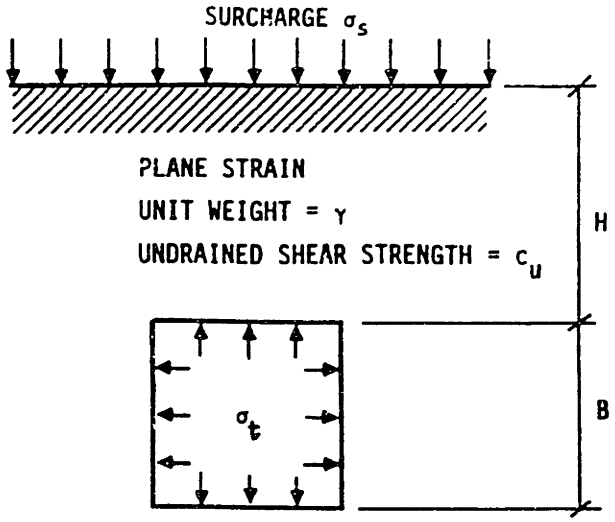

a) Geometry of square tunnel and loading

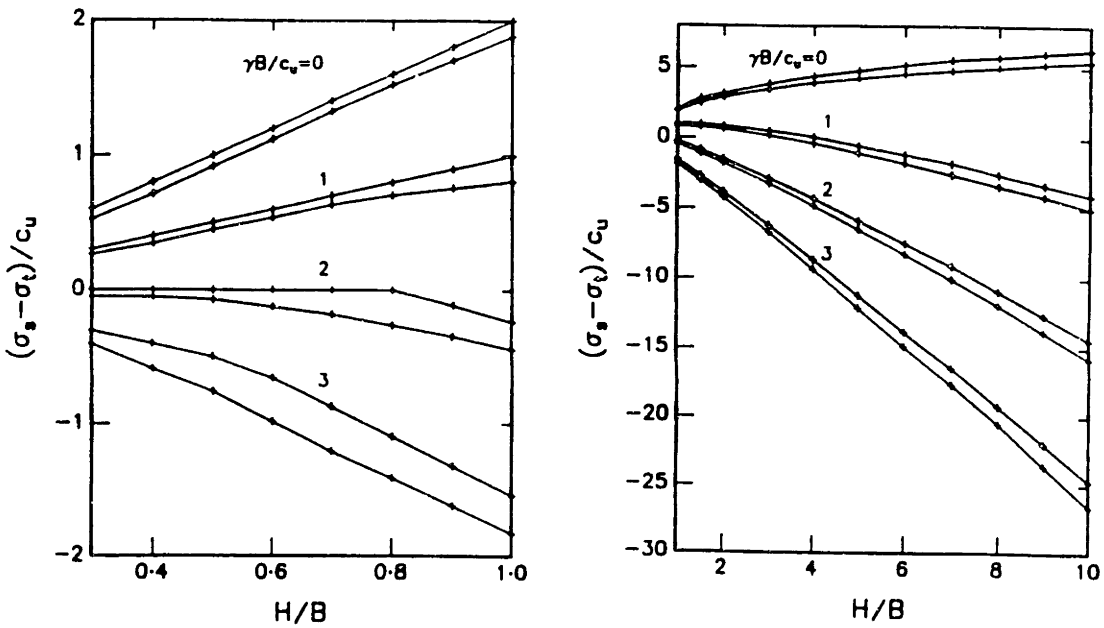

b) Stability factor

Fig. 2.24 Application of numerical limit analyses to undrained stability of square tunnel (after Sloan and Assadi, 1990)

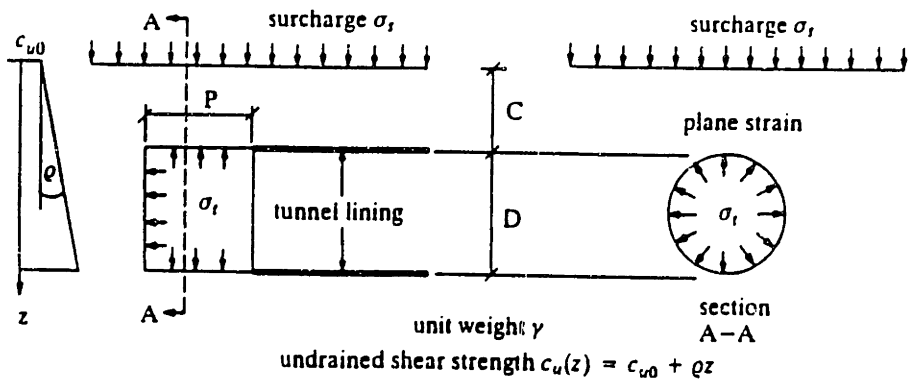

a) Geometry of circular tunnel and loading

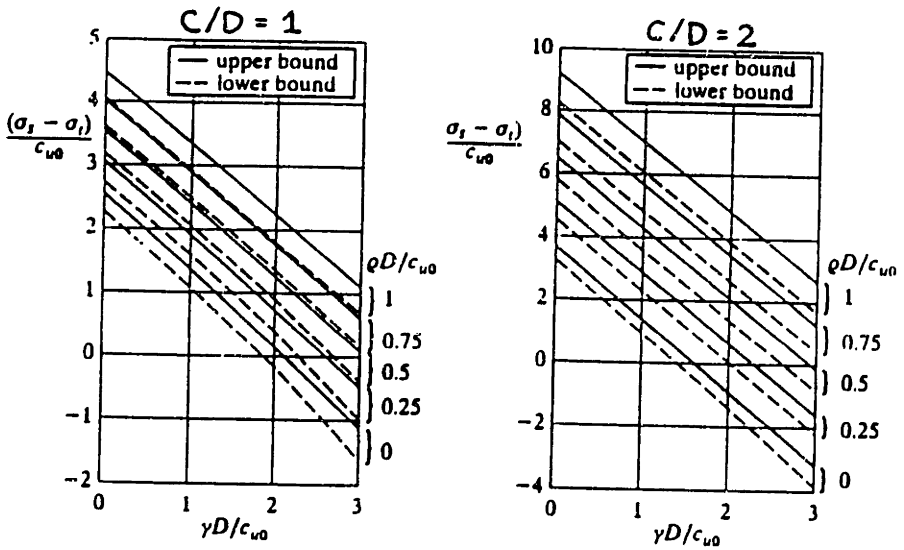

b) Stability factor

Fig. 2.25 Application of numerical limit analyses to undrained stability of circular tunnel (after Sloan and Assadi, 1993)

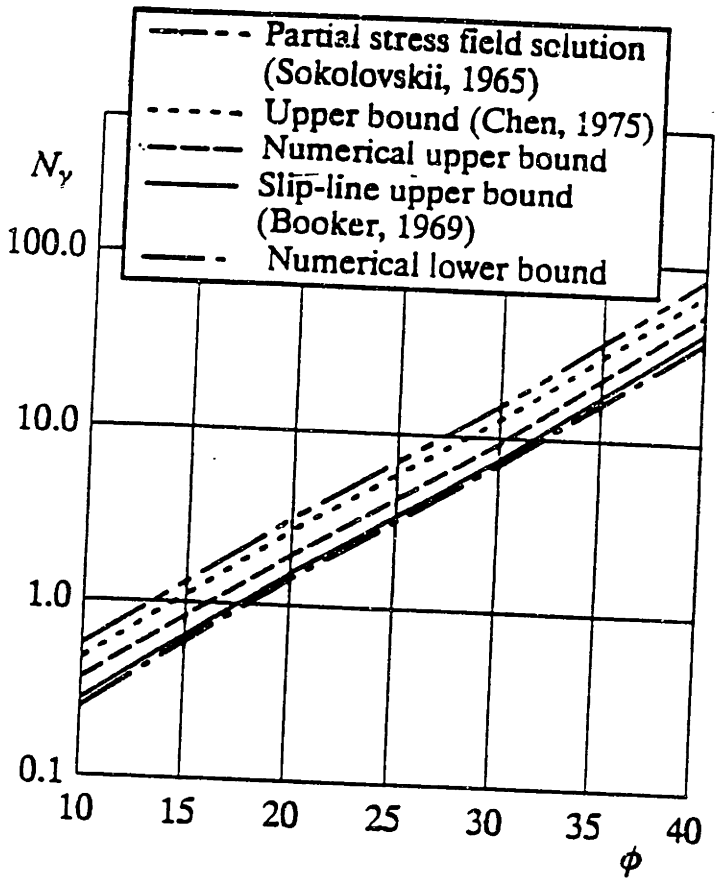

Fig. 2.26 Bearing capacity factor N_γ for a smooth footing on cohesionless soils (after Yu and Sloan, 1993)

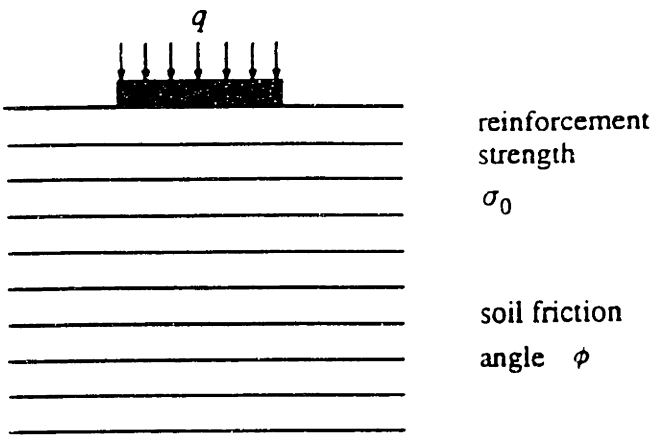

a) Geometry of a strip footing on cohesionless reinforced soil

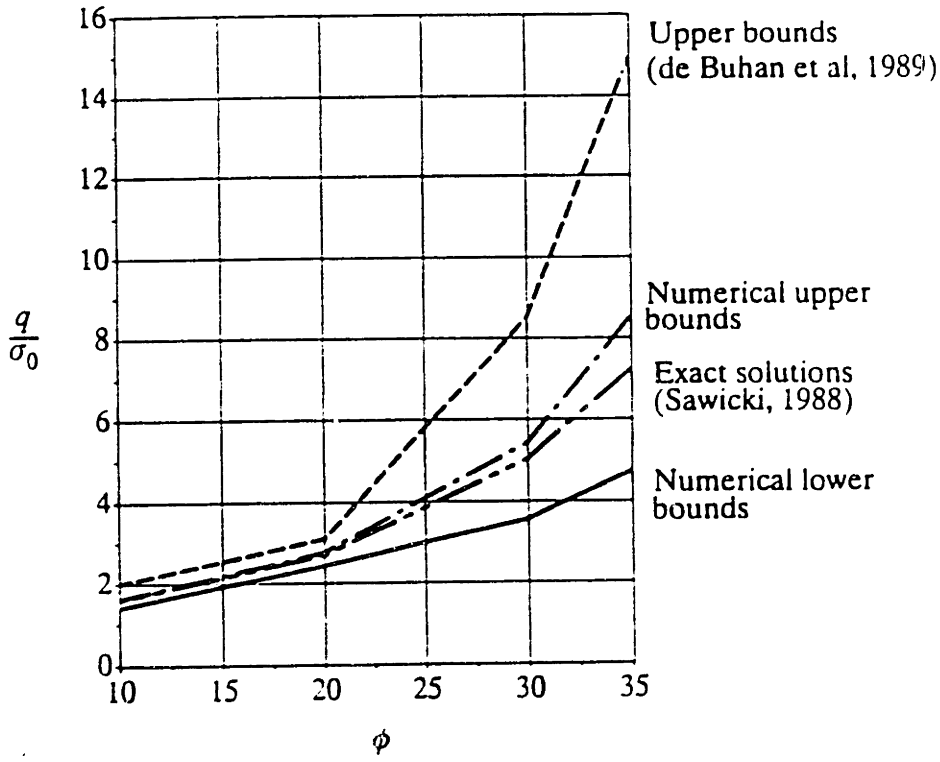

b) Normalized bearing capacity factor, q/σ_0

Fig. 2.27 Application of numerical limit analyses to a strip footing on cohesionless reinforced soil (after Yu and Sloan, 1994b)

3. Formulation of Limit Analysis Using Finite Elements and Linear Programming

3.1 Lower Bound Formulation

This section describes the formulation of the numerical lower bound method for plane strain problems, based on Sloan (1988a, 1988b) and Assadi and Sloan (1990). The main features of these formulations are: 1) the use of finite elements to discretize the continuum; 2) linearization of the Mohr-Coulomb yield criterion for cohesive-frictional materials; 3) the use of infinite extension elements, for modeling infinite half space conditions; and 4) the active set algorithm for solving the linear programming problem. The lower bound analysis is formulated as linear programming problem whose objective function is the maximization of the external load subjected to the constraints of a statically admissible stress field. The constraints include equilibrium equations, linearized yield criterion, and stress boundary conditions. The optimal stress field is obtained by means of the active set algorithm. Since this optimal stress field satisfies all of the requirements of the lower bound theorem, the external load associated with this optimal stress field provides a strict lower bound solution.

Formulation

3.1.1 Finite Element Discretization

For plane strain conditions, the soil mass is discretized into three types of finite element, 3-noded triangular element, 3-noded triangular extension element and, 4-noded rectangular extension element as shown in Figure 3.1. Each node of these elements is associated with three unknown stresses σ_x, σ_y, and τ_{xy} in the Cartesian (x-y) frame of reference. The stress components are assumed to vary linearly within each element according to:

$$\sigma_x = \sum_{i=1}^{3} N_i \sigma_{xi} \quad ; \qquad \sigma_y = \sum_{i=1}^{3} N_i \sigma_{yi} \quad ; \qquad \tau_{xy} = \sum_{i=1}^{3} N_i \tau_{xyi} \qquad (3.1a)$$

where

σ_{xi}, σ_{yi}, and τ_{xyi} ; i = 1, 2, 3 are the nodal stresses with respect to the Cartesian axis and N_i are linear shape functions[1] given by:

$$N_1 = [(x_2y_3 - x_3y_2) + y_{23}x + x_{32}y)]/2A \qquad (3.1b)$$
$$N_2 = [(x_3y_1 - x_1y_3) + y_{31}x + x_{13}y)]/2A$$
$$N_3 = [(x_1y_2 - x_2y_1) + y_{12}x + x_{21}y)]/2A$$

where

$$x_{32} = x_3 - x_2 \quad ; \quad y_{23} = y_2 - y_3 \qquad (3.1c)$$
$$x_{13} = x_1 - x_3 \quad ; \quad y_{31} = y_3 - y_1$$
$$x_{21} = x_2 - x_1 \quad ; \quad y_{12} = y_1 - y_2$$

and $2A = |(x_1-x_3)(y_2-y_3) - (x_3-x_2)(y_3-y_1)|$ is twice the area of the triangle.

Two types of extension elements (3-noded triangular and 4-noded rectangular elements) are necessary in order to obtain statically admissible solutions when dealing with an infinite half-space. The stresses for these two types of extension elements assume the same linear interpolations as the simple 3-noded triangle.

Statically admissible stress discontinuities are permitted at shared edges between adjacent elements, including those shared by adjacent extension elements. Stress discontinuities are modeled as each node is unique to a particular element. Therefore, it is possible that more than one node may share the same coordinate. Figure 3.2 illustrates the finite element mesh for these conditions which is completely different from the conventional finite element method, where each node is shared by the adjacent elements (and has one set of nodal degrees of freedom).

[1] The same shape functions are used in 3-noded constant strain triangular element in the standard displacement based finite element method (e.g. Zienkiewicz, 1970)

3.1.2 Element Equilibrium

The lower bound theorem states that stresses within the element must satisfy the static equilibrium equations given by:

$$\frac{\partial \sigma_x}{\partial x} + \frac{\partial \tau_{xy}}{\partial y} = 0 \qquad (3.2a)$$

$$\frac{\partial \sigma_y}{\partial y} + \frac{\partial \tau_{xy}}{\partial x} = \gamma$$

where γ is the unit weight of the soil

Figure 3.3a shows the sign convention used in the analyses which uses a right-handed Cartesian coordinate system, with tensile stress considered positive.

Differentiating equations 3.1a-3.1c and substituting into 3.2a gives rise to the equilibrium constraints on the nodal stresses as:

$$[A_{equi,\,3\text{-}n}]\{\sigma_{3\text{-}n}\} = \{b_{equi,\,3\text{-}n}\} \qquad (3.2b)$$

where

$$[A_{equi,\,3\text{-}n}] = \frac{1}{2A^e}\begin{bmatrix} y_{23} & 0 & x_{23} & y_{31} & 0 & x_{31} & y_{12} & 0 & x_{12} \\ 0 & x_{23} & y_{23} & 0 & x_{31} & y_{31} & 0 & x_{12} & y_{12} \end{bmatrix}$$

$$\{\sigma_{3\text{-}n}\}^T = \begin{bmatrix} \sigma^e_{x1} & \sigma^e_{y1} & \tau^e_{xy1} & \sigma^e_{x2} & \sigma^e_{y2} & \tau^e_{xy2} & \sigma^e_{xe} & \sigma^e_{y3} & \tau^e_{xy3} \end{bmatrix}$$

$\{b_{equi,\,3\text{-}n}\}^T = \{0 \;\; \gamma\}$; A^e = the area of the element

Equation 3.2b applies for all element types. However, additional constraints are necessary for the 4-noded triangular extension element, as the stresses at the 4th node (Figure 3.1c) must follow the linear expansion of the other three nodes. This leads to the following constraints for node-4:

$$\sigma_{x4} = \sigma_{x1} - \sigma_{x2} + \sigma_{x3} \qquad (3.2c)$$

$$\sigma_{y4} = \sigma_{y1} - \sigma_{y2} + \sigma_{y3}$$

$$\tau_{xy4} = \tau_{xy1} - \tau_{xy2} + \sigma_{xy3}$$

This equation is proved in Appendix C. This constraint may be rewritten in matrix form as:

$$[A_{equi,\ 4\text{-}n}]\{\sigma_{4-n}\} = \{b_{equi,\ 4\text{-}n}\} \qquad (3.2d)$$

where

$$[A_{equi,\ 4\text{-}n}] = \begin{bmatrix} I & -I & I & -I \end{bmatrix};\ I = \begin{bmatrix} 1 & 0 & 0 \\ 0 & 1 & 0 \\ 0 & 0 & 1 \end{bmatrix}$$

$$\{\sigma_{4-n}\}^T = \begin{bmatrix} \sigma^e_{x1} & \sigma^e_{y1} & \tau^e_{xy1} & \sigma^e_{x2} & \sigma^e_{y2} & \tau^e_{xy2} & \sigma^e_{xe} & \sigma^e_{y3} & \tau^e_{xy3} & \sigma^e_{x4} & \sigma^e_{y4} & \tau^e_{xy4} \end{bmatrix}$$

$$\{b_{equi,\ 3\text{-}n}\}^T = \{\ 0 \quad 0 \quad 0\ \}$$

3.1.3 Equilibrium along Stress Discontinuities

Figure 3.3b shows the stress discontinuities at the edges of adjacent triangles defined by the nodal pairs (1,2) and (3,4). For a statically admissible stress field, the shear and normal stress (τ, σ_n) must be equal at all points along the discontinuity. Since the stresses vary linearly along each element edge, this condition is satisfied by enforcing constraints at both ends of the discontinuity:

At node pairs (1,2) $\quad \sigma_{n1} = \sigma_{n2}\ ;\ \tau_1 = \tau_2 \qquad (3.3a)$

At node pairs (3,4) $\quad \sigma_{n3} = \sigma_{n4}\ ;\ \tau_3 = \tau_4$

Referring to Figure 3.3b, the normal and shear stresses acting on a plane inclined at an angle θ to the x-axis (defined positive in an anticlockwise direction) are given by:

$$\sigma_n = \sin^2\theta\ \sigma_x + \cos^2\theta\ \sigma_y - \sin 2\theta\ \tau_{xy} \qquad (3.3b)$$

$$\tau = -\sin\theta\cos\theta\ \sigma_x + \sin\theta\cos\theta\ \sigma_y + \cos 2\theta\ \tau_{xy}$$

Substituting equation 3.3b into 3.3a generates a matrix in the form:

$$[A_{dis}]\{\sigma_{dis}\} = \{b_{dis}\} \qquad (3.3c)$$

where

$$[A_{dis}] = \begin{bmatrix} T & -T & 0 & 0 \\ 0 & 0 & T & -T \end{bmatrix}$$

$$[T] = \begin{bmatrix} \sin^2\theta_d & \cos^2\theta_d & -\sin 2\theta_d \\ -\frac{1}{2}\sin 2\theta_d & \frac{1}{2}\sin 2\theta_d & \cos 2\theta_d \end{bmatrix}$$

$$\{\sigma_{dis}\}^T = \begin{bmatrix} \sigma^a_{x1} & \sigma^a_{y1} & \tau^a_{xy1} & \sigma^b_{x2} & \sigma^b_{y2} & \tau^b_{xy2} & \sigma^a_{xe} & \sigma^a_{y3} & \tau^a_{xy3} & \sigma^b_{x4} & \sigma^b_{y4} & \tau^b_{xy4} \end{bmatrix}$$

$$\{b_{dis}\}^T = \{0 \quad 0 \quad 0 \quad 0\}$$

where θ_d is the orientation of the discontinuity between two adjacent elements

3.1.4 Stress Boundary Conditions

To be statically admissible, the stress field must satisfy the prescribed stress boundary conditions according to the lower bound theorem. In most soil mechanics problems, stress boundary conditions are specified in terms of normal and shear stress as:

$$\sigma_n = q = \text{constant} \qquad (3.4a)$$

$$\tau = t = \text{constant}$$

Both normal stress and shear stress must satisfy equation 3.4a everywhere along the boundary edge of a element. In Figure 3.4, nodes 1 and 2 define the boundary edge. The prescribed normal and shear stresses at these nodes are equal to (q_1,t_1) and (q_2,t_2). Since the stresses vary linearly along the edge of each element, these specified stress boundary conditions are satisfied everywhere along the boundary edge by enforcing constraints at both node 1 and node 2 as:

At node 1 $\qquad \sigma^e_{n1} = q_1 \; ; \; \tau^e_{n1} = t_1 \qquad (3.4b)$

At node 2 $\qquad \sigma^e_{n2} = q_2 \; ; \; \tau^e_{n2} = t_2$

Substituting the stress transformation equations 3.3b to 3.4b, the stress boundary conditions may be written in matrix form as:

$$[A_{bound}]\{\sigma_{bound}\} = \{b_{bound}\} \qquad (3.4c)$$

where

$$[A_{bound}] = \begin{bmatrix} T & 0 \\ 0 & T \end{bmatrix}$$

$$[T] = \begin{bmatrix} \sin^2\theta_d & \cos^2\theta_d & -\sin 2\theta_d \\ -\frac{1}{2}\sin 2\theta_d & \frac{1}{2}\sin 2\theta_d & \cos 2\theta_d \end{bmatrix}$$

$$\{\sigma_{dis}\}^T = \begin{bmatrix} \sigma^e_{x1} & \sigma^e_{y1} & \tau^e_{xy1} & \sigma^e_{x2} & \sigma^e_{y2} & \tau^e_{xy2} \end{bmatrix}$$

$$\{b_{bound}\}^T = \{\, q_1 \;\; t_1 \;\; q_2 \;\; t_2 \,\}$$

It should be noted that equations 3.3a and 3.4b are applied to every element in the mesh, including those that are extension elements.

For problems where the loading is caused by a flexible structure, the normal surface traction is uniform. If nodes 1, 2, ..., k define the loading edge of flexible structure, the constraints required at these nodes are:

$$\sigma_{n1} = \sigma_{n2} = \sigma_{n3} = \ldots . \sigma_{nk} \qquad (3.4d)$$

For problems where the base is rigid, the normal stresses in the lower bound formulation are unrestricted[1].

3.1.5 Yield Criterion

For plane strain conditions with positive stresses in tension (Figure 3.3b), the Mohr-Coulomb yield criterion can be expressed as:

$$F = (\sigma_x - \sigma_y)^2 + (2\tau_{xy})^2 - (2c\cos\phi - (\sigma_x + \sigma_y)\sin\phi)^2 = 0 \qquad (3.5a)$$

where

c, ϕ = cohesion intercept and angle of internal friction of soil, respectively.

[1] This case corresponds to a displacement boundary condition and appears as a constraint in the upper bound formulation; section 3.2.7.1

According to the lower bound theorem, the stress field must not violate the yield criterion. That means $F \leq 0$ throughout each triangle. Since the lower bound method is formulated as a linear programming problem, equation 3.5a (a single non-linear function of the unknown stresses, σ_x, σ_y, τ_{xy}) must be linearized. In order to ensure that the solution obtained is a strict lower bound on the true collapse load, the actual Mohr-Coulomb yield surface must circumscribe the linearized yield surface. The linearization is accomplished by transforming the Mohr-Coulomb criterion using the following variables:

$$X = \sigma_x - \sigma_y \; ; \; Y = 2\tau_{xy} \; ; R = 2c\cos\phi - (\sigma_x + \sigma_y)\sin\phi \qquad (3.5b)$$

The Mohr-Coulomb yield criterion then becomes:

$$X^2 + Y^2 = R^2 \qquad (3.5c)$$

Equation 3.5c represents a circle in X, Y stress space, with radius, R as shown in Figure 3.5. The transformed yield surface can then be approximated by an interior polygon with p sides and p vertices (where p is an integer numbers). The X and Y coordinates of the k^{th} and $(k+1)^{th}$ vertices are given by:

$$X_k = R\cos\{\pi(2k-1)/p\} \; ; \; Y_k = R\sin\{\pi(2k-1)/p\} \qquad (3.5d)$$

$$X_{k+1} = R\cos\{\pi(2k+1)/p\} \; ; \; Y_{k+1} = R\sin\{\pi(2k+1)/p\}$$

Consider a stress state with coordinates X and Y. The lower bound theorem states that this stress point must lie inside or on the yield surface. With the convexity of the linearized yield criterion, this condition is satisfied if:

$$(X_{k+1} - X)(Y_k - Y) - (X_k - X)(Y_{k+1} - Y) \leq 0 \; ; \; k = 1,2 \ldots,p \qquad (3.5e)$$

Substituting equations 3.5b and 3.5d into 3.5e generates a set of inequality constraints:

$$F_k = A_k\sigma_x + B_k\sigma_y + C_k\tau_{xy} - D \leq 0 \; ; \; k = 1,2 \ldots,p \qquad (3.5f)$$

where

$$A_k = \cos(2\pi k/p) + \sin\phi\cos(\pi/p); \; B_k = \sin\phi\cos(\pi/p) - \cos(2\pi k/p) \qquad (3.5g)$$

$$C_k = 2\sin(2\pi k/p); \qquad D = 2c\cos\phi\cos(\pi/p)$$

It should be noted that F_k denotes the value of the k^{th} side of the linearized Mohr-Coulomb yield criterion.

Since the lower bound method is formulated as a linear programming problem, the soil cohesion can vary linearly throughout each triangular element according to:

$$c = \sum_{i=1}^{3} N_i c_i \qquad (3.5h)$$

where

N_i are the linear shape functions given by equation 3.1b

c_i is the cohesion at node i.

However, the friction angle, ϕ must be constant throughout each triangle. Since the parameter D in equation 3.5g is a function of the soil cohesion, it follows from equation 3.5h that the parameter D is also a linear function of x and y as:

$$D = \sum_{i=1}^{3} N_i D_i \qquad (3.5i)$$

where $D_i = 2c_i \cos\phi \cos(\pi/p)$

Substituting equations 3.1a and 3.5i into equation 3.5f leads to the linearized yield criterion for each triangular element:

$$F_k = \sum_{i=1}^{3} N_i (A_k \sigma_{xi} + B_k \sigma_{yi} + C_k \tau_{xyi}) - \sum_{i=1}^{3} N_i D_i \le 0 \qquad (3.5j)$$

where k = 1, 2, ..., p; i = 1, 2, 3

Equation 3.5j can be rearranged as:

$$F_k = \sum_{i=1}^{3} N_i (A_k \sigma_{xi} + B_k \sigma_{yi} + C_k \tau_{xyi} - D_i) \le 0 \qquad (3.5k)$$

where k = 1, 2, ..., p; i = 1, 2, 3

and thus

$$F_k = N_1 F_{k1} + N_2 F_{k2} + N_3 F_{k3} = \sum_{i=1}^{3} N_i F_{ki} \le 0 \qquad (3.5m)$$

where $F_{ki} = A_k \sigma_{xi} + B_k \sigma_{yi} + C_k \tau_{xyi} - D_i$; k = 1, 2,..., p ; i = 1, 2, 3

3.1.5.1 Required Constraints for the 3-Noded Triangular Element

Figure 3.6 shows the geometric representation of the linear shape functions for the 3-noded triangular element. It is obvious that they always lie within the range $0 \leq N_i \leq 1$, and thus, are non-negative. Therefore, in order to satisfy equation 3.5m throughout the element, it is sufficient to enforce the constraint at each node i:

$$F_{ki} \leq 0; \quad k=1, 2,..., p ; i = 1, 2, 3 \qquad (3.5n)$$

Thus, at each node i, the linearized yield criterion gives rise to p inequality constraints of the matrix form as:

$$[A_{yield,\ 3\text{-}n}]\{\sigma^i\} \leq \{b_{yield}\}; \quad i = 1, 2, 3 \qquad (3.5o)$$

where

$$[A_{yield,\ 3\text{-}n}] = \begin{bmatrix} A_1 & B_1 & C_1 \\ A_2 & B_2 & C_2 \\ \cdot\cdot & \cdot\cdot & \cdot\cdot \\ A_p & B_p & C_p \end{bmatrix}$$

$$\{\sigma^i\}^T = \{\sigma_{xi} \ \sigma_{yi} \ \tau_{xyi}\}$$

$$\{b_{yield}\}^T = \{D_i \ D_i, \ldots, D_i\}$$

3.1.5.2 Required Constraints for the 3-Noded Triangular Extension Element

A slightly different set of constraints must be enforced for 3-noded triangular extension elements in order to ensure that the stresses in both the non-extension and extension zones (Figure 3.1b) do not violate the linearized yield criterion. Since the stresses in these two zones are based on the same linear expansion as the standard triangular element (equation 3.1a), the linear shape functions do not always lie within the range $0 \leq N_i \leq 1$. However, it can be shown that for the 3-noded triangular extension element, the range of shape functions are:

$$N_1 \geq 0, \ N_2 \leq 1.0, \ N_3 \geq 0 \qquad (3.5p)$$

The stresses then satisfy the yield criterion throughout the zone by enforcing the following constraint:

$$F_{k1} \leq F_{k2}, \ F_{k2} \leq 0 \text{ and }, \ F_{k3} \leq F_{k2} \ ; k = 1, 2,..., p \qquad (3.5q)$$

The inequality constraints that are applied to the stresses at node 2 are identical to those described by inequality constraint 3.5o. At each nodes 1 and 3, the yield condition gives rise to p inequality constraints of the form:

$$[A_{yield,\ 3\text{-}n\ ext}]\{\sigma^i\} \leq \{b_{yield}\};\ i = 1 \text{ and } 3 \qquad (3.5r)$$

where

$$[A_{yield,\ 3\text{-}n\ ext}] = \begin{bmatrix} A_1 & B_1 & C_1 & -A_1 & -B_1 & -C_1 \\ A_2 & B_2 & C_2 & A_2 & B_2 & C_2 \\ .. & .. & .. & .. & .. & .. \\ A_p & B_p & C_p & A_p & B_p & C_p \end{bmatrix}$$

$\{\sigma^i\}^T = \{\sigma_{xi}\ \sigma_{yi}\ \tau_{xyi}\ \sigma_{x2}\ \sigma_{y2}\ \tau_{xy2}\}$

$\{b_{yield}\}^T = \{(D_i - D_2)\ (D_i - D_2), \ldots, (D_i - D_2)\}$

Inequality constraints 3.5p and 3.5q are proved in Appendix C.

3.1.5.3 Required Constraints for the 4-Noded Rectangular Extension Element

The stresses of the 4-noded rectangular extension element follow the same linear expansion of the 3-noded triangular element. In the extension zone, the stresses are also extrapolated by this linear expansion. The range of N_i is given by:

$$N_1 \geq 0,\ N_2 \leq 1.0,\ 0 \leq N_3 \leq 1 \qquad (3.5s)$$

This gives rise to the constraints required for the stresses to satisfy the yield criterion throughout the zone.

$$F_{k1} \leq F_{k2},\ F_{k2} \leq 0 \text{ and },\ F_{k3} \leq 0;\ k = 1, 2, \ldots, p \qquad (3.5t)$$

These are of the same form as inequality constraints (3.5o) and (3.5r). Inequality constraints 3.5s and 3.5t are proved in Appendix D.

3.1.6 Assembly of Constraint Equations

The statically admissible stress field is satisfied by assembling the following constraints.

1. Stress equilibrium equations

1.1 Within each element (all types of element)

$$[A_{equi,\ 3\text{-}n}]\{\sigma_{3\text{-}n}\} = \{b_{equi,\ 3\text{-}n}\} \qquad (3.2b)$$

1.2 Additional constraints for 4-noded rectangular extension element

$$[A_{equi,\ 4\text{-}n}]\{\sigma_{4\text{-}n}\} = \{b_{equi,\ 4\text{-}n}\} \qquad (3.2d)$$

1.3 At stress discontinuity

$$[A_{dis}]\{\sigma_{dis}\} = \{b_{dis}\} \qquad (3.3c)$$

2. Stress boundary conditions

$$[A_{bound}]\{\sigma_{bound}\} = \{b_{bound}\} \qquad (3.4c)$$

3. Linearized yield criterion

3.1 For 3-noded triangular element

$$[A_{yield,\ 3\text{-}n}]\{\sigma^i\} \le \{b_{yield}\};\ i = 1, 2, 3 \qquad (3.5o)$$

3.2 For 3-noded triangular extension element

$$[A_{yield,\ 3\text{-}n\ ext}]\{\sigma\} \le \{b_{yield}\};\ i = 1, \text{and } 3 \qquad (3.5r)$$

3.3 For 4-noded rectangular extension element

same form as inequality constraints 3.5o and 3.5r

All of these equality and inequality constraints can be summarized in the compact form as

$$[A_1]\{\sigma\} = \{b_1\} \qquad (3.6)$$
$$[A_2]\{\sigma\} \le \{b_2\}$$

where

$[A_1]$ is the constraint matrix of equilibrium and stress boundary conditions, while $[A_2]$ is the constraint matrix of the linearized yield criterion.

3.1.7 Objective Function

The lower bound theorem states that if a statically admissible stress can be found over the whole region, the load calculated from the stresses will be equal or lower than the true collapse load. This expression can be written in mathematical form as:

$$Q_{load} \leq Q_{collapse} \qquad (3.7a)$$

subject to a statically admissible stress field

where

Q_{load} = the load calculated from the statically admissible stress field

$Q_{collapse}$ = the true collapse load

This equation denotes that the true collapse is the maximum value of the load which can satisfy the requirements of a statically admissible stress field. In the linear programming problem, the lower bound formulation is a maximization problem. The collapse load is obtained by maximizing the load which is subject to constraints of statically admissible stress field. Since the lower bound method is formulated as linear programming problem, this maximization problem may be written as:

Maximize: Q_{load} (3.7b)

Subject to:

$$[A_1]\{\sigma\} = \{b_1\}$$

$$[A_2]\{\sigma\} \leq \{b_2\}$$

The objective function of this expression is to maximize Q_{load} which is a function of statically admissible stress. For most plane strain geotechnical problems, Q_{load} is the integral of the normal stress, σ_n acting over some part of the boundary, and thus:

$$Q_{load} = \int_s \sigma_n ds \qquad (3.7c)$$

Figure 3.7 illustrates an edge of a triangular element, defined by nodes 1 and 2, over which σ_n is to be maximized. Since the stresses vary linearly throughout each element, this equation can be evaluated analytically by:

$$Q_{load} = \frac{L}{2}(\sigma_{n1} + \sigma_{n2}) \qquad (3.7d)$$

where

L = the length of the edge

σ_{n1} and σ_{n2} = the normal stresses at nodes 1 and 2 of the element, respectively

Substituting the stress transformation equations 3.3b into 3.7d yields:

$$Q_{load} = \{c\}^T\{\sigma\} \qquad (3.7e)$$

where

$$\{c\}^T = \frac{L}{2}\{\sin^2\theta \quad \cos^2\theta \quad -\sin 2\theta \quad \sin^2\theta \quad \cos^2\theta \quad -\sin 2\theta\}$$

$$\{\sigma\} = \{\sigma_{x1} \quad \sigma_{y1} \quad \tau_{xy1} \quad \sigma_{x2} \quad \sigma_{y2} \quad \tau_{xy2}\}$$

In linear programming problems, {c} is known as the vector of objective function coefficients. Therefore, the problem of finding a statically admissible stress field that maximizes the load can be stated as follows:

Maximize: $\{c\}^T\{\sigma\}$ (3.7f)

Subject to:

$$[A_1]\{\sigma\} = \{b_1\}$$

$$[A_2]\{\sigma\} \leq \{b_2\}$$

When analyzing a slope stability problem which consists of only one soil stratum, the 'external load' can be equated with the unit weight of the soil[1]. Thus, the objective function changes to finding statically admissible stress which maximizes the unit weight of soil. The external load is given by:

$$Q_{load} = \{c\}^T\{Y\} \qquad (3.7g)$$

where

$\{c\}^T = \{1\}$

$\{Y\}^T = \{\gamma\}$

γ = the unit weight of soil

and the linear programming of this problem is similar to equation 3.7f as:

[1] The self weight of the soil is the driving force which leads to slope instability.

Maximize: $\{c\}^T\{Y\}$ (3.7i)

Subject to:

$$[A_3]\{\sigma\} = \{b_3\}$$

$$[A_4]\{\sigma\} \leq \{b_4\}$$

where $[A_3]$ is the matrix of all of the equality constraints and $[A_4]$ is the matrix of yield constraints.

3.1.8 Solution Procedure

Linear programming problems as given in equation 3.7f may be solved by the revised simplex algorithm (Sloan, 1988a). Before applying this algorithm, it is necessary to transform this linear programming problem into the standard form. This can be achieved by applying the transformation rules of linear programming. The standard form for linear programming is written:

Minimize: $\{c^*\}^T\{x^*\}$ (3.8a)

Subject to:

$$[A^*]\{x^*\} = \{b^*\}$$

$$\{x^*\} \geq 0$$

Although the lower bound linear programming problem can be solved by the revised simplex method, an even more elegant and efficient approach is to apply the active set algorithm developed by Best and Ritter (1985). The canonical form required by this algorithm is:

Minimize: $\{c^*\}^T\{x^*\}$ (3.8b)

Subject to:

$$[A^*_1]\{x^*\} = \{b^*_1\}$$

$$[A^*_2]\{x^*\} \leq \{b^*_2\}$$

The lower bound analysis of equation 3.7f can be written directly in this form by defining:

$$\{c\} = -\{c\};\ \{x^*\} = \{\sigma\}$$

$$[A^*_1] = [A_1];\ [A^*_2] = [A_2]$$

$$[b^*_1] = [b_1];\ [b^*_2] = [b_2]$$

It is obvious that the canonical form required by the active set scheme follows naturally from the formulation of the lower bound linear programming problem. Sloan (1988b) made modifications of the algorithm in order to improve efficiency and to reduce the storage requirement. The important modifications are as follows:

1. Only the nonzero entries in the constraint matrices $[A_1]$ and $[A_2]$ are stored.
2. The algorithm fully exploits the extreme sparsity of the overall constraint matrix.
3. A steepest-edge search is used to reduce the numbers of iterations to find the optimal solution.

The active set algorithm has proved to be a very efficient method for solving the lower bound linear programming problem (both in terms of storage and CPU time). In particular, large stability problems can be solved efficiently, even though they generate large number of constraints to be imposed at nodal stresses. More details of the active set algorithm may be found in Sloan (1988b).

3.2 Upper Bound Formulation

This section describes the formulation of the numerical upper bound method for plane strain problems, based on Sloan and Kleeman (1994). The formulation is analogous to the lower bound analysis described in section 3.1. It uses finite element interpolation, linearization of the non-linear yield criterion, and solves the linear programming problem using an active set algorithm. The soil mass is discretized into 3-noded triangular elements, with two unknown velocities at each node. To ensure that the finite element formulation leads to a linear programming problem, the non-linear yield criterion is linearized using a polygonal approximation, which circumscribes the original yield criterion so that the solution corresponds to a strict upper bound on the true collapse load. Linearization of the non-linear yield criterion results in additional sets of unknown velocities, and the plastic multiplier rates associated with each element. Kinematically admissible velocity fields are defined by the constraints of strain and velocity compatibility equations, associated flow, and velocity (displacement) boundary conditions. The external applied load is obtained by invoking the virtual work equation, expressed in terms of the unknown velocities and plastic multiplier rates. The upper bound formulation leads to a

linear programming problem whose objective function is the minimization of the external applied load subject to the constraints of kinematic admissibility. Finally, the optimal velocity field and the upper bound limit load are solved by applying the active set algorithm to the dual linear programming problem. Because the optimal velocity field satisfies all the requirements of the upper bound theorem, the corresponding limit load is a strict upper bound.

3.2.1 Finite Element Discretization

For plane strain conditions, the soil mass is discretized into 3-noded triangular elements as shown in Figure 3.8. Each node has two velocity components and each element has p plastic multiplier rates (where p is the number of sides in the linearized yield criterion, section 3.2.2). The velocities are assumed to vary linearly within each element according to:

$$u = \sum_{i=1}^{3} N_i u_i \qquad (3.9)$$

$$v = \sum_{i=1}^{3} N_i v_i$$

where u_i and v_i are the nodal velocities in the x and y directions, respectively, and N_i are linear shape functions which is given by equation 3.1b.

Plastic deformation may occur not only within triangles, but also in the velocity discontinuities along edges between adjacent elements. Kinematically admissible velocity discontinuities are permitted at all edges shared by adjacent triangles, and are modeled by assuming that each node is unique to its element. Therefore, nodes on either sides of the velocity discontinuity have the same coordinates. A simple mesh for a rigid footing which includes velocity discontinuities is shown in Figure 3.9. It should be noted that this representation is completely different from the conventional finite element method where each coordinate corresponds to a single nodal point.

3.2.2 Constraints for Plastic Flow within Triangular Elements

According to the upper bound theorem, the soil is assumed to be a perfectly plastic material with an associated flow rule. Plastic strain rates are allowed to occur throughout the element. To be kinematically admissible, the plastic strain rates must satisfy compatibility and associated flow equations given by:

$$\dot{\varepsilon}_x = \frac{\partial u}{\partial x} = \dot{\lambda}\frac{\partial F}{\partial \sigma_x} \qquad (3.10a)$$

$$\dot{\varepsilon}_y = \frac{\partial v}{\partial y} = \dot{\lambda}\frac{\partial F}{\partial \sigma_y}$$

$$\dot{\gamma}_{xy} = \frac{\partial v}{\partial x} + \frac{\partial u}{\partial y} = \dot{\lambda}\frac{\partial F}{\partial \tau_{xy}}$$

where

$\dot{\varepsilon}_x$, $\dot{\varepsilon}_y$ = normal plastic normal strain rates in x and y directions, respectively

$\dot{\gamma}_{xy}$ = plastic shear strain rates

F = the Mohr-Coulomb yield function

u, v = velocities in the x and y directions, respectively

$\dot{\lambda}$ = non-negative plastic multiplier rate

It should be noted that since the velocities are assumed to vary linearly throughout triangles, the plastic strain rates within each triangle are constant.

For plane strain conditions (assuming tensile stresses are positive), the Mohr-Coulomb yield function may be expressed as:

$$F = (\sigma_x - \sigma_y)^2 + (2\tau_{xy})^2 - (2c\cos\phi - (\sigma_x + \sigma_y)\sin\phi)^2 = 0 \qquad (3.5a, \text{bis})$$

where

σ_x, σ_y = normal stresses in x and y directions, respectively

τ_{xy} = shear stress

c, ϕ = cohesion intercept and angle of internal friction of soil, respectively

Since the upper bound method is formulated as a linear programming problem, equation 3.5a must be linearized using a polygonal approximation which describes the

stresses as a series of linear functions. In addition, in order to ensure that the solution obtained is a strict upper bound on the true collapse load, the polygon must circumscribe the original Mohr-Coulomb yield surface. The linearization method is similar to that used in the lower bound formulation, however, the polygonal yield surface externally circumscribes the actual Mohr-Coulomb surface for upper bound analyses.

Using transformed stresses;

$$X = \sigma_x - \sigma_y \; ; \; Y = 2\tau_{xy} \; ; \; R = 2c\cos\phi - (\sigma_x + \sigma_y)\sin\phi \qquad (3.5b, bis)$$

the Mohr-Coulomb yield criterion changes to:

$$X^2 + Y^2 = R^2 \qquad (3.5c, bis)$$

This equation represents a circle in terms of the variables X, and Y as shown in Figure 3.10. The rewritten Mohr-Coulomb yield surface is approximated by an exterior polygon with p sides and p vertices (Figure 3.10). The X and Y coordinates of the k^{th} and $(k+1)^{th}$ vertices of the exterior polygon are given by:

$$X_k = R\cos(\alpha_k - \beta)/\cos\beta \; ; \; Y_k = R\sin(\alpha_k - \beta)/\cos\beta \qquad (3.10e)$$

$$X_{k+1} = R\cos(\alpha_k + \beta)/\cos\beta \; ; \; Y_{k+1} = R\sin(\alpha_k + \beta)/\cos\beta$$

where $\beta = \pi/p$ and $\alpha_k = 2k\beta$.

A general stress point with, coordinates X and Y is located on the k^{th} side of the polygon if it satisfies the following condition:

$$(Y_{k+1} - Y_k)(X - X_k) - (X_{k+1} - X_k)(Y - Y_k) = 0 \; ; \; k = 1,2 \ldots,p \qquad (3.10f)$$

The value of the k^{th} side of the linearized yield function, F_k is obtained by substituting equation 3.10c and 3.10e into 3.10f.

$$F_k = A_k\sigma_x + B_k\sigma_y + C_k\tau_{xy} - 2c\cos\phi = 0 \; ; \quad k = 1,2 \ldots,p \qquad (3.10g)$$

where

$$A_k = \cos(\alpha_k) + \sin\phi \; ; \; B_k = \sin\phi - \cos(\alpha_k) \; ; \; C_k = 2\sin(\alpha_k)$$

For the linearized yield criterion defined by equation 3.10g, the associated flow rule of equation 3.10a can then be written in terms of the unknown plastic multiplier rates and the linearing coefficients, A_k, B_k, and C_k:

$$\dot{\varepsilon}_x = \sum_{k=1}^{p} \dot{\lambda}_k \frac{\partial F_k}{\partial \sigma_x} = \sum_{k=1}^{p} \dot{\lambda}_k A_k$$

$$\dot{\varepsilon}_y = \sum_{k=1}^{p} \dot{\lambda}_k \frac{\partial F_k}{\partial \sigma_y} = \sum_{k=1}^{p} \dot{\lambda}_k B_k \qquad (3.10i)$$

$$\dot{\gamma}_{xy} = \sum_{k=1}^{p} \dot{\lambda}_k \frac{\partial F_k}{\partial \tau_{xy}} = \sum_{k=1}^{p} \dot{\lambda}_k C_k$$

where $\dot{\lambda}_k$ is the non-negative plastic multiplier rates associated with the k^{th} side of the linearized yield surface.

Differentiating equation 3.9 with respect to the coordinates and substituting into equation 3.10i generates a series of nodal velocities and plastic multiplier rates within each element:

$$\sum_{i=1}^{3} \frac{\partial N_i}{\partial x} u_i - \sum_{k=1}^{p} \dot{\lambda}_k A_k = 0 \qquad (3.10j)$$

$$\sum_{i=1}^{3} \frac{\partial N_i}{\partial y} u_i - \sum_{k=1}^{p} \dot{\lambda}_k B_k = 0$$

$$\sum_{i=1}^{3} \frac{\partial N_i}{\partial x} v_i + \sum_{i=1}^{3} \frac{\partial N_i}{\partial y} u_i - \sum_{k=1}^{p} \dot{\lambda}_k C_k = 0$$

$$\dot{\lambda}_k \geq 0$$

Finally, substituting the linear interpolation function (equation 3.1b), the flow rule constraints can be expressed by constraint matrices:

$$[A_{11}]\{u\} - [A_{12}]\{\dot{\lambda}\} = \{0\} \qquad (3.10k)$$

$$\{\dot{\lambda}\} \geq 0$$

where

$$[A_{11}] = \begin{bmatrix} y_{23} & 0 & y_{31} & 0 & y_{12} & 0 \\ 0 & x_{32} & 0 & x_{13} & 0 & x_{21} \\ x_{32} & y_{23} & x_{13} & y_{31} & x_{21} & y_{12} \end{bmatrix}$$

$$[A_{12}] = \begin{bmatrix} A_1 & A_2 & A_3 & \dots & A_p \\ B_1 & B_2 & B_3 & \dots & B_p \\ C_1 & C_2 & C_3 & \dots & C_p \end{bmatrix}$$

$$\{u\}^T = \{u_1 \; v_1 \; u_2 \; v_2 \; u_3 \; v_3\}$$

$$\{\dot{\lambda}\}^T = \{\dot{\lambda}_1 \; \dot{\lambda}_2 \; \dots \; \dot{\lambda}_p\}$$

3.2.3. Constraints for Plastic Flow in Velocity Discontinuities

Velocity discontinuities are allowed to occur at all edges shared by adjacent triangles. Figure 3.11 shows a typical velocity discontinuity defined by the nodal pairs (1, 2) and (3, 4). In order to be kinematically admissible, the velocity discontinuities must satisfy the flow rule equation. For the Mohr-Coulomb yield criterion, the associated flow rule at a velocity discontinuity is given by:

$$\Delta v_n = | \Delta u_t | \tan\phi \qquad (3.11a)$$

where

Δu_t, Δv_n = the tangential and normal velocity jump (i.e. relative normal and tangential velocities)

The absolute value on the right hand side of this equation denotes that for a cohesionless material which possesses friction angle, ϕ , dilation must occur regardless of the sign of the tangential shearing.

Consider the discontinuity which is defined by nodal pair (i, j) as shown in Figure 3.11, the velocity jump in any direction with respect to node i is equal to the velocity of node j minus that of node i for the same direction. Therefore, the tangential and normal velocity jumps of nodal pair (i, j) are defined by:

$$\Delta u_{ij,t} = (u_j - u_i)\cos\theta + (v_j - v_i)\sin\theta \qquad (3.11b)$$

$$\Delta v_{ij,n} = (u_i - u_j)\sin\theta + (v_j - v_i)\cos\theta \qquad (3.11c)$$

where

$\Delta u_{ij,t}$, $\Delta v_{ij,n}$ = the tangential and normal velocity jump between nodal pairs (i, j)

u_i, u_j = nodal velocities in x-direction of nodes i and j, respectively

v_i, v_j = nodal velocities in y-direction of nodes i and j, respectively

θ = the angle of the discontinuity to the x-axis measured in a positive anticlockwise direction

It is clear from the equation 3.11b that the tangential velocity jump, $\Delta u_{ij,t}$ may be zero, negative or positive. From the linear programming point of view, this is referred to as a free variable or unrestricted-in-sign variable: Any unrestricted quantity can be decomposed into the difference of two non-negative quantities. Thus, the tangential velocity jump, $\Delta u_{ij,t}$ can be decomposed as:

$$\Delta u_{ij,t} = u^{+}_{ij,t} - u^{-}_{ij,t} \qquad (3.11d)$$

with the constraints

$$u^{+}_{ij,t} \geq 0 \qquad (3.11e)$$
$$u^{-}_{ij,t} \geq 0$$

Since these two equations are applied at the tangential velocity jump for both ends of the discontinuity, they also hold for the jump occurring at all points along the discontinuity:

$$\Delta u_t = u^{+}_t - u^{-}_t \qquad (3.11f)$$
$$u^{+}_t \geq 0$$
$$u^{-}_t \geq 0$$

In addition, it is also clear that the decomposition of the tangential velocity jump generates two non-negative variables, $u^{+}_{ij,t}$ and $u^{-}_{ij,t}$ at nodal pairs (i, j) of the velocity discontinuity. Therefore, for each discontinuity defined by node pairs (1, 2) and (3, 4), there are four unknown sets, namely $u^{+}_{12,t}$, $u^{-}_{12,t}$, $u^{+}_{34,t}$, and $u^{-}_{34,t}$. These unknowns are illustrated in Figure 3.12.

Substituting equation 3.11d into 3.11b gives rise to the following constraints:

$$u^{+}_{ij,t} - u^{-}_{ij,t} = (u_j - u_i)\cos\theta + (v_j - v_i)\sin\theta \qquad (3.11g)$$
$$u^{+}_{ij,t} \geq 0$$
$$u^{-}_{ij,t} \geq 0$$

The absolute sign in the flow rule in equation 3.11a prevents the upper bound method being formulated as a linear programming problem. In order to preserve the

structure of the linear programming problem, the absolute sign has to be eliminated. This can be achieved by two methods.

The first approach is to replace $| \Delta u_t |$ by $s\Delta u_t$, where $s = \pm 1$. This method requires additional constraints of the form $s\Delta u_t \geq 0$. This approach was used by Sloan (1989) and Bottero et al. (1980), but has the disadvantage that the direction of tangential velocity jump must be pre-specified. This severely restricts using large numbers of velocity discontinuities because it is not possible to pre-specify the correct sign of the tangential velocity jump of these discontinuities such that the mode of failure is kinematically admissible.

The second approach avoids the absolute sign from the flow rule equation by substituting $| \Delta u_t | = (u^+_t + u^-_t)$. From equations 3.11d and 3.11e, $\Delta u_t = u^+_t - u^-_t$, and both u^+_t and u^-_t are non-negative. Therefore, it is clear that substituting $| \Delta u_t |$ for $(u^+_t + u^-_t)$ is inexact if u^+_t and u^-_t are both positive simultaneously. Thus, the correct flow rule is satisfied only if either $u^+_t = 0$ or $u^-_t = 0$ at both end nodes of the discontinuity. Since u^+_t and u^-_t are constrained such that $u^+_t, u^-_t \geq 0$, it is possible that both of them may be positive. However, it turns out that by replacing $| \Delta u_t |$ by $(u^+_t + u^-_t)$ and decomposing of Δu_t to $(u^+_t - u^-_t)$, where u^+_t and u_t are non-negative, the upper bound solution always give either $u^+_t = 0$ or $u^-_t = 0$, thus the correct flow rule is always satisfied. This key result is proved in Appendix E. The advantage of this method is that it allows unlimited numbers of velocity discontinuities to be used in the upper bound analysis. Moreover, the direction of the tangential velocity jump is selected automatically during the optimization process (instead of being pre-specified).

Therefore, the absolute sign value in the flow rule equation, $| \Delta u_t |$ is replaced by $(u^+_t + u^-_t)$ and equation 3.11d becomes:

$$\Delta v_n = (u^+_t + u^-_t)\tan\phi \qquad (3.11h)$$

Since the velocities vary linearly along the discontinuity, the quantities u^+_t, u^-_t and Δu_t also follow the same linear variation. In order to satisfy the flow rule along the discontinuity, constraints 3.11h must be enforced at both nodal pairs (i, j) on discontinuities by:

$$\Delta v_{n,ij} = (u^{+}_{t,ij} + u^{-}_{t,ij})\tan\phi \qquad (3.11i)$$

where nodal pair (i, j) = (1, 2) and (3, 4)

Substituting the expression of $\Delta v_{n,ij}$ given by equation 3.11c, the final flow rule for each of the nodal pairs is given by:

$$(u_i - u_j)\sin\theta + (v_j - v_i)\cos\theta = (u^{+}_{t,ij} + u^{-}_{t,ij})\tan\phi \qquad (3.11j)$$

Equations 3.11g and 3.11j summarize all of the flow rule constraints which must be enforced on each nodal pair of the discontinuity. These constraints can be written in matrix form as:

$$[A_{21}]\{u\} - [A_{23}]\{u_3\} = \{0\} \qquad (3.11k)$$
$$\{u_3\} \geq 0$$

where

$$[A_{21}] = \begin{bmatrix} W & -W \\ W & -W \end{bmatrix}; \quad [W] = \begin{bmatrix} -\cos\theta & -\sin\theta \\ \cos\theta & -\sin\theta \end{bmatrix}$$

$$[A_{23}]^T = \begin{bmatrix} 1 & \tan\phi & 1 & \tan\phi \\ -1 & \tan\phi & -1 & \tan\phi \end{bmatrix}$$

$$\{u\}^T = \{u_1\ v_1\ u_2\ v_2\ u_3\ v_3\ u_4\ v_4\}$$

$$\{u_3\}^T = \{u^{+}_{t,12}\ u^{-}_{t,12}\ u^{+}_{t,34}\ u^{-}_{t,34}\}$$

3.2.4 Velocity Boundary Conditions

As stated in the upper bound theorem, the velocity field must satisfy the prescribed velocity boundary conditions. Consider node i on a boundary where the prescribed velocity in x and y direction are ($\bar{u}$, $\bar{v}$). Thus, the nodal velocities (u_i, v_i) must satisfy the following equaiities:

$$u_i = \bar{u} \qquad (3.12a)$$

$$v_i = \bar{v}$$

These constraints may be written in matrix form as:

$$[A_{31}]\{u\} = \{b_3\} \qquad (3.12b)$$

where

$$\{u\}^T = \{u_i\ v_i\}$$

$\{b_3\}^T = \{u_i \;\; v_i\}$

$[A_{31}]$ = the identity matrix

3.2.5 Objective Function

The upper bound theorem states that for a kinematically admissible velocity field, the load calculated from the virtual work equation will be equal or higher than the true collapse load. This expression can be written mathematically as:

$$Q_{load} \geq Q_{collapse} \qquad (3.13a)$$

subject to kinematically admissible velocity field

where

Q_{load} = the external load calculated from virtual work equation

$Q_{collapse}$ = the true collapse load

This equation expresses the collapse load as the minimum value of the sets of external loads which satisfy the requirement for a kinematically admissible velocity field. According to the linear programming problem, the upper bound analysis is a minimization problem and the objective function is the minimization of the external load (Min. Q_{load}). It should be noted that the term "external load" may denote the external applied force at the velocity boundary, or the body forces such as the unit weight of soil, depending on the type of stability problem. For example, if the problem covers the bearing capacity of a footing, the external load is the applied load of the footing. On the other hand, for slope stability problems, the external load is the unit weight of the soil.

Equation (3.13a) may be written as a linear programming problem:

Minimize: Q_{load} (3.13b)

Subject to: constraints of kinematically admissible velocity field

The external load, Q_{load} is linked with the velocity field by means of the virtual work equation, and is defined by equating the rate of work due to the external loads, with the internal power dissipated in the plastically deformed region. Thus, the virtual work equation is given by:

$$W_{ext} = W_{int} \tag{3.13c}$$

where

W_{ext} = the external rate of work due to the external loads

W_{int} = the internal dissipation of power in the plastic region

The external rate of work due to the external loads, and the internal dissipation of power are defined by:

$$W_{ext} = \int_A T_i u_i dA + \int_V F_i u_i dV \tag{3.13d}$$

$$W_{int} = \int_V \sigma_{ij} \dot{\varepsilon}_{ij} dV \tag{3.13e}$$

T_i, F_i = external surface forces and body forces, respectively

σ_{ij} = the internal stresses

u_i = the velocity field

$\dot{\varepsilon}_{ij}$ = the strain rates

V, A = the volume and surface area of the body

3.2.6 Internal Dissipation of Power

3.2.6.1 Power Dissipation in Triangular Elements

Since the plastic strain rates can occur both within the triangular element and along the velocity discontinuity, the internal dissipation of power may occur in both places. Within each element, the power dissipated by the plastic stresses is given by:

$$W_{ele} = \int_A (\sigma_x \dot{\varepsilon}_x + \sigma_y \dot{\varepsilon}_y + \tau_{xy} \dot{\gamma}_{xy}) dA \tag{3.14a}$$

Substituting equation 3.10i gives rise to the following equation:

$$W_{ele} = \int_A \sum_{k=1}^{p} [\dot{\lambda}_k (A_k \sigma_x + B_k \sigma_y + C_k \tau_{xy})] dA$$

The expression $(A_k\sigma_x + B_k\sigma_y + C_k\tau_{xy}) = 2c\cos\phi$ (equation 3.10g), hence the stress terms can be eliminated from this equation:

$$W_{ele} = 2\cos\phi \sum_{k=1}^{p} \dot{\lambda}_k \int_A c\,dA \qquad (3.14b)$$

Assuming that the cohesion varies linearly throughout the element, the integral part of equation 3.14b can be evaluated analytically. Thereafter, equation 3.14b can be written in matrix form as follows:

$$W_{ele} = \{c_2\}^T \{\dot{\lambda}\} \qquad (3.14c)$$

where

$$\{c_2\}^T = \frac{2}{3} A\,(c_1 + c_2 + c_3)\cos\phi\,[1 \;\; 1 \;\; 1 \;\; \ldots \;\; 1]$$

$$\{\dot{\lambda}\}^T = \{\dot{\lambda}_1 \;\; \dot{\lambda}_2 \;\; \ldots \;\; \dot{\lambda}_p\}$$

A = the area of a triangle

c_1, c_2, c_3 = the cohesion at nodes 1, 2 and 3 of the triangle, respectively

It should be noted that the power dissipated in each triangle is guaranteed to be non-negative as the plastic multiplier rates are constrained so that $\{\dot{\lambda}\} \geq 0$, and other terms also have positive values. Thus, the dissipation of power within the element is calculated correctly.

3.2.6.2 Power Dissipation in Discontinuities

Consider a velocity discontinuity of length, L, as shown in Figure 3.11. The dissipation of power along the discontinuity is expressed by the following:

$$W_{dis} = \int_L \{|\tau\,\Delta u_t| + \sigma_n \Delta v_n\}\,dL \qquad (3.14d)$$

where Δu_t, Δv_n are the tangential and normal velocity jumps, respectively

Substituting the flow rule equation (3.11a), and the Mohr-Coulomb yield criterion, the stress terms are removed, and thus:

$$W_{dis} = \int_L \{c|\Delta u_t|\}\,dL \qquad (3.14e)$$

As explained earlier, the absolute value of the tangential velocity jump, $|\Delta u_t|$ is substituted by $u^+_t + u^-_t$. Thus, this equation becomes:

$$W_{dis} = \int_L c \{u_t^+ + u_t^- \} dL \qquad (3.14f)$$

Since the velocity field varies linearly along the discontinuity, the terms, u^+_t and u^-_t also follow the same linear variation and can be expressed as:

$$u_t^+ = u_{12}^+ + \frac{t}{L}(u_{34}^+ - u_{12}^+) \qquad (3.14g)$$

$$u_t^- = u_{12}^- + \frac{t}{L}(u_{34}^- - u_{12}^-) \qquad (3.14h)$$

where L = the length of the discontinuity and $0 \le t \le L$

Substituting these two equations into 3.14f and integrating, the power dissipated in each discontinuity can be found:

$$W_{dis} = \{c_3\}^T \{u_3\} \qquad (3.14i)$$

$$\{c_3\}^T = \frac{L}{6} [(2c_1 + c_2) \quad (2c_1 + c_2) \quad (c_1 + 2c_2) \quad (c_1 + 2c_2)]$$

$$\{u_3\}^T = \{ u^+_{t,12} \; u^-_{t,12} \; u^+_{t,34} \; u^-_{t,34} \}$$

where c_1 and c_2 are the cohesion at the nodal pairs (1, 2) and (3, 4), respectively.

Note that the power dissipated in each discontinuity is always non-negative because the four additional variables at the discontinuity are constrained so that $\{u_3\} \ge 0$, and other terms are also positive. Thus, the dissipation of power in each discontinuity is calculated following the same line of reasoning presented in the previous section.

The total internal dissipation of power, W_{int} is obtained by summing the internal dissipation of power within the elements and along the velocity discontinuities:

$$W_{int} = W_{ele} + W_{dis} \qquad (3.14j)$$

Substituting equations 3.14c and 3.14i, the internal dissipation of power is expressed as:

$$W_{int} = \{c_2\}^T \{\dot{\lambda}\} + \{c_3\}^T \{u_3\} \qquad (3.14k)$$

3.2.7 Constraints due to Objective Function

As explained previously, the objective function of the upper bound method is the minimization of the external load (Min. Q_{load}). The expression for the external load is linked to the velocity field through equation of virtual work. This results in additional

constraints which depend on the type of stability problem. For most plane strain problems, the external loads involve the normal stress applied over some part of the boundary and the unit weight of soil. After equating the external work to the internal dissipation of power, the virtual work equation becomes

$$W_{ext} = \int_L \sigma_n v_n dL + \int_A \gamma v dA = W_{int} \qquad (3.15a)$$

where σ_n, v_n = normal stress and normal velocity for loading over a boundary of length, L

γ = the unit weight of soil

A = area of the whole soil mass

3.2.7.1 Rigid and Flexible Loading Boundary Conditions

For problems where part of the soil is loaded by an external force, such as a footing, the objective function is the minimization of the applied normal force.

$$Q_{load} = \int_L \sigma_n dL \qquad (3.15b)$$

For the rigid loading case, the normal velocity is constant over the loading boundary, but the normal stress is not. Therefore, the normal velocity can be moved out from the integration sign in equation 3.15a. After rearranging the terms, equation 3.15a becomes:

$$v_n \int_L \sigma_n dL = W_{int} - \int_A \gamma v dA \qquad (3.15c)$$

The applied normal force, Q_{load} can be obtained from equation 3.15c if the normal velocity over the boundary is enforced such that

$$v_n = 1 \text{ ; for all nodes of the loading boundary} \qquad (3.15d)$$

This additional constraint may be written in matrix form as:

$$[A_{41}]\{u\} = \{b_4\} \qquad (3.15e)$$

where

$[A_{41}]$ = the identity matrix

$\{u\}^T = \{u_1\ v_1\ u_2\ v_2\ u_3\ v_3\ .....\}$ (nodal velocity at loading boundary)

$\{b_4\}^T = \{1\ 1\ \ 1\ 1\ \ 1\ 1.....\ \}$

Substituting equation 3.15d in 3.15c gives the expression for the external load:

$$Q_{load} = \int_L \sigma_n dL = W_{int} - \int_A \gamma v dA \qquad (3.15f)$$

and the objective function is then:

$$Min.(Q_{load}) = Min.\{W_{int} - \int_A \gamma v dA\} \qquad (3.15g)$$

Assuming that the unit weight of soil is constant, the integral term, $\int_A \gamma v dA$ can be evaluated analytically:

$$\int_A \gamma v dA = \{c_1\}^T \{u_1\} \qquad (3.15h)$$

where

$\{c_1\}^T = \frac{\gamma}{3}[0\ A_1\ 0\ A_1\ 0\ A_1\ \ldots]$, A_1 = the area of the element

$\{u_1\}^T = \{u_1\ v_1\ u_2\ v_2\ u_3\ v_3\ \ldots\ldots\}$ (nodal velocities of each triangle)

Substituting equations 3.14k and 3.15h into 3.15g, the objective function for the rigid vertical loading is:

$$Min.(Q_{load}) = Min.[\{c_2\}^T\{\dot{\lambda}\} + \{c_3\}^T\{u_3\} - \{c_1\}^T\{u_1\}] \qquad (3.15i)$$

The boundary conditions for a flexible base comprise constant normal stress. Therefore, the virtual work can be re-arranged as follows:

$$\sigma_n \int_L v_n dL = W_{int} - \int_A \gamma v dA \qquad (3.15j)$$

The applied normal stress, σ_n is obtained from equation (3.15j) by imposing the constraint:

$$\int_L v_n dL = 1 \qquad (3.15k)$$

Since the velocities vary linearly, equation 3.15k can be expressed in terms of nodal velocities:

$$\frac{1}{2}\sum_{edge}[(v_i + v_j)\cos\theta_{ij} - (u_i + u_j)\sin\theta_{ij}]L_{ij} = 1 \qquad (3.15m)$$

where L_{ij} and θ_{ij} denote the length and inclination of each segment on L and each segment is defined by the end nodes (i, j).

This additional constraint can be written in matrix form as:

$$[A_{51}]\{u\}=\{b_5\} \tag{3.15n}$$

where

$[A_{51}] = [-L_{12}\sin\theta_{12} \quad L_{12}\cos\theta_{12} \quad -L_{12}\sin\theta_{12} \quad L_{12}\sin\theta_{12} \ldots..]$

$\{u\}^T = \{u_1 \quad v_1 \quad u_2 \quad v_2.....\}$ is the vector of nodal velocities along the loaded boundary

$\{b_5\}^T = \{1\}$

Substituting equation 3.15k into 3.15j gives the expression for the normal stress:

$$\sigma_n = W_{int} - \int_A \gamma v dA \tag{3.15o}$$

Since the normal stress is constant over the loading segment, the external load is simply obtained as:

$$Q_{load} = \sigma_n L = L(W_{int} - \int_A \gamma v dA) \tag{3.15p}$$

Finally, the objective function is given by:

$$\text{Min.}(Q_{load}) = \text{Min.}[L(W_{int} - \{c^T\}\{u_1\})] \tag{3.15q}$$

As the length of the loading boundary, L, is a constant value, it can be evaluated from both sides of the equation. This leads to an expression of the objective function in which the applied (uniform) normal stress is minimized directly:

$$\text{Min.}(\sigma_n) = \text{Min.}(W_{int} - \{c^T\}\{u_1\}) \tag{3.15r}$$

The collapse load is then calculated as the product of the optimal normal stress and the length of the loading segment.

Note that the objective function for flexible loading (equation 3.15g) is similar to that for rigid loading (equation 3.15r). The only difference is that the flexible case minimizes the normal stress while the rigid case minimizes the total applied force. The objective function for flexible vertical loading is then:

$$\text{Min.}(\sigma_n) = \text{Min.}[\{c_2\}^T\{\dot{\lambda}\} + \{c_3\}^T\{u_3\} - \{c_1\}^T\{u_1\}] \tag{3.15s}$$

Although both flexible and rigid base conditions can be modeled, the current formulation (Sloan and Kleeman, 1994) considers only the case where loads are applied normal to the boundary. Chapter 5 describes modifications of the objective function which enables the program to model eccentric and inclined footing loads.

3.2.7.2 Slope Stability Problem

For a slope stability problem (without surcharge loading), the objective function minimizes the unit weight of the soil. The virtual work equation in this case is written[1] as:

$$W_{ext} = \int_A (-\gamma) v dA = W_{int} \qquad (3.15t)$$

For situation where the unit weight is uniform (e.g. homogeneous soil), the term γ can be moved from the integration sign and equation 3.15t is then:

$$-\gamma \int_A v dA = W_{int} \qquad (3.15u)$$

The unit weight of soil is obtained from equation 3.15u by imposing the constraint on the vertical velocity such that

$$\sum_{elements} \int_A v dA = -1 \qquad (3.15v)$$

Since the velocity varies linearly throughout each triangle, equation 3.15v can be integrated analytically, and thus

$$\int_A v dA = \frac{A}{3}(v_1 + v_2 + v_3)$$

where v_1, v_2 and v_3 are the vertical velocity of nodes 1,2 and 3 of each triangular element

For each element, the constraint of equation 3.15v can be written in matrix form:

$$[A_{61}]\{u\} = \{b_6\} \qquad (3.15w)$$

where

$[A_{61}] = \frac{1}{3}[\,0\ \ A_1\ \ 0\ \ A_1\ \ 0\ \ A_1\ \ \ldots]$, A_1 = the area of the element considered

$\{u\}^T = \{u_1\ \ v_1\ \ u_2\ \ v_2\ \ u_3\ \ v_3\ \ldots\ldots\}$ (nodal velocities)

[1] Note that the negative sign of the unit weight results from the positive sign convention shown in Figure 3.8.

$$\{b_6\}^T = \{-1\}$$

Substituting equation 3.15v into 3.15u yields the expression of the unit weight of soil.

$$\gamma = W_{int}$$

Thus, the objective function is:

$$\text{Min.}(\gamma) = \text{Min.}(W_{int}) \tag{3.15x}$$

Substituting equation 3.14k, the objective function of the slope stability problem can be written in matrix form as:

$$\text{Min.}(\gamma) = \text{Min.}[\{c_2\}^T\{\dot{\lambda}\} + \{c_3\}^T\{u_3\}] \tag{3.15y}$$

3.2.8 Assembly of the Constraint Equations and Objective Function

The kinematically admissible velocity field is defined by assembling the following constraint equations:

1. Flow rule equation for each triangular element:

$$[A_{11}]\{u\} - [A_{12}]\{\dot{\lambda}\} = \{0\} \tag{3.10k}$$

2. Flow rule equation for each velocity discontinuity:

$$[A_{21}]\{u\} - [A_{23}]\{u_3\} = \{0\} \tag{3.11k}$$

3. Velocity boundary conditions:

$$[A_{31}]\{u\} = \{b_3\} \tag{3.12b}$$

4. Additional constraints due to the objective function:

   4.1 For vertical rigid loading:

$$[A_{41}]\{u\} = \{b_4\} \tag{3.15e}$$

   4.2 For vertical flexible loading:

$$[A_{51}]\{u\} = \{b_5\} \tag{3.15n}$$

   4.3 for slope stability problem:

$$[A_{61}]\{u\} = \{b_6\} \tag{3.15w}$$

5. Non-negative constraints on the plastic multiplier rates and additional variables for velocity discontinuities:

$$\{\dot{\lambda}\} \geq 0$$

$$\{u_3\} \geq 0$$

The objective function depends on the type of stability problem.

1. Rigid vertical loading

$$\text{Min.}(Q_{load}) = \text{Min.}[\{c_2\}^T\{\dot{\lambda}\} + \{c_3\}^T\{u_3\} - \{c_1\}^T\{u_1\}] \qquad (3.15i)$$

2. Flexible vertical loading

$$\text{Min.}(\sigma_n) = \text{Min.}[\{c_2\}^T\{\dot{\lambda}\} + \{c_3\}^T\{u_3\} - \{c_1\}^T\{u_1\}] \qquad (3.15s)$$

3. Slope stability

$$\text{Min.}(\gamma) = \text{Min.}[\{c_2\}^T\{\dot{\lambda}\} + \{c_3\}^T\{u_3\}] \qquad (3.15x)$$

3.2.9 Solution Procedure

The constraints that must be enforced are give by equations 3.10k, 3.11k, 3.12b, 3.15e, 3.15n, and 3.15w. The objective functions are defined by equations 3.15i, 3.15s, and 3.15x. Assembling these constraints gives rise to a linear programming problem of the form:

$$\text{Minimize: } \{C\}^T\{X\} \qquad (3.16a)$$

Subject to:

$$[A]\{X\} = \{B\}$$

$$\{X\} \geq 0$$

This type of linear programming is solved very efficiently by using the active set algorithm to the dual problem of equation 3.16a. The active set scheme is suited to this problem because it is well designed to deal with very sparse linear programming problems generated by these constraints. In addition, the algorithm employs the steepest search which can significantly reduce the number of iterations to arrive at the optimal solution (and hence greatly saves total computation time). The active set algorithm is also designed to reduce the storage requirement such that only the non-zero entries in the constraint matrices are stored. Therefore, the method can be used to analyze very large stability problems. More details of the active set algorithm may be found in Sloan (1988b).

3.3 Capabilities of Current Formulations

The computer codes of numerical limit analysis used to study stability problems in this thesis are written in FORTRAN 77 language by Prof. Sloan of University of Newcastle. The computer code of the lower bound is based on Assadi and Sloan (1990), and the upper bound is based on Sloan and Kleeman (1994). The capabilities of the current programs can be summarized as follows:

1. The analyses are for plane strain conditions only.
2. The unit weight of the soil is assumed to be constant over the whole body. Therefore, soil profiles with variable unit weight can not be solved.
3. The analysis assume an isotropic Mohr-Coulomb failure criterion with constant friction angle over the whole domain. However, the soil cohesion can be either constant, or vary linearly with depth. Anisotropic strength properties are not considered in the current program but have been implemented by Yu and Sloan (1994c).
4. For the lower bound program, the stress boundary condition can be specified by the normal or shear traction at the surface. For a rigid base, the normal stress is unrestricted and the optimization must maximize the normal force applied to the loading surface (instead of the normal stress). However, this option is not available in the current program.
5. For the upper bound program, the objective functions are available for both flexible and rigid loading normal to the surface, but are not able to handle inclined loading structures.
6. The analyses assumes associated flow and hence, overestimate the dilation rates for frictional materials compared to the measured behavior of real soils (cf. Pestana, 1994).
7. The programs do not consider pore water pressures and hence, are restricted to undrained total stress analyses ($\phi = 0$), or fully drained stability analyses.

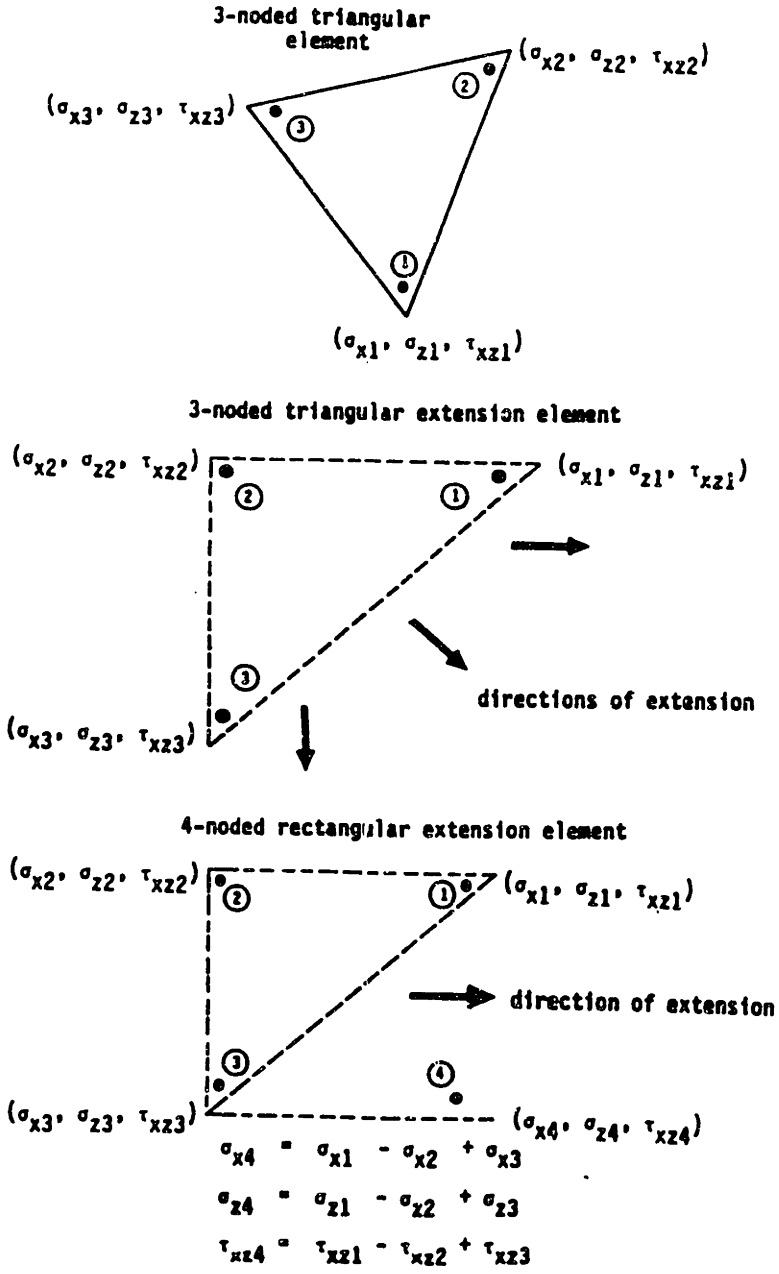

Fig. 3.1 Element types for lower bound limit analysis

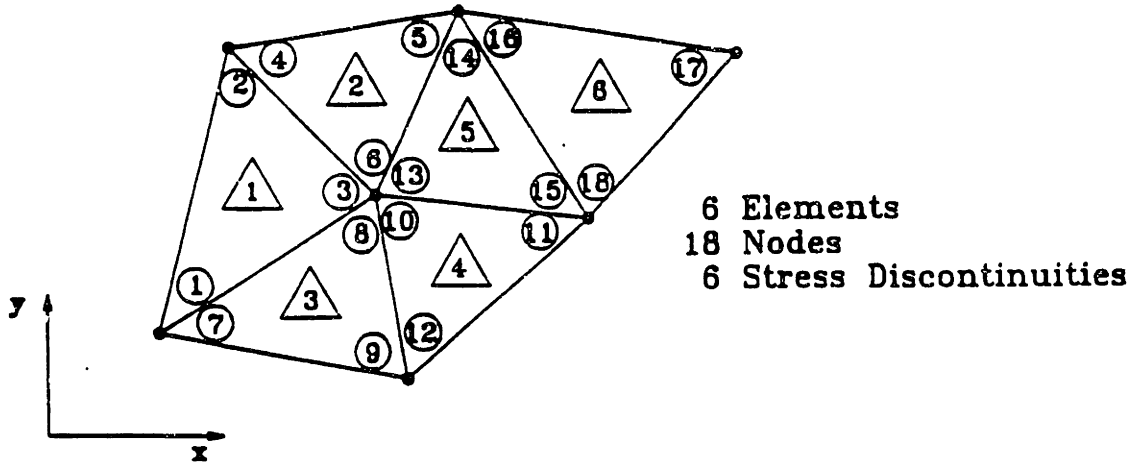

Fig. 3.2 Mesh of linear stress trinagle for the lower bound limit analysis

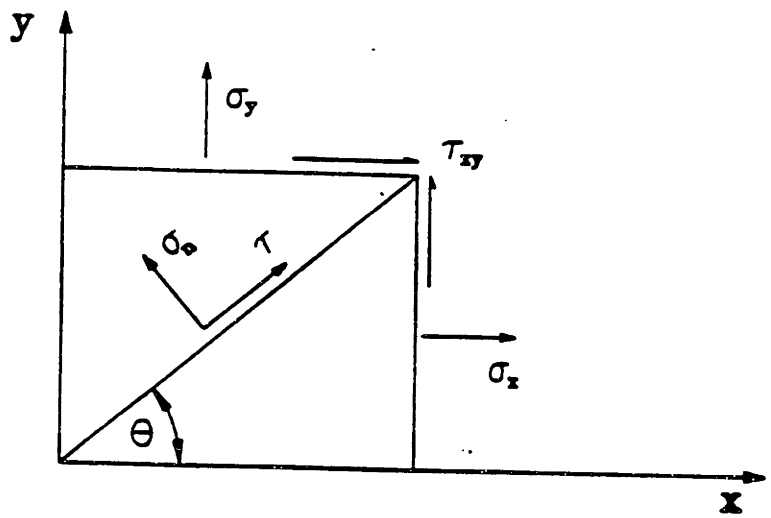

Fig. 3.3a Positive sign convention of stresses

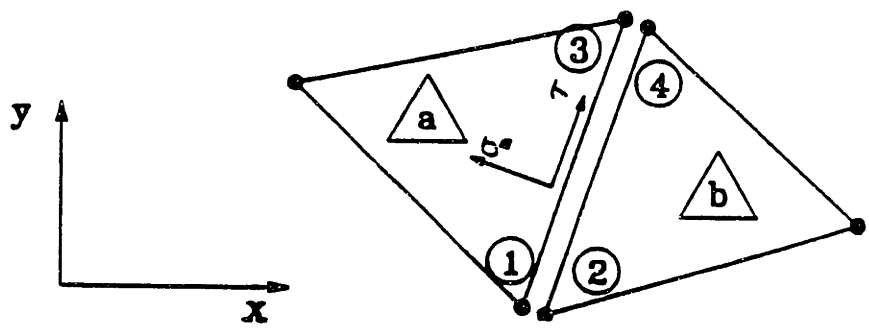

Fig. 3.3b Statically admissible stress discontinuity between adjacent triangles

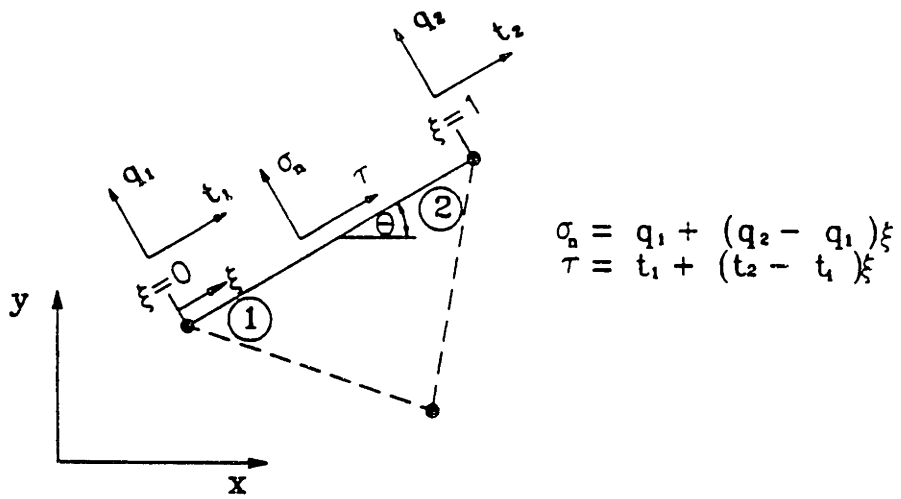

Fig. 3.4 Stress boundary conditions

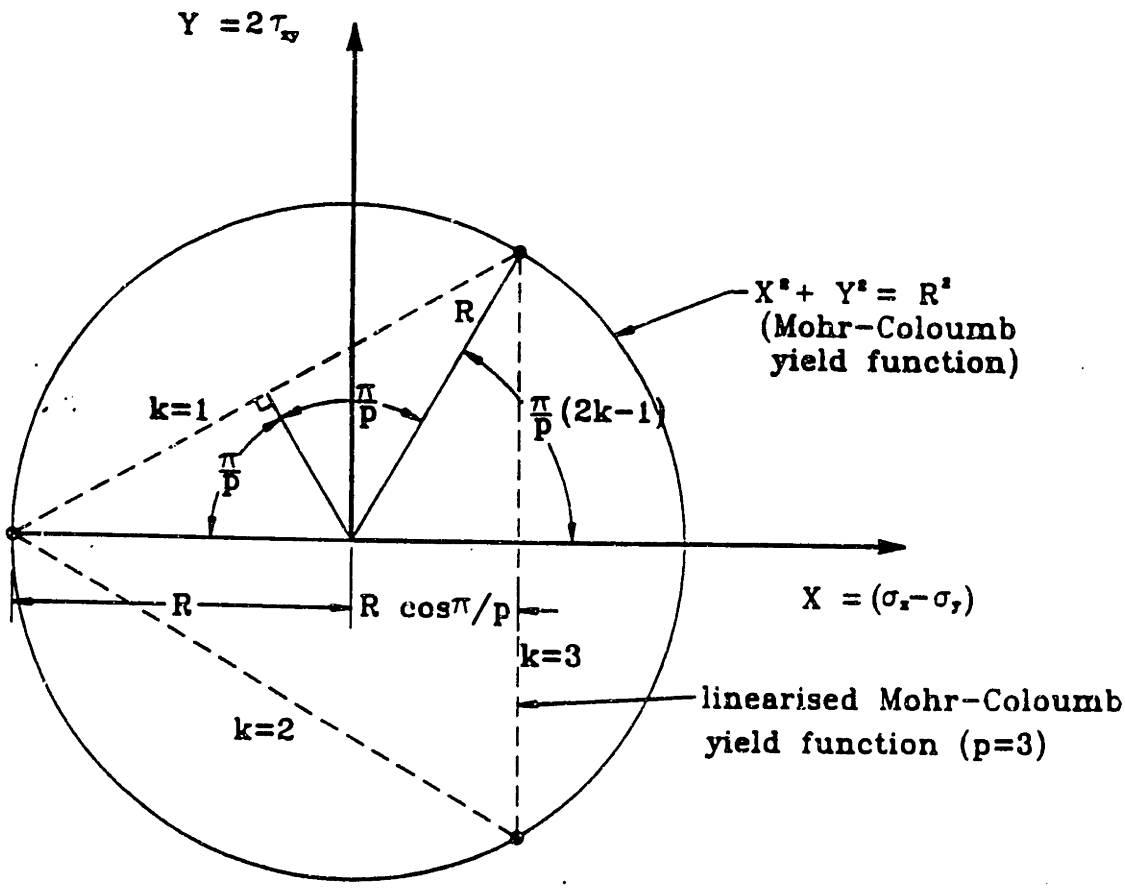

Fig. 3.5 Internal linear approximation to Mohr-Coulomb yield function
(p = number of sides in yield polygon = 3)

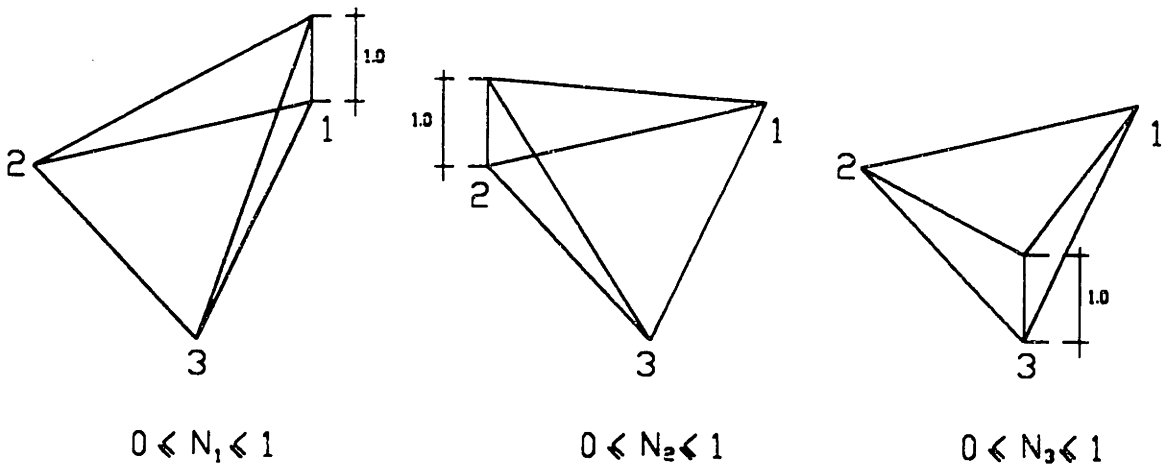

Fig. 3.6 Geometric representation of the linear shape functions for the 3-noded triangular element

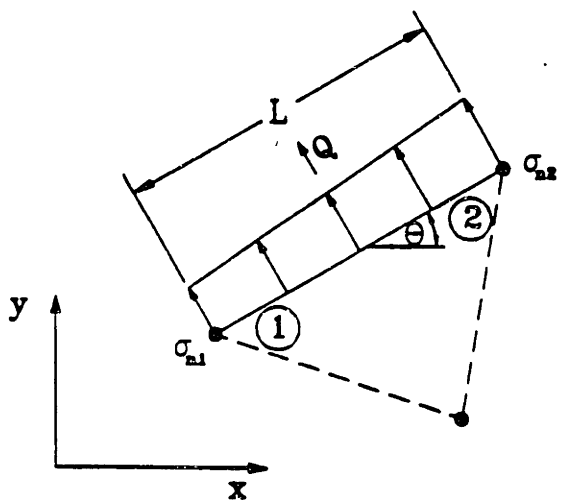

h = out-of-plane thickness

$Q = \frac{Lh}{2}(\sigma_{n1} + \sigma_{n2})$

= normal force

Fig. 3.7 External applied load in a direction normal to a boundary edge

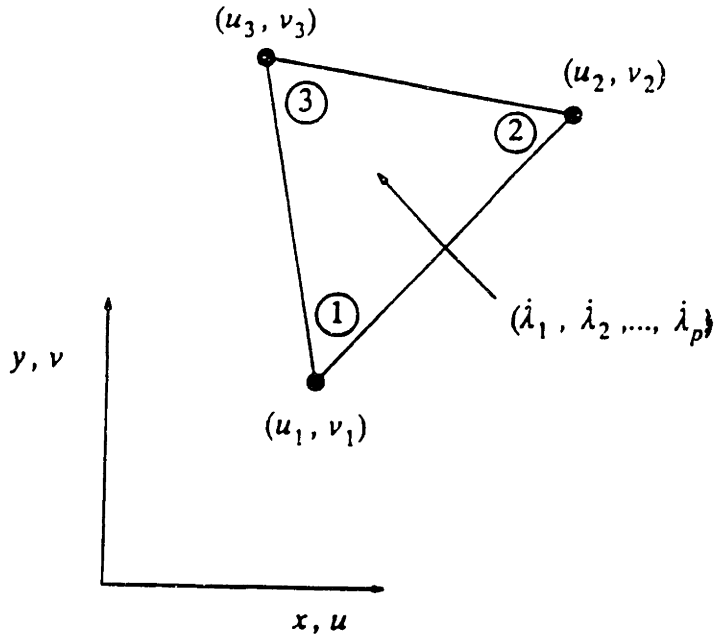

Fig. 3.8 Triangular element for upper bound limit analysis

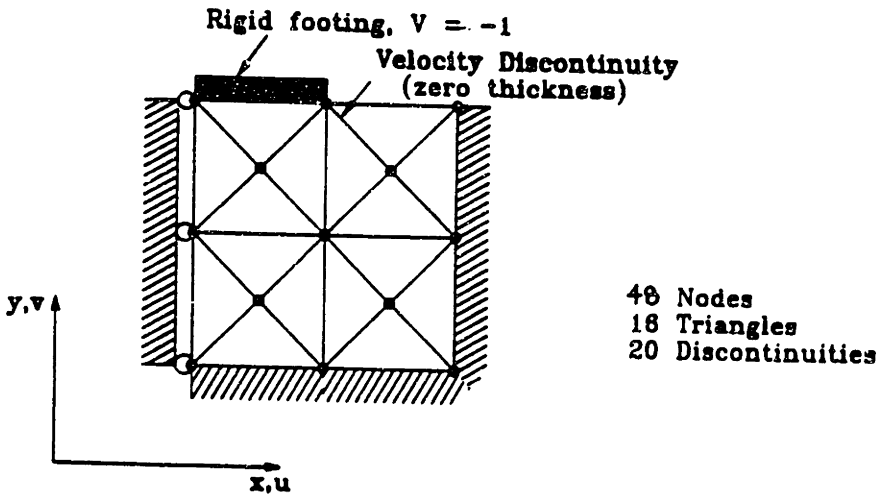

Fig. 3.9 Simple footing mesh for upper bound limit analysis

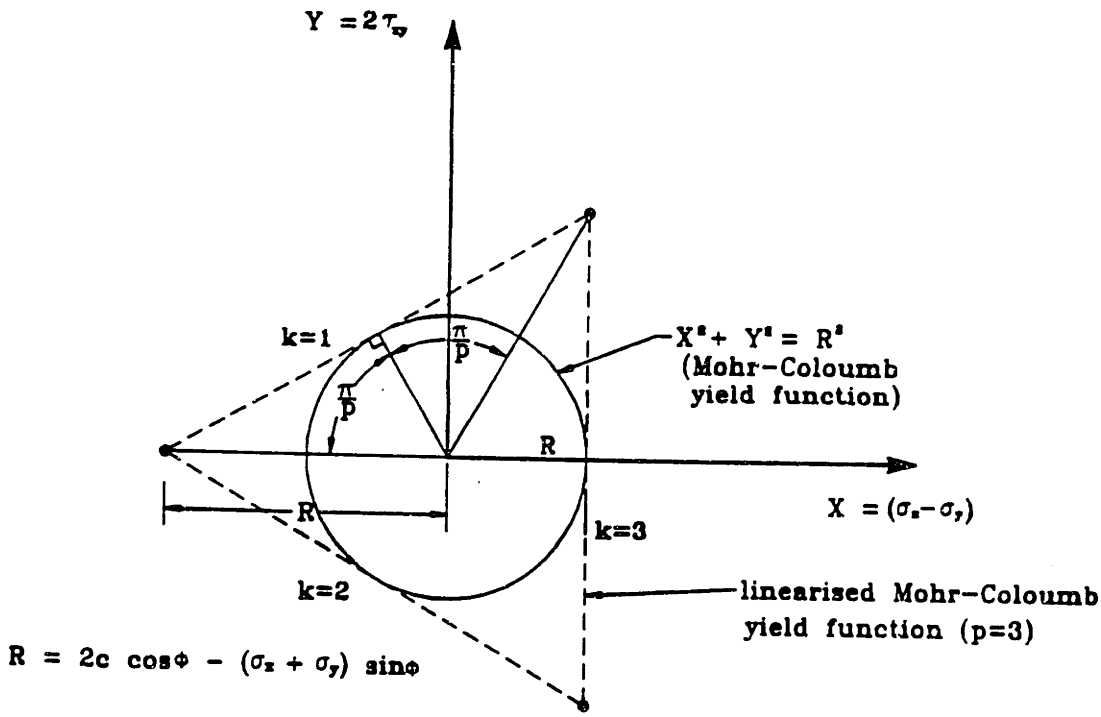

Fig. 3.10 External linear approximation to Mohr-Coulomb yield function (p = number of sides in yield polygon = 3)

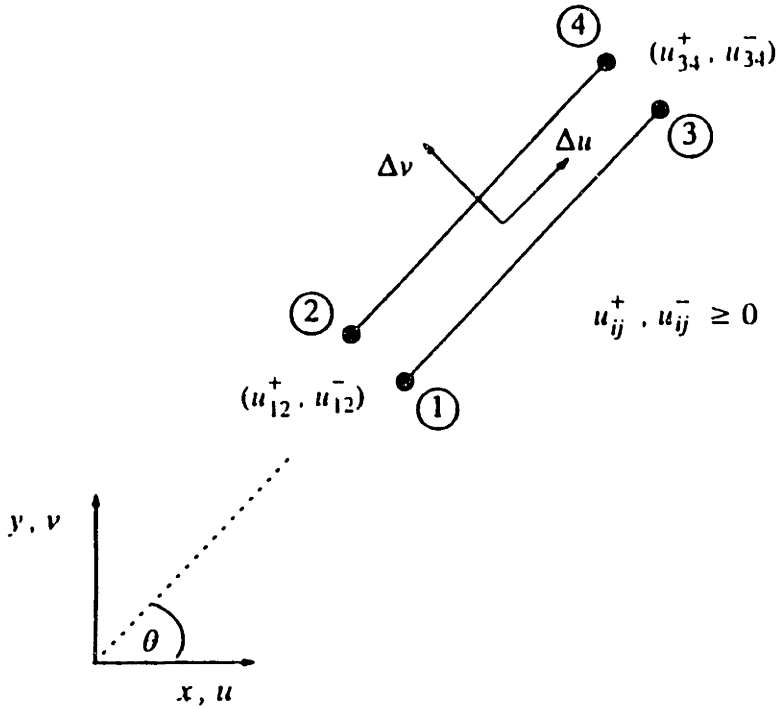

$$\Delta u_{ij} = u^+_{ij} - u^-_{ij} = (u_j - u_i)\cos\theta + (v_j - v_i)\sin\theta$$
$$\Delta v_{ij} = (u^+_{ij} + u^-_{ij})\tan\phi$$

Fig. 3.11 Velocity discontinuity geometry

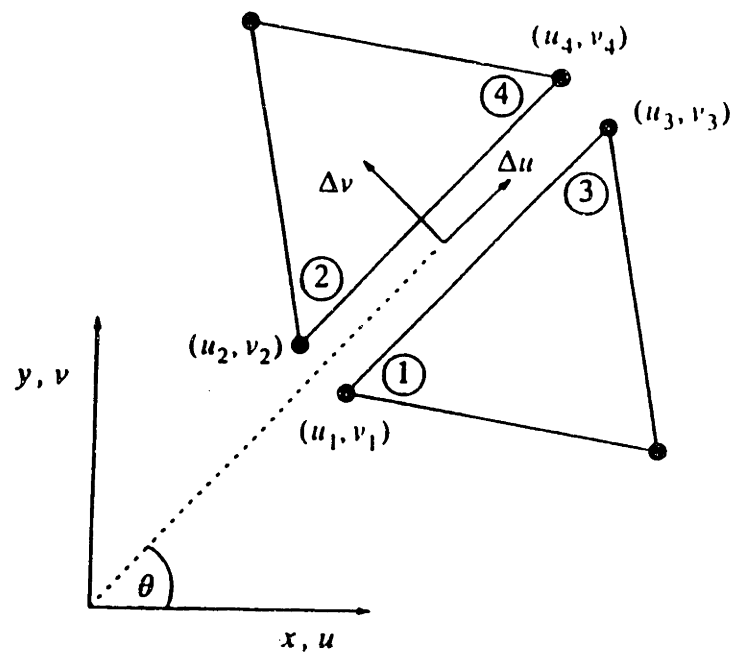

$$\Delta u_{ij} = (u_j - u_i)\cos\theta + (v_j - v_i)\sin\theta$$
$$\Delta v_{ij} = (u_i - u_j)\sin\theta + (v_j - v_i)\cos\theta$$

Fig. 3.12 Velocity discontinuity variables

4. Evaluation of Method: Undrained Loading of Footings on Clay

4.1 Introduction

This chapter evaluates the numerical limit analyses described in the previous chapter, through predictions of collapse loads for footings on cohesive soil. The analyses focus on rigid footings subject to vertical, concentric loading. Closed-form solutions for these classic bearing capacity problems, provide a useful basis for evaluating the accuracy of the numerical procedures.

Section 4.2 considers the effects of mesh refinement and yield surface approximations for smooth rigid footings on homogeneous clay. The studies are then extended for the case where the undrained shear strength increases linearly with depth (section 4.3), and the effects of base roughness on the collapse load (section 4.4). Results obtained from both numerical lower and upper bounds are compared with the exact solutions, while quoted CPU times are presented to illustrate the efficiency and practicality of the numerical limit analyses.

4.2 Smooth Rigid Footing on Homogeneous Clay

The exact collapse pressure for a smooth rigid footing on the surface of a homogenous clay layer is given by the well-known Prandtl (Prandtl, 1920) solution by $q_f = N_c c_u$, where c_u is the undrained shear strength and $N_c = [2 + \pi] \approx 5.14$. This section presents results of numerical limit analyses for this problem and considers the effects of mesh refinement, mesh arrangement, and yield surface approximations on lower and upper bound predictions of the collapse load.

4.2.1 Factors Affecting Numerical Lower Bound

4.2.1.1 Discretization Factors

Section 3.1.1 shows that numerical lower bound calculations for a deep soil layer (half space) must include special extension elements in order to ensure that the solution satisfies all requirements of static admissibility. However, it is not obvious how the application of these extension elements will affect the computed lower bound loads, or

how the extension elements can be used to reduce the size of the discretized domain. Thus, the first set of analyses consider the effects of the extension elements and the size of the discretized domain on computations of lower bound collapse loads.

Figures 4.1-4.3 show the lower bound meshes used in this investigation. The corresponding results are given in Table 4.1. Due to symmetry, only one-half of the problem is represented in the analyses. The meshes S1, S2 and S3 (Figures 4.1, 4.2 and 4.3) correspond to three sizes of the discretized domain increasing in both the lateral and vertical directions as shown in the figures. For each size of the discretized domain, analyses were performed with and without extension element (marked by "ext. ele.", Figures 4.1a vs 4.1b, Figures 4.1c vs 4.1d etc.). In addition, the effects of mesh refinement are investigated by increasing the node density within the discretized domain (coarse vs fine meshes, Figures 4.1a vs. 4.1c, Figures 4.1b vs 4.1d etc.). In all cases, the yield surface is approximated by a 24-sided polygon (p = 24; cf. equation 3.5d).

Figure 4.4 shows the stress boundary conditions for a smooth rigid footing. In the lower bound analyses (Figures 4.1-4.3), the rules of refinement are similar to those used in the conventional displacement finite element method, with the highest density of elements at locations of the highest expected stress gradients. Due to the singularity of the stresses at the edge of the footing, the highest concentration of elements are placed in that area and element density decreases radially away from the footing edge. The effects of mesh arrangement are discussed in more detail in section 4.2.1.3.

The results from Table 4.1 show the following:

1. For the smallest size of the discretized domain (S1), the error in N_c obtained with extension elements is larger than that without extension elements. (i.e. compare results of mesh S1-E-C vs S1-NE-C and S1-E-F vs. S1-NE-F). As the mesh is refined, there is a significant improvement in the computed collapse load without extension elements (N_c = 4.643 to 4.922, for S1 meshes), while the analyses with extension elements improve only slightly with mesh refinement (4.232 vs 4.325, for S1 meshes).

2. As the size of the discretized domain increases (S2, and S3), there is no difference in solution occurring with or without extension elements. In both cases, mesh refinement improves significantly the computed lower bound values of N_c.

3. For the analyses with extension elements, increasing the size of the discretized domain from size S1 to S2 improves the accuracy of solution (N_c = 4.325 vs 4.922 for the fine mesh). However, further enlargement of the discretized domain (S3 vs S2) produces only a very small change in the lower bound solutions.

The first and second result indicate that meshes with extension elements are much more sensitive to the size of the discretized domain than meshes without extension elements. If a relatively small discretized domain is used with extension elements, the solution is significantly less accurate, even with mesh refinement. These results clearly show that extension elements cannot be used to reduce the size of the discretized domain. The size of discretized domain must be large enough such that the extension elements do not cause a deterioration in solution accuracy. For this particular problem, the minimum lateral and vertical dimensions are 5B/2 x 4B/2 (i.e. S2), respectively. There is no improvement in accuracy for a fine mesh whose discretized domain is larger than this size (i.e. S2-E-F and S3-E-F both give N_c = 4.922). However, the only difference is that as the size of the discretized domain (and number of equations) increases, the CPU time required for solution also increases. Another observation is that if the effect of the discretized domain is eliminated, mesh refinement can improve the solution. It should be emphasized that extension elements are essential in order to obtain a strict lower bound solution for a half-space problem. (i.e. the extension elements ensure that the stress field can be extended throughout out the soil mass in statically admissible manner).

4.2.1.2 Yield Surface Linearization

The second study investigates the effect of approximations in the yield surface linearization. Calculations are performed using the fine mesh S2-E-F (Figure 4.2d) and vary the order (i.e. number of sides) of the polygon used to approximate the yield function, p as shown in Table 4.2. These results show that as the accuracy of the yield surface linearization increases, there is also an improvement in the computed collapse load. For this particular problem, the linearization error is small (error less than 3%) for p = 12-36, with little further improvement for p > 24. Hence, p = 24 is used in all subsequent calculations.

4.2.1.3 Mesh Arrangement

The last study investigates the effects of mesh arrangement and refinement on the accuracy of the solution. Figures 4.5-4.7 illustrate three different grid arrangements used for lower bound analyses. In each case, one coarse and one fine mesh were used for each grid arrangement. Simple, regular grid arrangements (type A) are generated by subdividing a mesh of rectangular elements, into four triangles, and represents a simple practical method for automatic mesh generation. Refinement is carried out throughout the entire discretized domain. Meshes shown in Figure 4.6 (type B) are identical to mesh S2-E-C and S2-E-F shown in Figure 4.2. In this case, refinements are based on radial sectors emanating from the edge of the footing. Meshes in Figure 4.7 (type C) are arranged so that elements form a series of fans of stress discontinuities extending from the edge of the footing. The similarity of meshes type B and type C is that the points which form triangles are distributed radially from the edge of the footing. The difference between those two types is that for mesh type C, the points are triangulated in such a way that their fans of stress discontinuities correspond to the exact solution proposed by Prandtl, while for mesh type B, the points are triangulated without any constraint. All analyses (meshes type A, B and C) use a fixed size of the discretized domain (5B/2 x 4B/2) together with extension elements and uniform linearization of the yield surface, with p = 24 (based on the previous studies).

Table 4.3 shows that there are substantial differences in the computed collapse loads for coarse meshes A1, B1 and C1. The smallest error occurs for mesh type C, followed by mesh types A and then B. As mentioned earlier, it is well known that the edge of the footing corresponds to a stress singularity and hence, more elements are required in this vicinity. Although the arrangement of mesh B1 followed this rule of refinement (and also contained more elements than mesh C1), the solution was less accurate than either C1 or A1. This result clearly shows that the solution accuracy of the lower bound analysis depends on the mesh arrangement. For a given mesh arrangement, refinement improves the solution (A2 vs A1, B2 vs B1, and C2 vs C1). Not surprisingly, the increase in accuracy of N_c by mesh refinement is accompanied by a corresponding increase in CPU time. The results in Table 4.3 indicate that initial discretization controls efficiency of the

solution (accuracy and CPU time) even though mesh refinement can produce more accurate solutions.

4.2.2 Factors Affecting Numerical Upper Bound Calculation

4.2.2.1 Discretization Factors

An analogous set of studies have been performed to investigate the effects of discretized domain size, yield surface linearization, mesh arrangement and refinement on the upper bound collapse load. Figure 4.8 shows three meshes used to investigate the effects of the discretized domain dimensions, with results summarized in Table 4.4. All three meshes are arranged in the same pattern but with different sizes of the discretized domain. Velocity boundary conditions for a smooth rigid footing are illustrated in Figure 4.9. All three calculations assume p = 24 in the linearization of the yield surface.

The results in Table 4.4 show that the size of the discretized domain has a much smaller effect on the upper bound collapse load than observed in the preceding analyses. All three meshes generate very accurate estimates of the collapse load (N_c error less than 2.5%). The minimum lateral and vertical dimensions required for the upper bound analyses are 4(B/2) x 2(B/2), in order to eliminate boundary effects in the analysis (i.e. N_c is the same for both su2 and su3 calculations; Table 4.4). This discretization domain is much smaller than that of the lower bound analyses [5(B/2) x 4(B/2)], where the stresses must be extended throughout the soil mass without violating equilibrium, stress boundary conditions, and yield criterion (indeed extension elements are necessary to satisfy these requirements for a half space). In contrast, for the upper bound analysis, the plastic deformation mechanism is restricted to a well defined zone beneath the footing. Figure 4.10 shows the plastic zone corresponding to the three meshes in Figure 4.8. These results show that there are no improvements in the computed upper bound load once the failure mechanism is fully contained within the discretized domain. Further enlargement of the discretized domain only increases the CPU time.

4.2.2.2 Yield Surface Linearization

Table 4.5 summarizes the upper bound calculations for the su2 mesh (Figure 4.8b) with various linearization approximation for the yield surface. These results are very similar to values quoted previously for lower bound analyses. The error in N_c associated with linearization of the yield surface is insignificant for $p \geq 24$.

4.2.2.3 Mesh Arrangement

The effects of mesh arrangement and refinement were studied using three geometric arrangements as shown in Figures 4.11-4.13. The first case of grid (mesh D; Figure 4.11) uses a regular rectangular grid, the second (mesh E; Figure 4.12) distributes elements within radial sectors emanating from the edge of footing. and the third (type F; Figure 4.13) has elements form the slip line of the exact solution (i.e. Prandtl mechanism). To distinguish between effects of grid arrangement and refinement, analyses have been performed using coarse and fine meshes for each arrangement (D2 vs D1 etc.) using similar procedures described for the lower bound analyses (cf. Table 4.3). The results of the upper bound calculations are summarized in Table 4.6.

For all grid arrangements, the error in N_c is small (less than 3 percent) and mesh refinement produces relatively small improvements in the accuracy of the solutions. These results show that the upper bound solution is less sensitive to mesh arrangement than the lower bound analyses. Good performance of the simple rectangular mesh can be related to the upper bound formulation, which allows plastic deformation to occur both within elements and along the velocity discontinuities. The rectangular mesh contains large numbers of velocity discontinuities or slip lines and hence, can describe a wide range of failure mechanisms. One important practical implication of these results is that relatively inexperienced users can achieve reliable upper bound collapse loads using simple (e.g. regular) mesh arrangements.

4.2.3 Results of the Numerical Lower and Upper Bound Analyses

This section describes in more detail the results of the numerical lower and upper bound analyses for the smooth rigid footing on a homogeneous clay half-space. The solutions provide very accurate collapse bounds from the preceding calculations using the discretizations shown in Figure 4.14. The lower bound mesh (mesh C2, Figure 4.7) has a high concentration of elements emanating in a radial fan from the edge of the footing, it is composed of 699 nodes, 220 triangular elements, one triangular extension element, 9 rectangular extension elements, and 330 stress discontinuities. The upper bound mesh (mesh D2, Figure 4.11b) uses a rectangular grid which consists of 642 nodes, 201 triangular elements, and 204 velocity discontinuities. The chosen sizes of the discretized domain were also based on the results of the studies of the effect of the discretized domain, and both analyses use p = 24 in the linearization of the yield surface. The corresponding results in Table 4.7 show that the numerical lower and upper bounds correspond to bearing capacity factors of 5.042 and 5.210, respectively. Thus, the exact collapse load is bracketed to within 3.3 percent. The CPU time required for both analyses is very small (less than 10 mins.)[1] .

Figures 4.15-4.18 illustrate the complete results of the lower and upper bound analyses for a clay layer with undrained strength $c_u = c_{u0}$. The lower bound results in Figure 4.15 include the contours of the major and minor principal stress (Figure 4.15a and 4.15b, respectively), the direction of the major principal stress to the vertical (Figure 4.15c), and the locations of the failure zone (Figure 4.15d). As expected from the known stress characteristics for this problem, the statically admissible stress field can be divided into three zones (Figure 4.15c). The first zone corresponds to active failure occurring beneath footing, where $\delta = 0°$ and $\sigma_1/c_{u0} = 5.0$. The second zone forms a radial shear fan, where the major principal stress rotates from the vertical to the horizontal direction ($\delta = 0° \rightarrow 90°$; Figure 4.15c) and the major principal stress reduces from $\sigma_1/c_{u0} = 5.0$ to 2.0. The third zone consists of passive shearing extending along a line at 45° from the edge of

[1] The author has not performed conventional displacement finite element for this problem. However, the expected CPU time required for a conventional displacement finite element calculation should be comparable to the numerical limit analysis for this simple problem.

the footing to the ground surface, where $\delta = 90°$ and $\sigma_1/c_{u0} = 2.0$. The three zones can also be seen from contours of the average in-plane stress $p = (\sigma_1 + \sigma_3)/2c_{u0}$ in Figure 4.16 (i.e. center of the Mohr circle). Figure 4.17 shows the normal contact stress distribution beneath the footing. This result indicates that the numerical lower bound analyses also correctly predicts a uniform normal contact stress beneath the footing with a magnitude of about 5.0, which is very close to the exact value of 5.141.

The upper bound results in Figure 4.18 include the deformed mesh (Figure 4.18a), which shows the reiative displacement of the individual element (note the large magnification scale in this figure); the plastic failure zone (Figure 4.18b) which shows the full shear strength of the soil mobilized within elements and along the velocity discontinuities, and the velocity field/velocity characteristics which show the direction of motion of the collapse mechanism (Figures 4.18c and d). The results show that the velocity characteristics correspond very well with the slip line mechanism proposed by Prandtl. In addition, the overall dimensions of the plastic zone (maximum width from the edge of the footing, x/B = 1.25 and maximum depth, y/B = 0.875) are in reasonable agreement with the locations of the failure zone analyzed by Prandtl (x/B = 1.0 and y/B = 0.707).

4.3 Smooth Rigid Footing on Non-Homogeneous Clay

Davis and Booker (1973) used the method of characteristics to solve the exact collapse load for a rigid strip footing on a purely cohesive soil, where the undrained shear strength increases linearly with depth. The bearing capacity factor, F, proposed by Davis and Booker can be expressed in the form as:

$$F = \frac{Q / (Bc_{u0})}{(2 + \pi) + (\rho B / c_{u0}) / 4} \qquad (4.1)$$

where Q = the collapse load

B = the width of footing

c_{u0} = the undrained shear strength at the soil surface

ρ = the change of undrained shear strength with depth (dc_u/dz)

The factor F is a function of the dimensionless strength profile parameter $\rho B/c_{u0}$ and is different for smooth and rough footings. Figure 4.19 summarizes the values of F_s and F_r reported by Davis and Booker (1973) for smooth and rough footings.

Figures 4.20 and 4.21 show the meshes used in the numerical lower bound and upper bound analyses of smooth rigid footings on non-homogeneous clay layers, respectively. These meshes were selected after experimenting with different arrangements and refinements. Note that the size of the discretized domain required for non-homogeneous strength is smaller than that of the homogeneous strength (for both lower and upper bound calculations). In addition, higher mesh refinement is required in the vicinity of the footing in the lower bound analyses. In all cases, the yield surface is linearized by a 24-sided polygon (p = 24).

Table 4.8 and Figure 4.22 summarize the bearing capacity factors computed for the smooth rigid footing on non-homogeneous clay, where the undrained shear strength varies linearly with depth. The results include the bearing capacity factor F_s, and the CPU time required for the analyses, the exact solutions, and the bounds on the exact collapse load. Provided that the error bound on the true collapse load is small (nominally less than 10%), it is reasonable to quote a best estimate value of the collapse as the mean of the lower and upper solutions. The difference between the best estimate collapse load and the exact solution are then quoted as the prediction 'accuracy'. The analyses consider a wide range of the strength parameter $\rho B/c_{u0}$, starting from the homogeneous case ($\rho = 0$) to the case where the undrained shear strength is zero at the ground surface ($c_{u0} = 0$; $\rho B/c_{u0} = \infty$). The results show the following:

1. For all possible strength profiles, the upper and lower bound solutions bracket the true collapse load to within 13.3%. For most practical problems, where the strength parameter $0 \leq \rho B/c_{u0} \leq 20$, the bounds are less than 5-6% (Figure 4.22a, b). If the best estimate is represented by the average of the lower and upper bound solutions, the error in predicting the collapse load (F_s error) is less than 6% for all ranges of $\rho B/c_{u0}$, and less than 1.5% for $0 \leq \rho B/c_{u0} \leq 20$.
2. The computation time for individual analysis (Figure 4.22c) is typically in the range of 400-700 CPU secs (i.e. 6-12 mins). No direct comparisons of CPU

time were made using the conventional displacement finite element method. However, Sloan (1988) quotes results of similar analyses and shows that the computation time required for numerical limit analysis was significantly faster than that required for the conventional displacement finite element analysis.

The results of the lower and upper bound of two cases, where $\rho B/c_{u0} = 3$ and $\rho B/c_{u0} \rightarrow \infty$ (zero undrained shear strength at surface) have been examined in more detail. Figure 4.23 shows the results of the lower bound analyses for $\rho B/c_{u0} = 3$. Notice that the failure zone ($[\sigma_1-\sigma_3]/2c_{u0} = 1.0$; Figure 4.23d) of the non-homogeneous case is much smaller in extent than that required previously for the homogeneous case (Figure 4.15d). Moreover, the direction of the major principal stress (δ; Figure 4.23c) varies at locations beneath the footing (i.e. no well defined active zone $\delta = 0°$) hence, the strength non-homogeneity causes a large change in the directions of shearing within the clay. Figure 4.24 compares contours of mean stress with the exact solution reported by Davis and Booker (1973). It is clear that there is good qualitative agreement between the numerical lower bound and the exact solution. Figure 4.25 compares the normal contact stress predicted from the lower bound method with the exact solution proposed by Davis and Booker (1973). The comparison shows that the contact stress predicted by the lower bound corresponds very well with that of the exact solution. Notice that the contact normal stress of the non-homogeneous case is not constant over the base of the footing like that of homogenous case, but instead increases from the edge towards the center of the footing.

Figure 4.26 shows the complete results of upper bound analyses for the case of $\rho B/c_{u0} = 3$. The plastic zone predicted by the upper bound analyses (Figure 4.26b) also corresponds closely with the failure zone predicted by the lower bound analysis (Figure 4.23d). Note that the velocity field/characteristics show that the failure mechanism involves a much larger horizontal component of displacement than was found in the previous calculations for the homogeneous clay (cf. Figure 4.18d). Figure 4.27 show that the predicted velocity characteristics for the upper bound analyses are qualitatively in good agreement with exact solutions given by Davis and Booker (1973).

Fig. 4.28 and 4.29 summarize the results of lower and upper bound analyses for the extreme case, where $\rho B/c_{u0} \rightarrow \infty$ (zero undrained shear strength at surface), respectively. Figure 4.28 shows that the lower bound analyses predicts that normal contact stress increase linearly from zero at the edge of the footing and is almost identical to that of the exact solution. Notice that the gradient of the normal contact stress across the footing is equal to the gradient in undrained shear strength with depth, ρ. The upper bound failure mechanism in Figure 4.29 consists of a very thin surface veneer of soil which moves horizontally beneath the footing. As mentioned in Davis and Booker (1973), this corresponds to a mud wave mechanism taking place at the surface of the clay.

4.4 Rough Rigid Footing on Non-Homogeneous Clay

4.4.1 Modifications for a Rough Rigid Footing

Davis and Booker (1971) describe two common methods for modeling the boundary conditions corresponding to a rough rigid soil-footing interface. In the first method, there are no velocity discontinuities along the interface, and no slip occurs. This method corresponds to the no-slip interface condition, and is termed a "narrow rough footing". A wedge of soil immediately beneath the footing is assumed to move as a rigid body; thus, it undergoes no plastic deformation. This model is often used to represent rough-rigid boundary conditions in conventional displacement finite element analyses. A second, more rigorous representation allows slip to occur, provided the boundary shear traction satisfies the Mohr-Coulomb failure criterion. The results show a rigid wedge of soil moving below the central zone of the footing. Outside this central zone, interface slip occurs from the edge of the footing. Davis and Booker (1971) state that these results correspond to the general case of a "wide rough footing"[1] .

In order to perform numerical limit analysis of this problem correctly, it is essential to include interface slip within the formulation. The following sections describe the

[1] These boundary conditions can be simulated in conventional displacement finite element methods by introducing special interface elements.

implementation of the frictional (rough) interface in the numerical lower and upper bound analyses.

4.4.1.1 Constraints for the Lower Bound Method

Since the lower bound method considers only the stress field, one additional constraint is required to enforce at the yield criterion at the soil nodes along the soil-footing interface. Consider the Mohr-Coulomb yield criterion, where the parameters c_i, and ϕ_i are the cohesion and friction angle at the soil-footing interface, respectively. The additional constraint of the yield criterion has the form:

$$|\tau| \leq c_i + \sigma_n \tan\phi_i \qquad (4.2)$$

where τ, σ_n = shear stress and normal stress along the soil-footing interface, respectively

This constraint is required to guarantee that the shear stress must not exceed the mobilized shear resistance at the interface. The absolute value in the left hand side of this equation is necessary, because it defines the convex Mohr-Coulomb yield surface in the space of τ-σ_n. For a perfectly rough footing, it is reasonable to assumed that $c_i = c_{soil}$ and $\phi_i = \phi_{soil}$, where c_{soil} and ϕ_{soil} are the cohesion and friction angle of the soil beneath the footing, respectively.

4.1.1.2 Constraints for the Upper Bound Method

In order to model both the narrow and wide rough footings within a single formulation, it is necessary to introduce the soil-footing interface as shown in Figure 4.30, such that the zone of interface slips because of part of the solution. Introducing a soil-footing interface allows both the soil and footing to move independently. By then enforcing constraints of kinematic admissibility, it is possible to describe the general behavior of rough footings. The conceptual modifications for the upper bound analyses can be summarized as follows:

1. According to Figure 4.30, soil-footing interfaces are composed of footing nodes (a-f), soil nodes (1-6) and interface elements (m-o). Note that the coordinates of nodes a-f are the same as those of nodes 1-6, respectively. Each footing node also has two unknown velocities (x and y directions) like other nodes in the mesh. Thus, the footing and soil

nodes form velocity discontinuities at the interfaces. The strength of all velocity discontinuities obeys the Mohr-Coulomb yield criterion with parameters, c_i and ϕ_i.

2. The first constraint arises because all interfaces are treated as velocity discontinuities. Therefore, they must satisfy the associated flow rule. The other constraint is due to the fact that the rigid footing moves only in a vertical direction with unit displacement (Figure 4.30a). Thus, the boundary conditions along all the footing nodes (a-f) are u = 0 (zero velocity in the x-direction), and v = -1 (one unit downward).

The associated flow rule constraint specifies that slip between the footing and soil must occur if the shear stress at the interface satisfies the yield criterion. Hence, the modification correctly models the behavior of wide rough footing. The constraint of unit vertical velocity (displacement) along the footing nodes allows the load from the footing to be minimized directly, as mentioned in the formulation of the upper bound analyses in section 3.2.7.

It should be noted here that no modification is needed for the interface upper bound analyses of a narrow rough footing as no slip occurs at any point along the interface. For this case, the soil and footing nodes coincide at collapse and it is not necessary to introduce soil-footing interface element (m-o; Figure 4.30b). Therefore, modeling can be simply achieved by specifying the velocity boundary conditions directly at the soil nodes on the surface.

In order to demonstrate that the modification can capture the behavior of both narrow and wide rough footings, comparisons have been made between the upper bound analyses with no slip, and with interface shear resistance (i.e. modified approach) for various selected values of the undrained strength parameter $\rho B/c_{u0}$. The corresponding results in Table 4.9 show that both methods of analyses give the same collapse load for the homogeneous clay ($\rho B/c_{u0} = 0$). Comparisons of the velocity fields and plastic zones for the homogeneous case in Figure 4.31 also show identical results. For small values of the strength parameter $\rho B/c_{u0} = 3$ (Table 4.9), the analysis with interface shear resistance provides a more accurate calculation of the exact collapse load than the no slip case. Figure 4.32 shows that the two solutions for this case produce small differences in the

plastic failure zone, although, there are quite significant differences in the directions of soil movement beneath the footing.

For very small values of $\rho B/c_{u0}$ ($c_{u0}/\rho B$ = 0.005 and 0.0; Table 4.9), the no slip analysis gives very large errors in the computed collapse loads, whereas the interface shear resistance provides an accurate representation of the exact failure mechanism. Note that the analysis for $c_{u0}/\rho B$ = 0.0 gives an error in the collapse load with the interface shear resistance of 13.3%, which reflects the singularity in the yield criterion caused by zero undrained shear strength (i.e. zero undrained shear strength allows the plastic strain rates to increase indefinitely). However, most of the error associated with results for $c_{u0}/\rho B \leq$ 0.005 is due to kinematic inadmissibility of the no-slip condition along the soil-footing interface. This behavior is confirmed by the results of the velocity fields and plastic zones shown in Figures 4.33 and 4.34 for $c_{u0}/\rho B$ =0.005 and 0.0, respectively. It is clear that the velocity field and plastic zone predicted by the no slip assumption are very different from those obtained by specifying the interface shear resistance. When interface shear resistance is included in the analysis, the plastic zone is much shallow than obtained by no slip calculation. According to Figure 4.19, the exact solutions of both smooth and rough footing are identical for c_{u0} = 0. Table 4.9 shows this agreement in which the collapse loads obtained from wide rough rigid footing and smooth rigid footing are more or less the same ($F_r = F_s$ for c_{u0} = 0). Moreover, Figure 4.34a and 4.34b illustrate the agreement between the velocity field and plastic zone of wide rough footing and smooth rigid footing obtained from the numerical upper bound, respectively (cf. Figure 4.29).

Based on these results, it can be concluded that the no-slip representation of a rough rigid footing can sometimes result in kinematic inadmissibility of the velocity field. All subsequent analyses impose the interface shear resistance in calculations for rough rigid footings.

4.4.2 Results of Lower Bound and Upper Bound Analyses for Rough Rigid Footings

Figures 4.35 and 4.36 show meshes used for lower bound and upper bound analyses of rough rigid footing on clay layers where the undrained shear strength increases linearly with depth. Meshes in these two figures were chosen after experimenting with a wide variety of mesh arrangements and refinements. For all meshes, the yield surface is approximated by using a 24-sided polygon. The corresponding results are summarized in Table 4.10 and Figure 4.37. The analyses consider a wide range of possible strength parameters $\rho B/c_{u0}$, starting from homogeneous case to the case where undrained shear strength is zero at the ground surface. The results show the following:

1. For all possible strength profiles, the true collapse load can be bracketed to within an accuracy of 13.8%. For most practical problems, where the strength parameter $\rho B/c_{u0}$ ranges from 0 to 20, the solutions are accurate to within 3-6% (Figure 4.37a, b) The error in predicting the collapse load (the average of both lower and upper bounds) is less than 7% for all ranges of $\rho B/cu_0$, and often less than 2.2%. Note that the accuracy of the computed collapse loads are comparable to results presented previously for smooth rigid footings.
2. Typical computation times for either lower or upper bound analysis (Figure 4.37c) are typically in the range 500-1000 CPU secs (i.e. 8-15 mins). A larger CPU time (i.e. 30-45 mins) may be required to solve only upper bound analysis for very large $\rho B/c_{u0}$. Note that the CPU time required for rough rigid footing is typically larger than that required for a comparable smooth rigid footing.

Figures 4.38-4.47 presents the results of lower and upper bound analyses for rough rigid footings on clay with three strength parameters, $\rho B/c_{u0}$ = 0, 3 and 200 (i.e. $c_{u0}/\rho B$ = 0.005). Figures 4.38 and 4.39 show the stress contours of the lower bound analysis for a rough rigid footing on homogeneous clay ($\rho B/c_{u0}$ = 0). Although the collapse load predictions for rough and smooth footings are almost identical, there are significant differences in the magnitudes of the principal stresses and stress directions at points beneath the footing (compare Figures 4.38 and 4.15). Figure 4.40 shows the normal and shear stress distribution along the rough soil-footing interface. The lower bound analysis predicts that the normal stress is nearly constant along the interface and corresponds very

closely with the exact solution. There are also significant shear stresses along the interface [at $x \geq 0.5(B/2)$], however the shear resistances are not fully mobilized ($\tau/c_{u0} \leq 1$) and thus, no slip takes place. This result is confirmed by the upper bound analysis for the same problem, shown in Figure 4.41. The failure mechanism (Figure 4.41b) shows two zones within the overall failure zone, where there is no plastic deformation (or slip). The velocity vectors (Figure 4.41c) also show a well defined zone below, where the soil moves vertically as a rigid footing. The lower bound analyses (Figure 4.38d) also show a small zone marked "X" beneath the footing [$(\sigma_1-\sigma_3)/2c_{u0} \approx 0.8$], where there is no failure. Hence, this indicates that no plastic occurs in this zone. The size of plastic zone for the rough case (Figure 4.41b) is comparable to that for the smooth case. The velocity field and velocity characteristics (Figures 4.41c and d) are in good agreement with Prandtl's mechanism.

Figures 4.42 and 4.43 show the stress contours obtained from the lower bound analysis for $\rho B/c_{u0} = 3$. The contour of the mean stress corresponds very well with that of the exact solution (Figure 4.43). Note that the contour of the mean stress for a rough footing (Figure 4.43a) is much more rounded than that for a smooth footing (Figure 4.24a). The normal and shear stress distributions along the interface are shown in Figure 4.44. The results in Figure 4.44b show that the shear resistance is fully mobilized towards the edge of the footing $X/(B/2) > 0.6$ and hence, slip occurs in this region. This behavior corresponds to 'wide rough footing' behavior, mentioned in Davis and Booker (1973). Figure 4.45 shows the results of the upper bound analysis of a rough rigid footing for $\rho B/c_{u0} = 3$. Evidence of slip at the interface marked by zone "X" (Figure 4.45c) also agrees with the lower bound analysis.

Figure 4.46 shows the normal and shear stress distributions for a rough footing with $c_{u0}/\rho B = 0.005$. The lower bound analysis predicts that the normal contact stress increases almost from zero at the edge of footing, while the interface shear resistance is fully mobilized for $X/(B/2) > 0.3$ (to the edge of footing). Notice that the slip zone in this case is larger than that of the previous case. Therefore, based on the results of $\rho B/c_{u0} = 3$ and $c_{u0}/\rho B = 0.005$, as the strength parameter increases, the slip begins to propagate from the edge of footing towards the center. The corresponding results of the upper bound

analysis are shown in Figure 4.47. These analyses show that slip occurs over all footing contacts. Note that the results of rough footing for $c_{u0}/\rho B = 0.005$ are much like those for smooth footing, for $c_{u0} = 0$ (cf. Figure 4.29).

Mesh	Mesh size		Number of			Extension elements	Mesh No.	N_c	N_c Error	CPU Time
			Nodes	Triangles	Discontinuities					
	X/(B/2)	Y/(B/2)	N	E	D				(%)	(sec)
S1	3.5	2.0	309	103	143	No	S1-NE-C	4.643	-9.69	35
			309	103	143	Yes	S1-E-C	4.232	-17.68	37
			507	169	241	No	S1-NE-F	4.922	-4.26	115
			507	169	241	Yes	S1-E-F	4.325	-15.87	138
S2	5.0	4.0	441	147	205	No	S2-NE-C	4.610	-10.33	76
			441	147	205	Yes	S2-E-C	4.610	-10.33	72
			603	201	205	No	S2-NE-F	4.922	-4.26	154
			603	201	205	Yes	S2-E-F	4.922	-4.26	182
S3	6.0	5.0	516	172	239	No	S3-NE-C	4.628	-9.98	85
			516	172	239	Yes	S3-E-C	4.628	-9.98	102
			687	229	325	No	S3-NE-F	4.922	-4.26	211
			687	229	325	Yes	S3-E-F	4.922	-4.26	246

Notes:
X = the lateral size of the domain boundary
Y = the vertical size of the domain boundary
B = the full width of the footing
CPU time = Run on DEC ALPHA 3000-300X workstation
For all meshes, the number of sides in linearized yield surface, p = 24

Table 4.1 Effect of extension elements and the sizes of domain boundary on lower bound analyses for a smooth rigid footing on homogeneous clay

p	N_c	N_c Error (%)	CPU Time (sec)
12	4.820	-6.24	14
24	4.922	-4.26	20
36	4.936	-3.99	23

Notes:

p = Number of sides in linearized yield surface

CPU time = Run on DEC ALPHA 3000-300X workstation

The mesh used in all analyses = S2-E-F

The lateral and vertical sizes of the domain boundary = 5(B/2) and 4(B/2)

Table 4.2 Effect of yield surface linearization on lower bound analyses for a smooth rigid footing on homogeneous clay

Mesh Arrangement	Mesh No.	Number of			N_c	N_c error	CPU Time
		Nodes N	Triangles E	Discontinuities D		(%)	(sec)
Type A	A1	279	80	129	4.661	-9.34	9
	A2	956	1033	1032	4.844	-5.78	263
Type B	B1	441	147	205	4.610	-10.33	72
	B2	603	201	304	4.922	-4.26	182
Type C	C1	390	117	178	4.975	-3.23	34
	C2	699	220	330	5.042	-1.93	213

Notes:

CPU time = Run on DEC ALPHA 3000-300X workstation

For all meshes, the number of sides in linearized yield surface, p = 24

Extension elements were used with all meshes

For all meshes, the lateral and vertical sizes of the domain boundary = 5(B/2) and 4(B/2)

Table 4.3 Effect of mesh arrangement on lower bound analyses for a smooth rigid footing on homogeneous clay

Mesh	Mesh size		N_o	N_o error	CPU Time
	X/(B/2)	Y/(B/2)		(%)	(sec)
su1	3.0	1.5	5.261	2.33	6
su2	4.0	2.0	5.252	2.16	20
su3	4.5	2.5	5.252	2.16	40

Notes:

X = the lateral size of the domain boundary

Y = the vertical size of the domain boundary

B = the full width of the footing

CPU time = Run on DEC ALPHA 3000-300X workstation

For all meshes, the number of sides in linearized yield surface, p = 24

Table 4.4 Effect of the discretized domain size in upper bound analyses for a smooth rigid footing on homogeneous clay

p	N_c	N_c Error (%)	CPU Time (sec)
12	5.292	2.94	14
24	5.252	2.16	20
36	5.249	2.10	23

Notes:

p = Number of sides in linearized yield surface

CPU time = Run on DEC ALPHA 3000-300X workstation

The mesh used in all analyses = su2

The lateral and vertical sizes of the domain boundary = 4(B/2) and 2(B/2)

Table 4.5 Effect of yield surface linearization on upper bound analyses for a smooth rigid footing on homogeneous clay

Mesh Arrangement	Mesh No.	Numbers of			N_c	N_c error	CPU Time
		Nodes N	Triangles E	Discontinuities D		(%)	(sec)
Type D	D1	384	128	180	5.252	2.16	19
	D2	1536	512	744	5.210	1.34	560
Type E	E1	378	126	174	5.293	2.96	39
	E2	510	170	238	5.274	2.59	98
Type F	F1	291	97	133	5.252	2.16	17
	F2	405	135	187	5.201	1.17	38

Notes:

CPU time = Run on DEC ALPHA 3000-300X workstation

For all meshes, the number of sides in linearized yield surface, p = 24

Extension elements were used with all meshes

For all meshes, the lateral and vertical sizes of the domain boundary = 4(B/2) and 2(B/2)

Table 4.6 Effect of mesh arrangement on upper bound analyses for a smooth rigid footing on homogeneous clay

Numerical Solution	Mesh No.	Nc	Nc Error (%)	CPU Time (sec.)
Lower Bound (LB)	D2	5.042	-1.93	213
Upper Bound (UB)	C2	5.210	1.34	560

Notes:
Bounds = 3.3%
CPU time = Run on DEC ALPHA 3000-300X workstation
For both meshes, the number of sides in linearized yield surface, p = 24

Table 4.7 Summary of the results of numerical limit analyses for a smooth rigid footing on homogeneous clay

$c_{u0}/(\gamma B)$	Lower bound		Upper bound		F_s bounds	Exact Solution	Best Estimate, F_s	F_s error
	F_s	CPU Time (sec.)	F_s	CPU Time (sec.)	(%)	F_s	=0.5(LB.+UB.)	(%)
0	0.992	120	1.133	1566	13.3	1.000	1.062	6.2
0.0025	1.112	206	1.233	1655	10.4	1.218	1.172	-3.7
0.005	1.184	228	1.314	409	10.4	1.310	1.249	-4.7
0.01	1.276	199	1.402	426	9.4	1.382	1.339	-3.1
0.02	1.357	201	1.466	495	7.7	1.435	1.412	-1.6
0.03	1.394	212	1.489	489	6.6	1.453	1.442	-0.8
0.04	1.404	221	1.492	546	6.1	1.453	1.448	-0.3
0.05	1.403	216	1.502	407	6.8	1.447	1.453	0.4

$\gamma B/c_{u0}$	Lower bound		Upper bound		F_s bounds	Exact Solution	Best Estimate, F_s	F_s error
	F_s	CPU Time (sec.)	F_s	CPU Time (sec.)	(%)	F_s	=0.5(LB.+UB.)	(%)
16.0	1.397	227	1.487	556	6.2	1.435	1.442	0.5
12.0	1.379	244	1.461	416	5.8	1.412	1.420	0.5
8.0	1.337	256	1.409	499	5.2	1.368	1.373	0.4
5.0	1.278	286	1.336	531	4.5	1.305	1.307	0.1
3.0	1.208	300	1.260	622	4.2	1.218	1.234	1.3
1.5	1.127	354	1.169	667	3.6	1.132	1.148	1.4
0.0	0.981	213	1.013	560	3.3	1.000	0.997	-0.3

Notes:

$$F_s = \frac{(Q / B)}{(2 + \pi)c_{u0} + \rho B / 4}$$

where Q = Collapsed load

r = change of undrained shear strength with depth

B = width of footing

c_{u0} = undrained shear strength at surface

Exact Solutions are based on Davis and Booker (1973)

Table 4.8 Summary of lower and upper bound analyses for a smooth rigid footing on non-homogeneous clay, where strength increases linearly with depth

Strength parameter	F_r				
	Interface shear resistance (i.e. $c_i = c_{u0}$)		No slip allowed		Exact solutions
	UB.	error	UB.	error	
$rB/c_{u0}=0$	1.018	1.8	1.018	1.8	1.000
$rB/c_{u0}=3$	1.455	2.6	1.498	5.6	1.418
$c_{u0}/(rB)=0.005$	1.446	0.3	1.962	36.1	1.442
$c_{u0}/(rB)=0.0$	1.133	13.3	1.873	87.3	1.000

Notes:

$$F_r = \frac{(Q/B)}{(2+\pi)c_{u0} + \rho B/4}$$

where Q = Collapsed load

r = change of undrained shear strength with depth

B = width of footing

c_{u0} = undrained shear strength at surface

UB. = Numerical upper bound

Exact Solutions are based on Davis and Booker (1973)

Interface shear resistance = the wide rough footing

No Slip allowed = the narrow rough footing

Table 4.9 Comparison of numerical upper bound analyses with two types of boundary condition for rough rigid footings on non-homogeneous clay layers

$c_{u0}/(rB)$	Lower bound		Upper bound		F_r bounds	Exact Solution	Best Estimate, F_r	F_r error
	F_r	CPU Time (sec.)	F_r	CPU Time (sec.)	(%)	F_r	=0.5(LB.+UB.)	(%)
0	0.987	405	1.133	1550	13.8	1.000	1.060	6.0
0.0025	1.201	642	1.337	1993	10.7	1.318	1.269	-3.7
0.005	1.321	577	1.446	2200	9.0	1.442	1.384	-4.0
0.01	1.452	632	1.579	2307	8.3	1.577	1.516	-3.9
0.02	1.578	597	1.693	2500	7.0	1.691	1.635	-3.3
0.03	1.628	731	1.734	2672	6.3	1.733	1.681	-3.0
0.04	1.651	686	1.747	2805	5.7	1.745	1.699	-2.6
0.05	1.655	775	1.746	2780	5.4	1.738	1.700	-2.2

$(rB)/c_{u0}$	Lower bound		Upper bound		F_r bounds	Exact Solution	Best Estimate, F_r	F_r error
	F_r	CPU Time (sec.)	F_r	CPU Time (sec.)	(%)	F_r	=0.5(LB.+UB.)	(%)
16.0	1.647	824	1.762	672	6.7	1.729	1.704	-1.4
12.0	1.624	645	1.729	732	6.3	1.688	1.677	-0.7
8.0	1.571	707	1.662	927	5.6	1.618	1.617	-0.1
5.0	1.487	783	1.567	975	5.2	1.529	1.527	-0.1
3.0	1.389	830	1.455	1123	4.6	1.418	1.422	0.3
1.5	1.264	934	1.332	386	5.3	1.270	1.298	2.2
0.0	0.981	238	1.018	571	3.7	1.000	0.999	-0.1

Notes:

$$F_r = \frac{(Q / B)}{(2+\pi)c_{u0} + \rho B / 4}$$

where Q = Collapsed load

r = change of undrained shear strength with depth

B = width of footing

c_{u0} = undrained shear strength at surface

Exact Solutions are based on Davis and Booker (1973)

Table 4.10 Summary of lower and upper bound analyses for a rough rigid footing on non-homogeneous clay, where strength increases linearly with depth

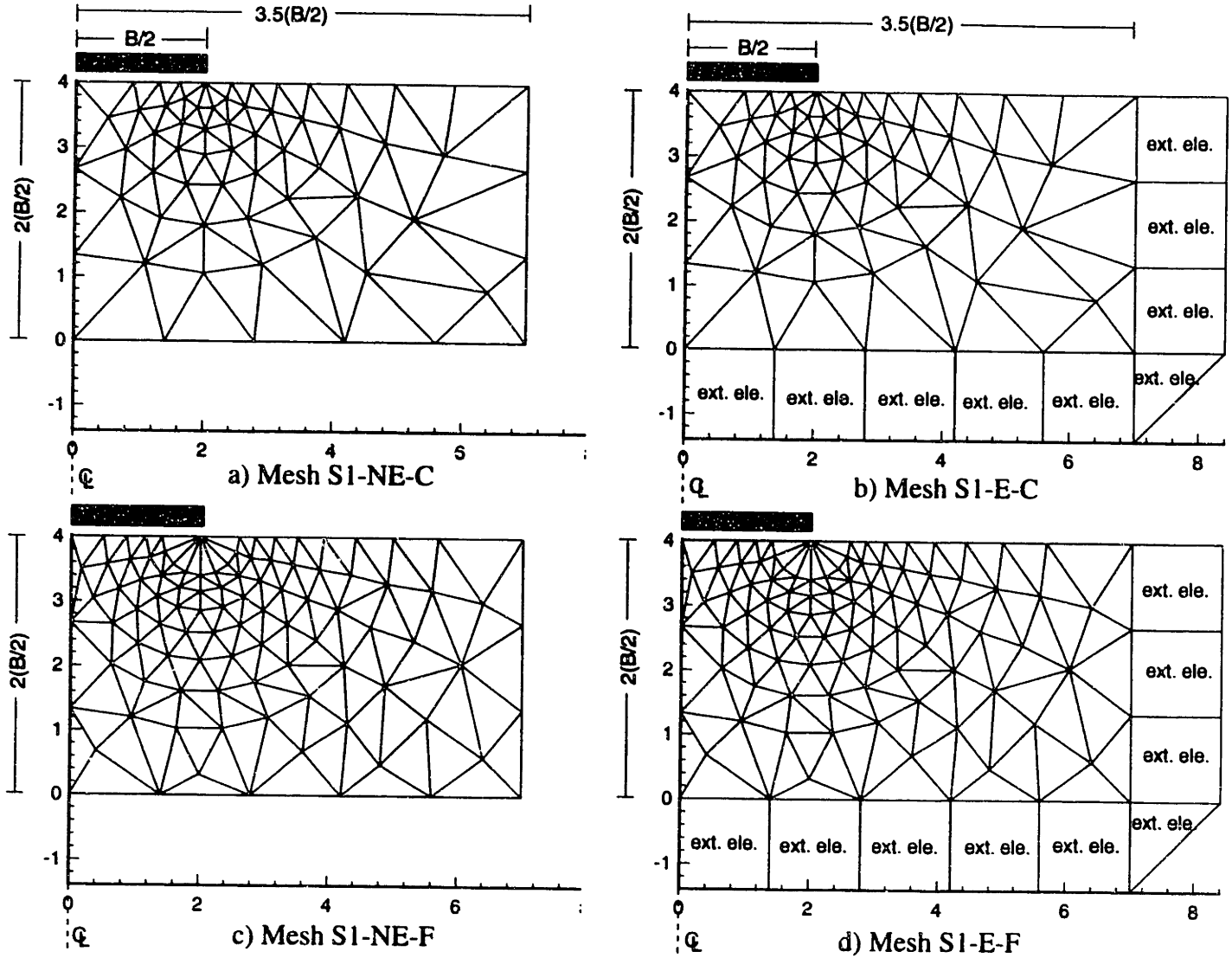

Fig. 4.1 S1 meshes used to study the effects of discretization in lower bound analyses

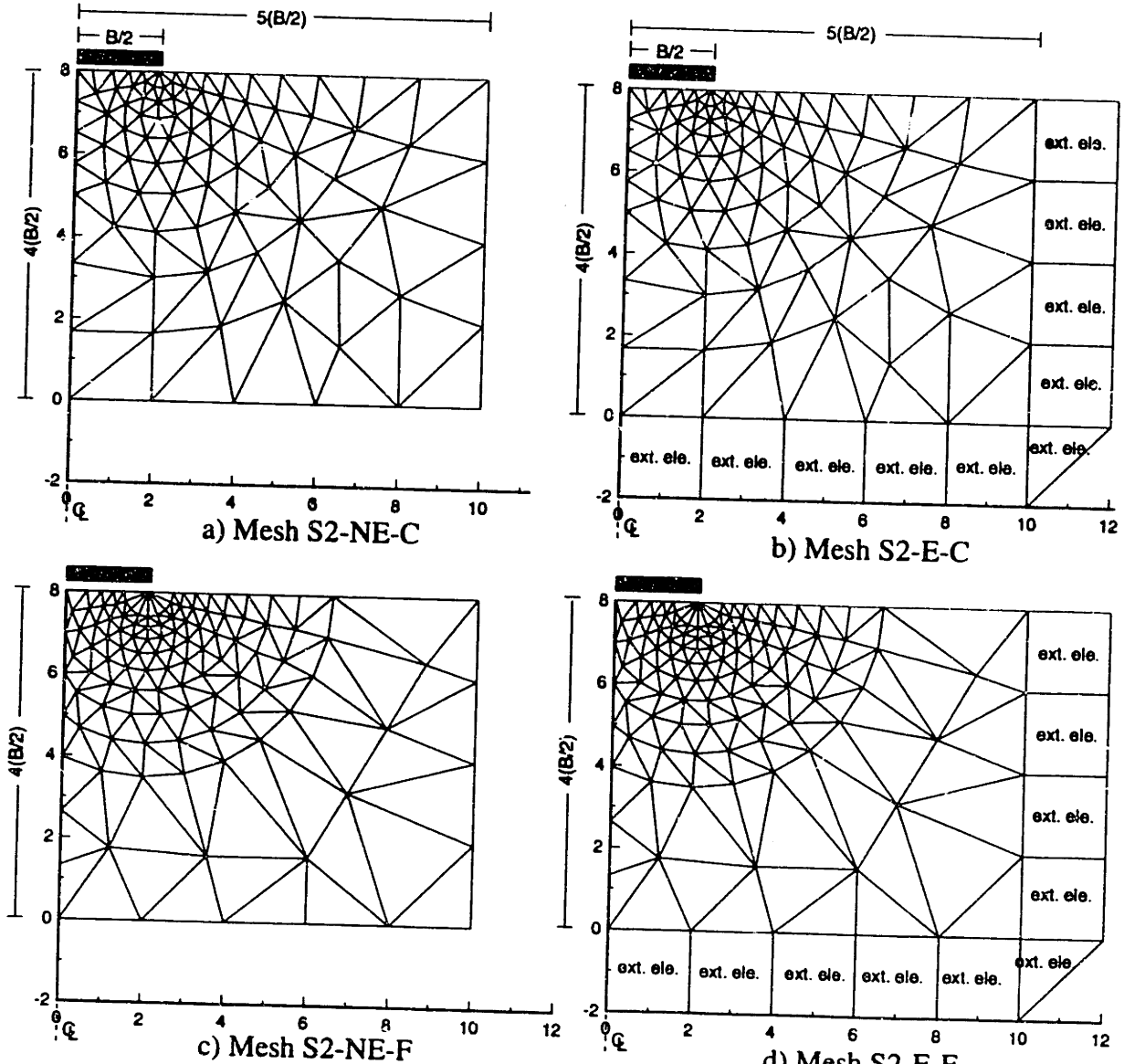

Fig. 4.2 S2 meshes used to study the effects of discretization in lower bound analyses

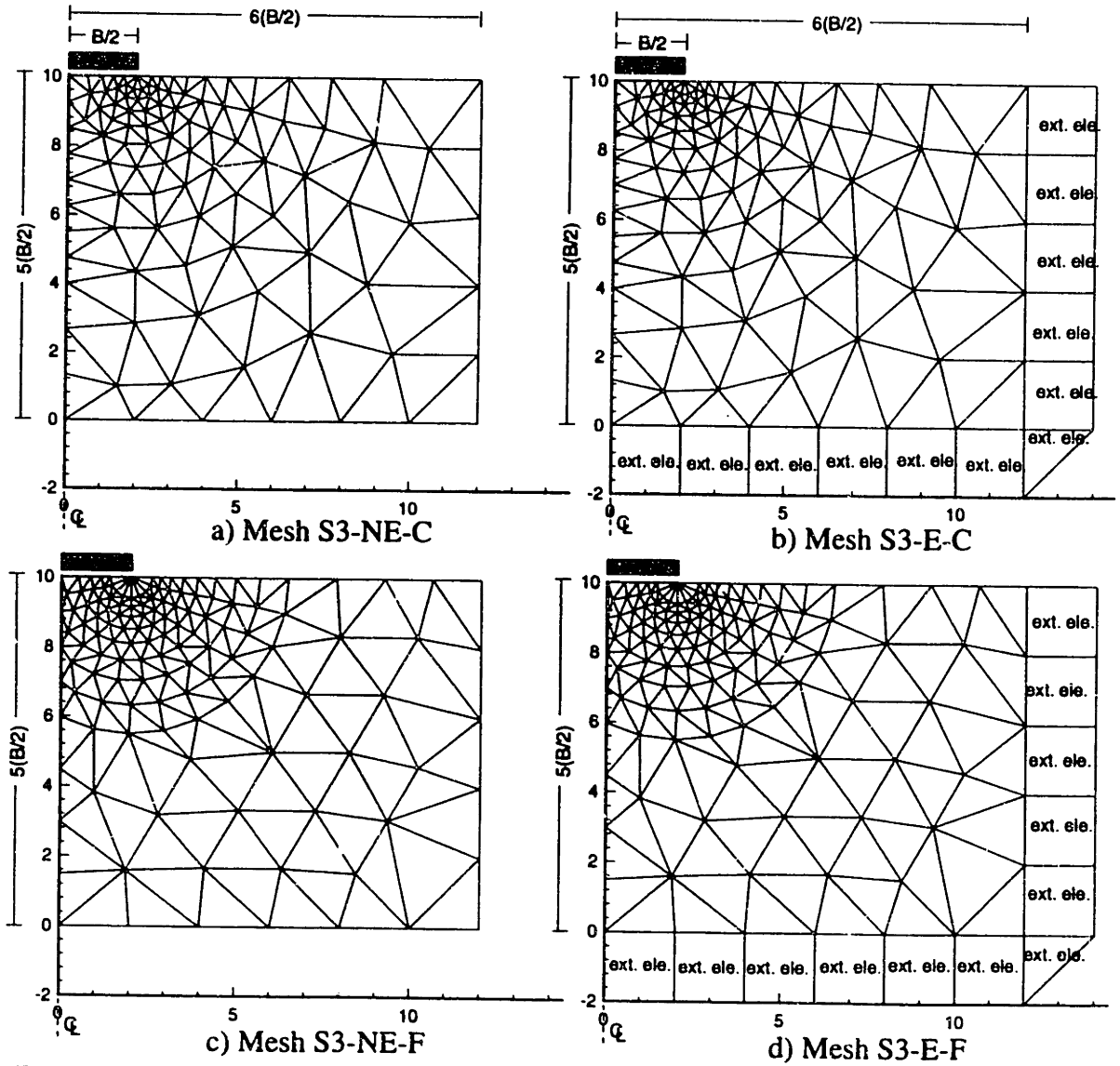

Fig. 4.3 S3 meshes used to study of the effects of discretization in lower bound analyses

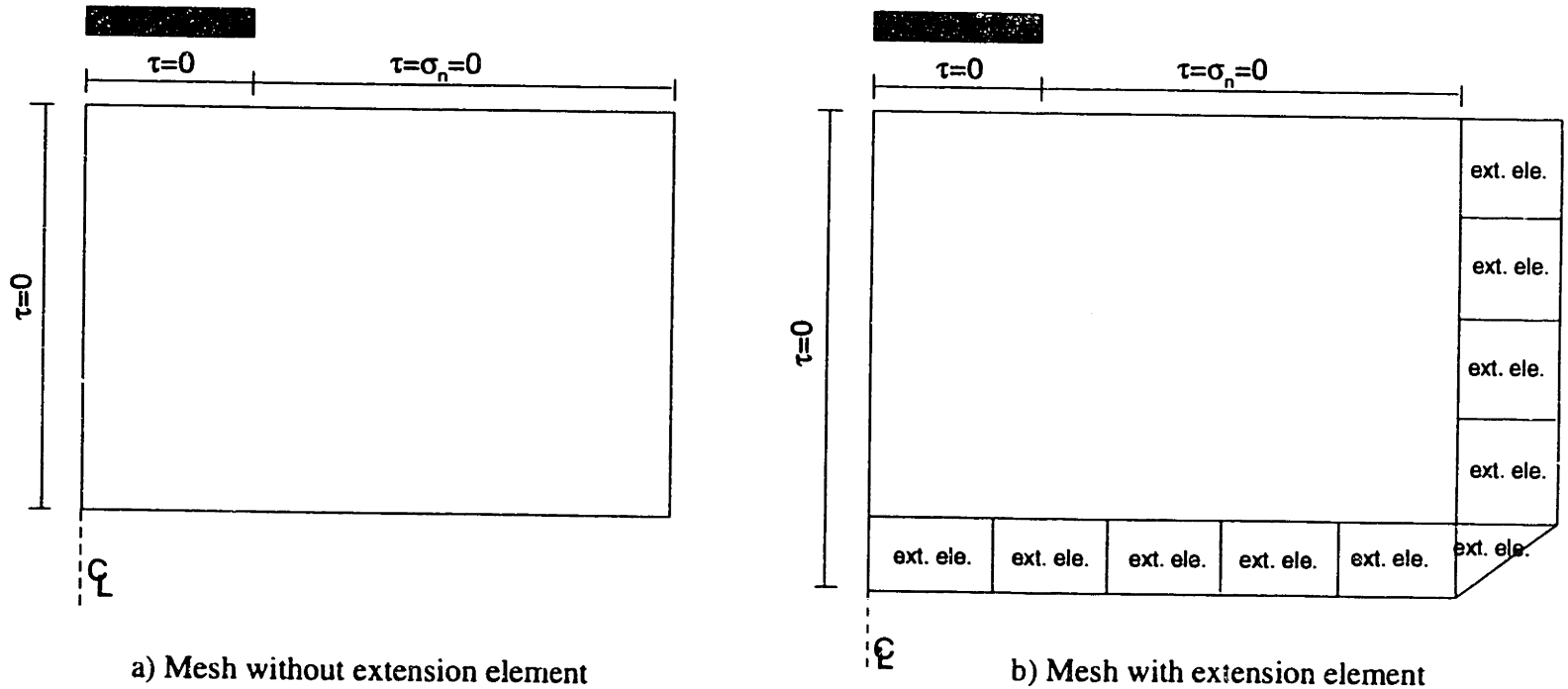

a) Mesh without extension element

b) Mesh with extension element

Fig. 4.4 Stress boundary conditions for lower bound analyses of a smooth rigid footing

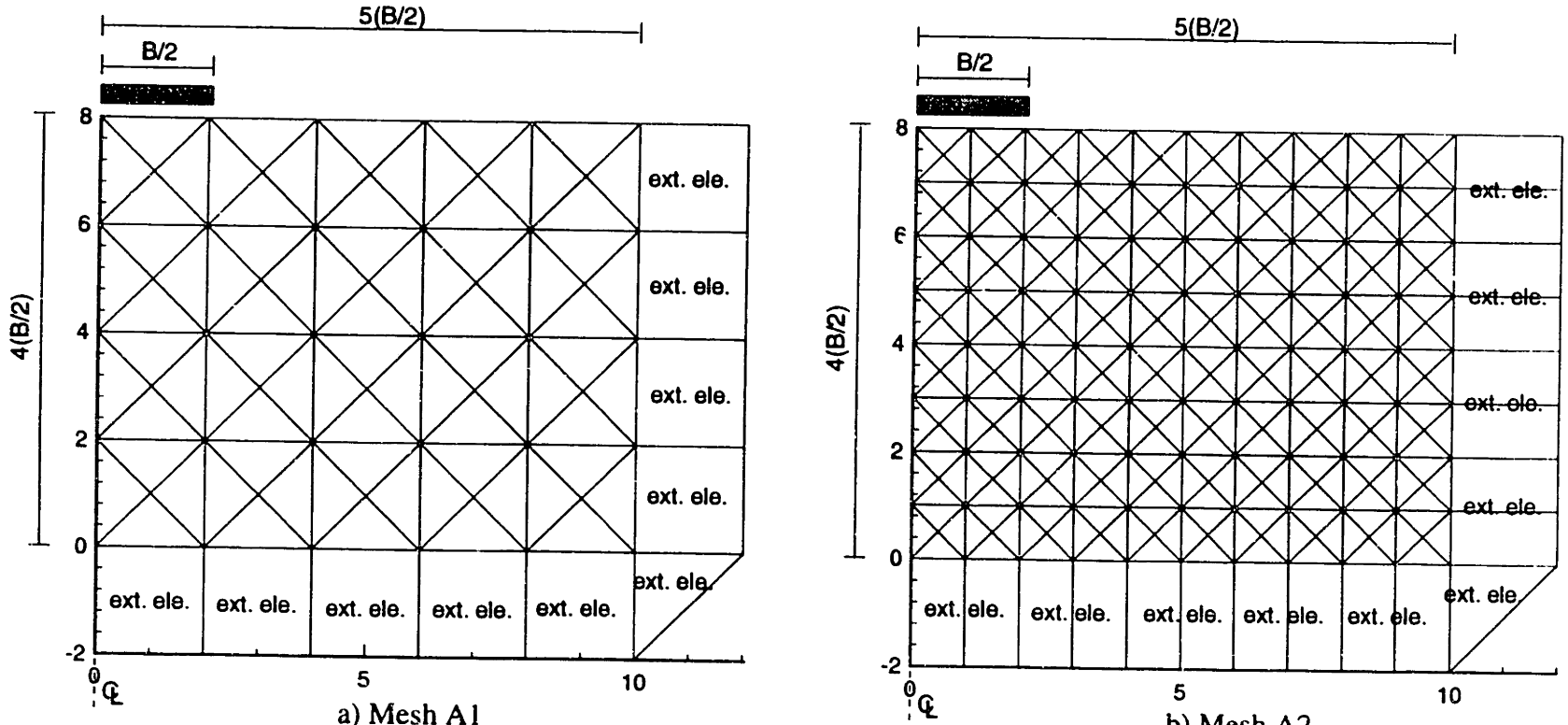

a) Mesh A1 b) Mesh A2

Fig. 4.5 Type A meshes used to study the effect of mesh arrangement in lower bound analyses

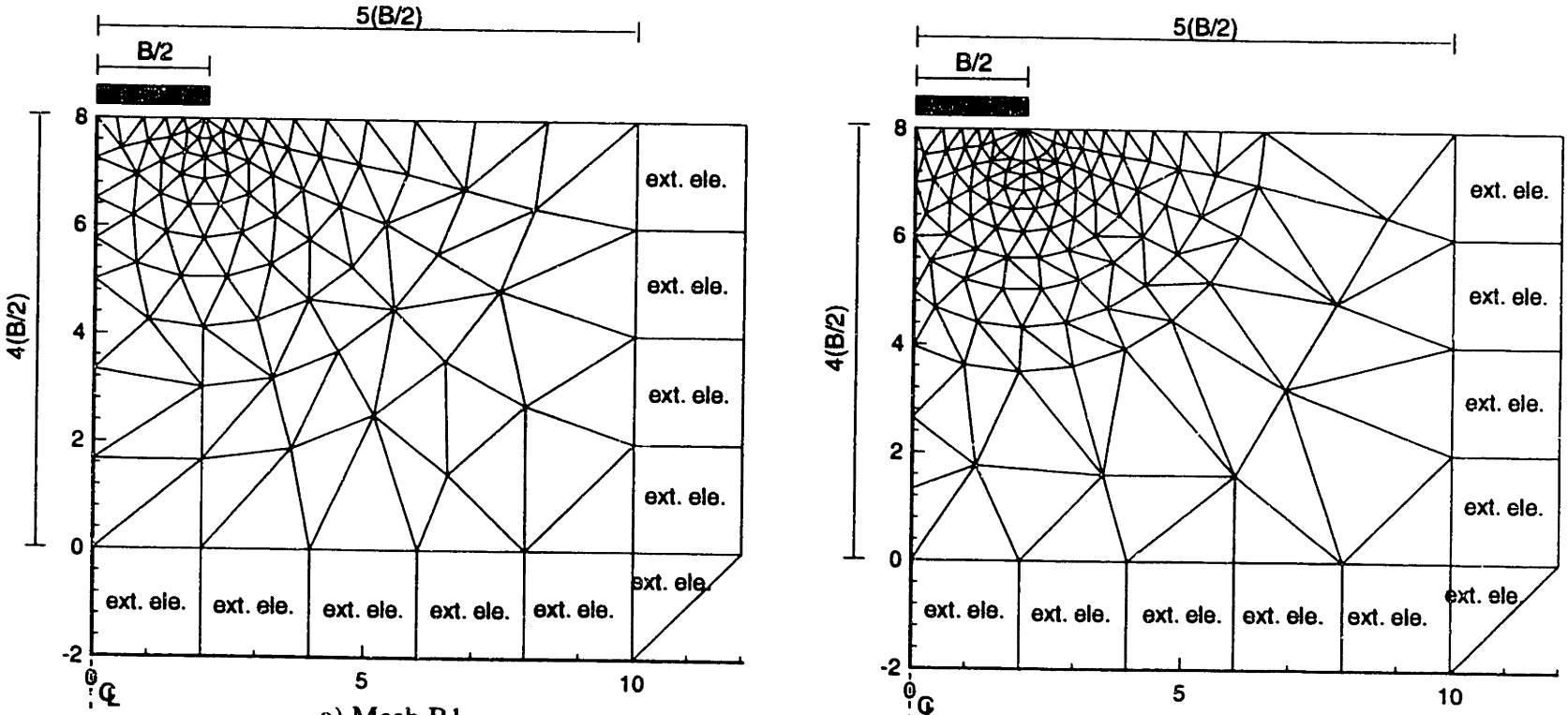

a) Mesh B1 b) Mesh B2

Fig. 4.6 Type B meshes used to study the effect of mesh arrangement in lower bound analyses

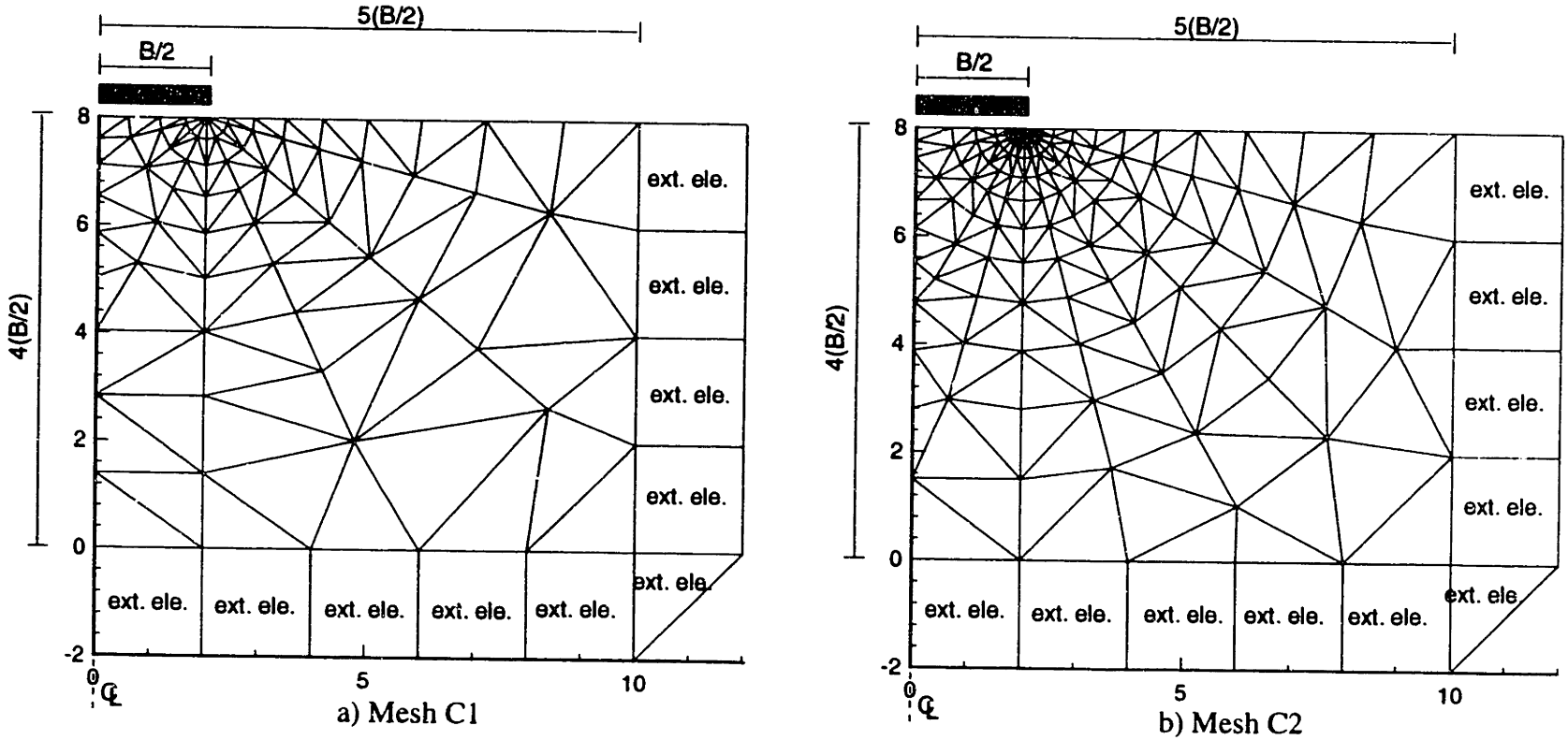

Fig. 4.7 Type C meshes used to study the effect of mesh arrangement in lower bound analyses

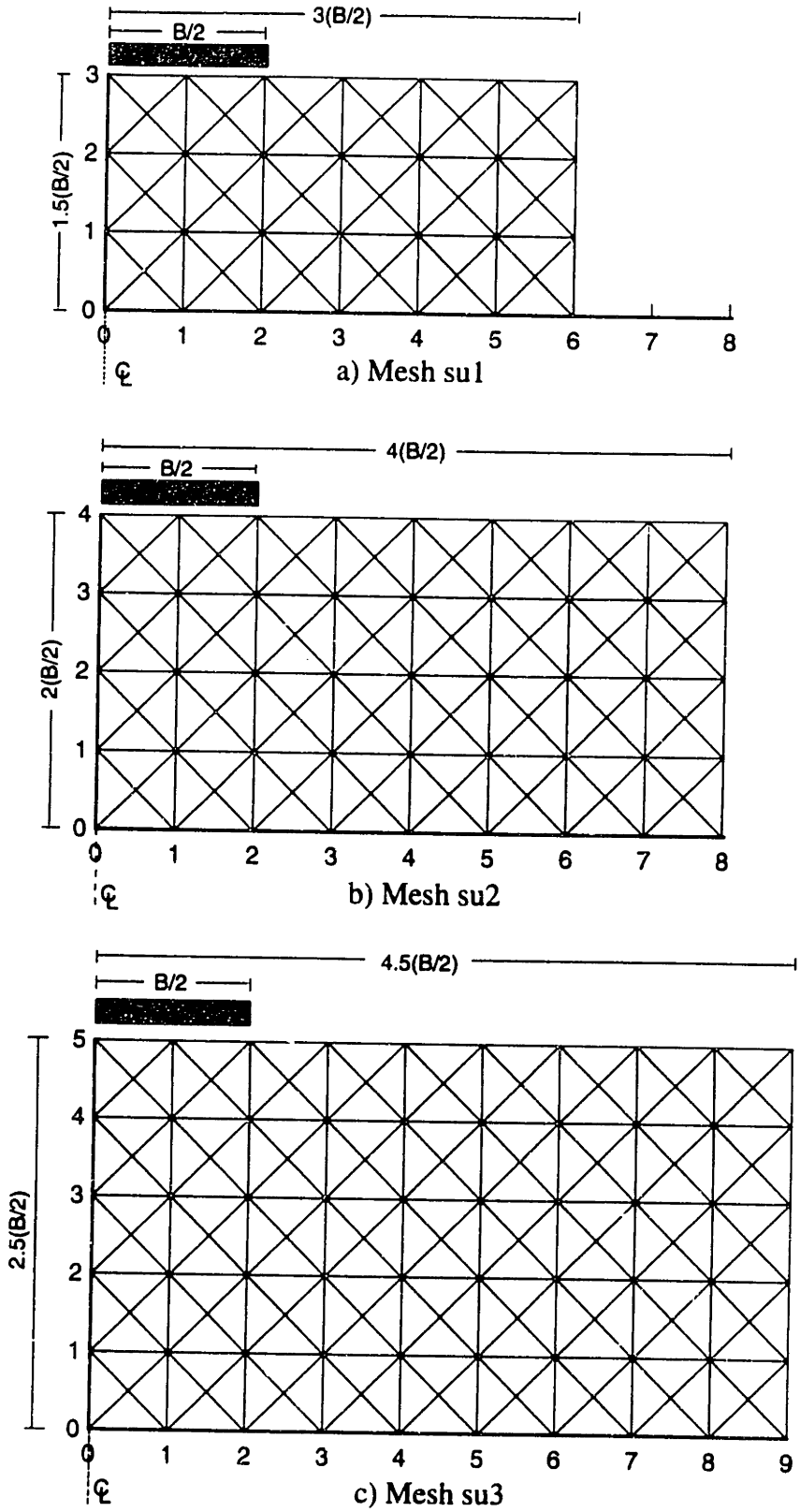

Fig. 4.8 Meshes used to study the effect of size of the discretized domain in upper bound analyses

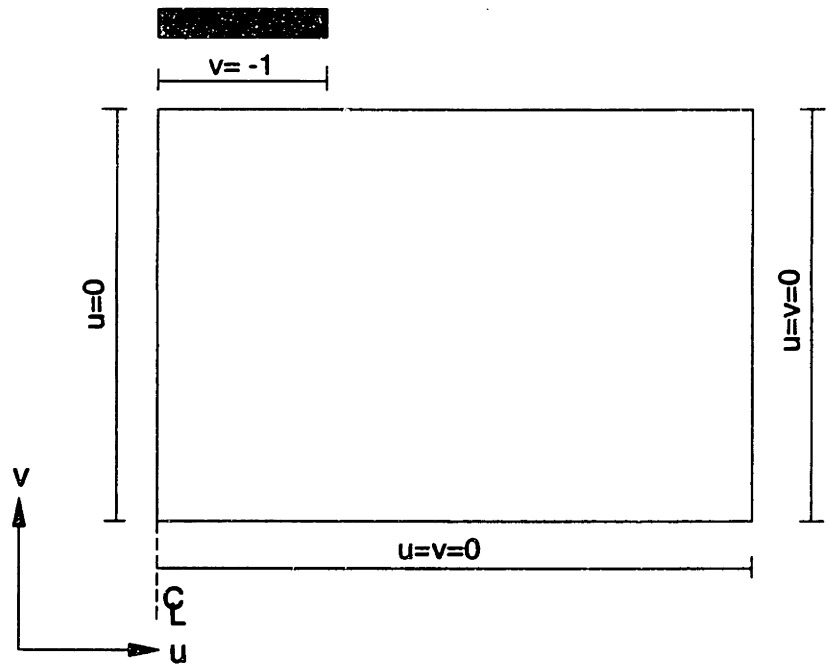

Fig. 4.9 Velocity boundary conditions for upper bound analysis of a smooth rigid footing

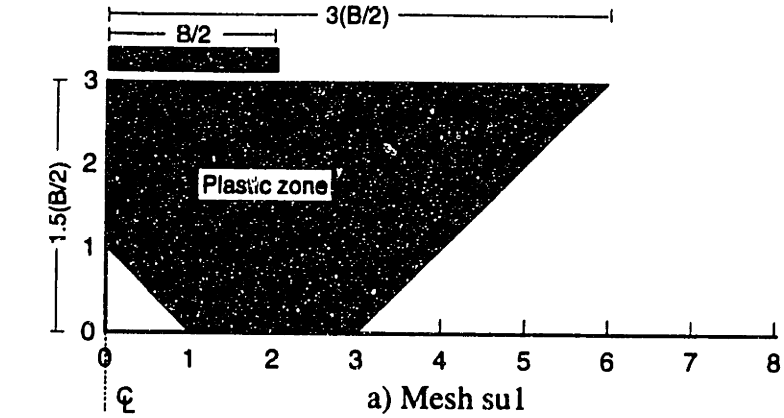

a) Mesh su1

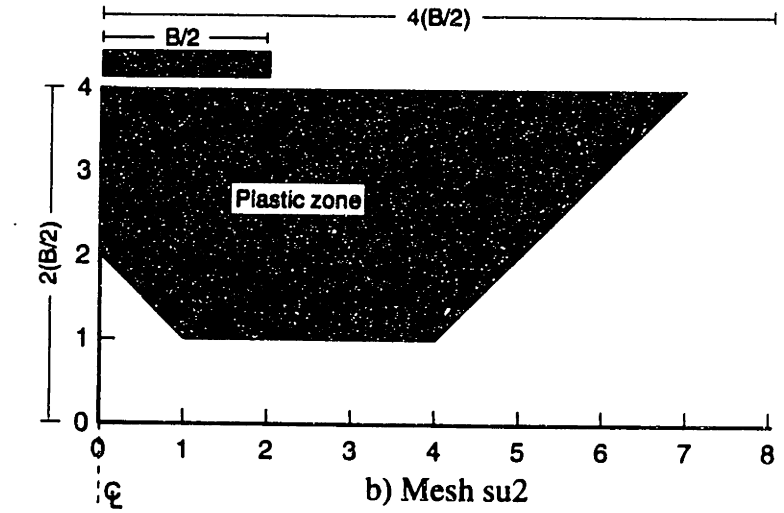

b) Mesh su2

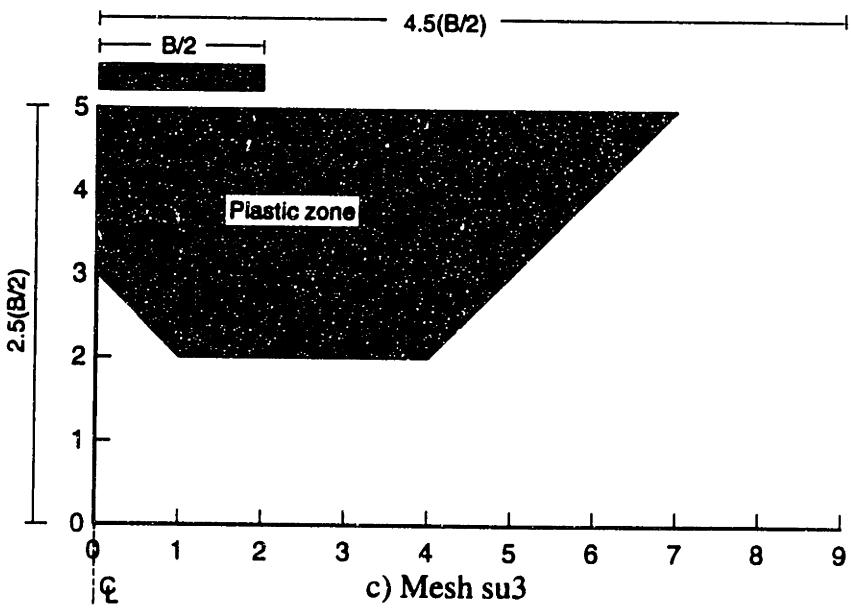

c) Mesh su3

Fig. 4.10 Plastic zone of meshes with different sizes of domain boudary

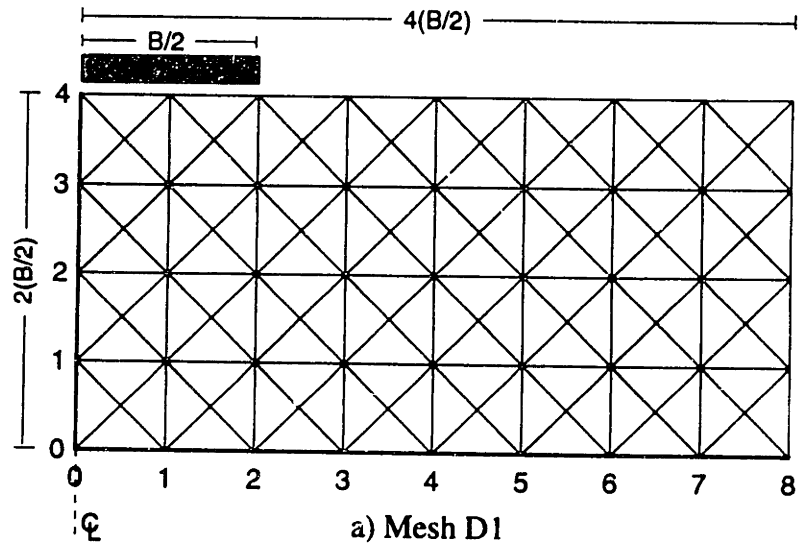

a) Mesh D1

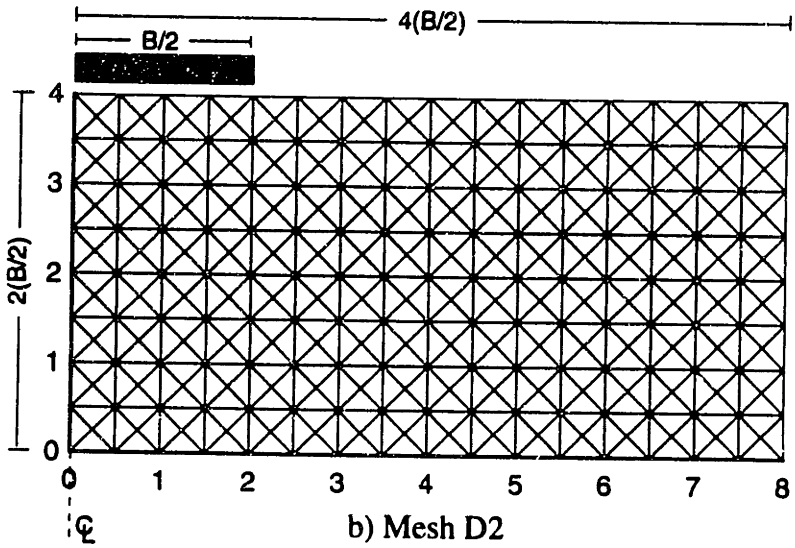

b) Mesh D2

Fig. 4.11 Type D meshes used to study the effects of mesh arrangement for upper bound analyses

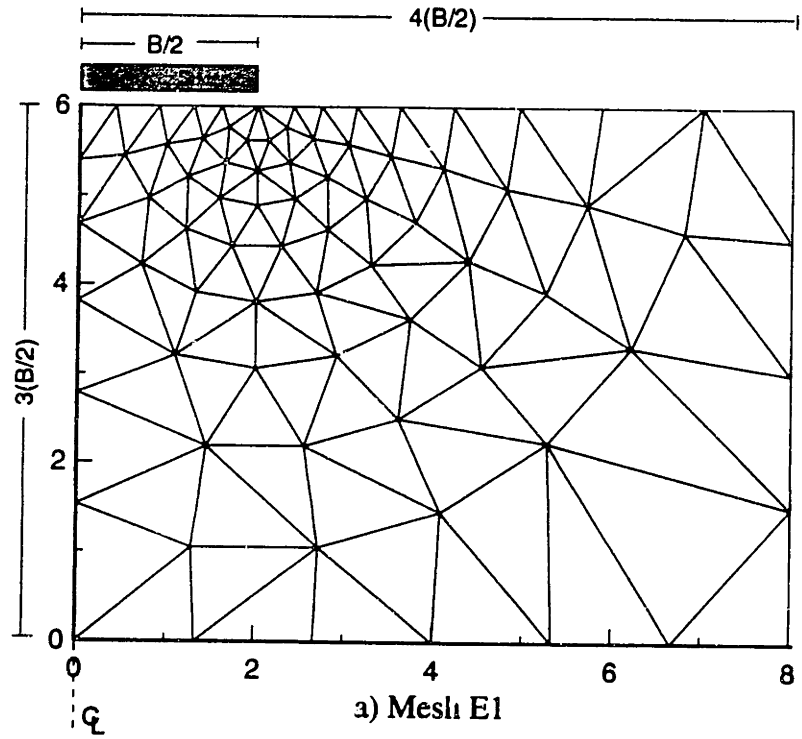

a) Mesh E1

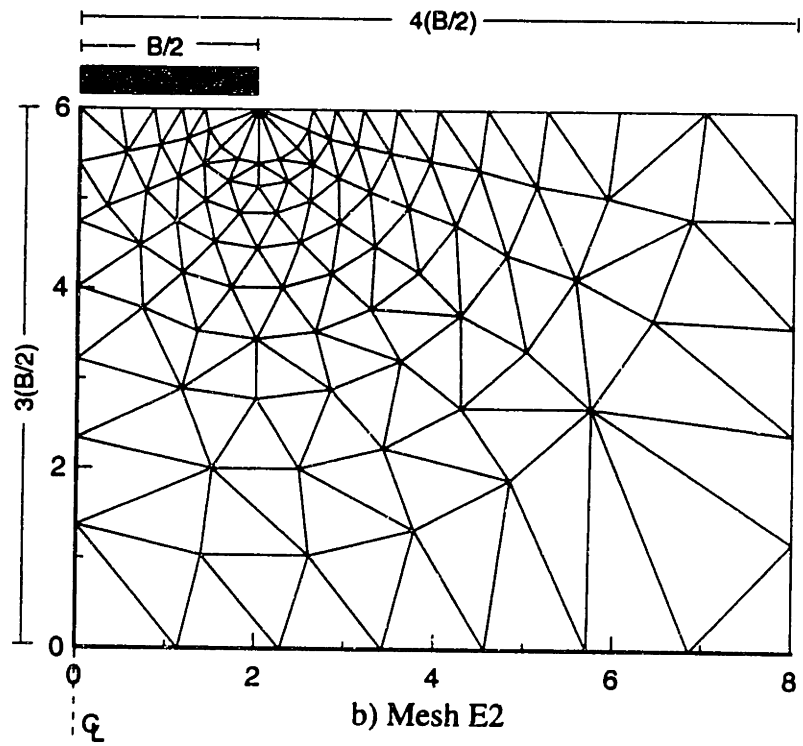

b) Mesh E2

Fig. 4.12 Type E meshes used to study the effects of mesh arrangement for upper bound analyses

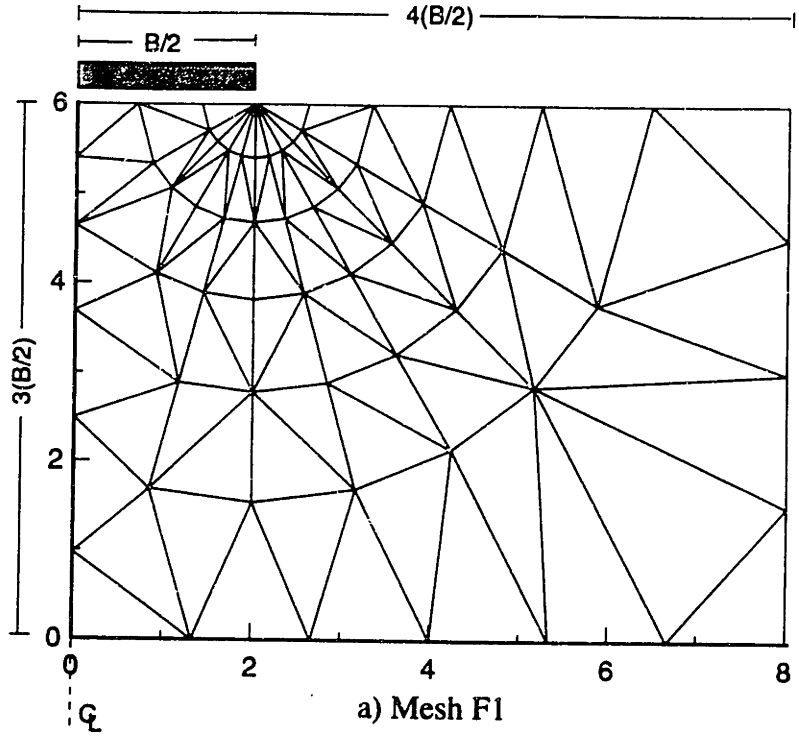

a) Mesh F1

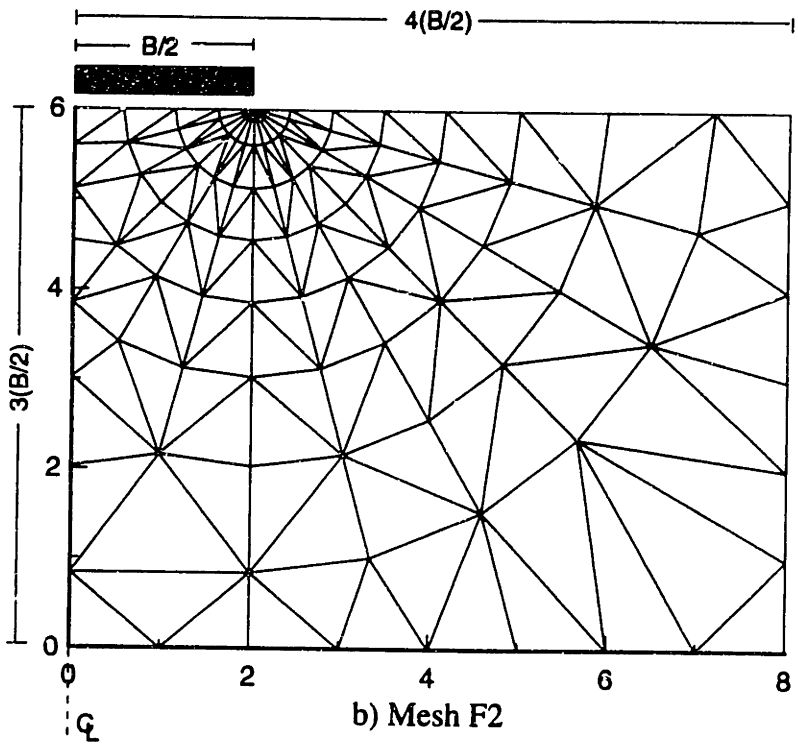

b) Mesh F2

Fig. 4.13 Type F meshes used to study the effects of mesh arrangement for upper bound analyses

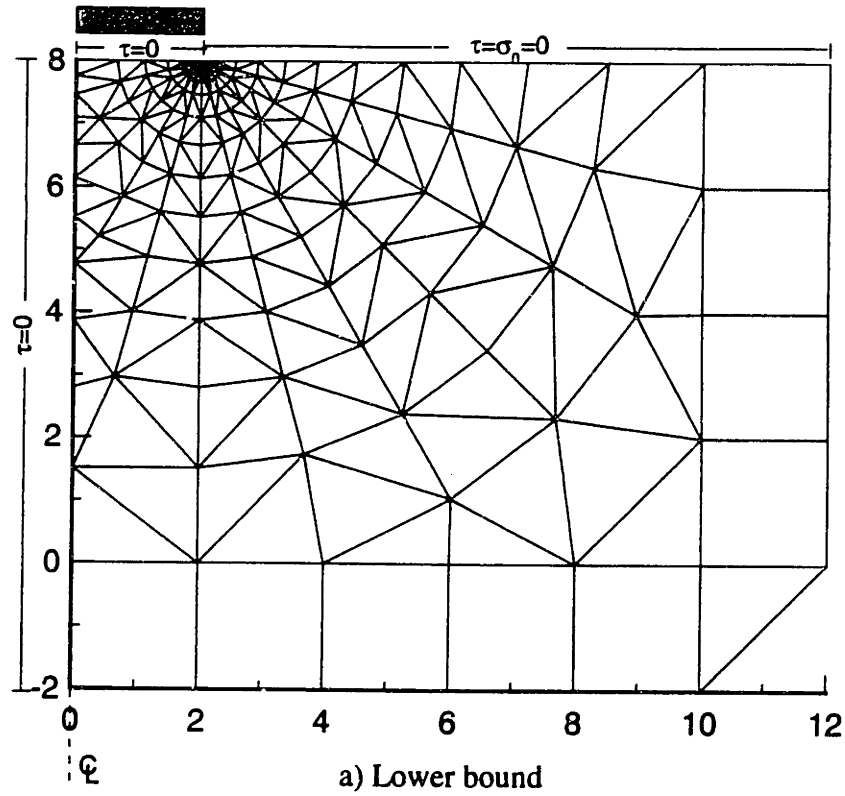

a) Lower bound

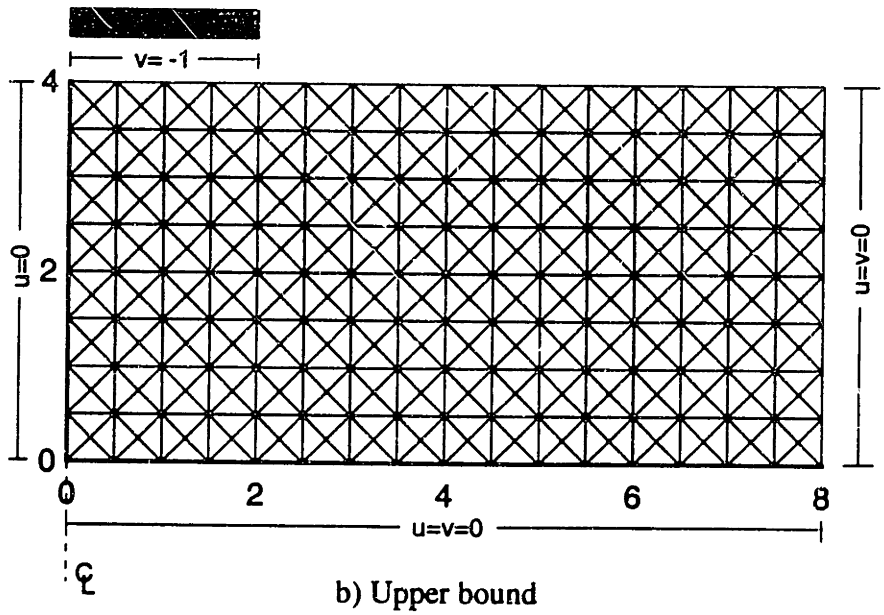

b) Upper bound

Fig. 4.14 Meshes used in a smooth rigid footings on homogeneous clay

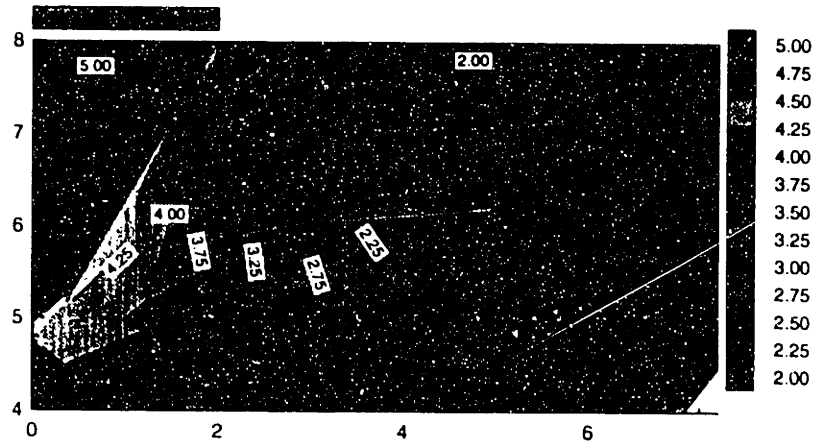

a) Major principal stress, σ_1/c_{u0}

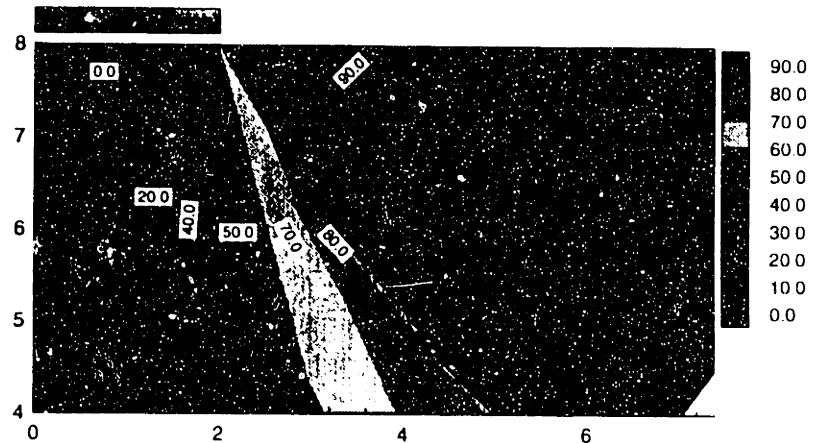

c) Direction of major principal stress to vertical, δ

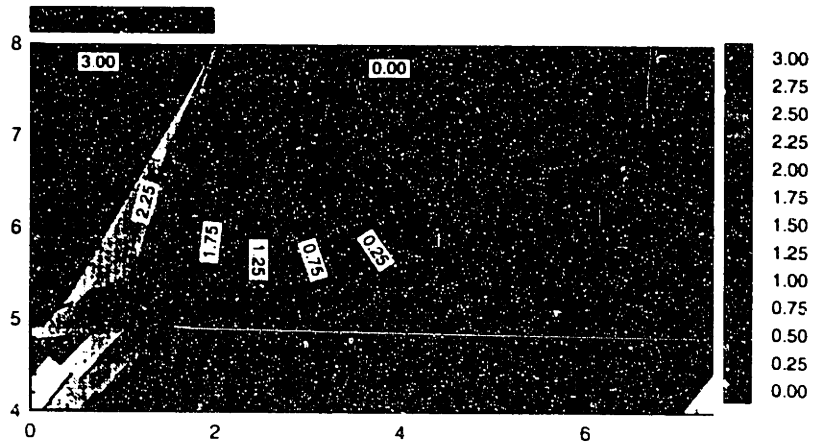

b) Minor principal stress, σ_3/c_{u0}

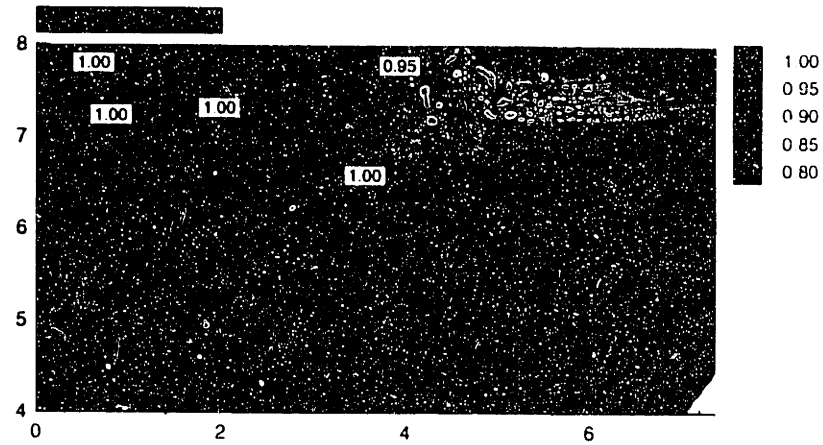

d) Failure zone, $(\sigma_1-\sigma_3)/2c_{u0}$

Fig. 4.15 Summary of lower bound results for a smooth rigid footing on homogeneous clay

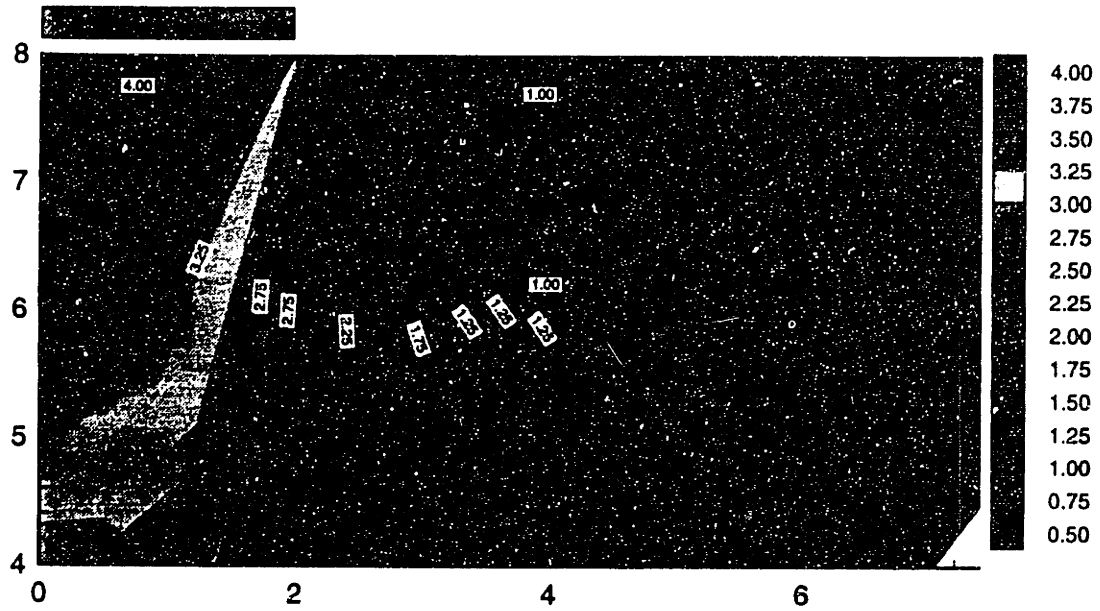

Fig. 4.16 Lower bound calculations of mean stress of for a smooth rigid footing on homogeneous clay, p/c_{u0}

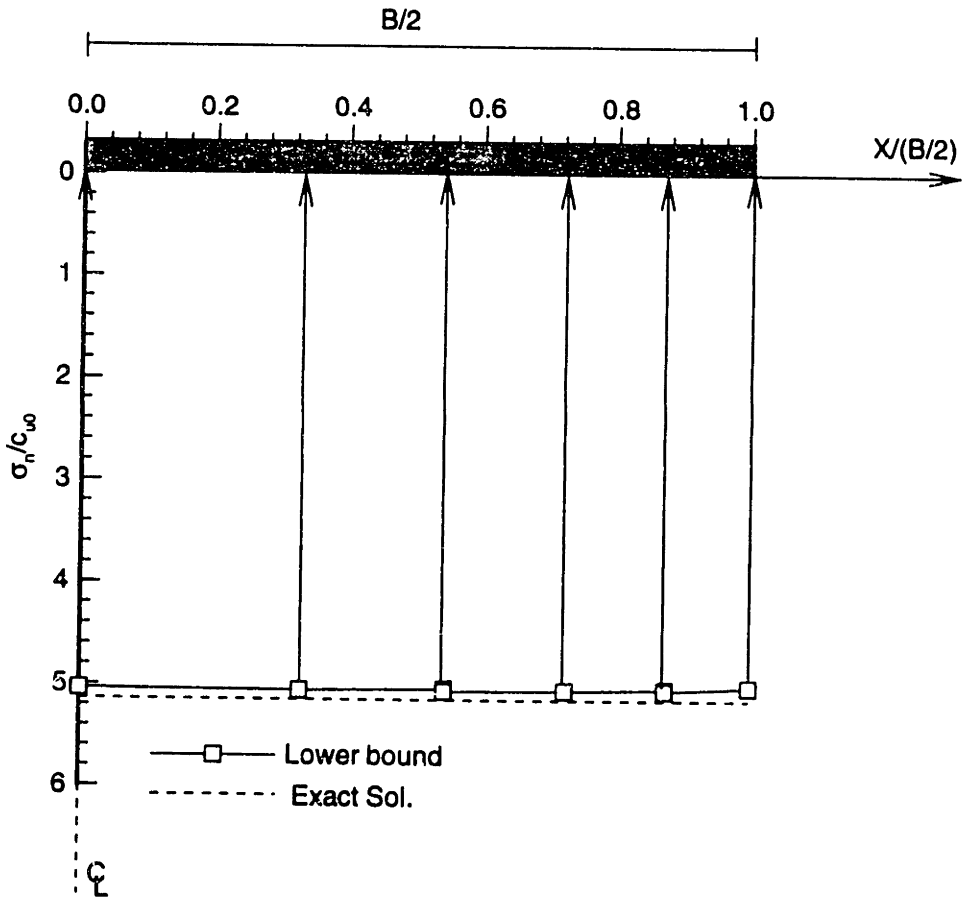

Fig. 4.17 Lower bound and exact solutions for normal contact stress beneath a smooth rigid footing on homogeneous clay

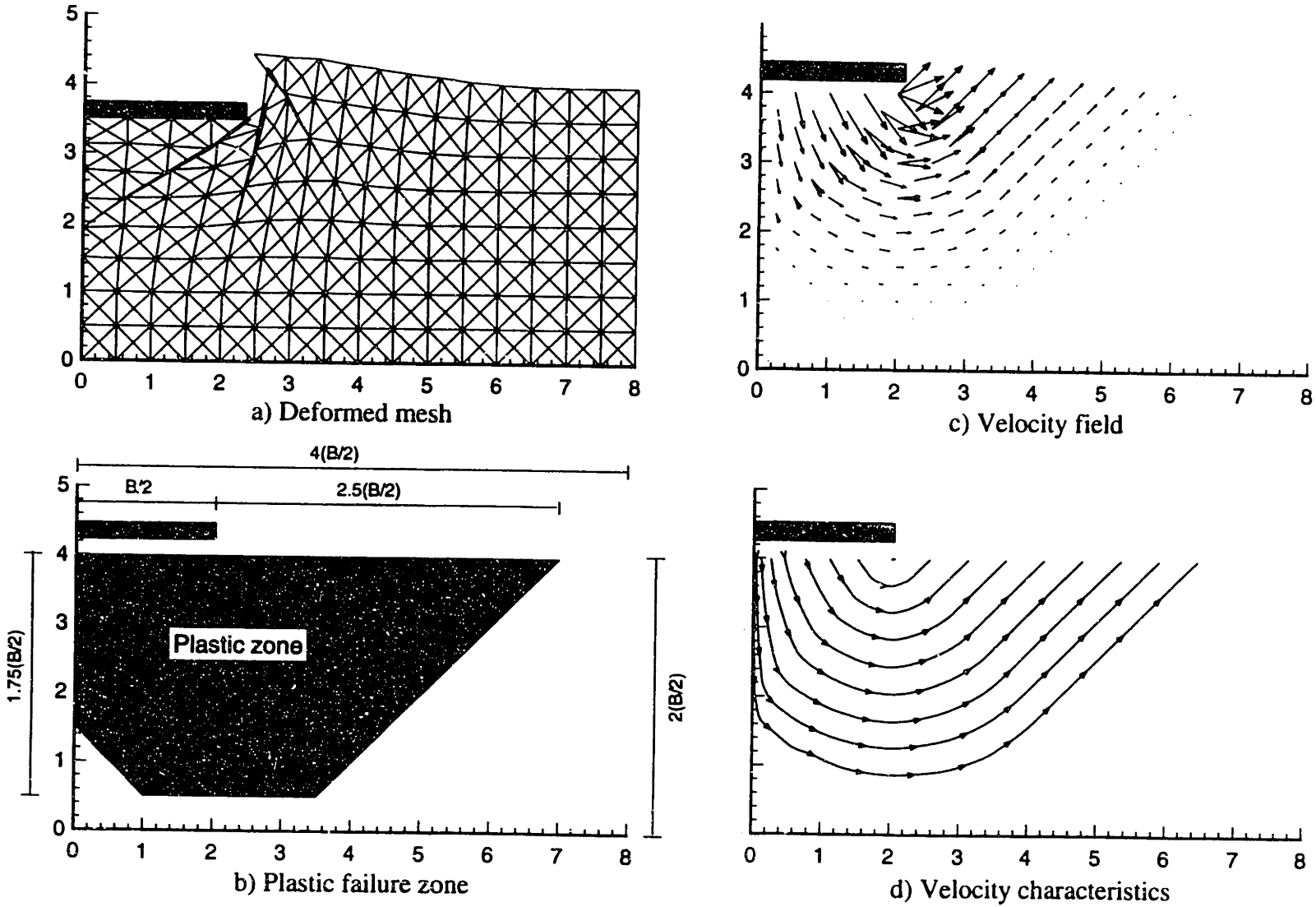

Fig. 4.18 Summary of upper bound results for smooth rigid footing on homogeneous clay

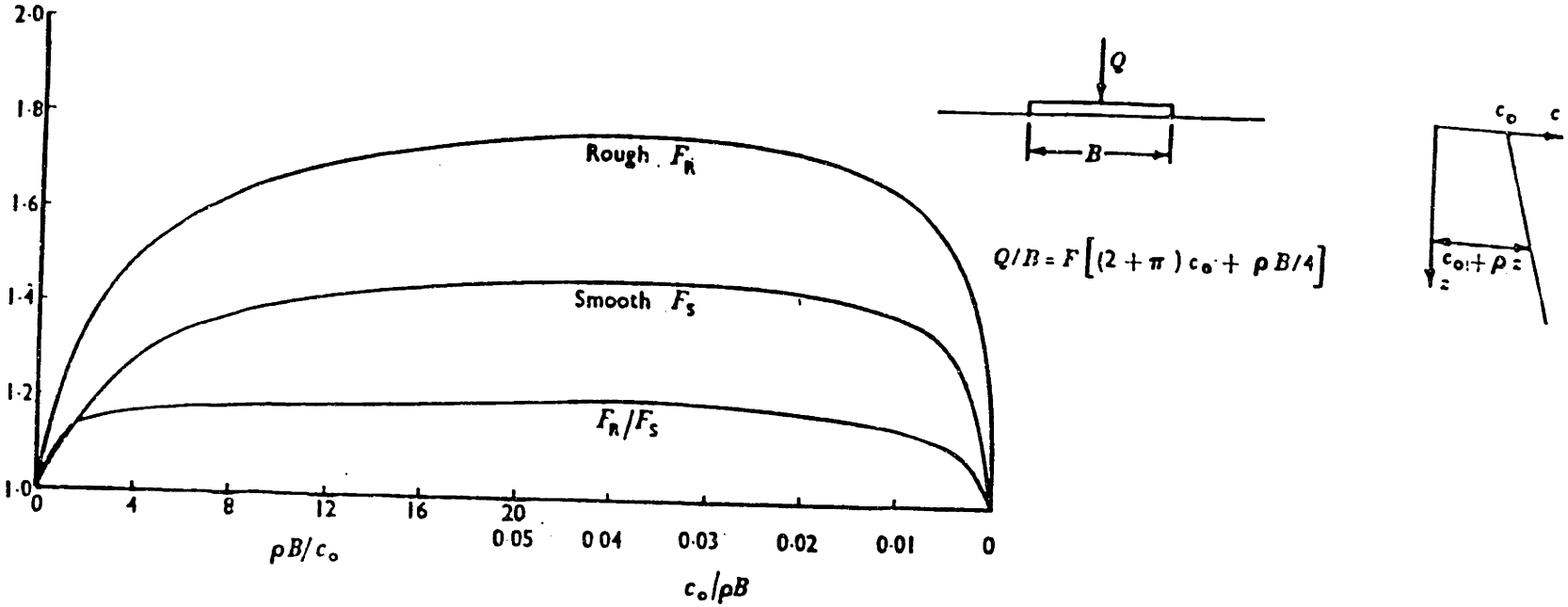

Fig. 4.19 Exact solutions for a smooth and rough rigid footings on non-homogeneous clay, where strength increases linearly with depth (After Davis and Booker, 1973)

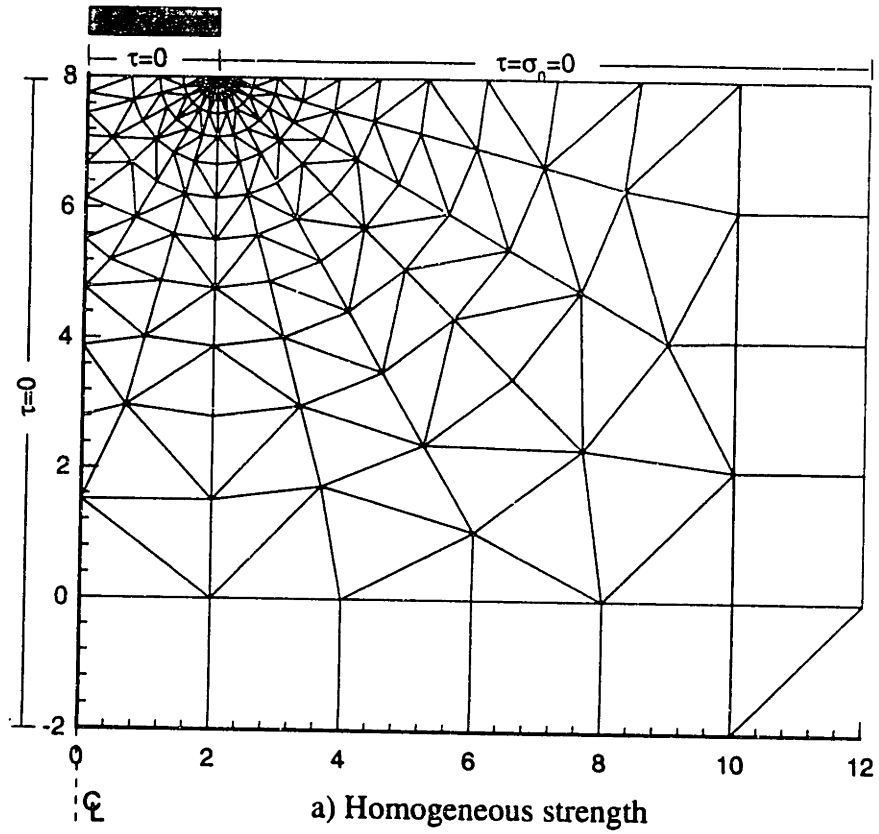

a) Homogeneous strength

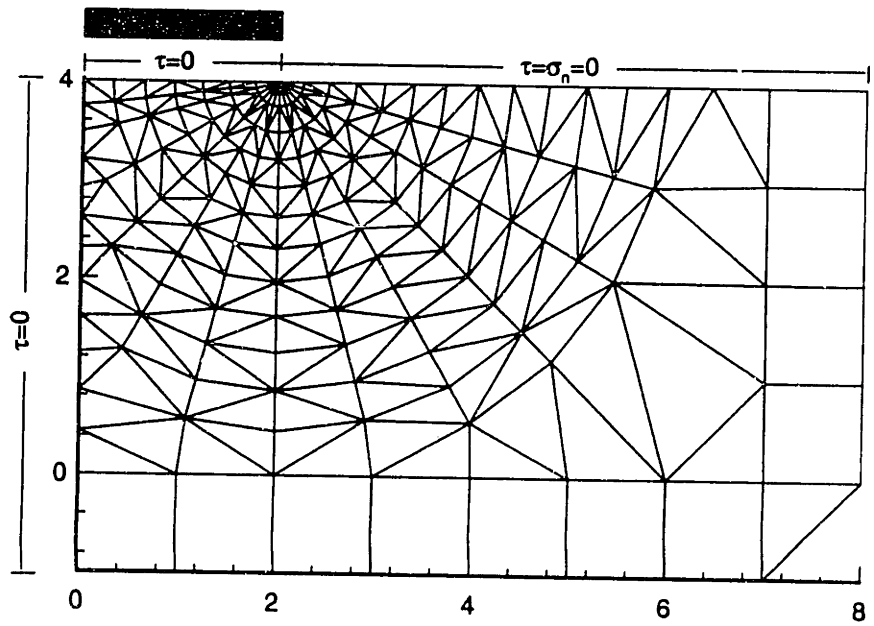

b) Strength increasing with depth (all range of $\rho B/c_{u0}$)

Fig. 4.20 Meshes used in lower bound analyses of smooth rigid footings on non-homogeneous clay, where strength increases linearly with depth

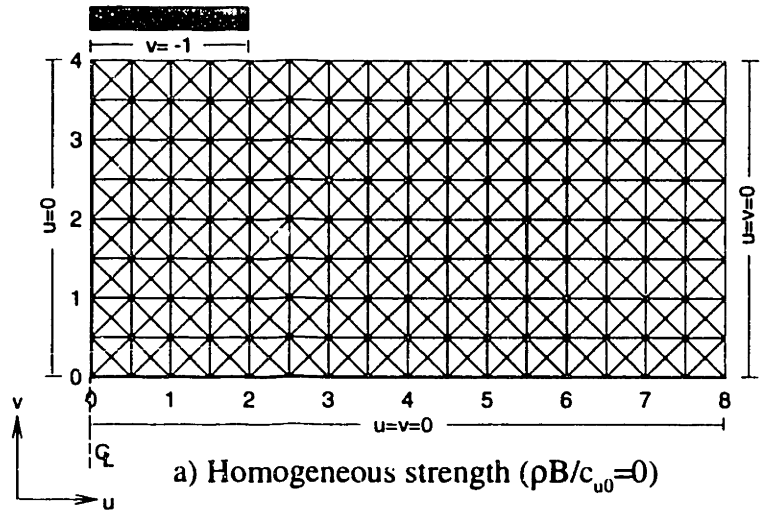

a) Homogeneous strength ($\rho B/c_{u0}=0$)

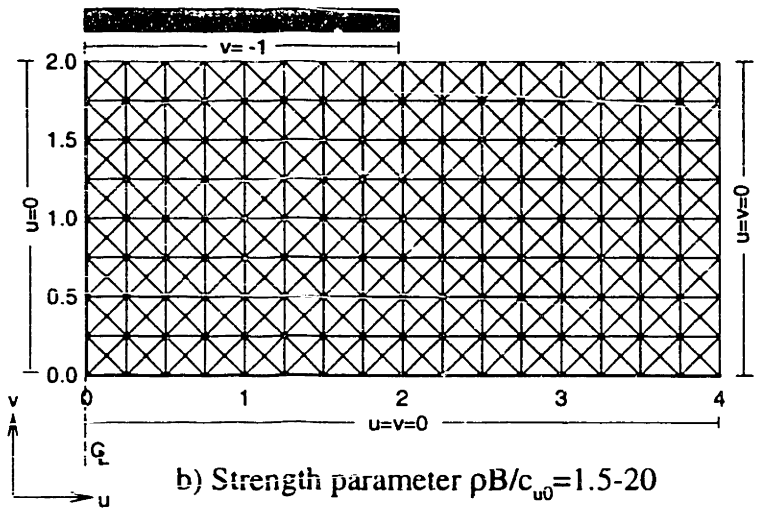

b) Strength parameter $\rho B/c_{u0}=1.5\text{-}20$

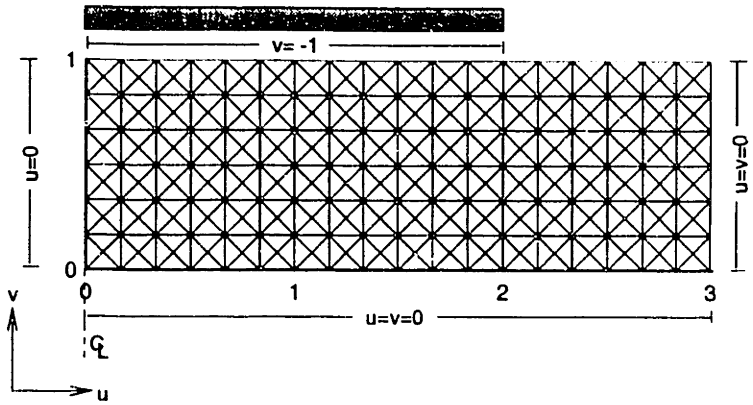

c) Strength parameter $c_{u0}/(\rho B)=0.005\text{-}0.04$

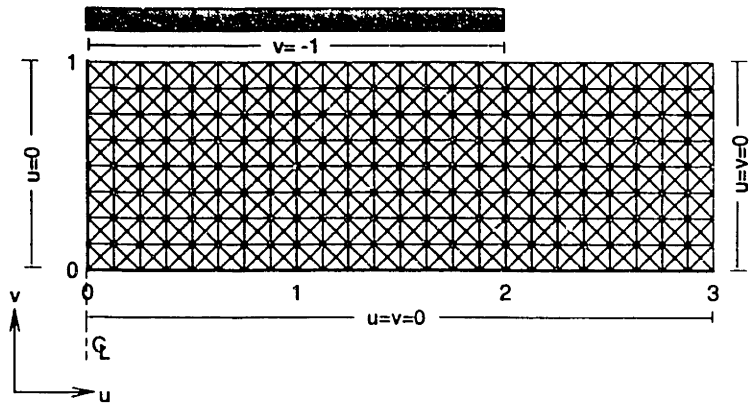

d) Strength parameter $c_{u0}/(\rho B)=0,\ 0.0025$

Fig. 4.21 Meshes used in upper bound analyses of smooth rigid footings on non-homogeneous clay, where strength increases linearly with depth

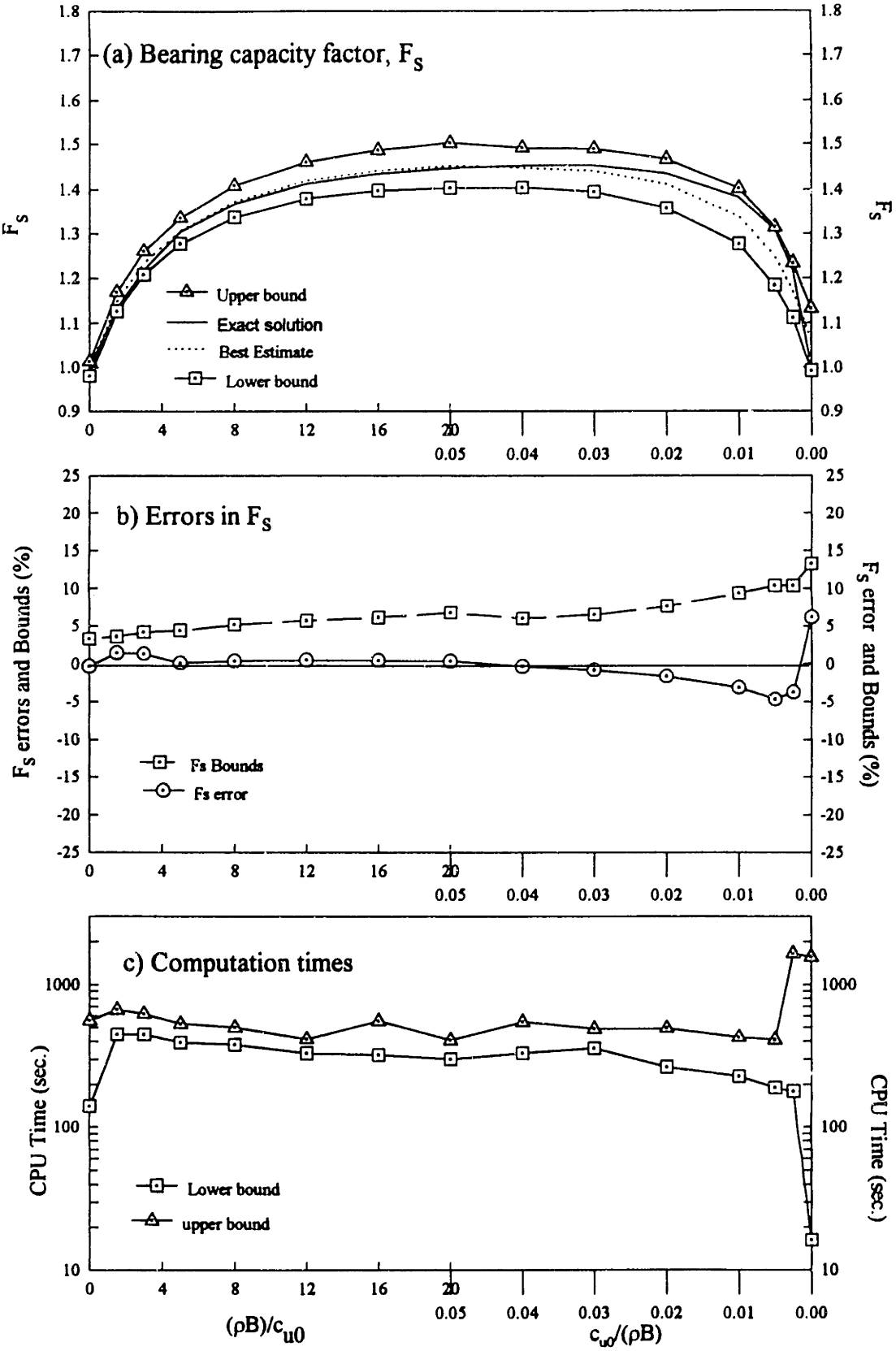

Fig. 4.22 Comparisons of numerical and analytical solutions for bearing capacity of a smooth rigid footing on clay, where strength increases linearly with depth

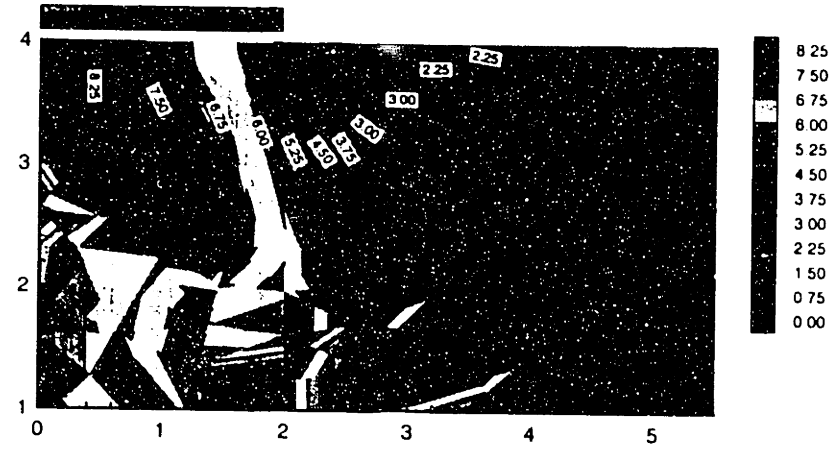

a) Major principal stress, σ_1/c_{u0}

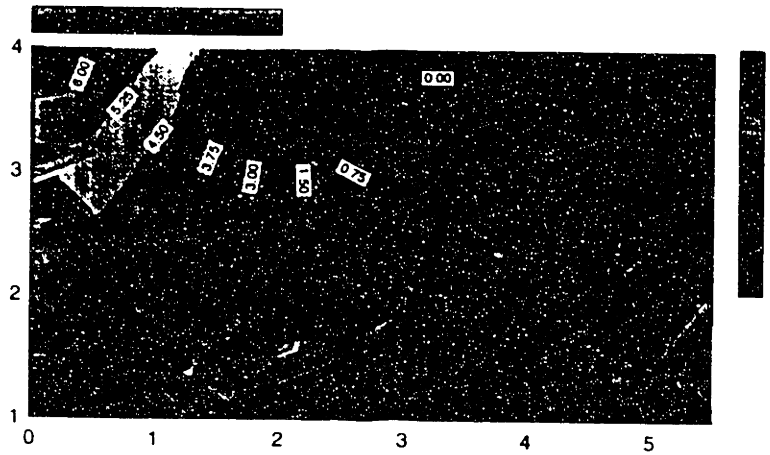

b) Minor pricipal stress, σ_3/c_{u0}

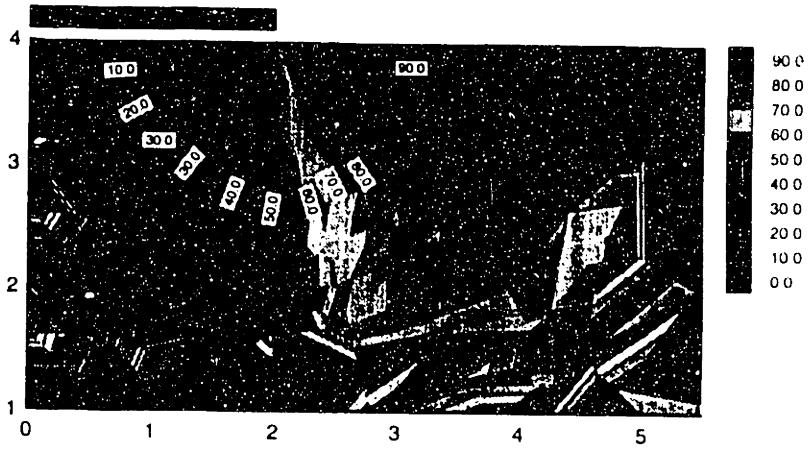

c) Direction of major pricipal stress to vertical, δ

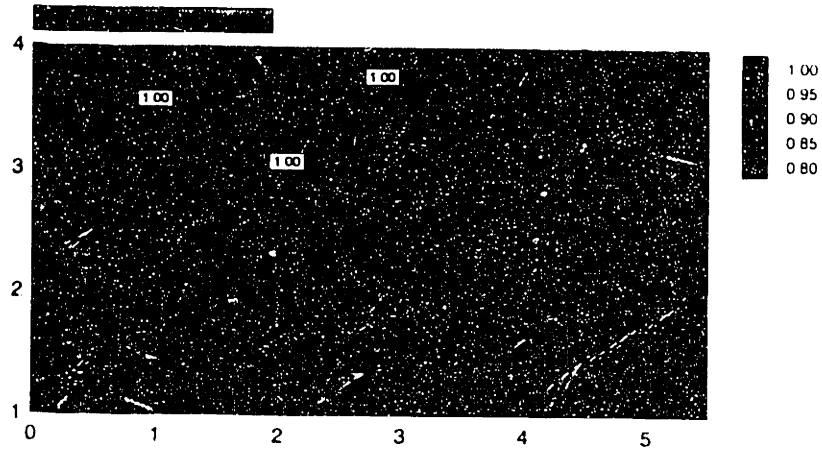

d) Failure zone, $(\sigma_1-\sigma_3)/2c_{u0}$

Fig. 4.23 Summary of lower bound analyses for smooth rigid footings on non-homogeneous clay, where $\rho B/c_{u0}=3$

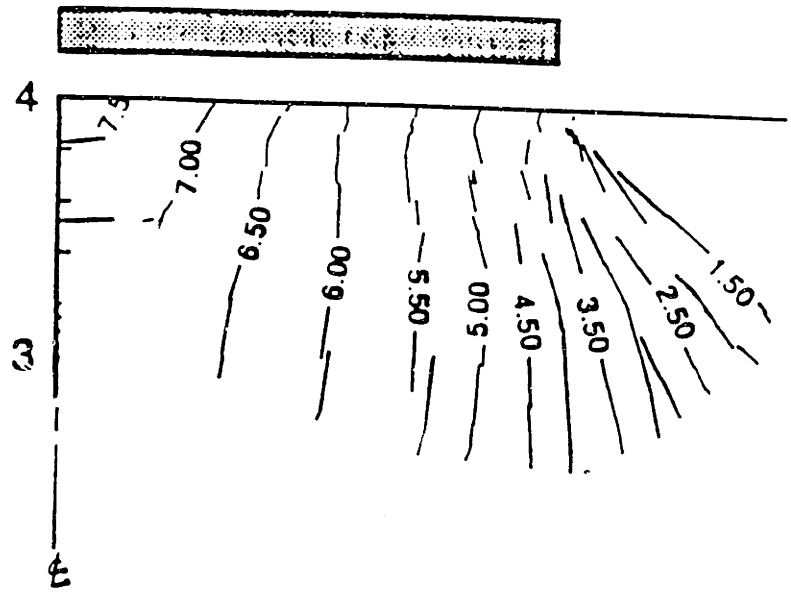

a) Numerical lower bound

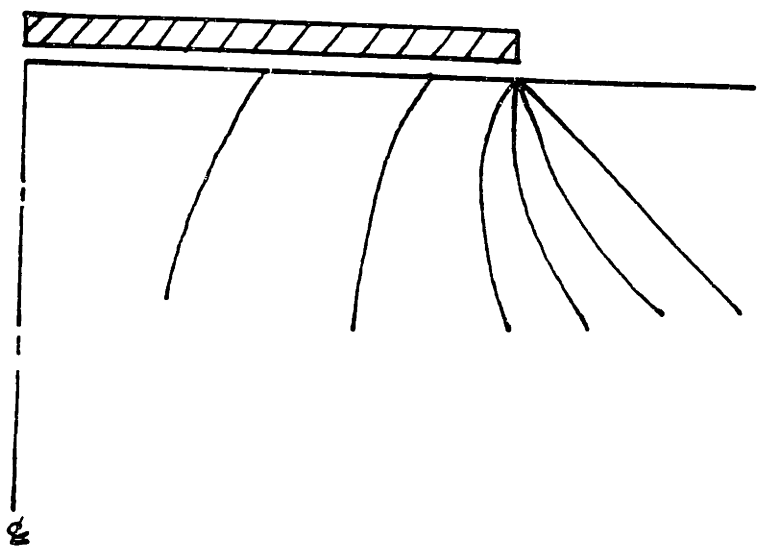

b) Exact solution (Davis and Booker, 1973)

Fig. 4.24 Comparisons of mean stress contours between numerical and analytical solutions for a smooth rigid footing on non-homogeneous clay, where $\rho B/c_{u0} = 3$

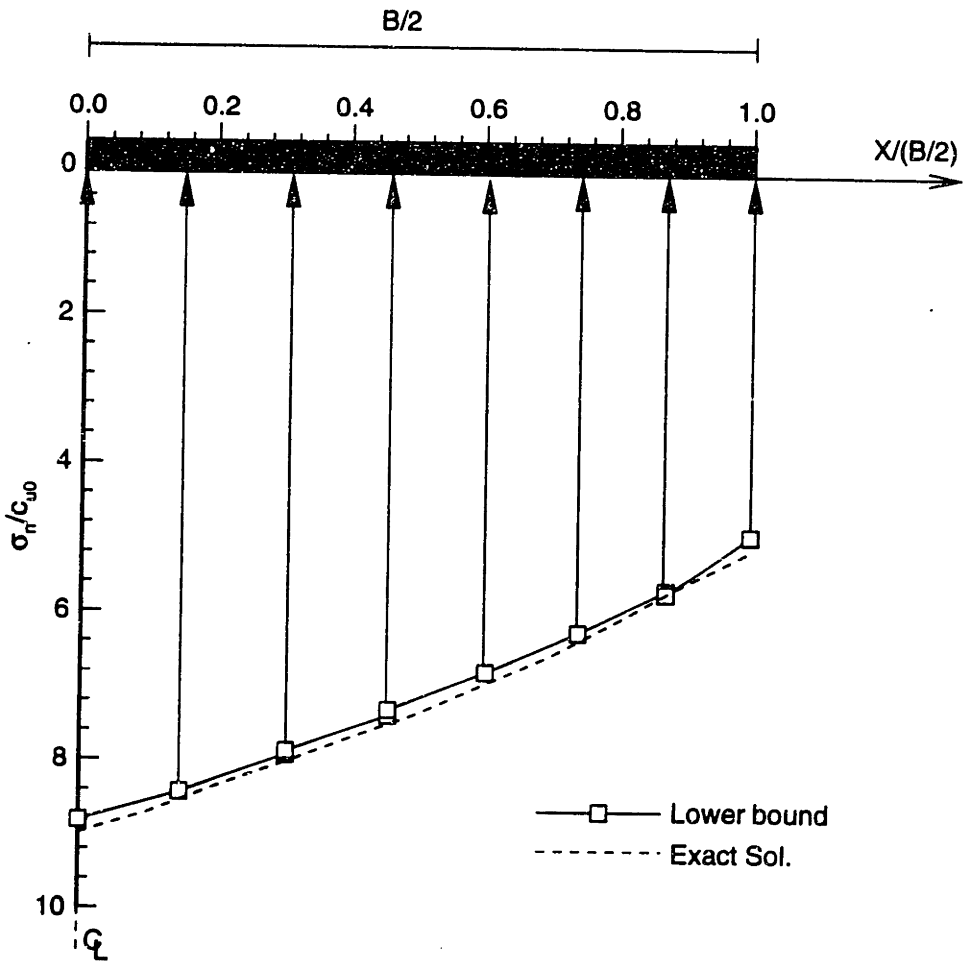

Fig. 4.25 Lower bound and exact solutions for normal contact stress beneath a smooth rigid footing on non-homogeneous clay, where $\rho B/c_{u0}=3$

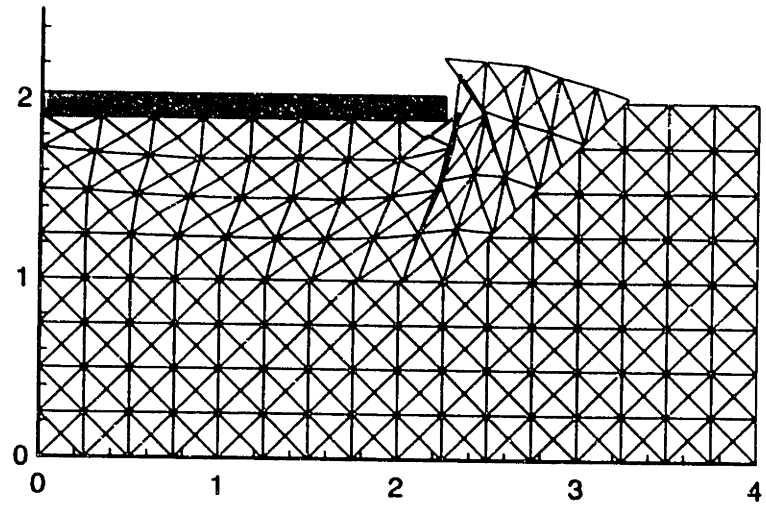

a) Deformed mesh

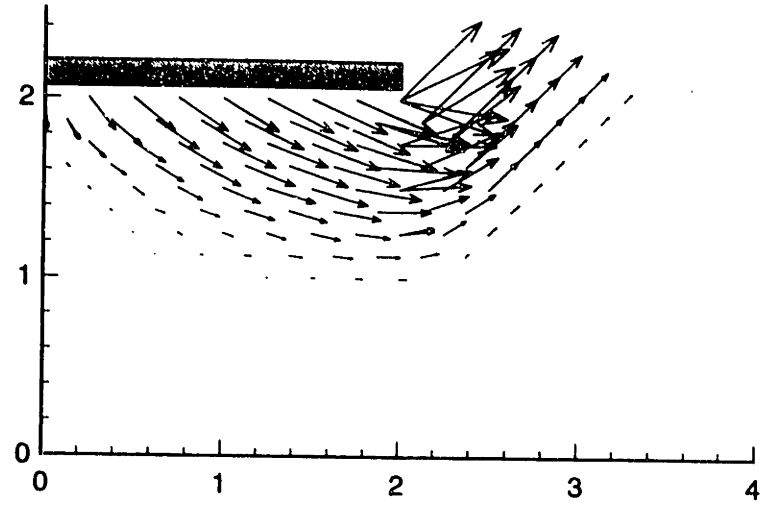

c) Velocity field

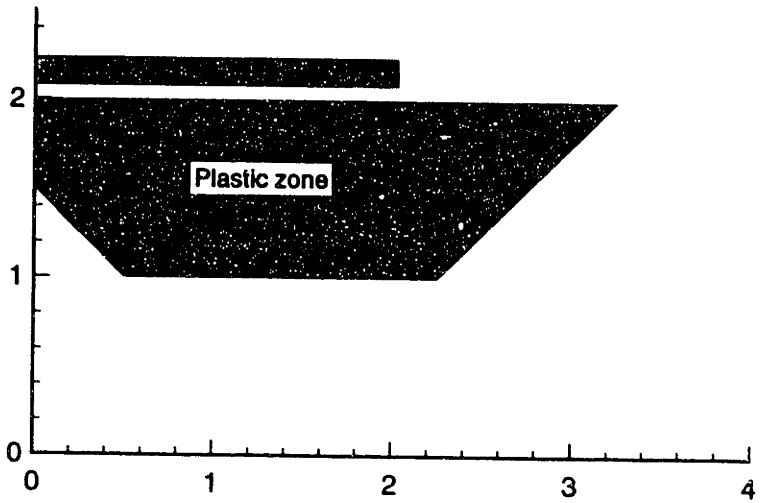

b) Plastic failure zone

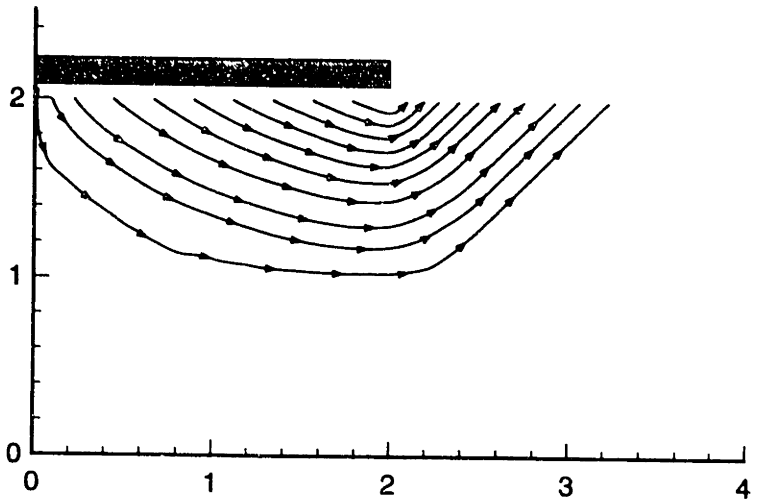

d) Velocity characteristics

Fig. 4.26 Summary of upper bound results for smooth rigid footing on non-homogeneous clay, where $\rho B/c_{u0}=3$

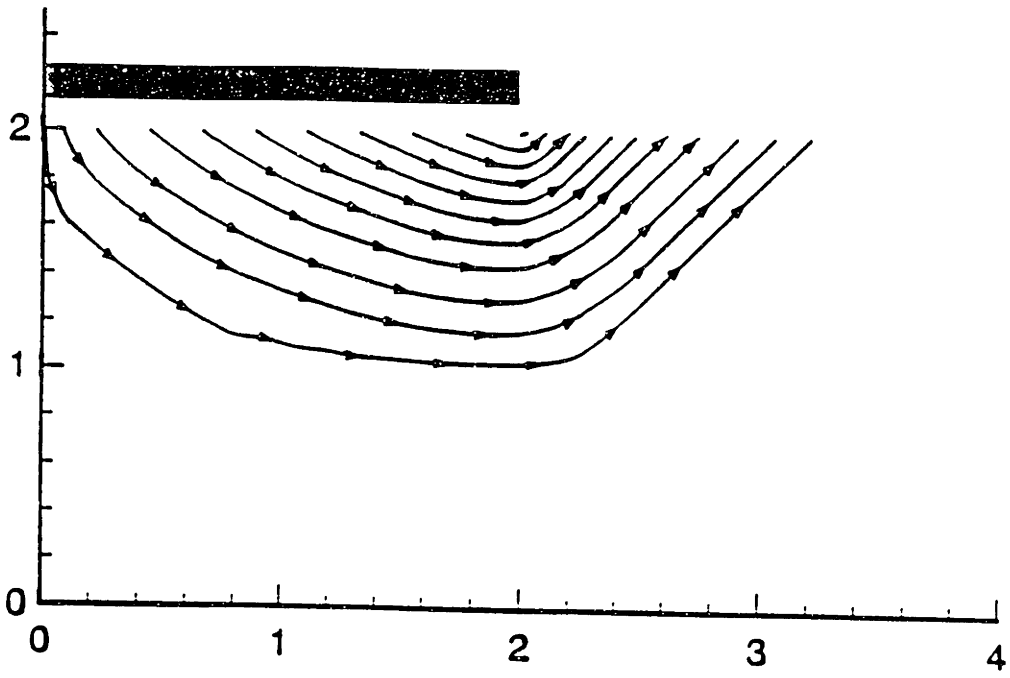

a) Numerical upper bound

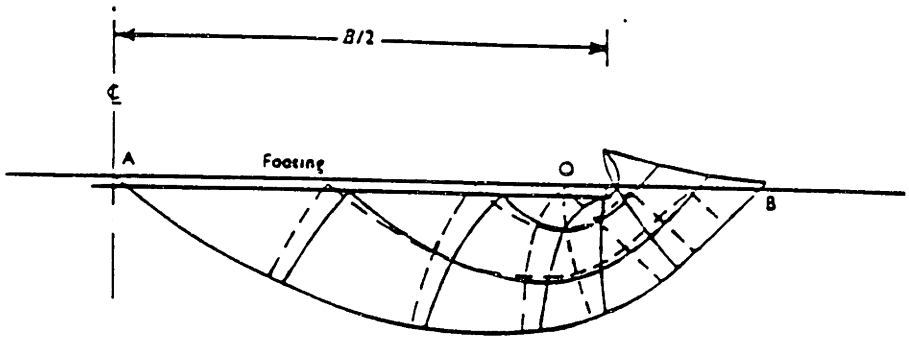

b) Exact solution (Davis and Booker, 1973)

Fig. 4.27 Comparisons of velocity field between numerical and analytical solutions for a smooth rigid footing on non-homogeneous clay, where $\rho B/c_{u0} = 3$

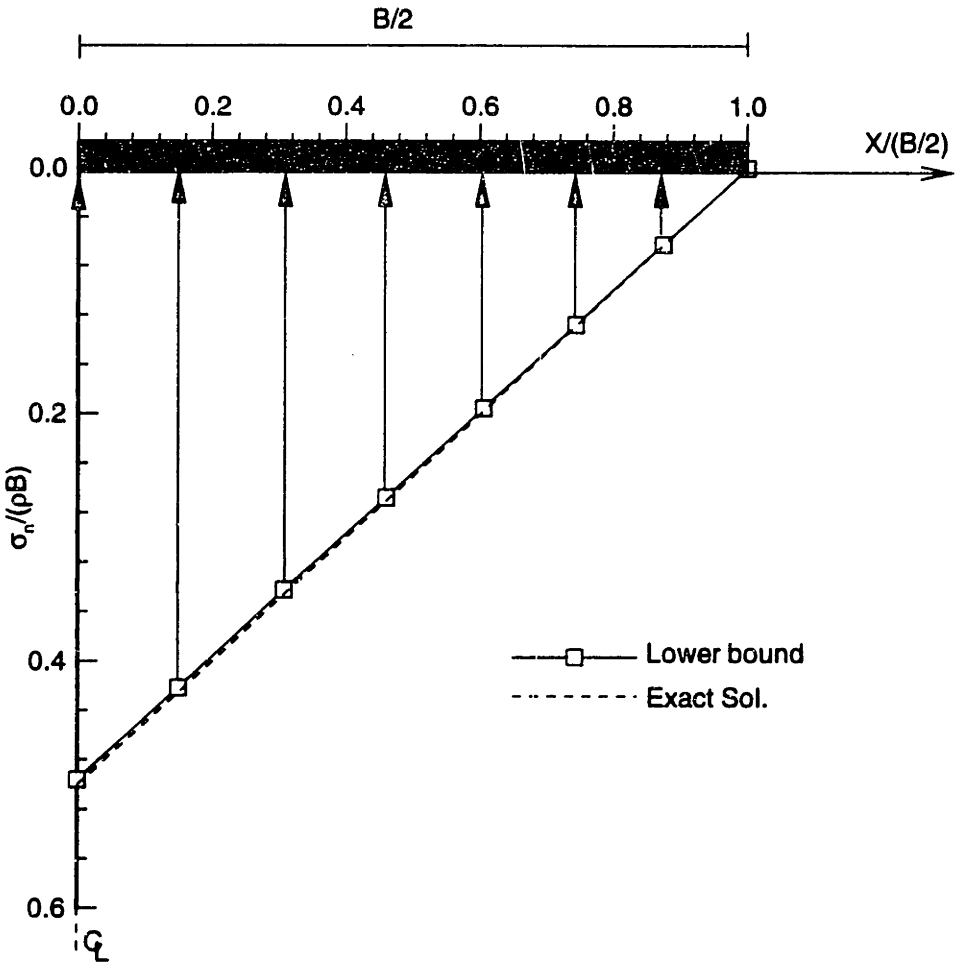

Fig. 4.28 Lower bound and exact solutions for normal contact stress beneath a smooth rigid footing on non-homogeneous clay, where $c_{u0}/(\rho B)=0$

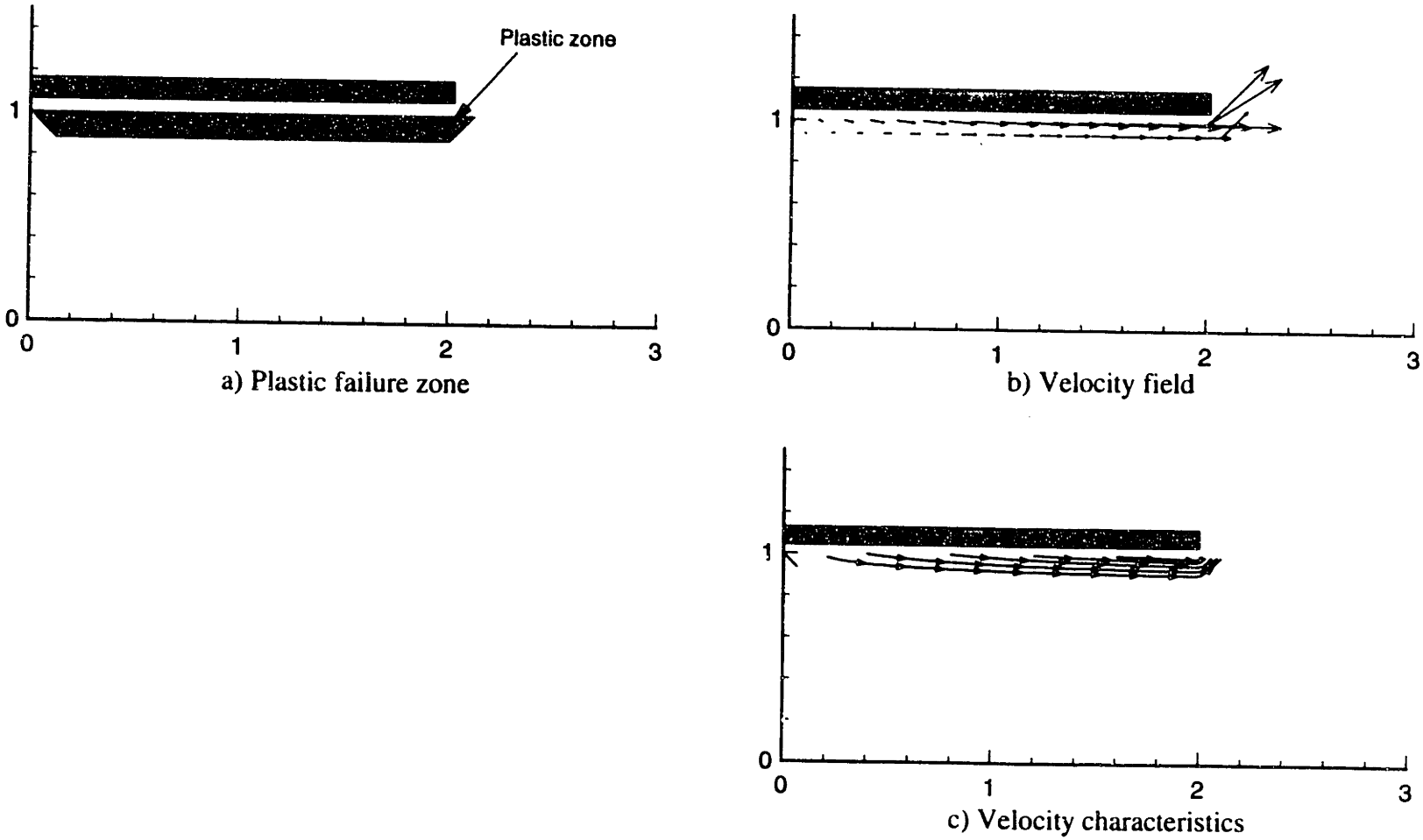

Fig. 4.29 Summary of upper bound results for smooth rigid footing on non-homogeneous clay, where $c_{u0}/(\rho B)=0$

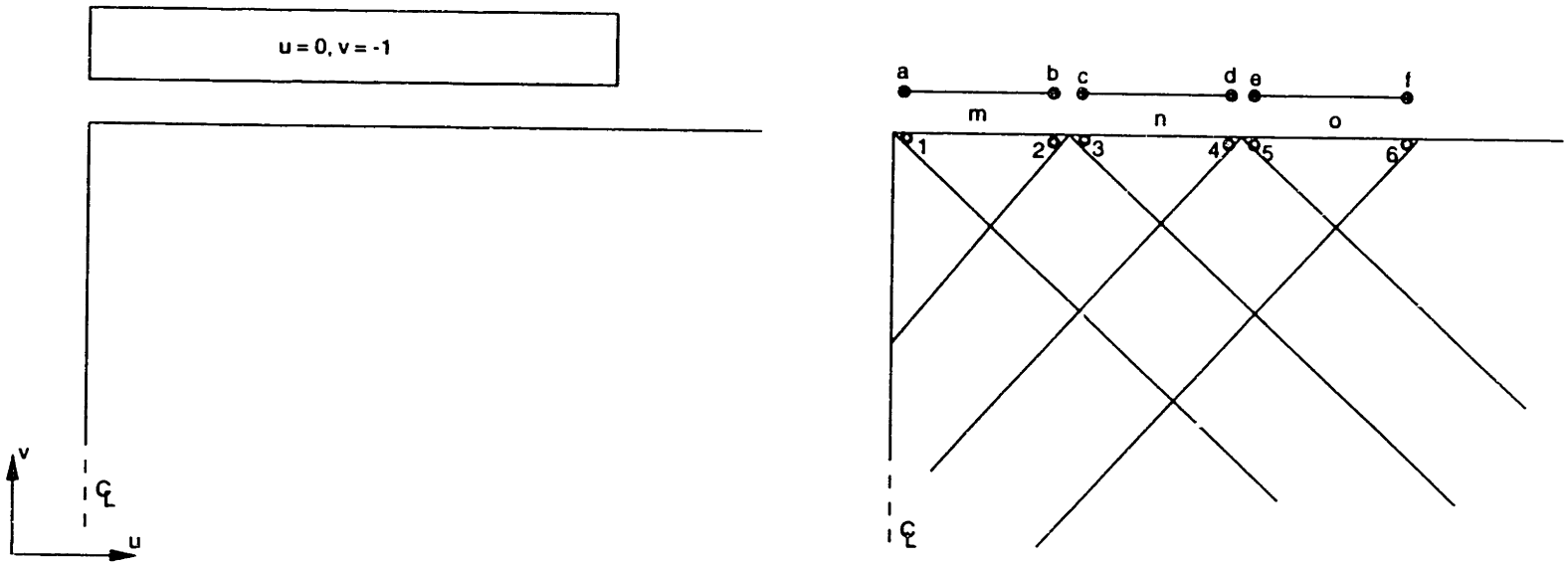

a) Rough rigid footing

b) Modelling

Fig. 4.30 Modelling of rough rigid footings for upper bound analyses

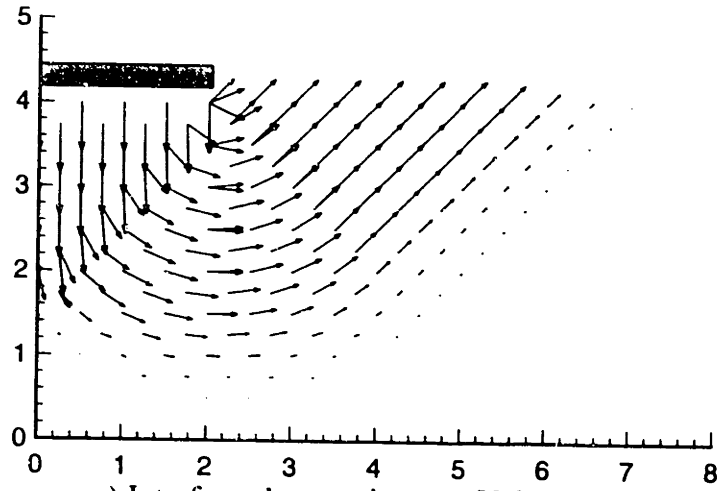

a) Interface shear resistance: Velocity field

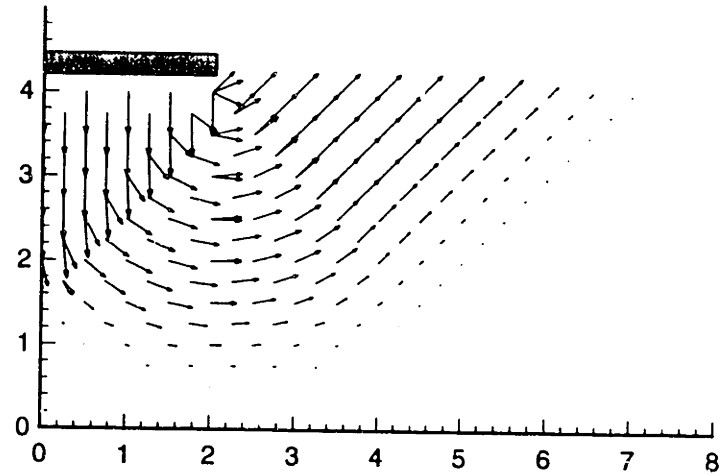

c) No slip: Velocity field

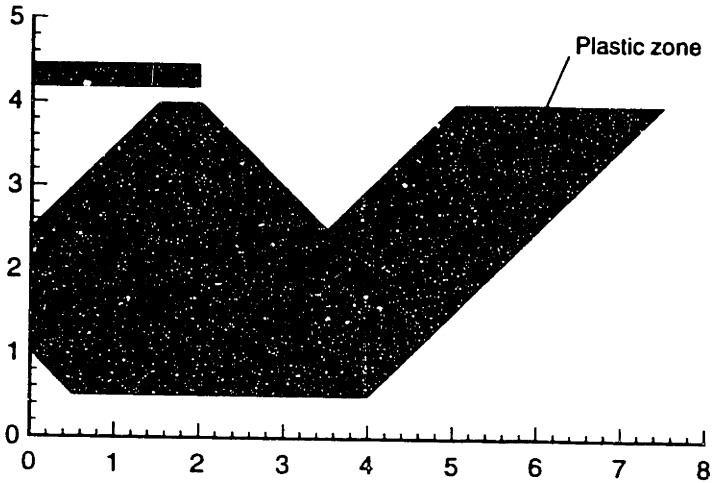

b) Interface shear resistance: Plastic Failure zone

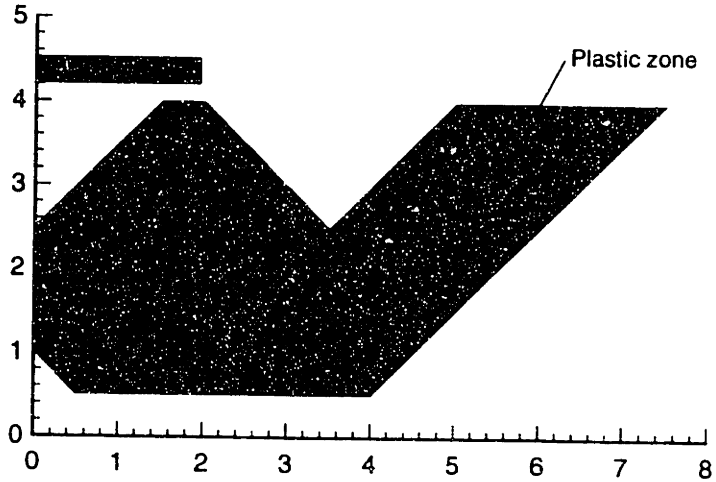

d) No slip: Plastic zone

Fig. 4.31 Comparisons of the upper bound analyses between interface shear resistance and no slip bounadary condition for a rough rigid footing on homogeneous clay

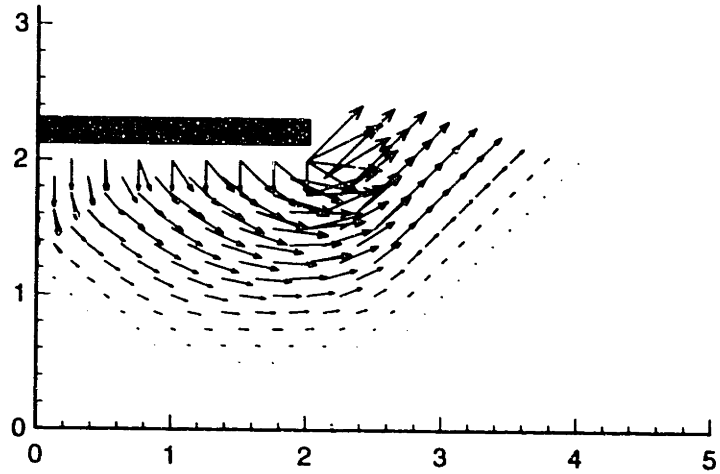

a) Interface shear resistance: Velocity field

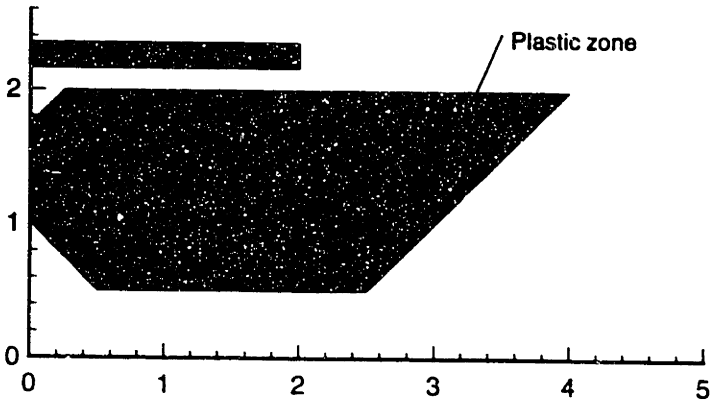

b) Interface shear resistance: Plastic Failure zone

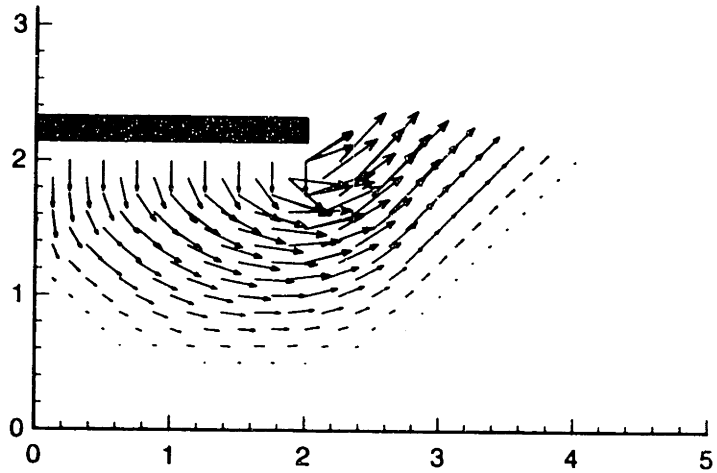

c) No slip: Velocity field

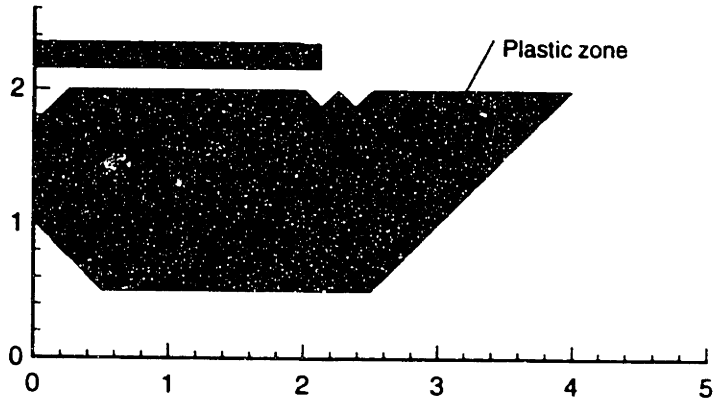

d) No slip: Plastic zone

Fig. 4.32 Comparisons of the upper bound analyses with interface shear resistance and no slip boundary condition for a rough rigid footing on non-homogeneous clay, where $\rho B/c_{u0}=3$

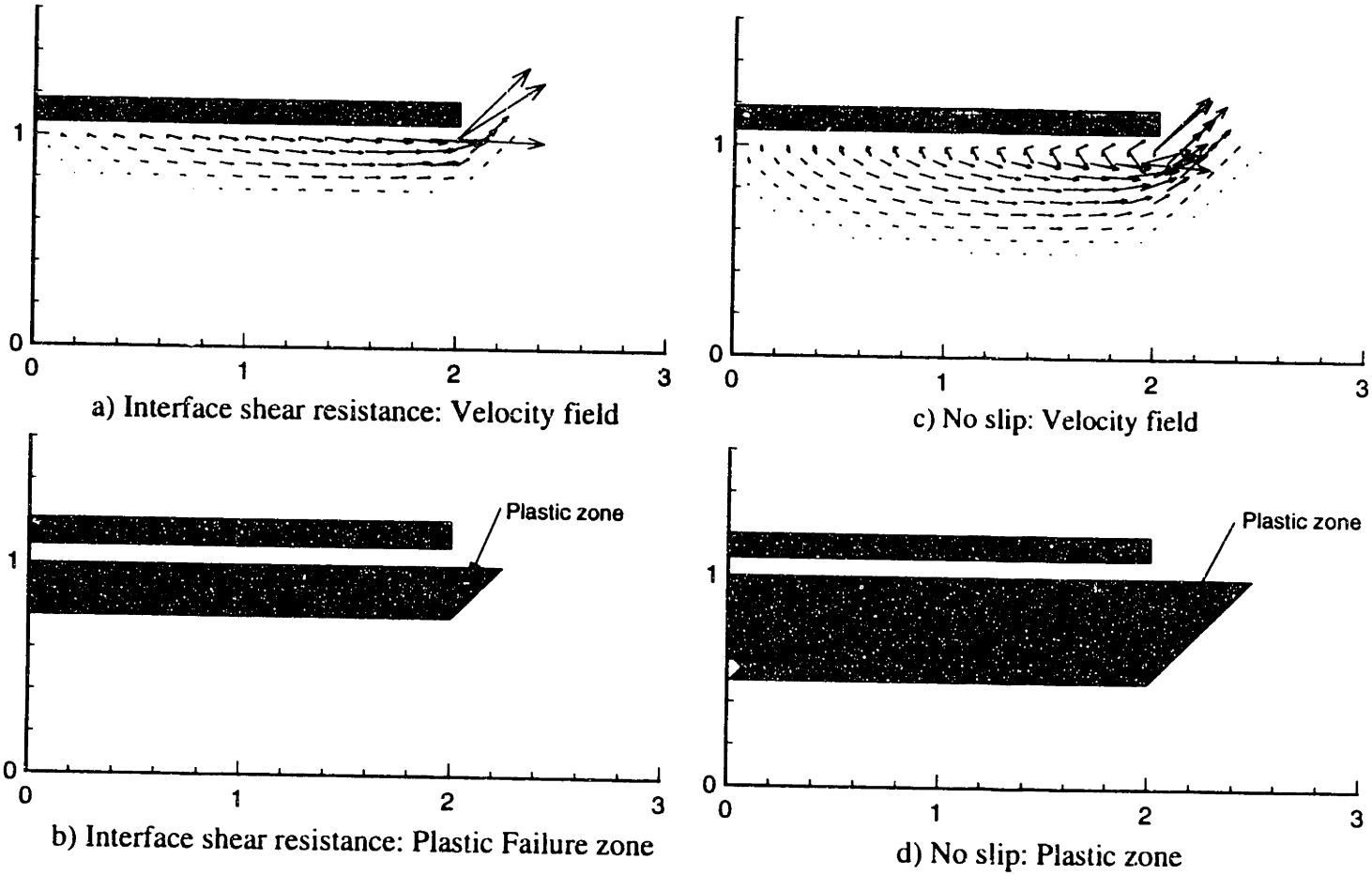

a) Interface shear resistance: Velocity field

c) No slip: Velocity field

b) Interface shear resistance: Plastic Failure zone

d) No slip: Plastic zone

Fig. 4.33 Comparisons of the upper bound analyses with interface shear resistance and no slip boundary condition for a rough rigid footing on non-homogeneous clay, where $c_{u0}/(\rho B)=0.005$

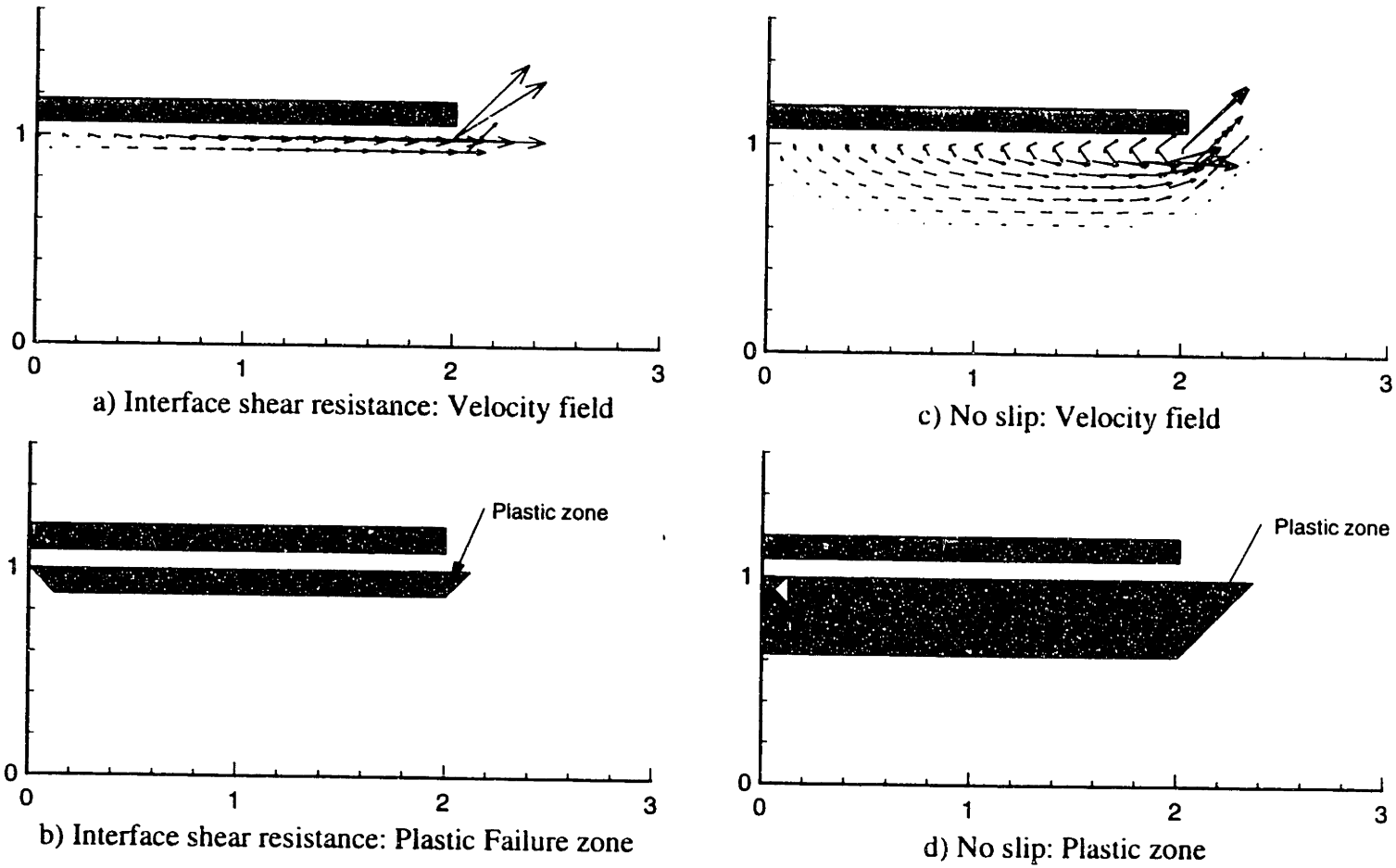

a) Interface shear resistance: Velocity field

c) No slip: Velocity field

b) Interface shear resistance: Plastic Failure zone

d) No slip: Plastic zone

Fig. 4.34 Comparisons of the upper bound analyses with interface shear resistance and no slip condition for a rough rigid footing on non-homogeneous clay, where $c_{\omega 0}/(\rho B)$=0.0

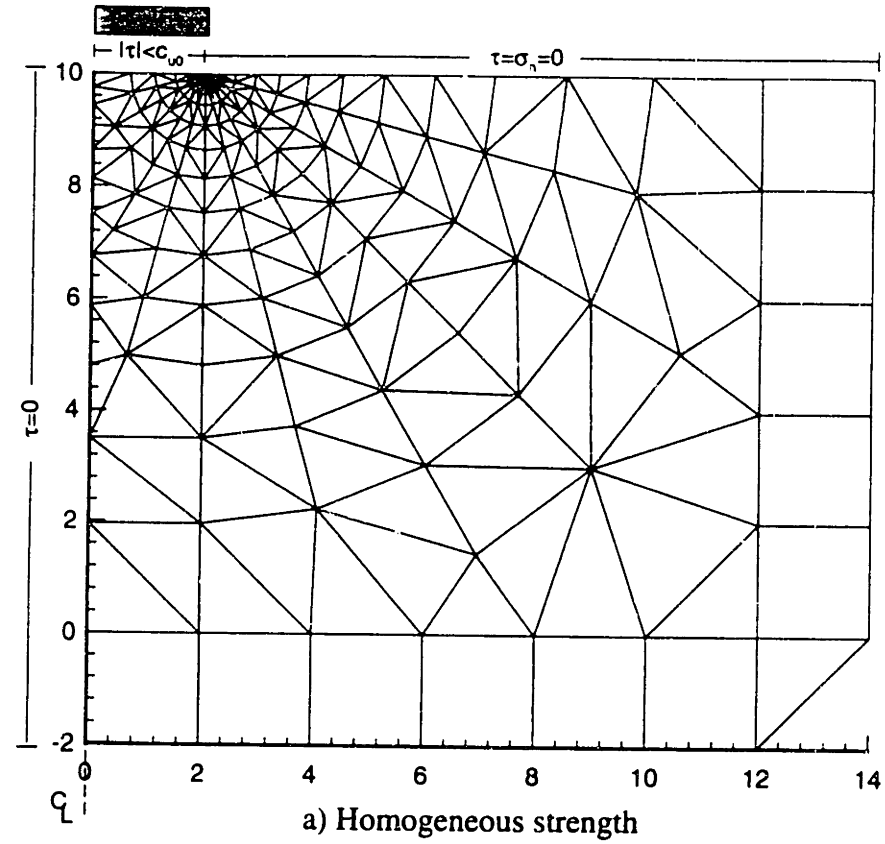

a) Homogeneous strength

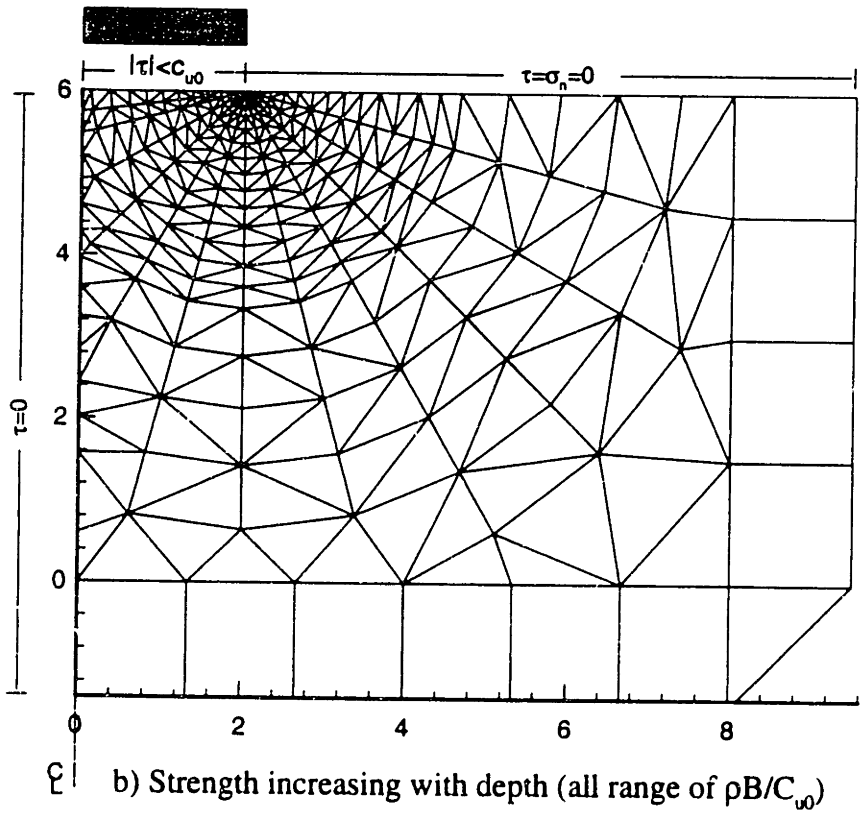

b) Strength increasing with depth (all range of $\rho B/C_{u0}$)

Fig. 4.35 Meshes used in lower bound analyses of rough rigid footings on non-homogeneous clay, where strength increases linearly with depth

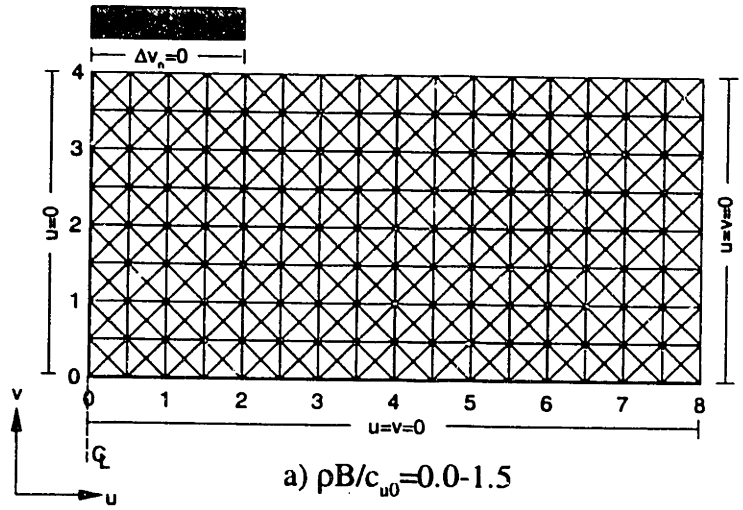

a) $\rho B/c_{u0}$=0.0-1.5

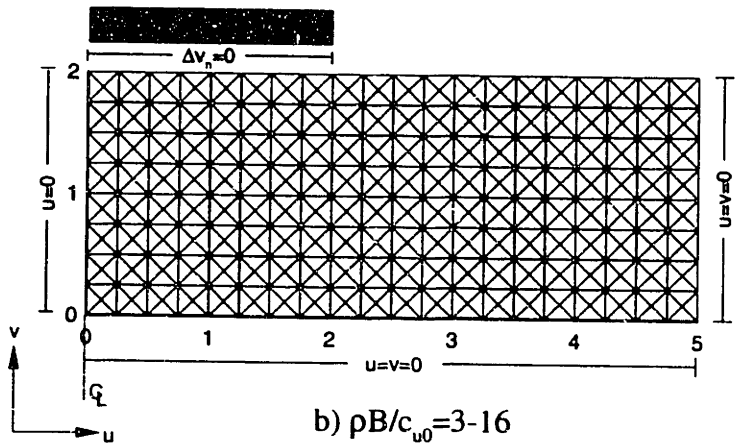

b) $\rho B/c_{u0}$=3-16

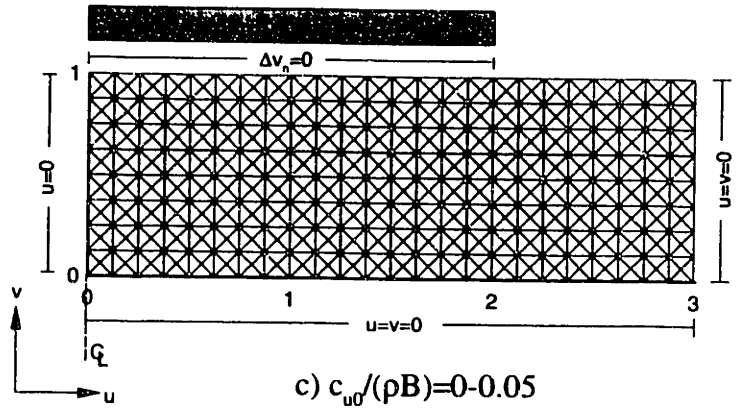

c) $c_{u0}/(\rho B)$=0-0.05

Fig. 4.36 Meshes used in upper bound analyses of rough rigid footings on non-homogeneous clay, where strength increases linearly with depth

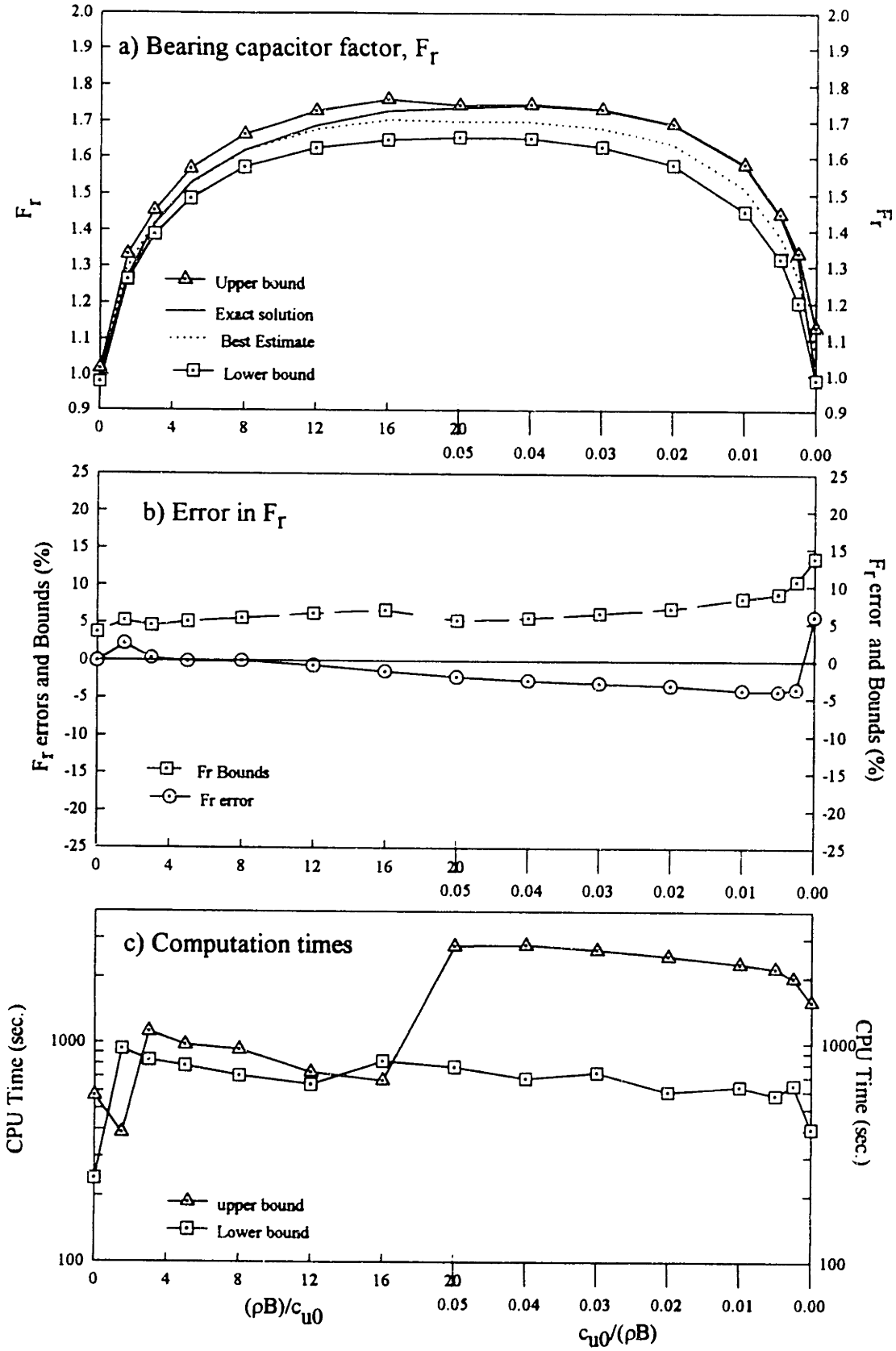

Fig. 4.37 Comparisons of numerical and analytical solutions for bearing capacity of a rough rigid footing on clay, where strength increases linearly with depth

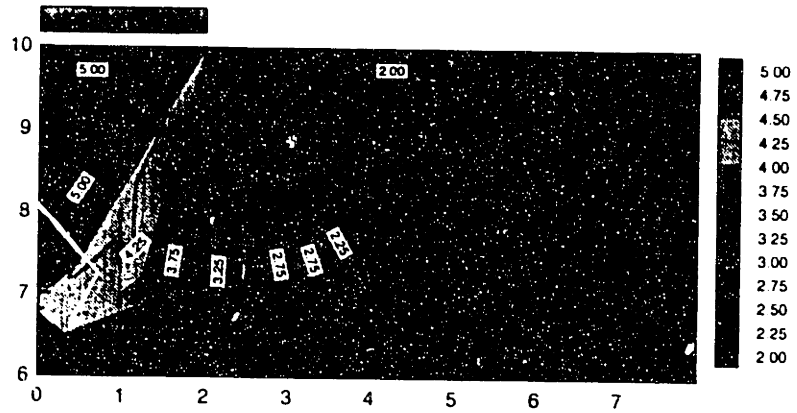

a) Major principal stress, σ_1/c_{u0}

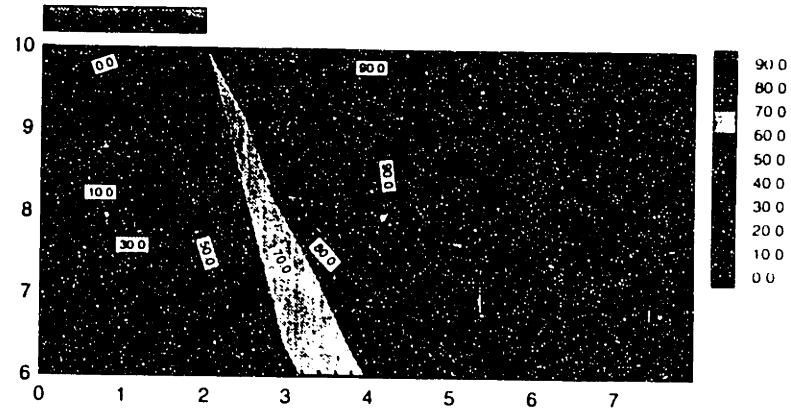

c) Direction of major pricipal stress to vertical, δ (deg.)

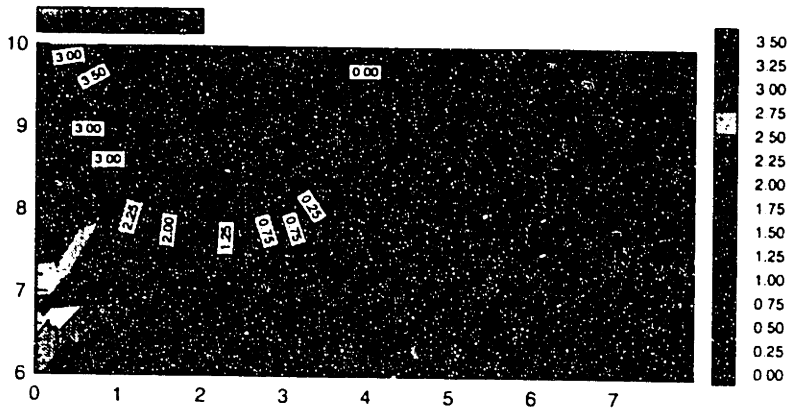

b) Minor principal stress, σ_3/c_{u0}

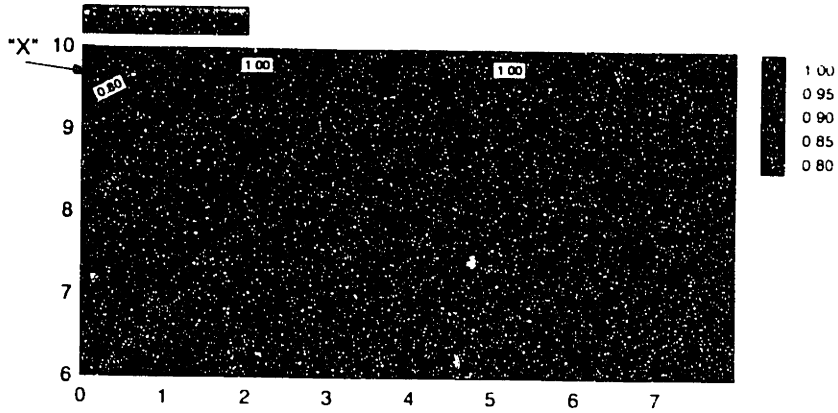

d) Failure zone, $(\sigma_1-\sigma_3)/2c_{u0}$

Fig. 4.38 Summary of lower bound results for rough rigid footings on homogeneous clay

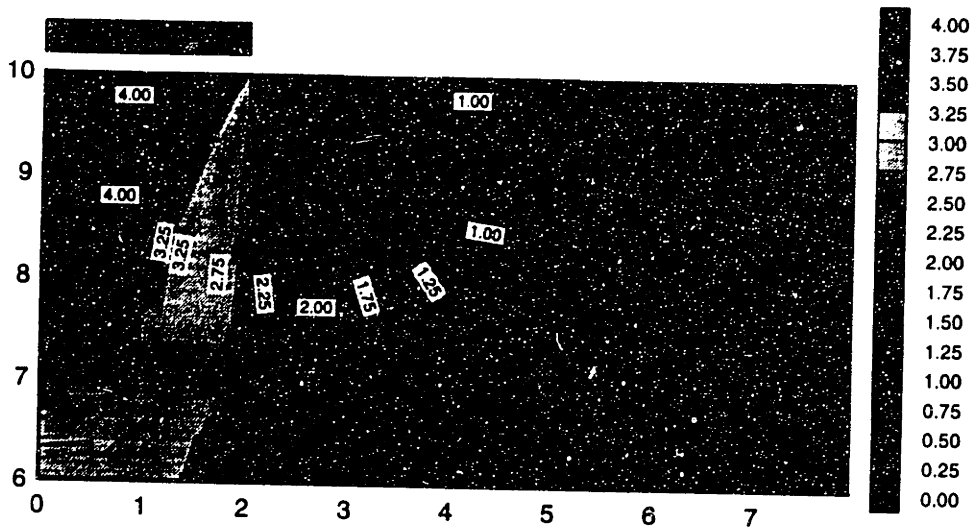

Fig. 4.39 Lower bound for contour of mean stress of rough rigid footings on homogeneous clay

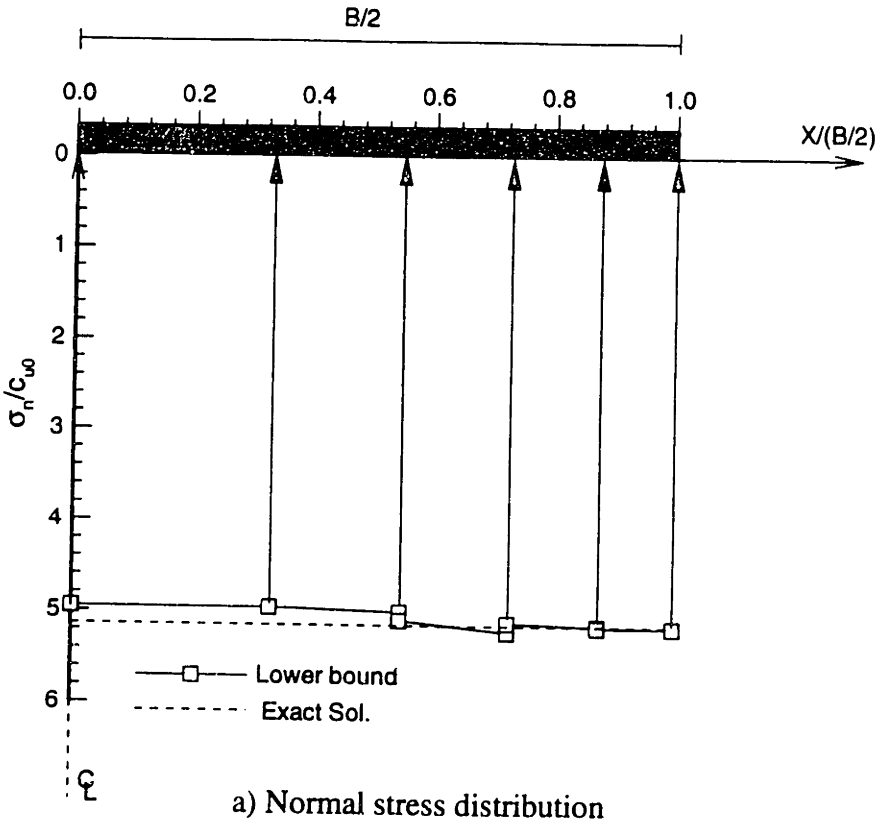

a) Normal stress distribution

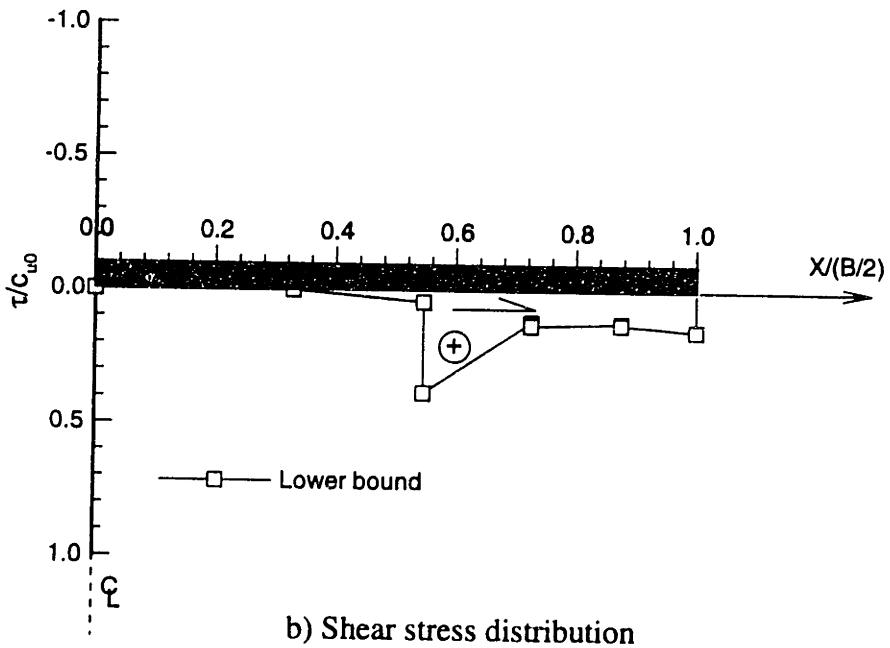

b) Shear stress distribution

Fig. 4.40 Lower bound for normal stress and shear stress beneath rough rigid footings on homogeneous clay

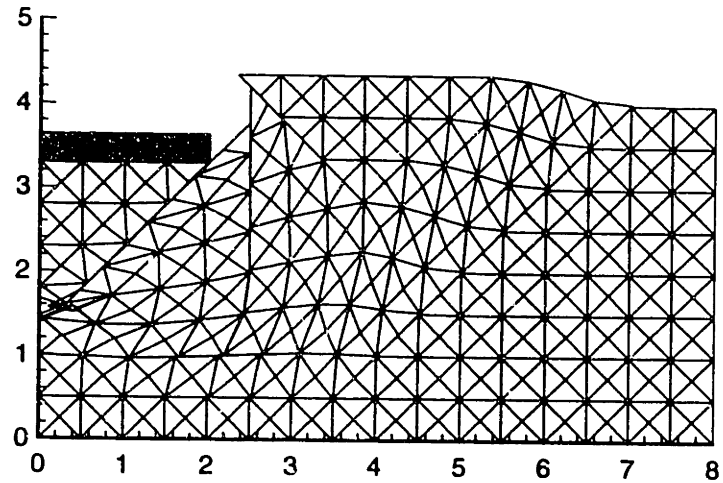

a) Deformed mesh

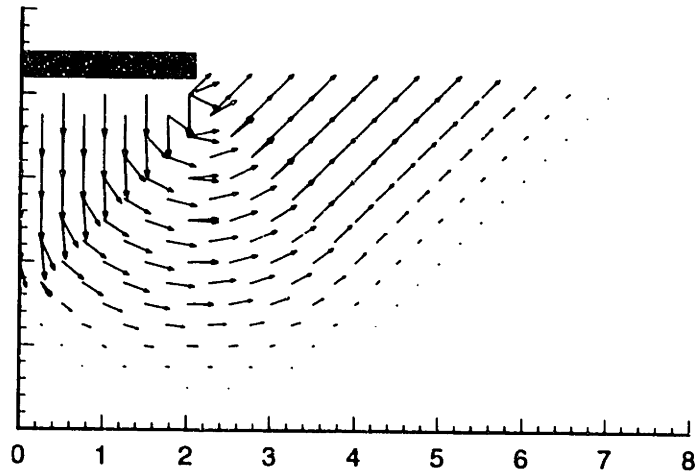

b) Velocity field

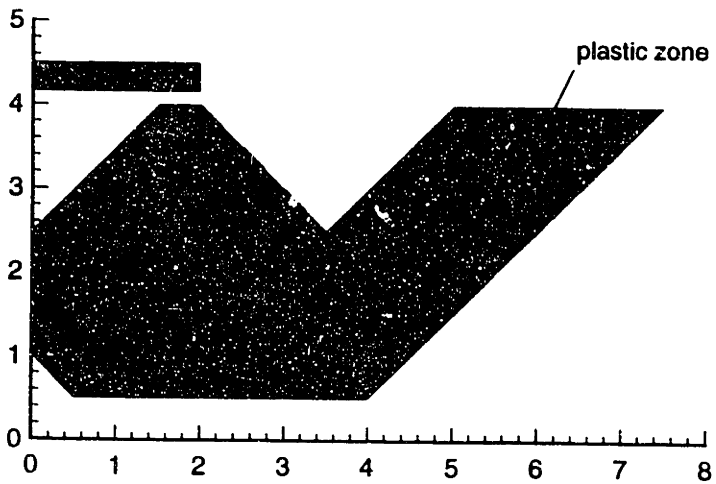

b) Plastic failure zone

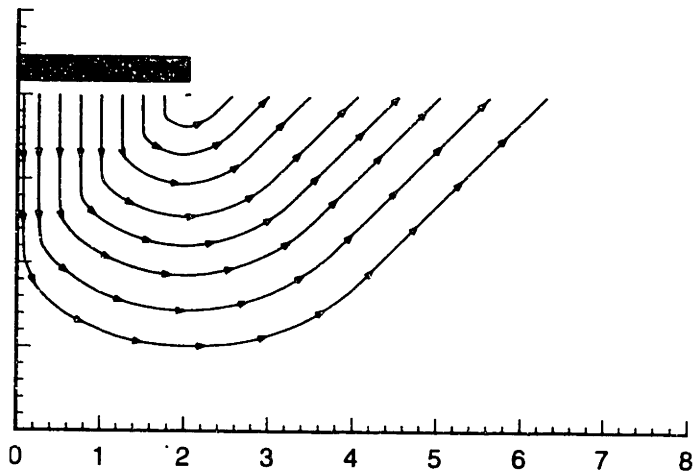

d) Velocity characteristics

Fig. 4.41 Summary of upper bound results for rough rigid footings on homogeneous clay

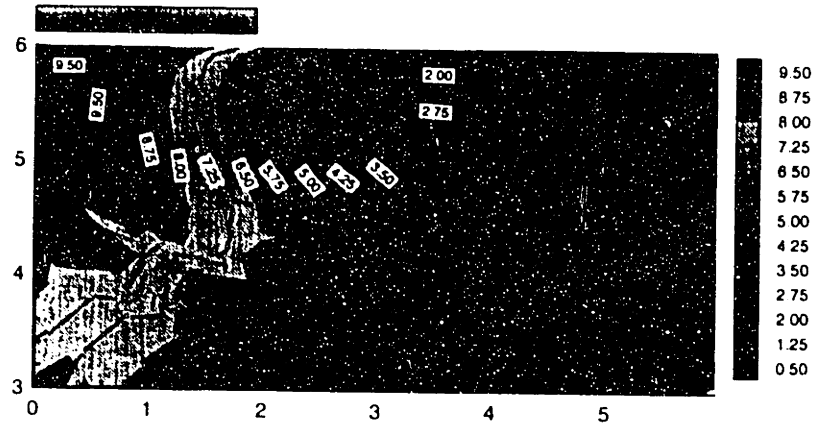

a) Major principal stress, σ_1/c_{u0}

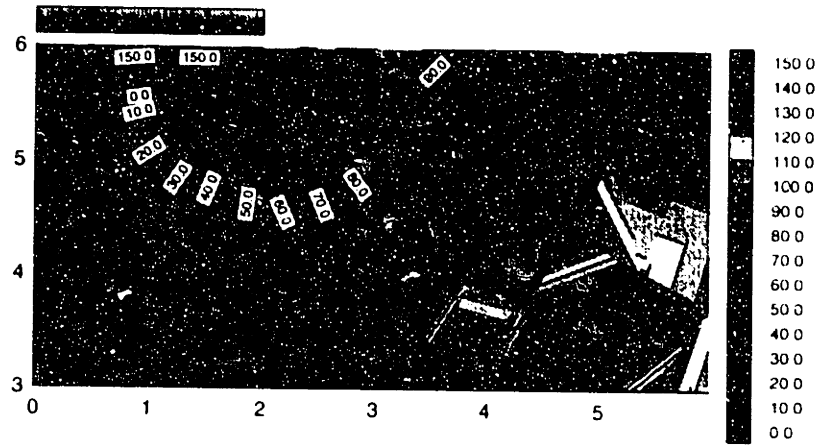

c) Direction of major principal stress to vertical, δ (deg.)

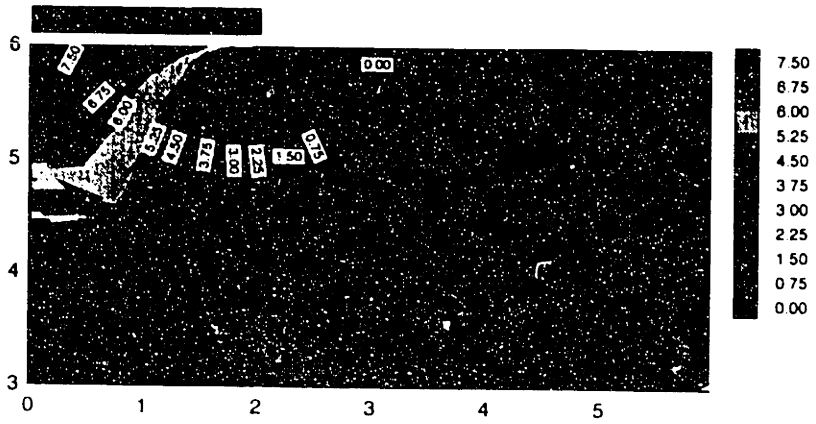

b) Minor principal stress, σ_3/c_{u0}

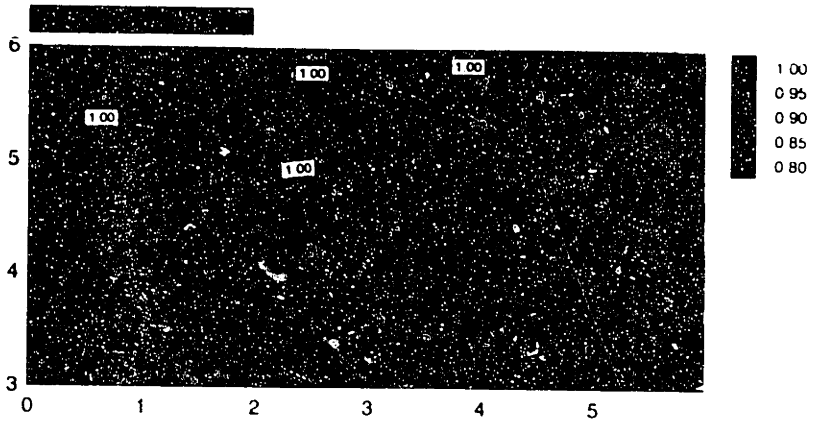

d) Failure zone, $(\sigma_1-\sigma_3)/2c_{u0}$

Fig. 4.42 Summary of lower bound results for rough rigid footings on non-homogeneous clay, where $\rho B/c_{u0}=3$

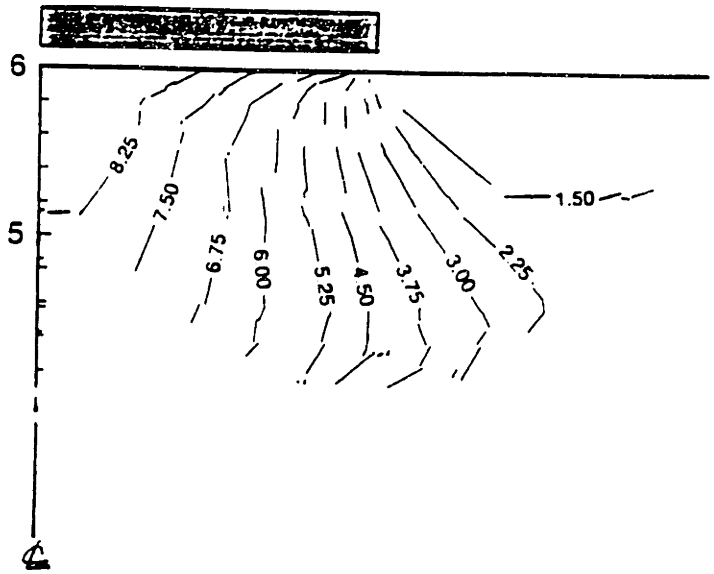

a) Numerical lower bound

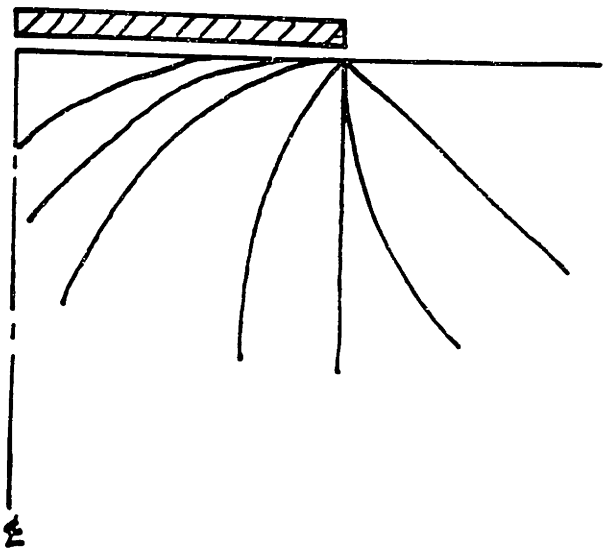

b) Exact solution (Davis and Booker, 1973)

Fig. 4.43 Comparisons of mean stress contours between numerical and analytical solutions for a rough rigid footing on non-homogeneous clay, where $\rho B/c_{u0} = 3$

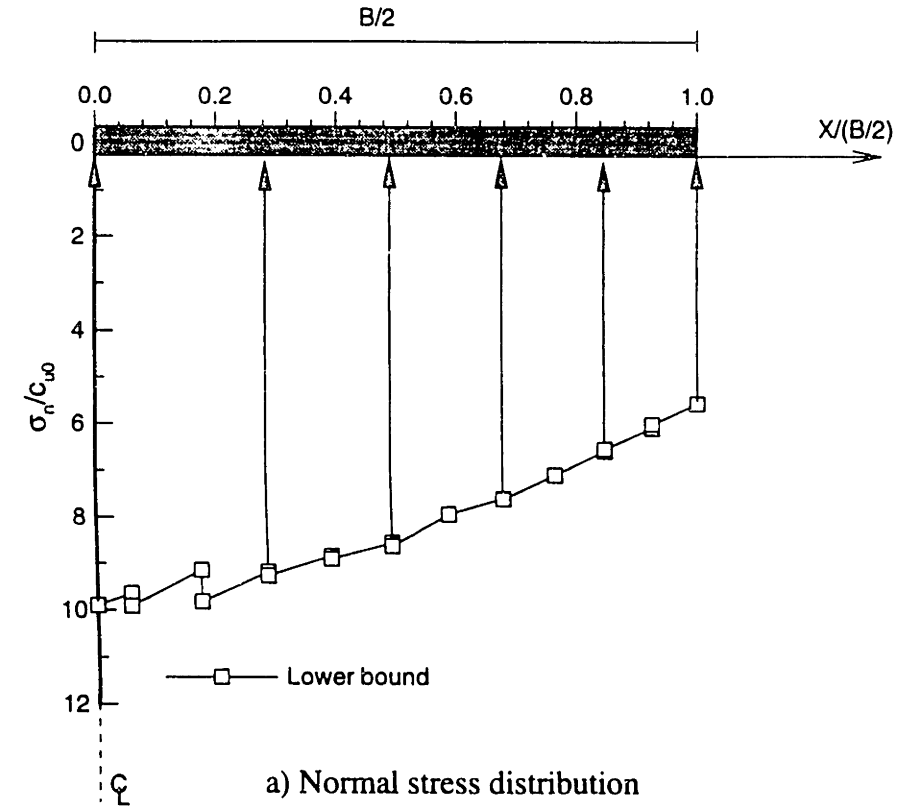

a) Normal stress distribution

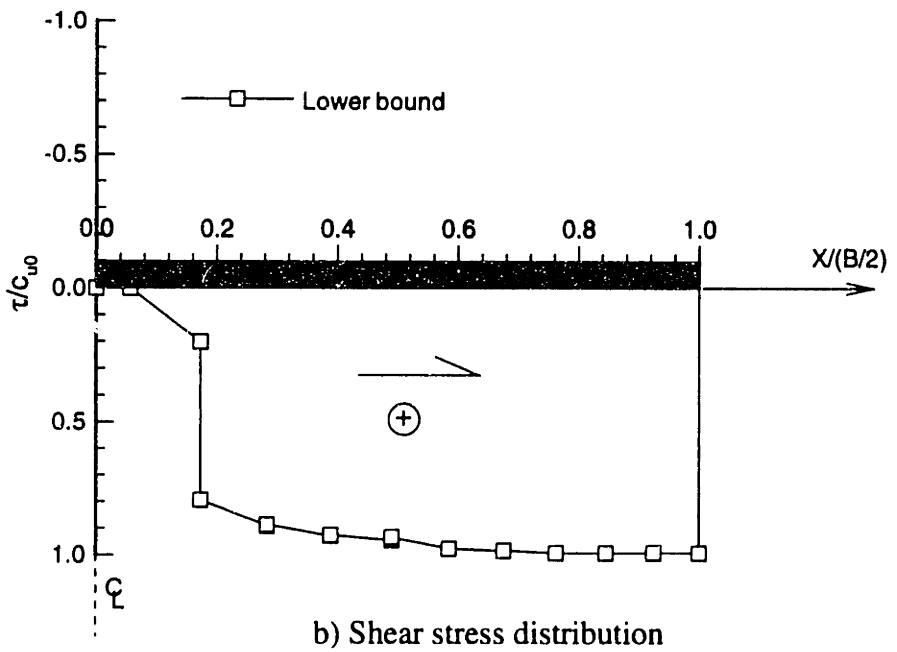

b) Shear stress distribution

Fig. 4.44 Lower bound for normal stress and shear stress beneath rough rigid footings on non-homogeneous clay, where $\rho B/c_{u0} = 3$

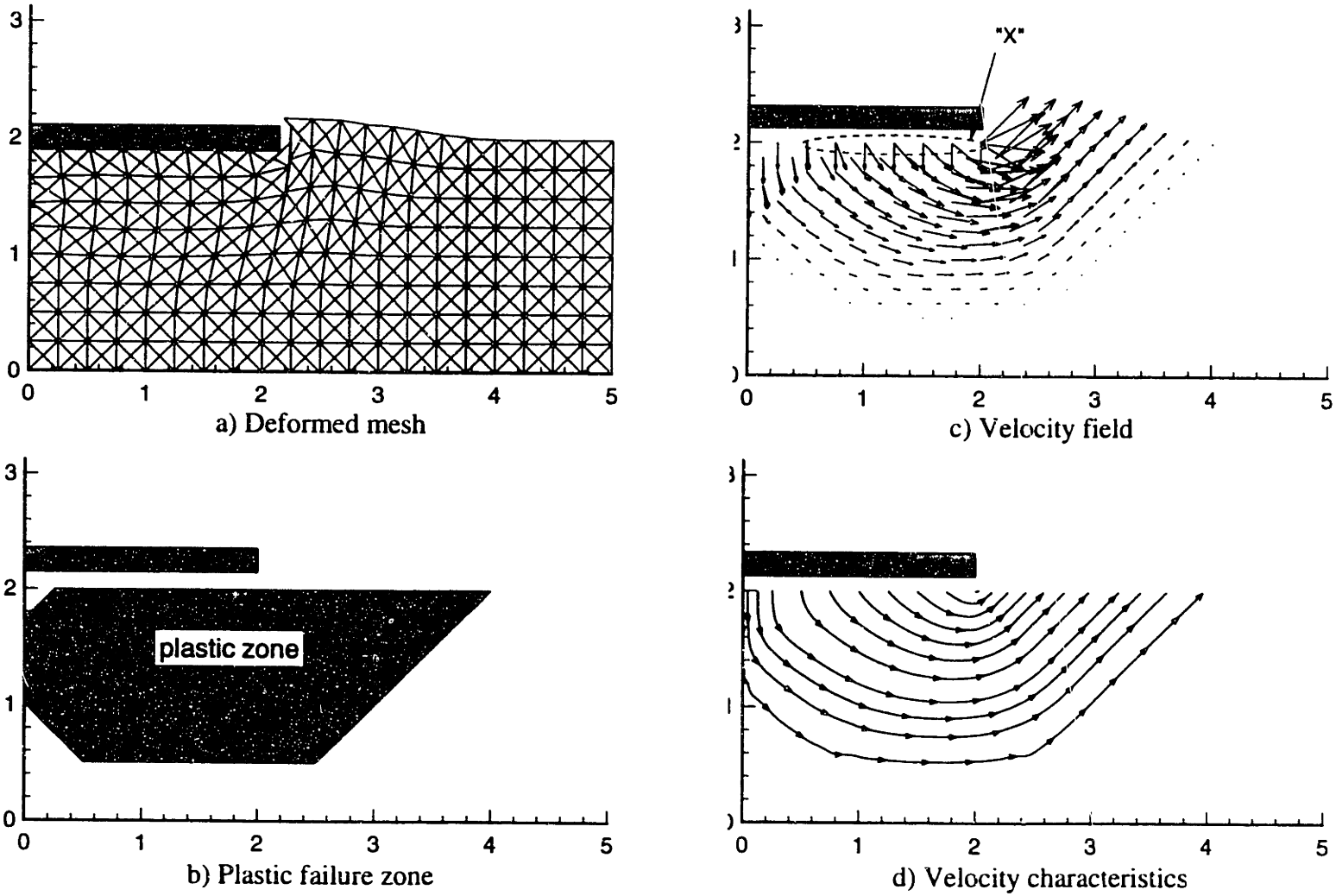

Fig. 4.45 Summary of upper bound results for rough rigid footings on non-homogeneous clay, where $\rho B/c_{u0}=3$

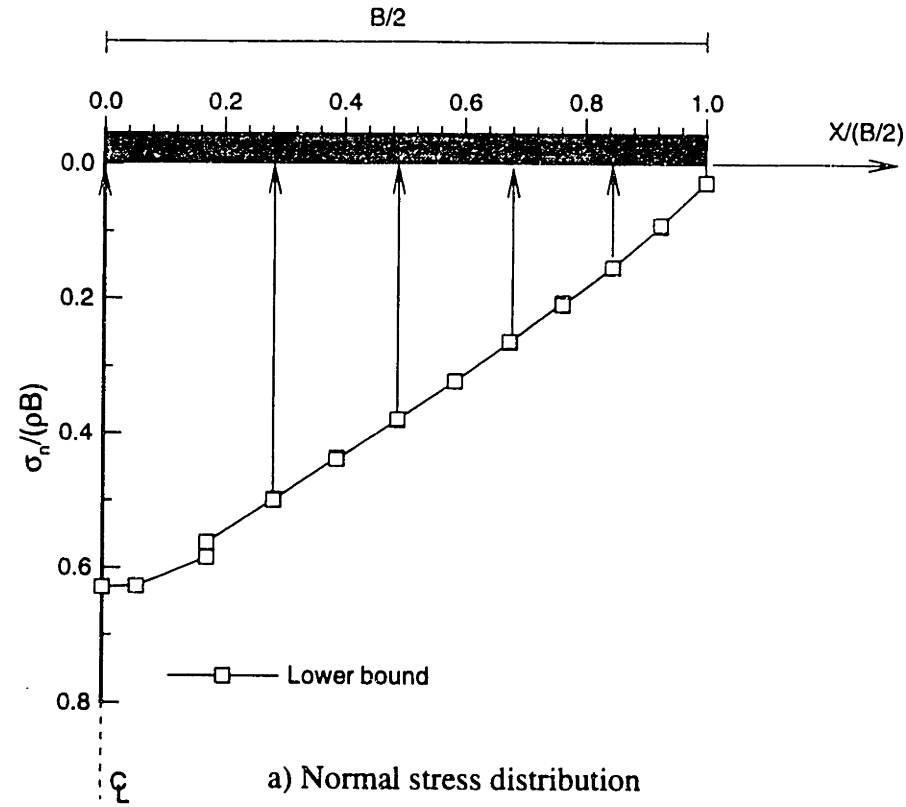

a) Normal stress distribution

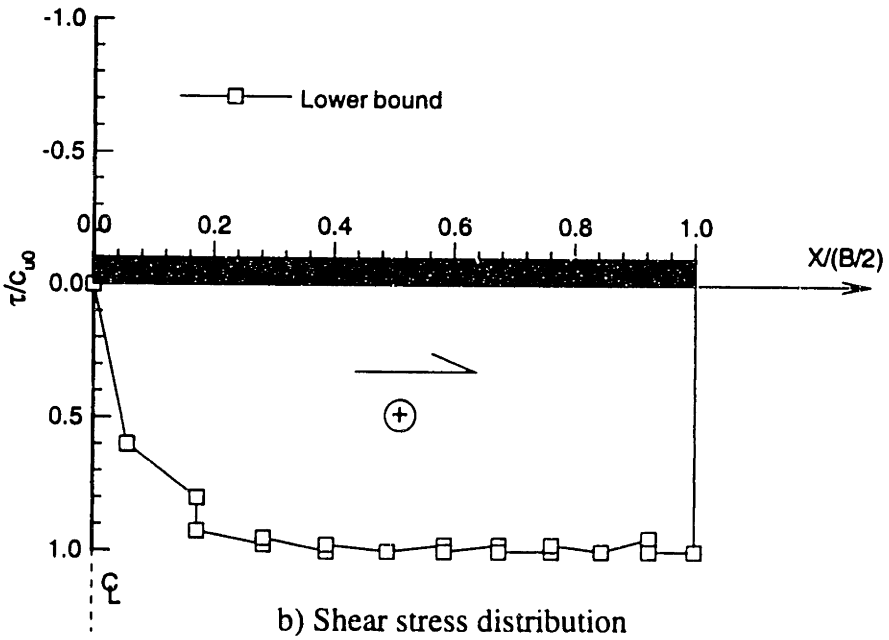

b) Shear stress distribution

Fig. 4.46 Lower bound for normal stress and shear stress beneath rough rigid footings on non-homogeneous clay, where $c_{u0}/(\rho B) = 0.005$

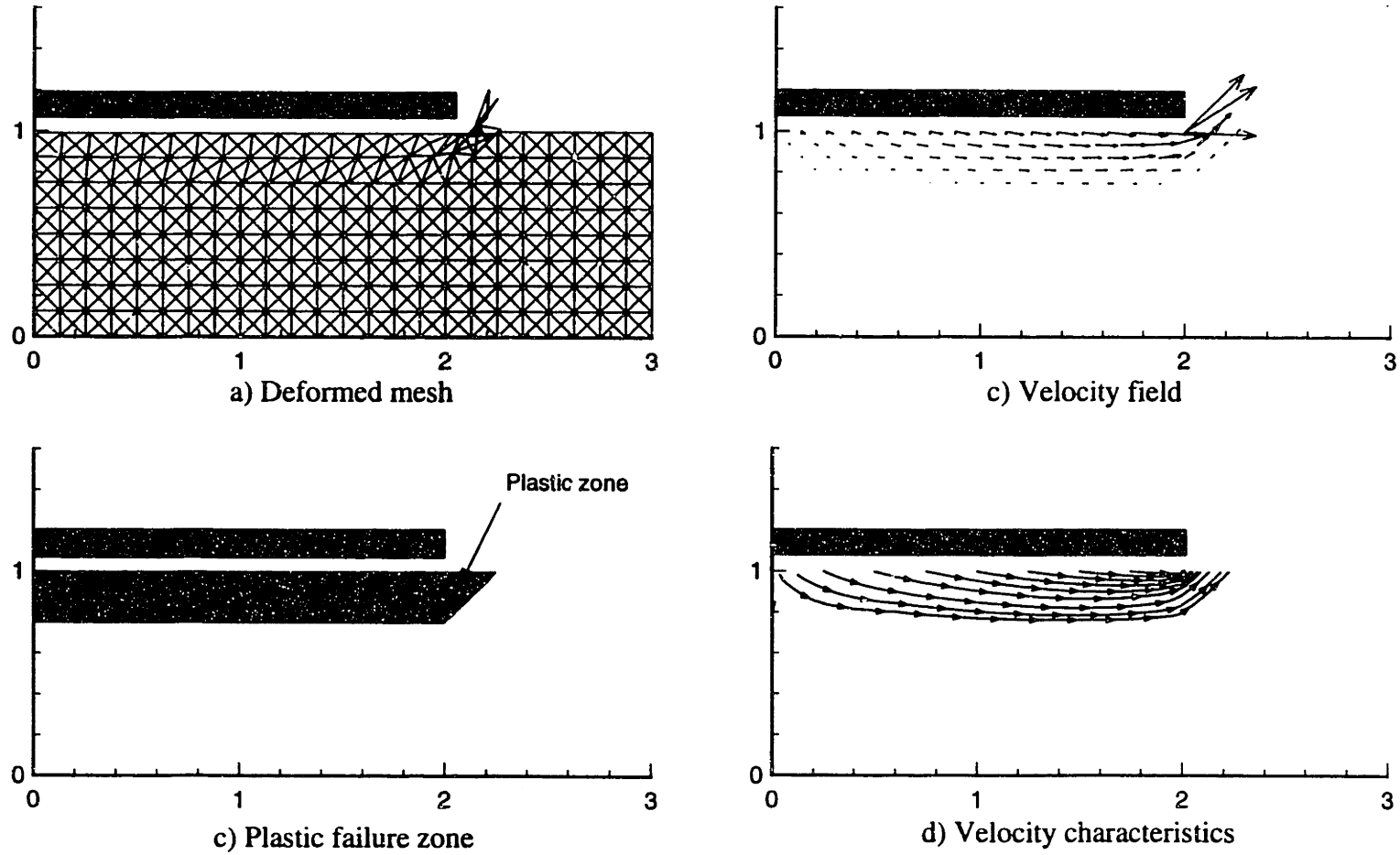

Fig. 4.47 Summary of upper bound results for rough rigid footings on non-homogeneous clay, where $c_{u0}/(\rho B)=0.005$

5. Undrained Bearing Capacity for Footings on Clay with Inclined and Eccentric Loads

5.1 Introduction

This chapter describes the application of the numerical limit analyses for computing the undrained bearing capacity of a rough rigid footing on a homogeneous clay layer with inclined and eccentric loads. There are no exact collapse loads published for this problem and hence, the results are evaluated through comparison with published empirical solutions. The analyses are then extended to include the situation where undrained shear strength increases linearly with depth. This application demonstrates the capabilities of the numerical limit analyses to deal simultaneously with complex boundary conditions (associated with inclined, eccentric loads) and non-homogeneities of the soil. The results also represent the first step towards the use of limit analyses for problems of soil-structure interaction.

Section 5.2 describes modifications of the lower and upper bound programs to incorporate the general interface conditions between a rough rigid footing (with inclined and eccentric loads) and the underlying soil. These modifications represent generalizations of the boundary conditions within the existing programs supplied by Sloan (1994). Section 5.3 describes the results of analyses performed for a succession of increasingly complex cases: 1) eccentric vertical loading; 2) centric inclined loading; and 3) combined eccentric and inclined loading. Section 5.4 gives further solutions for non-homogeneous clay layers. Solution accuracy is controlled by the range of the collapse load obtained from the numerical lower and upper bound calculations. Bearing capacity factors represented, as dimensionless functions of the inclination angle, eccentricity-to-width ratio, and undrained shear strength of the clay, are compared with existing empirical solutions. The analyses are also summarized in the form of a three-dimensional failure envelope in terms of the (three) statically equivalent forces on the footing (vertical, horizontal and moment loads). Section 5.5 describes the development of general mathematical functions to describe the failure surface.

5.2 Footing-Soil Interface Conditions for Eccentric and Inclined Loading

When a footing is subjected to inclined and/or eccentric loads, the representation of interface boundary conditions become more complicated as the failure mechanisms are related to the inclination angle and eccentricity of the applied load as well as the strength profile of the clay (cf. Chapter 4). For example, as the inclination angle of the applied load increases, the failure changes from a bearing capacity mechanism to direct sliding along the interface. Similarly, as the load eccentricity increases, the base of the footing will tends to separate from the underlying soil assuming that the interface can not sustain (negative) tensile stresses. In contrast to the preceding analyses (vertical, concentric loading) in Chapter 4, there are no exact analytical solutions for combined loading of a rough rigid footing. The published solutions are approximations based on empirical measurements from model tests or using limit equilibrium methods. The following sections describe modifications of the original lower and upper bound programs to handle the interface boundary conditions imposed by combined inclined and eccentric loads.

5.2.1 Modifications to the Lower Bound Program

The first modification of the lower bound program is to constrain the shear resistance at the soil-footing interfaces. This is achieved by introducing special interface constraints (section 4.4). Figure 5.1 shows a schematic of the interface which is characterized by footing nodes (a-f), soil nodes (1-6) and interface elements (m-o). Nodes a-f have the same coordinates as nodes 1-6, respectively. Each footing node has three unknown stress (σ_x, σ_y, τ_{xy}) like other nodes in the mesh. Along each interface, the shear and normal stresses must remain equal on either side of the interface (a-b and 1-2, etc), while the tangential normal stress can be discontinuous across the interface. The strength of all interfaces follows the Mohr-Coulomb yield criterion with parameters c_i and ϕ_i, the interface cohesion and the interface friction angle, respectively. For a perfectly rough footing, the interface cohesion and friction angle are assumed to be equal to those of the underlying soil. Since the soil in this study is purely cohesive, the interface cohesion is equal to undrained shear strength of clay at the surface, and the interface friction angle is zero.

The second modification enables inclined and eccentric loads to be used in the analysis by enforcing additional equilibrium constraints along each loaded segment of the footing. For a rigid footing, the normal stress and shear stress are not necessarily uniform at all points along the base of footing. Instead, they may be discontinuous or even change sign at any point. However, the normal stress and shear stress must satisfy the equilibrium with the external applied load. Consider a rigid footing subjected to an inclined and eccentric load, Q in Figure 5.2. The net load, Q is inclined at an angle $\alpha°$, and is applied through point K located a distance, e from the center of the footing. Thus, to be statically admissible, the stresses over the loading segment must satisfy two equations of force equilibrium:

$$\Sigma F_t = 0: \qquad Q\sin\alpha = \int_s \tau dx \tag{5.1}$$

$$\Sigma F_n = 0: \qquad Q\cos\alpha = \int_s \sigma_n dx \tag{5.2}$$

where τ, σ_n = shear normal and stress along the footing nodes, respectively

s = surface area of footing base

x = distance measured from the point of load application

Combining equations 5.1 and 5.2 gives rise to the following equation:

$$\sin\alpha \int_s \sigma_n dx = \cos\alpha \int_s \tau dx \tag{5.3}$$

The stresses must also satisfy moment equilibrium:

$$\Sigma M_K = 0: \qquad \int_s x\sigma_n dx = 0 \tag{5.4}$$

Hence, equations 5.3 and 5.4 summarize the equilibrium constraints which must be enforced over the loading segment.

Equilibrium also requires that the shear and normal stresses remain equal on all points, along both sides of the interface. Since the stresses vary linearly along each discontinuity, this condition is satisfied by enforcing constraints at the end nodes of each interface segment:

Normal direction: $\sigma_{n1} = \sigma_{na}$; $\sigma_{n2} = \sigma_{nb}$; . . . ; $\sigma_{n6} = \sigma_{nf}$ (5.5)

Tangential direction: $\tau_{n1} = \tau_{na}$; $\tau_{n2} = \tau_{nb}$; . . . ; $\tau_{n6} = \tau_{nf}$ (5.6)

By enforcing the constraints given in equations 5.3-5.6, lower bound analyses can be performed for inclined and eccentric loading of footings, while satisfying all the requirements for a statically admissible stress field.

The third modification is introduced in order to model the separation which can occur between the footing and the soil at large load eccentricity. The lower bound analysis states that yield conditions must be satisfied at all points in the soil. Assuming that no tension can be sustained across the interface, the Tresca yield criterion must be modified to include a tension cutoff, shown in Figure 5.3 The stresses along soil-footing interfaces must satisfy the modified Tresca yield criterion as:

Tresca yield criterion: $|\tau| \leq c_i$ (5.7)

Tension cutoff: $\sigma_n \geq 0$ (5.8)

The shaded area in Figure 5.3 shows the intersection of the inequality constraints given in equations 5.7 and 5.8.

Finally, the objective function (i.e. maximization of the applied load, Q) must be modified to account for the inclination angle, α as follows:

$$\text{Max.}\{Q\} = \text{Max.}\ \{\frac{1}{\cos\alpha}\int_s \sigma_n dx\} \qquad (5.9)$$

Alternatively, the objective function can be expressed in terms of the shear stress based on equation 5.1:

$$\text{Max.}\{Q\} = \text{Max.}\ \{\frac{1}{\sin\alpha}\int_s \tau dx\} \qquad (5.10)$$

Since the stresses are constrained by equation 5.3, either equation 5.9 or 5.10 can represent the objective function for the lower bound, linear programming problem.

5.2.2 Modifications to the Numerical Upper Bound Program

Modifications of the upper bound analyses for inclined and eccentric loading are conceptually similar to those described above for the lower bound analyses. Soil-footing interfaces are introduced explicitly in the formulation (cf. section 4.4). Figure 5.4 shows

the interface representation which is composed of footing nodes (a-f), soil nodes (1-6) and interface elements (m-o). Nodes a-f have the same coordinates as node 1-6, respectively. Each of the footing nodes has two unknown velocities, (u, v), like other nodes in the mesh. The velocities vary linearly along the interface from one end to another. The soil-footing interfaces form velocity discontinuities which enable the footing to move independently from the underlying soil. As a result, the interfaces permit all kinds of failure mechanisms to occur ranging from bearing capacity to sliding failure, as well as separation between the footing and soil due to eccentric loading.

When a rigid footing is subjected to inclined and eccentric load, its motions can be fully defined by three degree of freedom, either horizontal and vertical translations and rotation about the center of the footing (or combinations of these). Thus, the second modification is to introduce the rigid body movement for the footing as shown in Figure 5.5. The motions of the rigid footing can be described by three unknown velocities at the center of its base in the horizontal u_{cg}, and vertical directions v_{cg}, and one angular velocity, w_{cg} (rotation). To be kinematically admissible, the velocities along footing nodes must be compatible with these three unknown velocities describing the rigid body movement. Consider point A located on the base of the footing which is inclined at an angle of θ to the x-axis (anti-clockwise direction is positive). The horizontal and vertical velocities of this point must satisfy the following equation:

$$u_A = u_{cg} - w_{cg} \times \sin\theta \qquad (5.11)$$

$$v_A = v_{cg} + w_{cg} \times \cos\theta \qquad (5.12)$$

where u_A, v_A = horizontal and vertical velocities of point A, respectively

x = distance from the center of footing to point A

Since the velocities vary linearly along the base of the footing, these kinematic conditions are satisfied everywhere along the base by enforcing constraints at each of the footing nodes (a-f; Figure 5.4).

In order to model the mechanisms of separation between the footing and the soil, it is necessary to enforce the flow rule at the soil-footing interfaces. Assuming that the interface can not sustain tensile (normal) stress, a tension cut-off is included in the yield criterion (equations 5.7 and 5.8). To be kinematically admissible, the flow must remain

associated with this modified Tresca yield criterion. Figure 5.6 illustrates the direction of the tangential (Δu_t) and normal (Δu_n) velocity jump at the soil-footing interface corresponding to the Tresca yield criterion with tension cut-off. The velocity jumps in the tangential and normal directions correspond to the three line segments marked in Figure 5.6:

$$(1) \qquad \Delta u_t \geq 0 \; ; \; \Delta u_n = 0 \qquad (5.13)$$

$$(2) \qquad \Delta u_t = 0 \; ; \; \Delta u_n \leq 0 \qquad (5.14)$$

$$(3) \qquad \Delta u_t \leq 0 \; ; \; \Delta u_n = 0 \qquad (5.15)$$

Combining these three equations gives rise to the constraint of the flow rule at the soil-footing interface.

$$\Delta u_t = \text{unspecified sign} \qquad (5.16)$$

$$\Delta u_n \leq 0 \qquad (5.17)$$

Since Δu_t can be positive, zero or negative (unspecified signed), it is not necessary to enforce equation 5.16. However, constraint 5.17 must be enforced at all soil-footing interfaces. The physical interpretation of equation 5.16 is that the base of the footing can slip in either direction along the interface ($\Delta u_t < 0$ or $\Delta u_t > 0$), or may stick to the soil. ($\Delta u_t = 0$). The constraint imposed by equation 5.17 implies that the base of the footing can either remain in contact with the soil ($\Delta u_n = 0$), or separate from it ($\Delta u_n < 0$). Therefore, all types of possible failure mechanisms can be captured by these two constraints.

The final modification of the program adjusts the objective function to account for the general case of inclined and eccentric loading. The upper bound analysis finds the minimum value of the applied load, Q for a kinematically admissible velocity field. Thus, the objective function minimizes the applied load, Q. Consider the footing subjected to an inclined and eccentric load, as shown in Figure 5.5. The external work done by the applied load, Q is:

$$W_{ext} = Q \{ \sin(\alpha + \theta) u_{cg} - \cos(\alpha + \theta) v_{cg} - e \cos(\alpha) w_{cg} \} \qquad (5.18)$$

The external work done by the applied load is then equated with the internal dissipation of power through the principle of virtual work:

$$Q \{ \sin(\alpha + \theta) u_{cg} - \cos(\alpha + \theta) v_{cg} - e \cos(\alpha) w_{cg} \} = W_{int} \qquad (5.19)$$

The internal dissipation of power, W_{int} is based on equation 3.14j as described in Chapter 3. Hence, the applied load, Q can be obtained from equation 5.19 by enforcing the constraint that:

$$\sin(\alpha + \theta)\, u_{cg} - \cos(\alpha + \theta)\, v_{cg} - e\cos(\alpha)\, w_{cg} = 1 \qquad (5.20)$$

Substituting this equation to (5.19) yields the expression of the external load.

$$Q = W_{int} \qquad (5.21)$$

Therefore, the objective function for the upper bound linear programming problem is given by:

$$\text{Min. } \{Q\} = \text{Min. } \{W_{int}\} \qquad (5.22)$$

The physical interpretation of equation 5.20 is that the point of load application is constrained to move in the same direction as the applied load with a unit virtual displacement. Thus, by enforcing constraint 5.20, the problem of finding the minimum value of the applied load is equivalent to the problem of finding the least amount of internal dissipation of power (equation 5.22). This interpretation confirms the fact that in nature, the critical failure mechanism corresponds with the one which yields the least amount of energy dissipation.

5.3 Results of Inclined and Eccentric Loaded Footing on Homogeneous Clay

5.3.1 Introduction

Figure 5.7 summarizes the general loading geometry with a total applied load, Q, applied on a footing of width, B. The applied load acts at an angle of inclination, α, to the vertical, and an eccentricity, e (relative to the center of the footing). Sign conventions of α and e are also shown in the figure. The loading conditions can also be represented by a set of statically equivalent loads, the vertical load V, horizontal load H, and moment M, acting at the center of the base (Figure 5.7c). For combined loading of the footing, two sets of load combinations are considered in the analyses: 1) $\alpha > 0$ and $e/B > 0$; and 2) $\alpha > 0$ and $e/B < 0$ (Figure 5.7a, b). Due to the symmetry, the analyses consider inclination angles $\alpha = 0°$- $90°$ and eccentricity ratios, $-0.35 \leq e \leq 0.35$. The remaining combinations for $\alpha < 0°$ can be inferred from the symmetry of the problem.

All lower bound analyses were performed using the mesh shown in Figure 5.8 while three different discretizations were used in the upper bound calculations (Table 5.1). Figures 5.8 and 5.9 also show the stress and velocity boundary conditions considered in the analyses.

The following sections describe the results of numerical limit analyses for three situations: 1) vertical, eccentric loading ($\alpha = 0°$, e); 2) inclined concentric loading (α, e = 0) and 3) combined loading for Type 1 and 2 geometries (α, e) (Figure 5.7).

5.3.2 Vertical and Eccentric Loading

Figure 5.10a shows the bearing capacity factor, $N_c = Q/(Bc_{u0})$, where c_{u0} is the undrained shear strength of the clay (at the surface), as a function of eccentricity ratio, e/B, for footings on homogeneous clay under vertical, eccentric loading. The computed values are also listed in Table 5.2. For all values of e/B, the upper bound and lower bound analyses bracket the true collapse load to within 3-10%. As this range of uncertainty is very small, the average of the upper and lower bound calculations is reported as the 'best estimate' of the collapse load in Table 5.2. The bearing capacity factor decreases almost linearly from 5.147 to 0 as the eccentricity ratio increases from 0 to 0.5. A more complete representation of the collapse load is also given in Figure 5.10b which plots the failure surface in terms of the vertical load capacity, $V/(Bc_{u0})$, and the moment capacity, $M/(B^2c_{u0})$. The values in this figure correspond to best estimate collapse loads. Figure 5.10b show that as the eccentricity increases, the vertical capacity decreases from 5.147 to 0, but the moment capacity increases from 0 to a maximum value of 0.65 at e/B = 0.25 and then decreases at higher eccentricities.

Figures 5.11 through 5.14 show detailed results of the lower bound and upper bound calculations for three loading cases e/B = 0.0, 0.1 and 0.25 (i.e. concentric load, small eccentricity and large eccentricity), respectively. Figure 5.11 compares the mean stress contours from lower bound analyses of these three cases[1]. The results clearly show how the pressurized zone follows the point of load application and reduces in magnitude

[1] Notice that for e/B = 0, the mean stress contours are almost perfectly symmetrical and correspond to solutions reported previously in Figure 4.39.

with increasing eccentricity. The corresponding results of contact normal stresses are summarized in Figure 5.12. For zero eccentricity, the contact normal stress is almost constant over the base of footing. For large eccentricity (e/B = 0.25), the contact normal stress is zero over a large portion of the base, where there is no adhesion between the soil and the footing, while the maximum stress over the remaining portion of the base , $\sigma_n/c_{u0} \approx$ 2-5.1.

Figures 5.13 and 5.14 compare the velocity characteristics and the deformed mesh for the same loading cases. For the concentric load, both the velocity characteristics and the deformed mesh are symmetrical with soil displacing to either side of the footing (Figure 5.13a). As the eccentricity increases, the size of the failure zone decreases significantly and the mechanism dividing line (marked x-x') moves beyond the point of load application towards the edge of the footing (Figures 5.13b, c). Comparisons of the deformed meshes show that for small eccentricity, (e/B = 0.1; Figure 5.14b), the base of footing remains in contact with the soil at all points. However, for large eccentricity (e/B = 0.25; Figure 5.14c), there is a physical separation between the rigid footing and the underlying soil at the distal edge of the footing. The results in Figures 5.11-5.14 clearly show that the constraints governing soil-footing interfaces are able to model correctly a rough, rigid footing subjected to vertical and eccentric load.

5.3.3 Inclined and Concentric Loading

Figure 5.15 summarizes the results of analyses for inclined, concentrically loaded footings on homogeneous clay, which are also tabulated in Table 5.3. For all values of inclination angles, the true collapse loads can be bracketed to within 1-3%. For $\alpha > 15°$, the solutions bracket the collapse load very precisely (< 1% error) and thus, the numerical solutions are almost exact. The upper bound analyses show that failure is caused by sliding of footing along the interface for $\alpha > 15°$. Figure 5.15b shows the failure surface for inclined, concentrically loaded footings in terms of the vertical and horizontal load capacities, $V/(Bc_{u0})$ and $H/(Bc_{u0})$, respectively. As the inclination angle increases from 0° to 90°, the vertical capacity decreases from 5.147 to 0, whereas the horizontal capacity increases to a maximum value of 1.0 (interface sliding). The figure also indicates that the

minimum inclination angle which causes the footing to slide along the interfaces is between 15° and 20°.

Figures 5.16 and 5.17 compare the contact normal stress and shear stress along the interfaces for three load inclinations, α = 0°, 15°, and 45°, respectively. The lower bound analyses predict that contact normal stress is almost constant along the soil-footing interfaces for all 3 inclination angles. At α = 0°, the contact shear stresses is only significant towards the edges of the footing (Figure 5.17a). However, as α increases, the full shear resistance, τ/c_{u0} =1 is mobilized at all points along the base (Figure 5.17b, c).

The corresponding results of velocity characteristics and deformed meshes from upper bound analyses of the same load cases are shown in Figures 5.18 and 5.19, respectively. These results show the transition from a bearing capacity failure under vertical loading (α = 0°; Figure 5.18a) to sliding on the surface at α = 45° (Figures 5.18c and 5.19c), where there is no failure within the soil mass itself.

5.3.4 Type 1 Combined Inclined and Eccentric Loading

Table 5.4 summarizes the bearing capacity factor N_c, and upper and lower bounds on the collapse load obtained from limit analyses for Type 1 combined loading (cf. Figure 5.7) on a homogeneous clay layer. Figure 5.20 shows the bearing capacity factor plotted as functions of the eccentricity ratio, e/B and inclination angle, α. The best estimate of the bearing capacity factor given by the average of the lower bound and upper bound values, is replotted in the same format in Figure 5.21. The results show that for all cases, the collapse loads can be bounded to within 1-9%. The most accurate solutions (bounds $\leq$ 1%) correspond to cases, where $\alpha \geq 30°$ and failure is due to sliding along the soil-footing interface. There is greater uncertainty bounds in the range for loading combinations, where $0.25 \leq e/B \leq 0.35$ and $0° \leq \alpha \leq 15°$. However, taking the average of lower bound and upper bound values as the best estimate, the true collapse loads can be estimated to an accuracy $\pm$ 3 - 4% in all cases.

The results in Figures 5.20 and 5.21 show that the bearing capacity factors generally decrease with increasing inclination angle and/or eccentricity of the loading.

However, for $\alpha > 30°$, changes in eccentricity have no influence on the results which correspond to interface sliding. For $\alpha = 0°$, the bearing capacity factor decreases almost linearly with increasing eccentricity ratio, e/B, and correspond to the situation where the effective width of the footing decreases, until separation occurs at the distal edge of the footing when $e/B \geq 0.20$. Failure mechanisms for combined loading are discussed later in this section.

Note that for loading Type 1 (Figure 5.7), the effects of eccentricity and inclination angle tend to counteract each other. This is because for Type 1 loading combinations, increasing the eccentricity will cause separation to occur at the distal edge (left side of the base) of the footing, but as the load inclination increases, soil is pushed in the direction of the horizontal load component. Hence, combined loading can increase the area of contact between the soil and the footing, and generate higher bearing capacity factors. This observation is confirmed by the results of limit analyses shown in Figure 5.21b. For $0.30 \leq e/B \leq 0.35$, increasing the inclination angle from 0° to 15° results in a small increase in the bearing capacity.

The failure surface of the footing can also be represented in terms of the dimensionless statically equivalent loads: $V/(Bc_{u0})$, $H/(Bc_{u0})$, and $M/(B^2c_{u0})$, as shown in Figure 5.22 (The figure shows only the average of the computed upper and lower bound collapse loads). The data are projected as contour lines corresponding of constant α and e/B in two orthogonal planes $V/(Bc_{u0})$ vs. $M/(B^2c_{u0})$, and $V/(Bc_{u0})$ vs. $H/(Bc_{u0})$, respectively. These two orthogonal plots can be combined to construct a three-dimensional failure surface for Type 1 inclined, eccentric loading. The data form a closed convex surface, Figure 5.23, which defines the combinations of vertical, horizontal, and (centrically-applied) moment which cause failure of the footing on homogeneous clay, F(V, H, M):

$F(V, H, M) = 0$	Failure occurs
$F(V, H, M) < 0$	No failure
$F(V, H, M) > 0$	Physically impossible local condition

The construction of a general failure surface provides clearer meaning and better understanding of the factor of safety when dealing with stability problems where there are

several variables governing the collapse (different mechanisms, etc). For a footing subjected to three statically equivalent loads, V_l, H_l, M_l (applied at the center of the footing), the factor of safety can be defined by the proximity of the loading state to the failure surface[1] .

5.3.5 Type 2 Combined Inclined and Eccentric Loading

Figure 5.24 and Table 5.5 summarize the limit analyses for Type 2 combined inclined and eccentric loading. For all combinations of inclination angles and eccentricities, the collapse loads can be bracketed to within 1-10%. The accuracy of the bounds for loading Type 2 are comparable to those for loading Type 1. Again, the narrow bounds (1%) correspond to the failure caused by sliding of the footing along the surface, whereas the larger bounds (> 9%) correspond to large load eccentricity, e/B = 0.35. The average values of lower bound and upper bound data which are plotted in Figure 5.25 enable the collapse load to be accurately predicted to within ±4-5%. Note that for all cases, increasing eccentricity ratio and inclination angle give rise to reductions in the bearing capacity factor. The failure envelope for Type 2 combined loading is shown in two orthogonal spaces, $V/(Bc_{u0})$ vs. $M/(B^2c_{u0})$ and $V/(Bc_{u0})$ vs. $H/(Bc_{u0})$ in Figure 5.26, and as a three-dimensional surface in Figure 5.27. Type 2 loading generates a closed convex failure surface similar to that described in the preceding section.

5.3.6 Comparison between Type 1 and Type 2 Combined Loading

Figure 5.28 compares the average bearing capacity factors for Type 1 and Type 2 combined loading cases shown as function of α and $|e/B|$. The differences between the bearing capacity factor of loading Type 1 and Type 2 are given in Table 5.6. For all cases (except α = 7.5 and $|e/B|$ = 0.05), the bearing capacity factors of loading Type 1 are greater than those of loading Type 2. The differences range from 1 - 22%. Small differences correspond to large inclination angles or small eccentricity ratios, whereas large differences correspond to large eccentricity ratios $|e/B|$ = 0.25 - 0.35, and moderate

[1] Several definitions of factor of safety are possible from Figure 5.23, for example using homeothetic functions $F(xV_l, xH_l, xM_l) = 0$; where $x \geq 1.0$ is the factor of safety.

inclination angles, α = 15°-30°. Large differences in the bearing capacity factors for Type 1 and Type 2 loading can be explained by differences in the failure mechanism as discussed in section 5.3.4.

Figures 5.29a and b compare the failure surface of Type 1 and Type 2 loading in two orthogonal planes $V/(Bc_{u0})$ vs. $M/(B^2c_{u0})$ and $V/(Bc_{u0})$ vs. $H/(Bc_{u0})$. These comparisons show the lack of symmetry for the two load cases. Figure 5.30 shows the complete 3-D failure surface (which is closed and convex) that defines failure for any combination of the three statically equivalent loads applied at the center of the footing.

Two detailed comparisons were made between the Type 1 and Type 2 loading for the same inclination angle, 1) small eccentricity (α = 7.5°, e/B = ±0.10), and 2) large eccentricity (α = 7.5°, e/B = ±0.25). Figures 5.31 and 5.32 show the upper bound results for loading Type 1 and Type 2, respectively. There are large differences in the velocity characteristics and failure mechanisms for these two cases. In both cases, increased eccentricity causes the proximal edge (right side for Type 1, left side for Type 2) of the footing to plough into the soil, while the distal edge (left side for Type 1, right side for Type 2) separates. Figure 5.31a shows that for small inclination angle of Type 1 loading case, soil fails only one side of the footing, canceling out the effects of the eccentricity load. In contrast, for similar Type 2 loading combinations (Figure 5.32a), the failure occurs below the whole footing showing that the inclination and eccentricity act together in reducing the load capacity.

For large eccentricity (e/B = 0.25) of Type 1 loading (Figure 5.31b), failure occurs on both sides (i.e. mechanism dividing line forms below point of load application, x-x′ in Figure 5.31b) and the size of failure zone remain almost constant. These results which indicate that the eccentricity controls the failure mechanism rather than the inclination angle. On the other hand, for Type 2 loading (Figure 5.32b), the failure zone reduces in size with increasing eccentricity, and hence there is a larger reduction in the bearing capacity factor (29.9% reduction for Type 1 vs. 37.3% for Type 2). These results explained why the bearing capacity factor for Type 1 loading is greater than that of Type 2.

5.3.7 Computation Times

Tables 5.7 summarizes the computation times (CPU times) required for the analyses of a rough rigid footing subjected to an inclined and eccentric load for Type 1 and Type 2 loading. The analyses were performed on DEC ALPHA 3000-300X workstation. For most practical problems, each analysis typically requires CPU times in the range 10-30 minutes. Larger CPU time (up to 50 mins.) may be required when dealing with large eccentricities. However, this amount of CPU time is still expected to be highly competitive with existing methods, such as the non-linear displacement finite element analyses. Notice that the CPU times for the upper bound analyses are typically 1.5-2.0 times larger than those for the lower bound analyses.

5.3.8 Comparisons of the Numerical Limit Analyses and the Existing Solutions

Several authors (Meyerhof, 1953; Vesic, 1975; Saran & Agarwal, 1991) have presented solutions for the bearing capacity factor, N_c, for inclined and eccentric loading of footings on homogeneous clay. For a vertical, eccentric load, both Meyerhof (1953) and Vesic (1975) adopt the concept of effective width area, which assumes that the vertical load acts over an apparent footing width, $B' = (B - 2e)$ (i.e. the collapse load, $Q = (2+\pi)B'c_{u0}$). However, for an inclined and concentric load, both authors propose inclination factors, λ_c which are applied by multiplying this factor with the bearing capacity for the vertical load. Values of λ_c were obtained empirically from experiments on model footings. The resulting bearing capacity factors for combined loading are then given as:

Meyerhof (1953)
$$N_c = (2+\pi)\frac{(1-\alpha/90)^2}{\cos\alpha}(1-2e/B) \qquad (5.23)$$

Vesic (1973)
$$N_c = (2+\pi)\frac{1}{\cos\alpha + 2\sin\alpha}(1-2e/B) \qquad (5.24)$$

It should be noted that neither Meyerhof (1953) nor Vesic (1975) consider differences between Type 1 and Type 2 loading conditions.

More recently, Saran and Agarwal (1991) have applied limit equilibrium methods to solve the footing problem subjected combined inclined and eccentric loading. Their

method allows separation to occur between the footing and soil but requires extensive trial and errors search in order to obtain reliable solutions. They also neglect Type 2 loading condition.

Comparisons have been made between the numerical limit analyses and the published solutions for four cases: 1) vertical, eccentric load (α = 0, e/B); 2) inclined, concentric load (e/B = 0, α); 3) combined Type 1 loading (α, e/B $\geq$ 0) and 4) Type 2 combined loading (α, e/B $\leq$ 0). Figure 5.33 compares these published solutions with results of limit analyses for the first two cases. Figure 5.33a shows that the solutions of Meyerhof (1953) and Saran and Agarwal (1991) match almost exactly the lower bound limit analyses for eccentric, vertical loading with a linear decrease in N_c as a function of the eccentricity, e/B. These results indicate that the effective width concept for vertical and eccentric load corresponds to a lower bound solutions. Figure 5.33b shows that the inclined bearing capacity factors proposed by Meyerhof (1953) and Saran and Agarwal (1991) do not match the limit analyses, as they do not take account correctly for the sliding mechanism. Hence, these solutions overestimate the true value of N_c at inclinations $20° \leq \alpha \leq 60°$, and underestimate the sliding resistance of the footing for $\alpha \geq 60°$. In contrast, the solutions given by Vesic (1975) are in excellent agreement with the results of the lower bound limit analyses.

Figures 5.34 and 5.35 compare the published solutions with the results of limit analyses for Type 1 and Type 2 combined loading, respectively. The comparisons show significant limitations of all three published solutions for combined eccentric and inclined loading. In many of these cases, the published solutions underestimate the bearing capacity factor by 20-25% for Type 1 and Type 2 combined loading. These results show clearly the theoretical limitation of the existing solutions. However, it is also clear that the existing solutions are generally conservative. As a result, the modified bearing capacity factors from limit analyses imply larger allowable loads in design, and will require further validation before these recommendations can permeate into geotechnical practice.

5.4 Results of Inclined and Eccentric Loaded Footings on Non-Homogeneous Clay

5.4.1 Introduction

This section extends the calculations for inclined and eccentrically loaded footings to the situations where the clay profile is non-homogeneous. Figure 5.36 summarizes the loading geometry and the sign conventions of the inclination angle, α, and eccentricity, e. The analyses were performed for two cases: 1) vertical, eccentric loading with e/B = 0-0.35 and 2) inclined, concentric loading with inclination angles, α = 0°-30°. Also shown in this figure is a set of statically equivalent loads - vertical load (V), horizontal load (H), and moment load (M), which act at the center of the base of footing.

For the situation where undrained shear strength increases linearly with depth, the bearing capacity factor is governed by the strength parameter $\rho B/c_{u0}$, where ρ is the gradient of undrained shear strength with depth, B is the width of the footing and c_{u0} is the undrained shear strength at the surface. For most practical problems[1], the range of $\rho B/c_{u0}$ is between 0 - 12. Note that the homogeneous case corresponds to the strength parameter, $\rho B/c_{u0} = 0$.

5.4.2 Vertical and Eccentric Loading

Table 5.8 summarizes the bearing capacity factor obtained from the limit analyses for a footing subjected to vertical, eccentric loading (α = 0, e/B) on non-homogeneous clay. The bounds of the collapse load are also shown in this table. For all of the cases considered, the collapse loads can be bracketed within to 3.3% - 9.2%. Using the mean of lower bound and upper bound data as the best estimate enables the true collapse loads be accurately predicted to within ± 2 - 4.5%.

Figure 5.37 summarizes the bearing capacity factors (average of upper and lower bound collapse loads) plotted as a function of the eccentricity ratio, e/B, and the strength parameter, $\rho B/c_{u0}$. For selected strength profile ($\rho B/c_{u0}$), the bearing capacity decreases almost linearly with increasing eccentricity (Figure 5.37a). Fig. 5.37b shows that for a give eccentricity of loading, the bearing capacity factor increases with the ratio $\rho B/c_{u0}$ (over the

[1] Note on exception: For offshore foundations on deep layers of normally consolidated clay $c_{u0} = 0$, and therefore $\rho B/c_{u0} = \infty$.

range $\rho B/c_{u0} \leq 12$. The rate of increase in N_c depends on the eccentricity ratio, e/B. For small eccentricity, small changes in $\rho B/c_{u0}$ can substantially alter the bearing capacity. On the other hand, at large eccentricity (e/B = 0.25), the bearing capacity is largely independent of the strength profile ($\rho B/c_{u0}$ = 0 - 12).

Figure 5.38 illustrates the failure envelope for vertical, eccentric loading of footings on non-homogenous clay. The bearing capacity factors are reported in terms of the statically equivalent vertical and moment loads $V/(Bc_{u0})$, and $M/(B^2c_{u0})$. The results show that the size of the failure envelope is controlled by the strength profile parameters, $\rho B/c_{u0}$.

Figure 5.39 - 5.41 compare results of velocity fields and velocity characteristics from upper bound analyses at $\rho B/c_{u0}$ = 0 and 2, for three eccentricity ratios, e/B = 0, 0.10 and 0.25. Notice that non-homogeneity in shear strength reduces the size of the failure zone in all cases. but has little effect on the actual failure mechanism for the selected values of $\rho B/c_{u0}$.

5.4.3 Inclined and Concentric Loading

Table 5.9 summarizes the results of limit analyses for inclined and concentric load on non-homogeneous clay. For all cases, the collapse loads can be bracketed within to 1% - 7.3%. Small bounds (1%) correspond to the failure due to the sliding of footing along surface. The prediction of the collapse load is accurate to within ± 1-3.5% using the mean of lower bound and upper bound values.

Figure 5.42 shows the bearing capacity factors plotted as function of inclination angle, α, and the strength profile parameter, $\rho B/c_{u0}$. The data are the average of lower bound and upper bound solutions. The results show that for a selected value of the strength profile parameter, the bearing capacity factor reduces with increased load inclination, α. Substantial reductions in the bearing capacity occur as $\rho B/c_{u0}$ increases. For load inclinations $\alpha < 10°$, the bearing capacity increases significantly with $\rho B/c_{u0}$ (Figure 5.42b). However, for $\alpha \geq 10°$, the bearing capacity factors remain constant for all strength profiles as the failure corresponds to interface sliding.

Figure 5.43 shows the failure envelope in $V/(Bc_{u0})$ vs. $H/(Bc_{u0})$ space for inclined and concentric loading of footings on non-homogenous clay. The data form contour lines corresponding to constant values of α and $\rho B/c_{u0}$. The results show that increasing the strength profile parameter enlarges the size of the failure envelope. For $\alpha \geq 15°$, the failure envelopes coalesce to the same line, corresponding to interface sliding.

Figure 5.44 compares the velocity field and velocity characteristics for the same inclination angle ($\alpha = 10°$) but different strength profile parameters ($\rho B/c_{u0} = 0$ and 2). The comparisons show that strength non-homogeneity reduces the size of the failure zone but increases the horizontal component of velocity. Hence, failure approaches interface sliding conditions for much smaller load inclination angles.

5.4.4 Computation Times

Table 5.10 summarizes the computation times for non-homogeneous clay layers with a) vertical, eccentric loading, and b) inclined, concentric loading. Typical CPU time are in range 15 - 35 mins. Larger CPU times may be required when dealing with large strength profile parameters and eccentricity. There are several cases which the analyses require very small CPU times (<10 mins.). These again correspond to failure due to interface sliding.

5.5 Mapping the Failure Surface of Combined Inclined and Eccentric Loading

The purpose of this section is to develop reliable analytical representations for inclined and eccentric loading of footings on clay through functions which map the shape of the failure surface. Based on the results of analyses presented in section 5.3 and 5.4, the bearing capacity factor for combined loading is governed by three parameters:

1. Inclination angle, α
2. Eccentricity ratio, e/B
3. Strength profile parameter, $\rho B/c_{u0}$

The three-dimensional failure surface can be described by mapping a series of projection in the V′ - M′ space (cf. Figure 5.22a). For a selected value of the strength

profile parameter, the projected failure surface in V′ - M′ space can be described by the function shown in Figure 5.45:

$$M' = 0.5V'[1-(\frac{V'}{a})^c]^b \qquad (5.25)$$

where $V' = V/(Bc_{u0})$

$M' = M/(B^2c_{u0})$

V = the equivalent vertical load

a, *b*, *c* = parameters

The three parameters, *a*, *b*, and *c* control the shape of the failure envelope projection, and have physical meaning. Figure 5.45 shows that parameter *a* represents the vertical capacity of the footing under inclined and concentric loading. It is a function of both the strength profile parameter and inclination angle [$a(\rho B/c_{u0}, \alpha)$]. Even though the other two parameters *b* and *c* can not be seen in the figure, they control the shape (y_1 and θ_2) of the projected failure envelope. Parameter *b* shows the effects of the combining the inclination angle and loading Type [$b(\alpha$, loading Type)]. For a given value of the strength profile parameter $\rho B/c_{u0}$, the size of the failure envelope is controlled by $c(\rho B/c_{u0})$. In other words, this parameter shows the effect of non-homogeneity on the collapse loads. Three parameters *a*, *b* and *c* can be found from the results of limit analyses as follows.

Based on equation 5.25, the parameter *a* corresponds to the vertical capacity $V/(Bc_{u0})$ of inclined concentric loading. Thus, we can directly obtain this parameter using the results of limit analyses for inclined concentrically loaded footings on non-homogeneous clay (Figure 5.43). For each point [$V/(Bc_{u0})$, $H/(Bc_{u0})$] on the failure envelope shown in Figure 5.46a, the parameter *a* corresponds to the horizontal distance and is a function of strength profile parameter and inclination angle.

On the other hand, an indirect method must be used in order to obtained parameters *b* and *c*. After rearranging the terms, equation (5.25) becomes:

$$\frac{M'}{V'} = 0.5[1-(\frac{V'}{a})^c]^b$$

Substituting the term on the left hand side with |e/B| gives rise to:

$$|e/B| = 0.5[1-(\frac{V'}{a})^{c}]^{b} \qquad (5.26)$$

Since parameter *c* is only a function of strength profile parameter, it can be evaluated by considering the results of vertical eccentric loaded of footings on non-homogenous clay (Figure 5.38). For vertically loaded (α = 0°), analyses of the projected failure envelope (equation 5.25) show that the value of *b* is equal to 1.0. Rearranging the terms and taking logarithmic function to both sides yields the expression for vertical eccentric loading on non-homogenous clay :

$$\text{Log}(\frac{V'}{a}) = \frac{1}{c}\text{Log}(1-2|e/B|) \qquad (5.27)$$

Hence, for a selected value of the strength profile parameter $\rho B/c_{u0}$, the parameter *c* corresponds to the inverse of the slope for the plot between log(1- 2|e/B|) versus log(V'/*a*) as shown in Figure 5.46b, and is obtained from the results of numerical limit analyses using the linear regression method shown in Figure 5.47. For all cases, the least square error (r^2) ranges from 0.999 - 1.0, which indicates that the parameter *c* is very accurately.

The parameter *b* can be obtained similarly but using the results of inclined eccentric loaded footing on homogeneous clay (Figures 5.22, 5.26). It should be noted that the parameter b is dependent on not only load inclination angle, but loading Type (1 or 2; Figure 5.7) as well. Evaluation of parameter *c* from equation 5.27 shows that $c \approx 1.0$ for homogeneous case. Since we now know the value of parameter *c*, rearranging equation 5.26 leads to the expression for inclined eccentric loading on homogenous clay:

$$\text{Log}(1-\frac{V'}{a}) = \frac{1}{b}\text{Log}(2|e/B|) \qquad (5.28)$$

Hence, for a given loading Type and an inclination angle, the parameter *b* corresponds to the inverse of the slope for the plot between log(2|e/B|) versus log(1-V'/*a*) as shown in Figure 5.46c, and is obtained from the results of numerical limit analyses using the linear regression method shown in Figure 5.48. For all case, the least square error (r^2) ranges from 0.9 - 0.99, which indicates that there are some errors associated with the parameter *b*.

After we have obtained these three parameters described above, a curve fitting technique is used to get the mathematical functions of these parameters, which are given in Table 5.11. These functions are relatively complicated as the shape of the failure surface reflects changes in the mechanism of failure. For example, the parameter *a* reflects the transition from a failure in the clay to interface sliding resistance of the footing (with vertical component of the sliding resistance, $1/\tan\alpha$). It should be mentioned that all equations listed in Table 5.11 are valid for inclination angles $0° \le \alpha \le 30°$, and strength profile parameters $0 \le \rho B/c_{u0} \le 25$. Numerical values of the parameters *a*, *b*, *c* are tabulated in Table 5.12.

By rearranging equation 5.26, the expression for the bearing capacity factor can be obtained.

$$N_c = \frac{a}{\cos\alpha}\{1-(2|e/B|)^{1/b}\}^{1/c} \qquad (5.29)$$

In order to demonstrate the performance of the proposed failure envelope, comparisons between the proposed equation and the numerical limit analyses are made for three cases, namely 1) inclined, concentric load with strength increasing with depth (Figure 5.49); 2) vertical, eccentric load with strength increasing with depth (Figure 5.50); and 3) combined inclined and eccentric load with homogeneous strength (Figures 5.51-5.54). The evaluations include the comparisons of bearing capacity factors, and the comparisons of failure envelope either in the space V-H or V-M or both. The comparisons show that the proposed failure envelope matches very well with the results of numerical limit analyses for two loading cases: 1) inclined, concentric loading (Figure 5.49); and 2) vertical, eccentric loading (Figure 5.50). This indicates that the parameters *a* and *c* are very reliable. There are some approximations which occur in Type 1 and 2 combined loading (Figures 5.51-5.54) and are related to the parameter *b*. Because the maximum errors are less than 10% (5.5% for Type 1; 8.7% for Type 2), in engineering practice the proposed failure envelope is sufficiently accurate to represent the exact solution for an inclined and eccentric loaded footing on clay.

α (deg.) \ e/B	0.00	0.05	0.10	0.15	0.20	0.25	0.30	0.35
0	*A1*	*A1*	A2	A2	A2	A2	*A3*	*A3*
7.5	*A1*	A2	A2	A2	A2	A2	*A3*	*A3*
15	A2	A2	A2	A2	A2	A2	*A3*	*A3*
30	A2	A2	A2	A2	A2	A2	*A3*	*A3*
45	A2	-	-	-	-	-	A2	A2
60	A2	-	-	-	-	-	-	A2
75	A2	-	-	-	-	-	-	A2
90	A2	-	-	-	-	-	-	-

a) Loading Type 1

α (deg.) \ e/B	0.00	-0.05	-0.10	-0.15	-0.20	-0.25	-0.30	-0.35
0	*A1*	*A1*	A2	A2	A2	A2	*A3*	*A3*
7.5	*A1*	A2	A2	A2	A2	*A3*	*A3*	*A3*
15	A2	A2	A2	*A3*	*A3*	*A3*	*A3*	*A3*
30	A2	A2	*A3*	*A3*	*A3*	*A3*	*A3*	*A3*
45	A2	*A3*	*A3*	*A3*	*A3*	*A3*	*A3*	*A3*
60	A2	-	-	-	-	*A3*	*A3*	*A3*
75	A2	-	-	-	-	-	-	*A3*
90	A2	-	-	-	-	-	-	-

Note: "-" = no analysis, failure of soil is due to sliding of footing

b) Loading Type 2

Table 5.1 Meshes used for upper bound analyses of inclined and eccentric loading

Eccentricity ratio e/B	Lower bound (LB)		Upper bound (UB)		Bounds (%)	Best Estimate 0.5*(LB+UB)
	N_c	CPU Time (min.)	N_c	CPU Time (min.)		N_c
0.00	5.061	22	5.232	66	3	5.147
0.05	4.608	17	4.856	64	5	4.732
0.10	4.107	18	4.329	29	5	4.218
0.15	3.592	15	3.804	27	6	3.698
0.20	3.085	15	3.290	24	6	3.188
0.25	2.565	13	2.758	21	7	2.662
0.30	2.030	11	2.208	37	8	2.119
0.35	1.528	11	1.695	32	10	1.612

Table 5.2 Bearing capacity factor, N_c of vertical eccentric loading of footings on homogeneous clay

Inclination angle α (deg.)	Lower bound (LB)		Upper bound (UB)		Bounds (%)	Best Estimate 0.5*(LB+UB)
	N_c	CPU Time (min.)	N_c	CPU Time (min.)		N_c
0	5.061	22	5.232	66	3	5.146
7.5	4.346	17	4.553	44	5	4.449
15	3.498	13	3.685	19	5	3.591
30	1.983	6	2.000	8	1	1.992
45	1.402	6	1.414	7	1	1.408
60	1.145	7	1.155	5	1	1.150
75	1.027	6	1.035	6	1	1.031
90	0.992	6	1.000	5	1	0.996

Table 5.3 Bearing capacity factor, N_c of inclined concentric loading of footings on homogeneous clay

α (deg.) \ e/B		0.00	0.05	0.10	0.15	0.20	0.25	0.30	0.35
0	UB	5.232	4.856	4.329	3.804	3.290	2.759	2.192	1.675
	LB	5.061	4.608	4.107	3.592	3.085	2.566	2.031	1.528
7.5	UB	4.553	4.371	4.040	3.685	3.310	2.831	2.235	1.689
	LB	4.346	4.175	3.845	3.516	3.139	2.640	2.076	1.550
15	UB	3.685	3.592	3.418	3.207	2.960	2.668	2.271	1.734
	LB	3.498	3.401	3.227	3.023	2.794	2.492	2.121	1.591
30	UB	2.000	2.000	2.000	2.000	2.000	2.000	1.892	1.706
	LB	1.983	1.983	1.983	1.983	1.974	1.914	1.803	1.624
45	UB	1.414	1.414	1.414	1.414	1.414	1.414	1.414	1.414
	LB	1.402	1.402	1.402	1.402	1.402	1.402	1.402	1.377
60	UB	1.155	1.155	1.155	1.155	1.155	1.155	1.155	1.155
	LB	1.145	1.145	1.145	1.145	1.145	1.145	1.145	1.145
75	UB	1.035	1.035	1.035	1.035	1.035	1.035	1.035	1.035
	LB	1.027	1.027	1.027	1.027	1.027	1.027	1.027	1.027
90	UB	1.000	-	-	-	-	-	-	-
	LB	0 992	-	-	-	-	-	-	-

a) Bearing capacity factor, N_c

α (deg.) \ e/B	0.00	0.05	0.10	0.15	0.20	0.25	0.30	0.35
0	3.3	5.2	5.3	5.7	6.4	7.3	7.6	9.2
7.5	4.7	4.6	4.9	4.7	5.3	7.0	7.3	8.6
15	5.2	5.5	5.8	5.9	5.8	6.8	6.9	8.6
30	0.9	0.9	0.9	0.9	1.3	4.4	4.8	5.0
45	0.9	0.9	0.9	0.9	0.9	0.9	0.9	2.7
60	0.9	0.9	0.9	0.9	0.9	0.9	0.9	0.9
75	0.8	0.8	0.8	0.8	0.8	0.8	0.8	0.8
90	0.9	-	-	-	-	-	-	-

b) Bounds of N_c (%) between LB and UB

Table 5.4 Bearing capacity factors for Type 1 inclined and eccentric loading on homogeneous clay

α (deg.) \ e/B		0.00	-0.05	-0.10	-0.15	-0.20	-0.25	-0.30	-0.35
0	UB	5.232	4.856	4.329	3.804	3.290	2.759	2.192	1.675
	LB	5.061	4.608	4.107	3.592	3.085	2.566	2.031	1.528
7.5	UB	4.553	4.395	3.997	3.522	3.031	2.504	2.071	1.652
	LB	4.346	4.187	3.796	3.318	2.840	2.359	1.915	1.495
15	UB	3.685	3.588	3.331	2.919	2.557	2.213	1.889	1.565
	LB	3.498	3.400	3.132	2.776	2.400	2.070	1.749	1.429
30	UB	2.000	2.000	1.995	1.928	1.828	1.705	1.559	1.383
	LB	1.983	1.972	1.909	1.818	1.708	1.589	1.442	1.272
45	UB	1.414	1.414	1.414	1.414	1.398	1.367	1.315	1.234
	LB	1.402	1.402	1.389	1.365	1.332	1.288	1.231	1.148
60	UB	1.155	1.155	1.155	1.155	1.155	1.155	1.145	1.123
	LB	1.145	1.145	1.145	1.138	1.128	1.114	1.093	1.060
75	UB	1.035	1.035	1.035	1.035	1.035	1.035	1.035	1.035
	LB	1.027	1.027	1.027	1.027	1.027	1.026	1.022	1.015
90	UB	1.000	1.000	1.000	1.000	1.000	1.000	1.000	1.000
	LB	0.992	0.992	0.992	0.992	0.992	0.992	0.992	0.992

a) Bearing capacity factor, N_c

α (deg.) \ e/B	0.00	-0.05	-0.10	-0.15	-0.20	-0.25	-0.30	-0.35
0	3.3	5.2	5.3	5.7	6.4	7.3	7.6	9.2
7.5	4.7	4.9	5.2	6.0	6.5	6.0	7.8	10.0
15	5.2	5.4	6.1	5.0	6.3	6.7	7.7	9.1
30	0.9	1.4	4.4	5.9	6.8	7.0	7.8	8.4
45	0.9	0.9	1.8	3.5	4.8	5.9	6.6	7.3
60	0.9	0.9	0.9	1.5	2.3	3.6	4.6	5.8
75	0.8	0.8	0.8	0.8	0.8	0.9	1.3	2.0
90	0.9	-	-	-	-	-	-	-

b) Bounds of N_c (%) between LB and UB

Table 5.5 Bearing capacity factors for Type 2 inclined and eccentric loading on homogeneous clay

α (deg.) \ |e/B|	0.00	0.05	0.10	0.15	0.20	0.25	0.30	0.35
0	0.0	0.0	0.0	0.0	0.0	0.0	0.0	0.0
7.5	0.0	-0.4	1.2	5.1	9.4	11.8	7.8	2.9
15	0.0	0.1	2.8	9.0	14.9	18.6	18.8	10.5
30	0.0	0.3	2.0	6.1	11.7	17.2	20.7	22.6
45	0.0	0.0	0.5	1.3	3.2	5.9	10.1	15.8
60	0.0	0.0	0.0	0.3	0.7	1.4	2.7	5.2
75	0.0	0.0	0.0	0.0	0.0	0.0	0.2	0.6
90	0.0	-	-	-	-	-	-	-

Notes: N_c values of both loading types are the mean of lower bound and upper bound

Difference = N_c(Type 1) - N_c(Type 2)

Table 5.6 Difference of N_c (%) between Type 1 and Type 2 combined loading

α (deg.) \ e/B		0.00	0.05	0.10	0.15	0.20	0.25	0.30	0.35
0	UB	66	64	29	27	24	21	49	42
	LB	22	17	18	15	15	13	11	11
7.5	UB	44	24	23	25	25	22	51	44
	LB	17	15	14	17	18	14	12	11
15	UB	19	20	20	19	20	17	45	36
	LB	13	13	14	15	13	13	13	12
30	UB	8	7	7	9	9	10	31	29
	LB	6	7	7	7	9	9	11	11
45	UB	7	-	-	-	-	-	7	7
	LB	6	-	-	-	-	-	6	10
60	UB	5	-	-	-	-	-	-	6
	LB	7	-	-	-	-	-	-	6
75	UB	5	-	-	-	-	-	-	6
	LB	6	-	-	-	-	-	-	5
90	UB	5	-	-	-	-	-	-	-
	LB	6	-	-	-	-	-	-	-

a) Loading Type 1

α (deg.) \ e/B		0.00	-0.05	-0.10	-0.15	-0.20	-0.25	-0.30	-0.35
0	UB	66	64	29	27	24	21	49	42
	LB	22	17	18	15	15	13	11	11
7.5	UB	44	25	25	25	20	50	43	38
	LB	17	16	15	14	15	13	11	11
15	UB	19	19	18	47	44	45	39	34
	LB	13	13	12	12	10	11	9	9
30	UB	8	23	28	30	30	28	29	29
	LB	6	7	10	9	7	8	24	7
45	UB	7	17	17	18	22	20	23	21
	LB	6	7	6	8	7	6	7	6
60	UB	5	-	-	-	-	16	18	19
	LB	7	6	7	7	6	6	6	6
75	UB	5	-	-	-	-	-	-	16
	LB	6	-	-	-	6	6	6	6
90	UB	5	-	-	-	-	-	-	-
	LB	6	-	-	-	-	-	-	-

Notes: "-" = no analysis, failure of soil is due to sliding of footing

b) Loading Type 2

Table 5.7 CPU times (mins) required for analyses of inclined and eccentric loading of footings on homogeneous clay

$\rho B/c_{u0}$ \ e/B		0.00	0.05	0.10	0.15	0.20	0.25	0.30	0.35
0	UB	5.232	4.856	4.329	3.804	3.290	2.759	2.192	1.675
	LB	5.061	4.608	4.107	3.592	3.085	2.566	2.031	1.528
2	UB	7.829	6.895	5.993	5.124	4.257	3.468	2.712	1.970
	LB	7.426	6.540	5.673	4.830	4.019	3.243	2.506	1.799
4	UB	9.374	8.257	7.120	6.032	5.009	3.996	3.068	2.150
	LB	8.838	7.774	6.680	5.632	4.644	3.703	2.813	1.981
6	UB	10.729	9.416	8.073	6.738	5.564	4.433	3.310	2.332
	LB	9.996	8.785	7.520	6.304	5.160	4.073	3.055	2.134
8	UB	11.873	10.365	8.848	7.430	6.103	4.834	3.571	2.495
	LB	11.157	9.714	8.275	6.907	5.641	4.411	3.298	2.302
12	UB	14.079	12.251	10.404	8.691	7.078	5.422	4.036	2.787
	LB	13.121	11.380	9.613	7.992	6.452	4.985	3.684	2.542

a) Bearing capacity factor, N_c

$\rho B/c_{u0}$ \ e/B	0	0.05	0.1	0.15	0.2	0.25	0.3	0.35
0	3.3	5.2	5.3	5.7	6.4	7.3	7.6	9.2
2	5.3	5.3	5.5	5.9	5.7	6.7	7.9	9.0
4	5.9	6.0	6.4	6.8	7.6	7.6	8.7	8.2
6	7.1	6.9	7.1	6.6	7.5	8.5	8.0	8.9
8	6.2	6.5	6.7	7.3	7.9	9.1	7.9	8.1
12	7.3	7.7	8.2	8.8	9.7	8.8	9.6	9.6

b) Bounds of N_c (%) between LB and UB

Table 5.8 Bearing capacity factors for vertical, eccentric loading of footings on non-homogeneous clay

$\rho B/c_{u0}$ \ α (deg.)		0	5	10	15	20	30
0	UB	5.232	4.792	4.285	3.685	2.924	2.000
	LB	5.061	4.610	4.066	3.498	2.899	1.983
2	UB	7.829	6.621	5.208	3.864	2.924	2.000
	LB	7.426	6.290	4.975	3.807	2.899	1.983
4	UB	9.374	7.695	5.581	3.864	2.924	2.000
	LB	8.838	7.260	5.356	3.831	2.899	1.983
6	UB	10.729	8.499	5.749	3.864	2.924	2.000
	LB	9.996	8.019	5.575	3.831	2.899	1.983
8	UB	11.873	9.075	5.759	3.864	2.924	2.000
	LB	11.157	8.639	5.682	3.831	2.899	1.983
12	UB	14.079	10.115	5.759	3.864	2.924	2.000
	LB	13.121	9.605	5.710	3.831	2.899	1.983

a) Bearing capacity factor, N_c

$\rho B/c_{u0}$ \ α (deg.)	0	5	10	15	20	30
0	3.3	3.9	5.3	5.2	0.9	0.9
2	5.3	5.1	4.6	1.5	0.9	0.9
4	5.9	5.8	4.1	0.9	0.9	0.9
6	7.1	5.8	3.1	0.9	0.9	0.9
8	6.2	4.9	1.3	0.9	0.9	0.9
12	7.3	5.3	0.9	0.9	0.9	0.9

b) Bounds of N_c (%) between LB and UB

Table 5.9 Bearing capacity factors for inclined, concentric loading of footings on non-homogeneous clay

$\rho B/c_{u0}$ \ e/B		0.00	0.05	0.10	0.15	0.20	0.25	0.30	0.35
0	UB	66	64	29	27	24	21	49	42
	LB	22	17	18	15	15	13	11	11
2	UB	32	31	29	25	46	44	38	25
	LB	38	29	27	27	22	21	18	17
4	UB	30	28	25	23	21	35	28	85
	LB	28	23	23	24	20	20	15	15
6	UB	25	27	27	47	39	33	87	74
	LB	29	25	18	22	20	18	31	13
8	UB	31	30	24	24	21	18	84	68
	LB	30	30	29	24	24	21	18	17
12	UB	27	26	24	22	18	93	80	59
	LB	31	28	26	24	20	19	15	14

a) Vertical eccentric load

$\rho B/c_{u0}$ \ α (deg.)		0	5	10	15	20	30
0	UB	66	49	25	8	12	8
	LB	22	17	15	13	11	7
2	UB	32	26	20	1	1	1
	LB	38	27	22	9	6	5
4	UB	30	24	17	1	1	1
	LB	28	24	19	6	5	5
6	UB	25	22	15	1	1	1
	LB	29	25	18	5	6	6
8	UB	31	25	14	1	1	1
	LB	30	25	17	5	6	4
12	UB	27	22	10	1	1	1
	LB	31	30	12	4	8	8

b) Inclined concentric load

Table 5.10 CPU times (mins) required for limit analyses of footings on non-homogeneous clay

Parameter		
a	*b*	*c*
Min. $\begin{cases} r\,(1+s\,(rB/c_{u0})t\,) \\ 1/\tan\alpha \end{cases}$ where $r = (2+\pi)(1 - 1.4781(\sin\alpha)^{1.15})$ $s = 0.3 - 1.3390(\sin\alpha)^{1.2828}$ $t = 0.6828 - 27.5677(\sin\alpha)^{2.7162}$	Type 1: $1 - 1.4672(\sin\alpha)^{0.89}$ Type 2: $1 - 1.3286(\sin\alpha)^{1.0946}$	$1.0201 - 0.1302(\rho B/c_{u0})^{0.3259}$

Notes:

1. The proposed failure envelope: $M' = \pm 0.5V'\{1 - (\frac{V'}{a})^c\}^b$
   where $V'=V/(Bc_{u0})$ and $M'=M/(B^2c_{u0})$
2. Three parameters are valid for $\alpha = 0° - 30°$, and $\rho B/c_{u0} = 0 - 25$

Table 5.11 Mathematical expressions for three parameters of the failure envelope under combined loading conditions

$\rho B/c_{u0}$ \ α (deg.)	0.0	2.5	5.0	7.5	10.0	15.0	20.0	30.0
0	5.142	4.934	4.682	4.411	4.127	3.536	2.747	1.717
2	7.618	7.111	6.452	5.735	5.016	3.732	2.747	1.679
4	9.116	8.416	7.452	6.381	5.338	3.732	2.747	1.714
6	10.384	9.516	8.282	6.897	5.578	3.732	2.747	1.716
8	11.522	10.501	9.017	7.343	5.671	3.732	2.747	1.717
10	12.572	11.409	9.690	7.596	5.671	3.732	2.747	1.717
12	13.557	12.260	10.316	7.596	5.671	3.732	2.747	1.717
16	15.384	13.836	11.430	7.596	5.671	3.732	2.747	1.717
20	17.069	15.288	11.430	7.596	5.671	3.732	2.747	1.717
25	19.033	16.977	11.430	7.596	5.671	3.732	2.747	1.717

a) Parameter *a*

α (deg.)	0.0	2.5	5.0	7.5	10.0	15.0	20.0	30.0
Load Type 1	1.000	0.910	0.833	0.760	0.691	0.559	0.435	0.208
Load Type 2	1.000	0.957	0.908	0.857	0.805	0.697	0.589	0.378

b) Parameter *b*

$\rho B/C_{u0}$	*c*
0	1.020
2	0.857
4	0.816
6	0.787
8	0.764
10	0.744
12	0.727
16	0.699
20	0.674
25	0.648

b) Parameter *c*

Table 5.12 Parameters for analytical representation of the failure surface under combined loading conditions

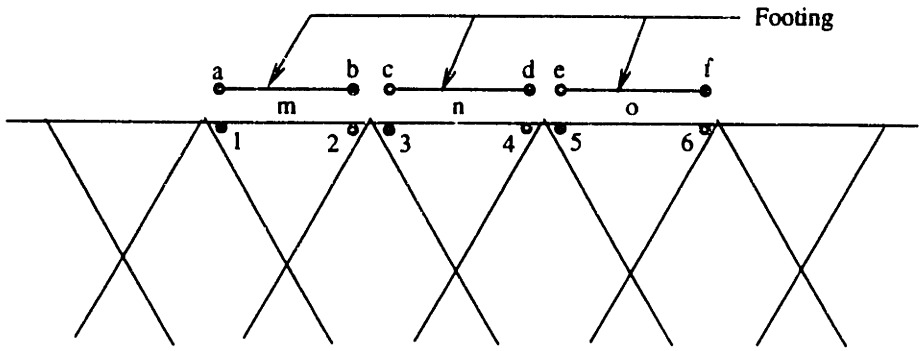

Fig. 5.1 Soil-footing interfaces for the lower bound method

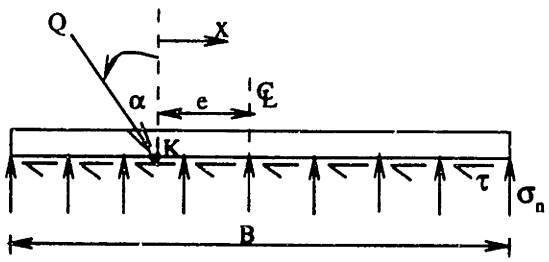

Fig. 5.2 Inclined and eccentric loaded footing

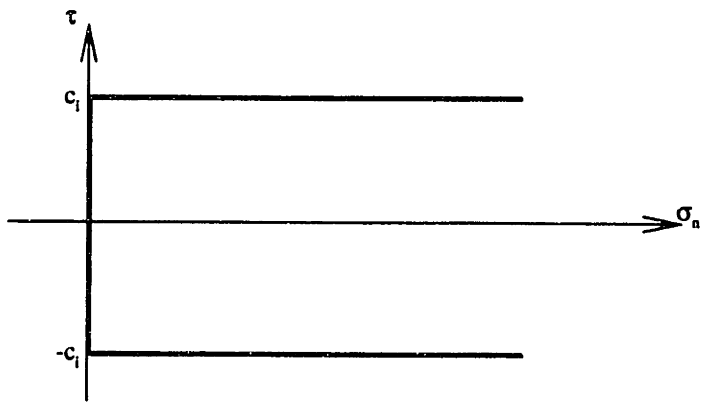

Fig. 5.3 Modified Tresca yield criterion with tension cutoff

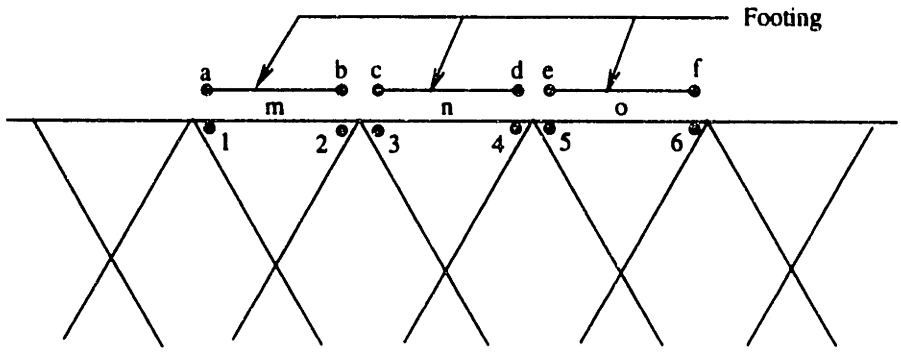

Fig. 5.4 Soil-footing interfaces for the upper bound method

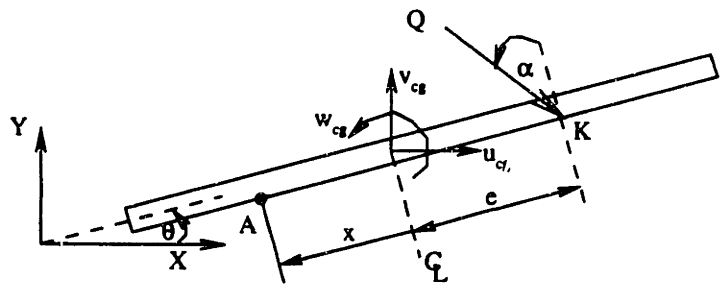

Fig. 5.5 Rigid body movement of a rigid footing

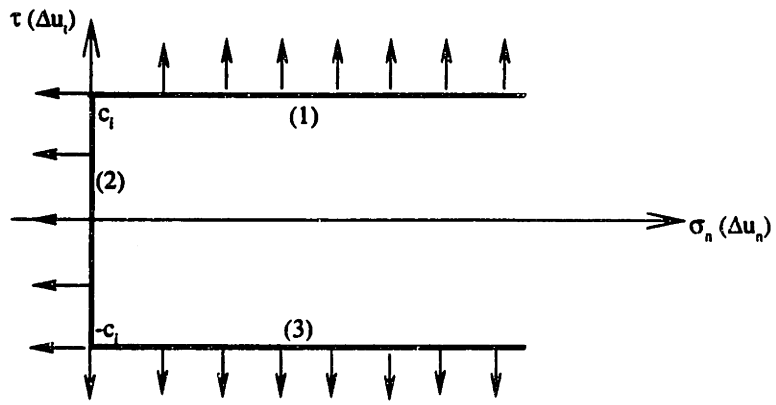

Fig. 5.6 Associated plastic flow direction of modified Tresca yield criterion with tension cutoff

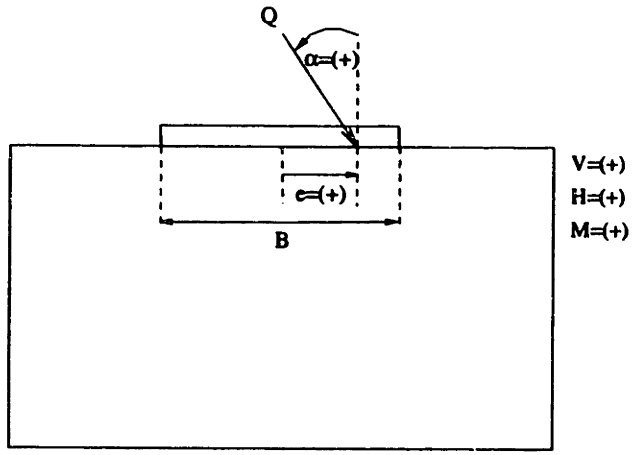

a) Loading type 1

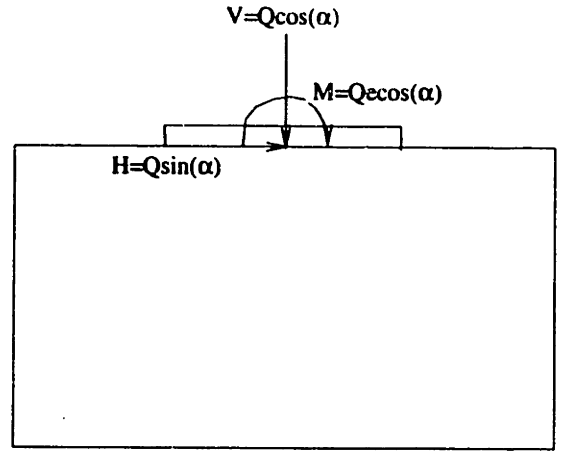

c) Positive sign convention for equivalent forces V,H and M

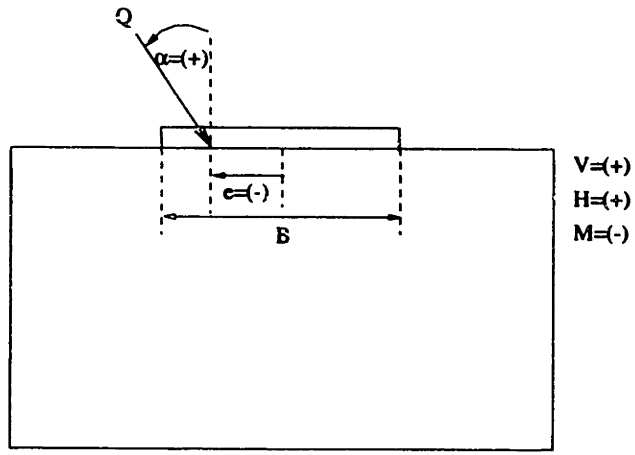

b) Loading type 2

Range of e and α

e/B = 0.00-0.35, increment of 0.05

α =0, 7.5, 15, 30, 45, 60, 75, 90 degree

Fig. 5.7 Load geometry of combined inclined and eccentric loaded footings

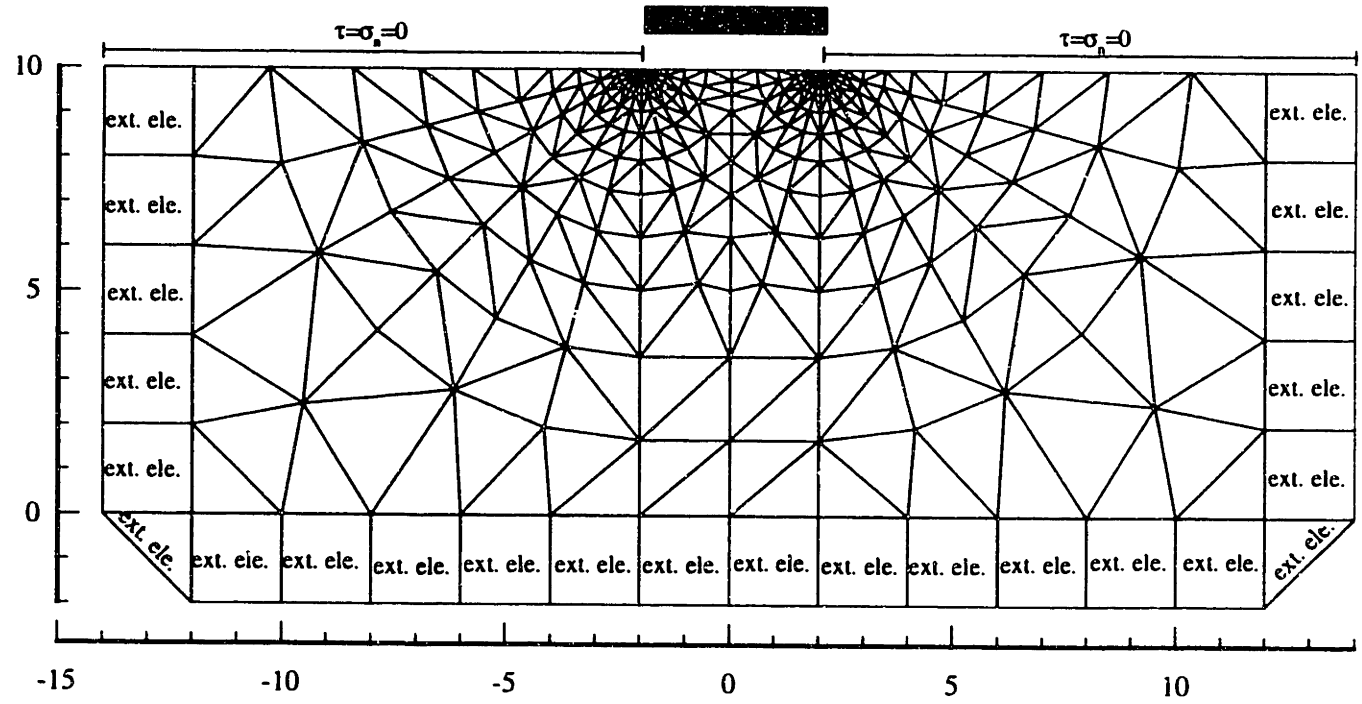

Fig. 5.8 Mesh for lower bound analysis of inclined, eccentric loading
(Note: for all inclination angles and eccentricity ratios)

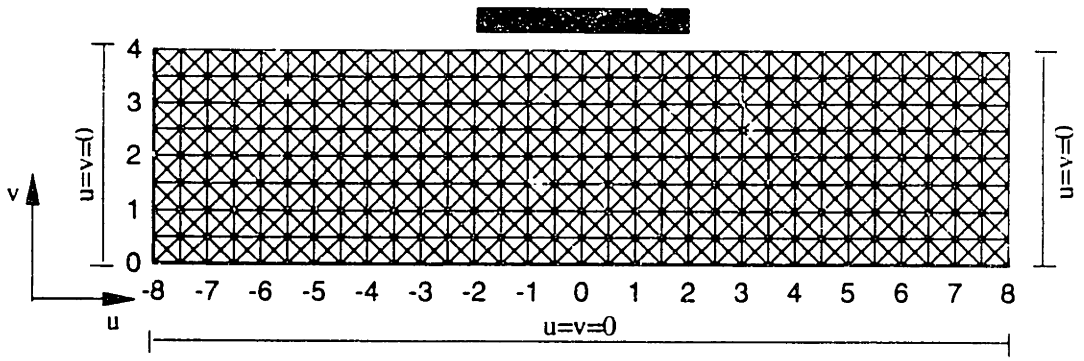

a) Mesh A1

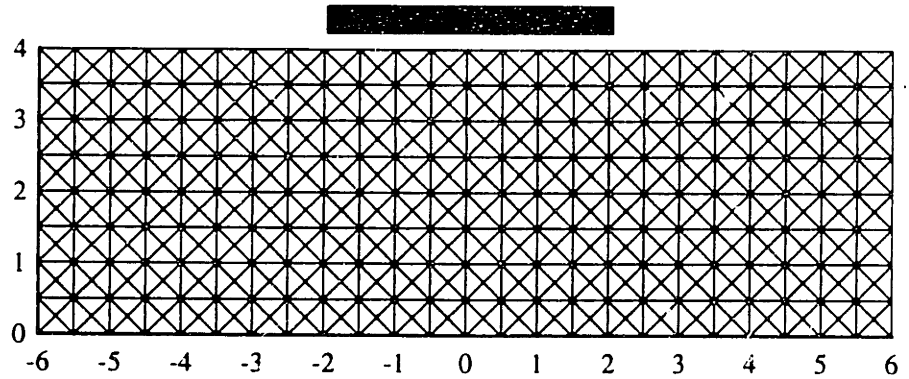

b) Mesh A2

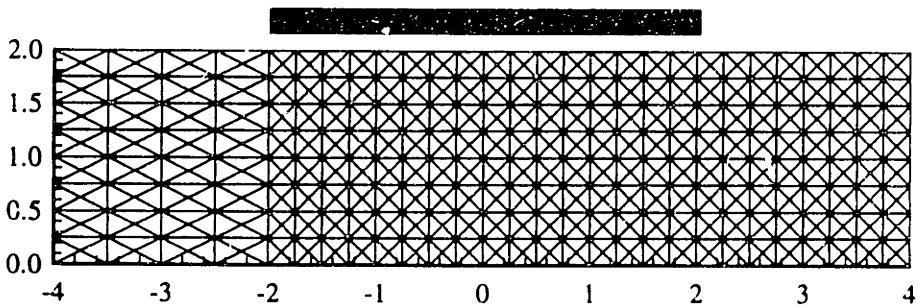

c) Mesh A3

Fig. 5.9 Meshes used for upper bound analyses of inclined eccentric loading (see Table 5.1)

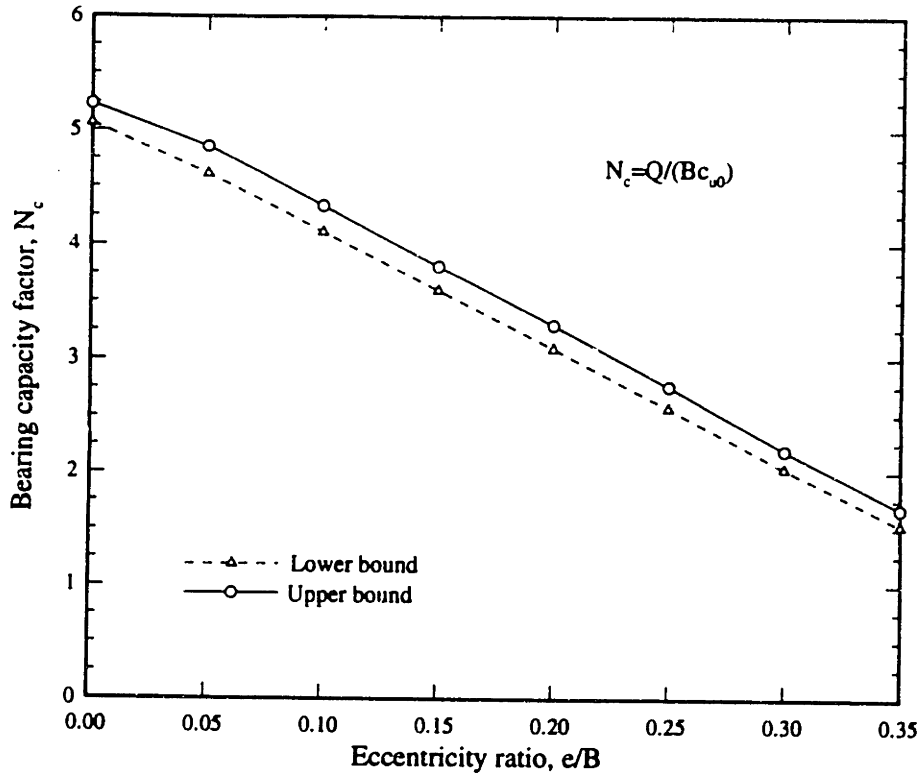

a) Bearing capacity factor versus eccentricity ratio

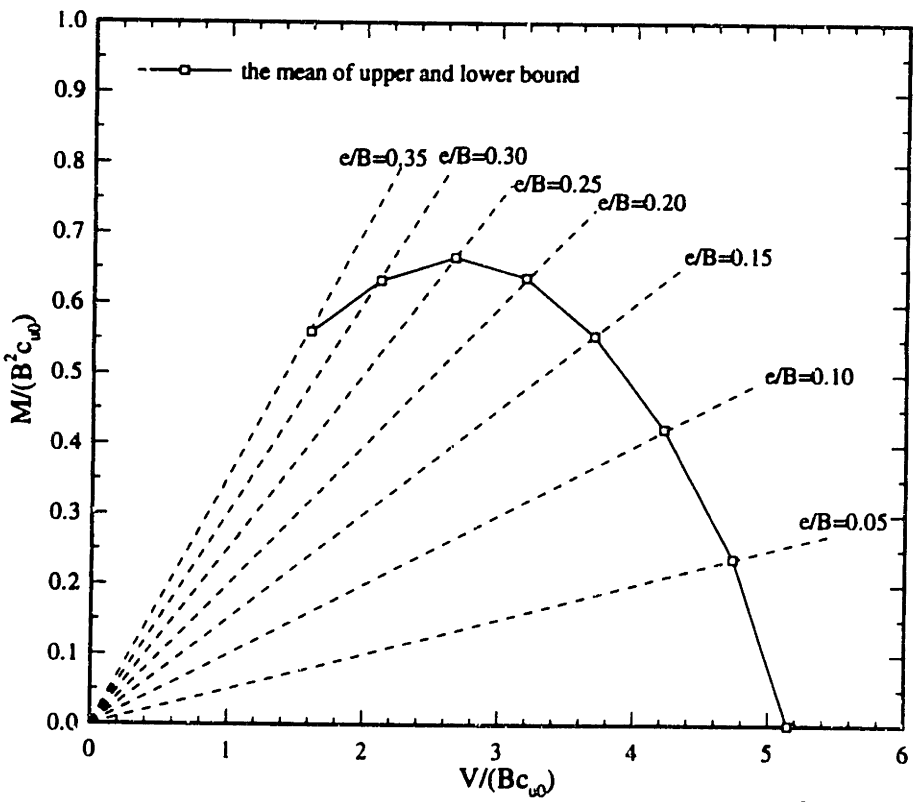

b) Failure envelope in the space $V/(Bc_{u0})$ vs. $M/(B^2c_{u0})$

Fig. 5.10 Predictions of collapse for vertical and eccentric loading

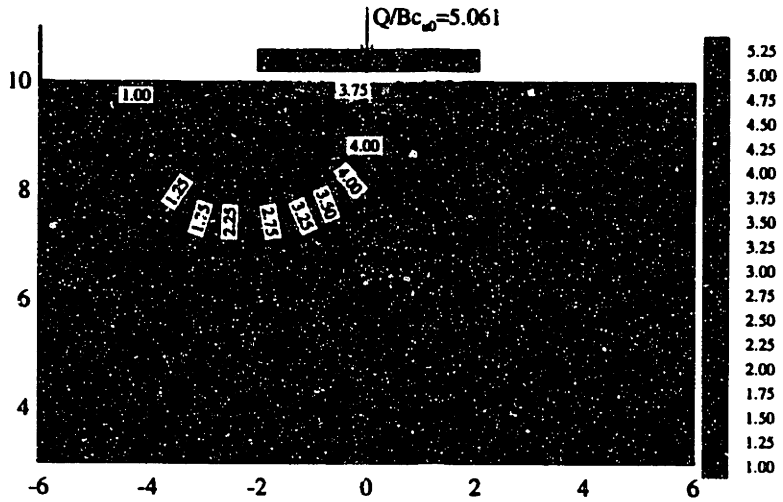

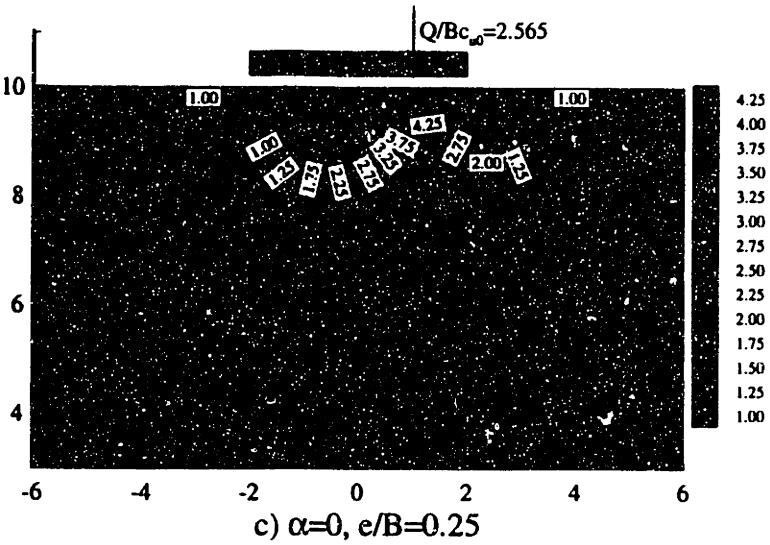

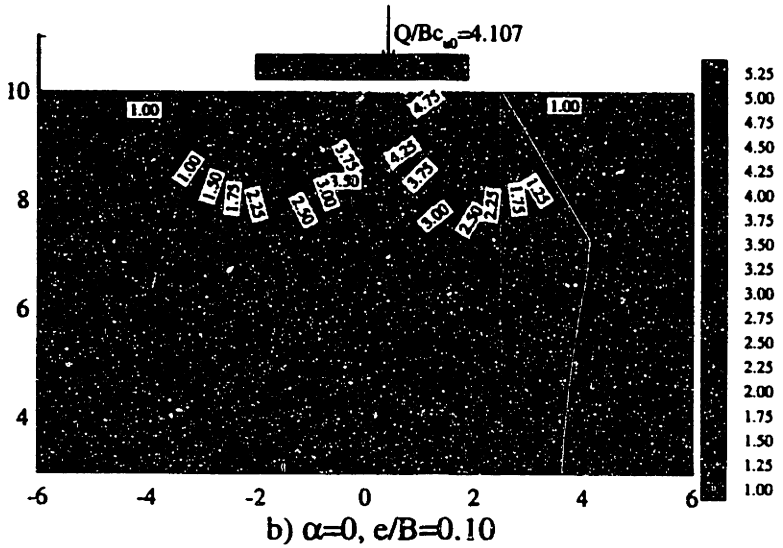

Fig. 5.11 Comparisons of mean stress contours from lower bound analyses of vertically loaded footings at three eccentricity ratios

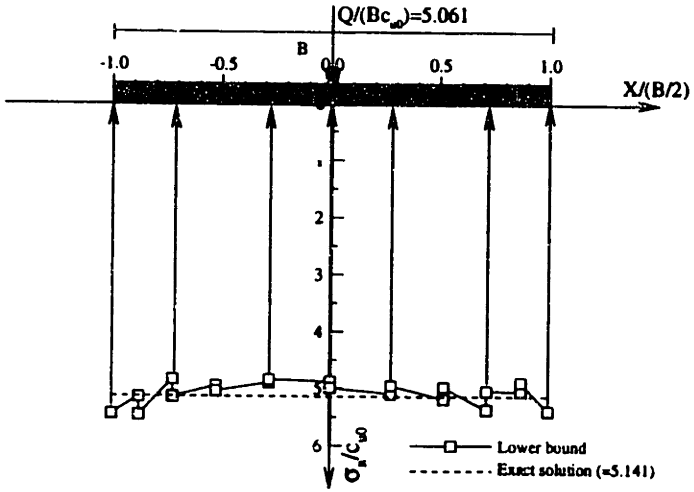

a) α=0, e/B=0.0

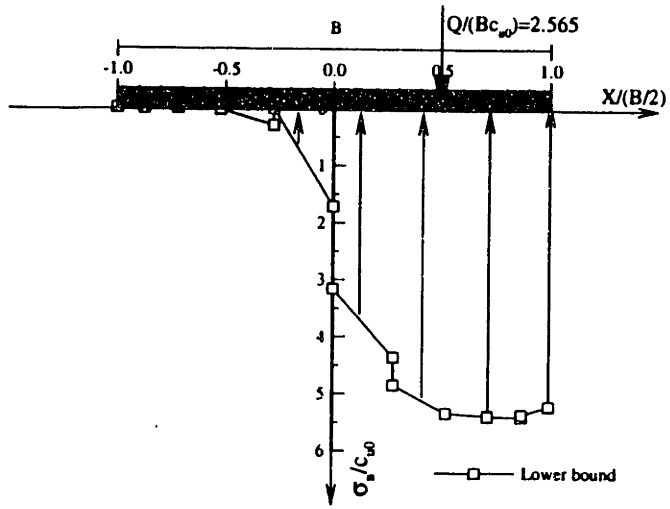

c) α=0, e/B=0.25

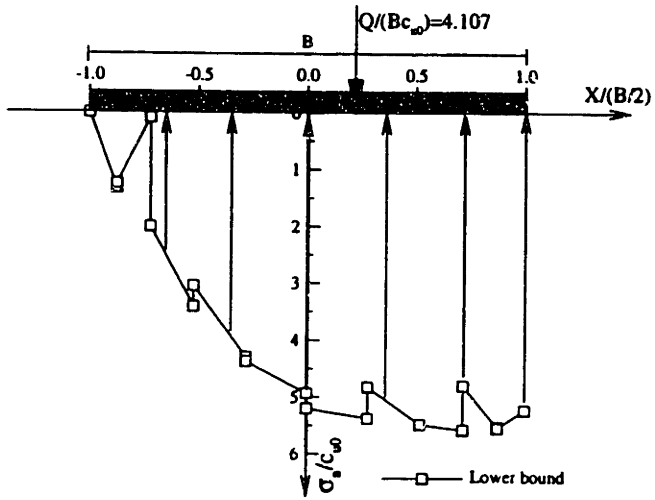

b) α=0, e/B= 0.10

Fig. 5.12 Comparisons of contact normal stress from lower bound analyses of vertically loaded footings at three eccentricity ratios

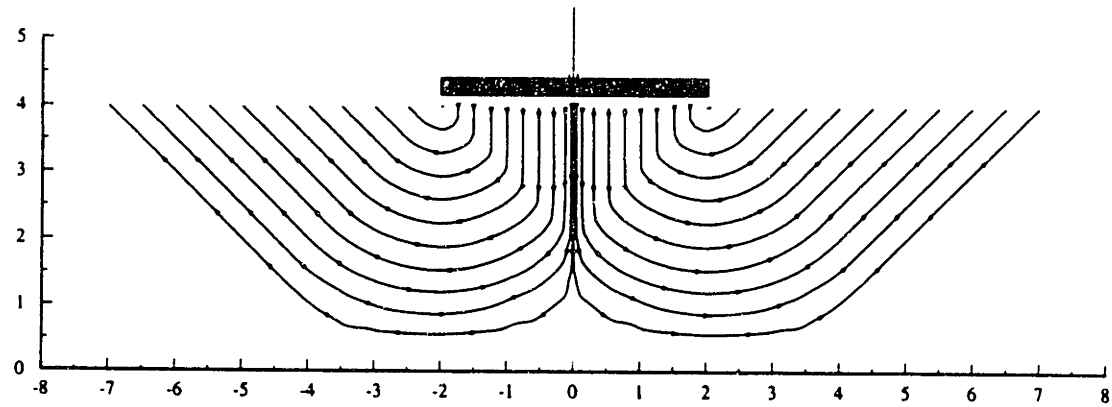

a) α=0, e/B=0.0

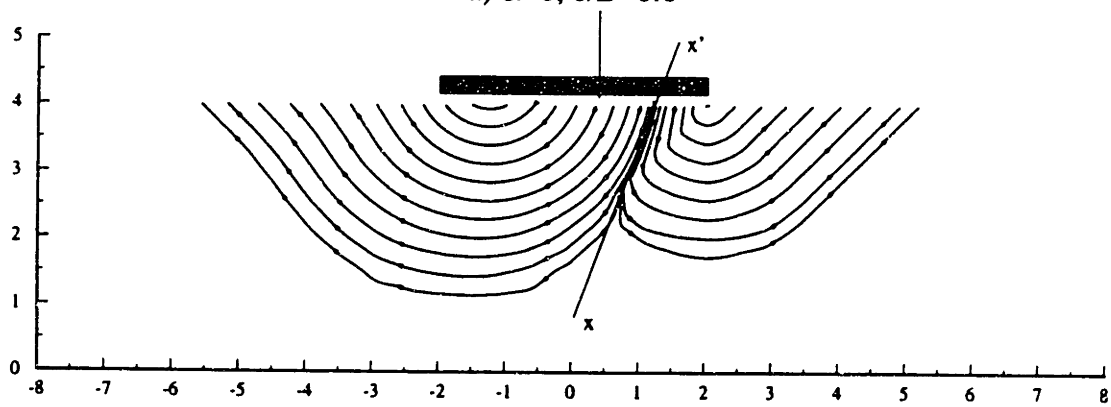

b) α=0, e/B=0.10

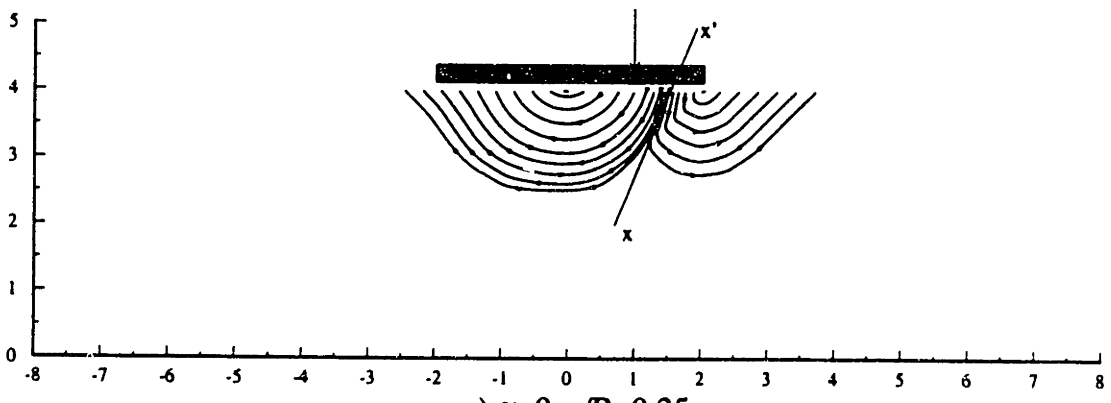

c) α=0, e/B=0.25

Fig. 5.13 Comparisons of velocity characteristics from upper bound analyses of vertically loaded footings at three eccentricity ratios

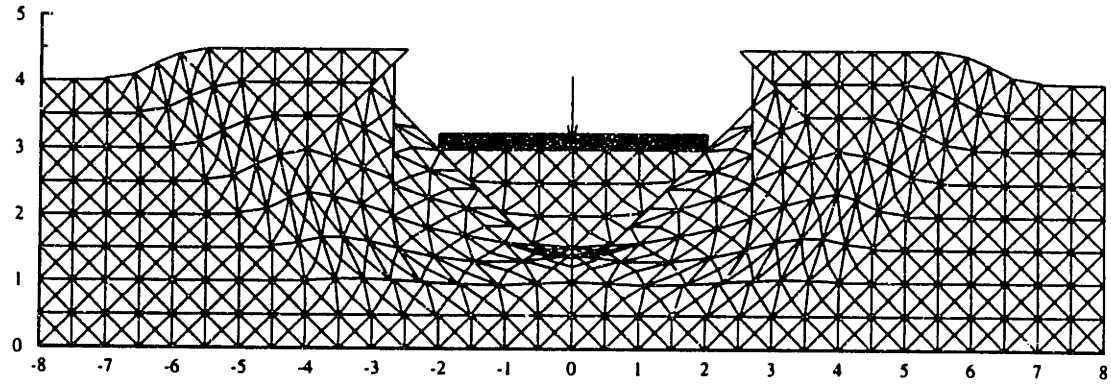

a) α=0, e/B=0.0

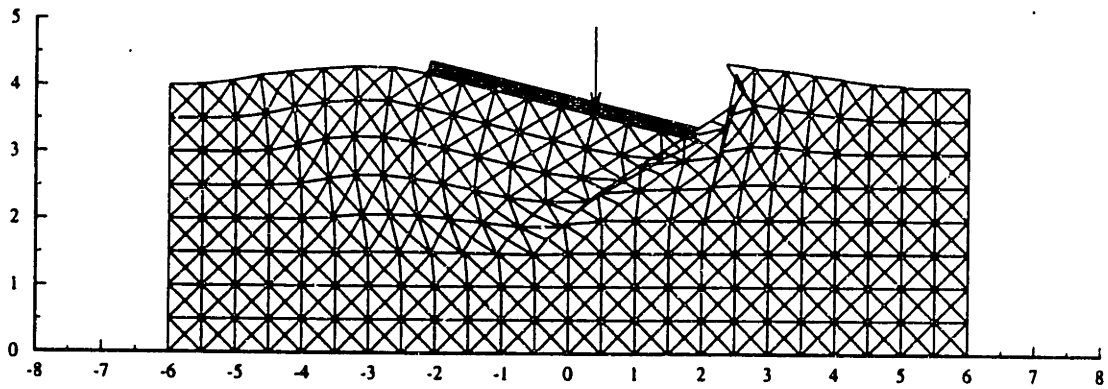

b) α=0, e/B=0.10

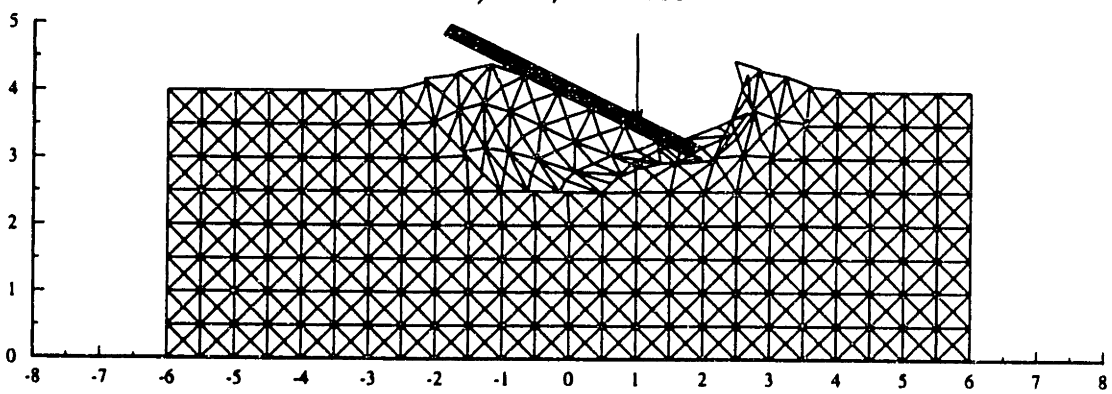

c) α=0, e/B=0.25

Fig. 5.14 Comparisons of deformed mesh from upper bound analyses of vertically loaded footings at three eccentricity ratios

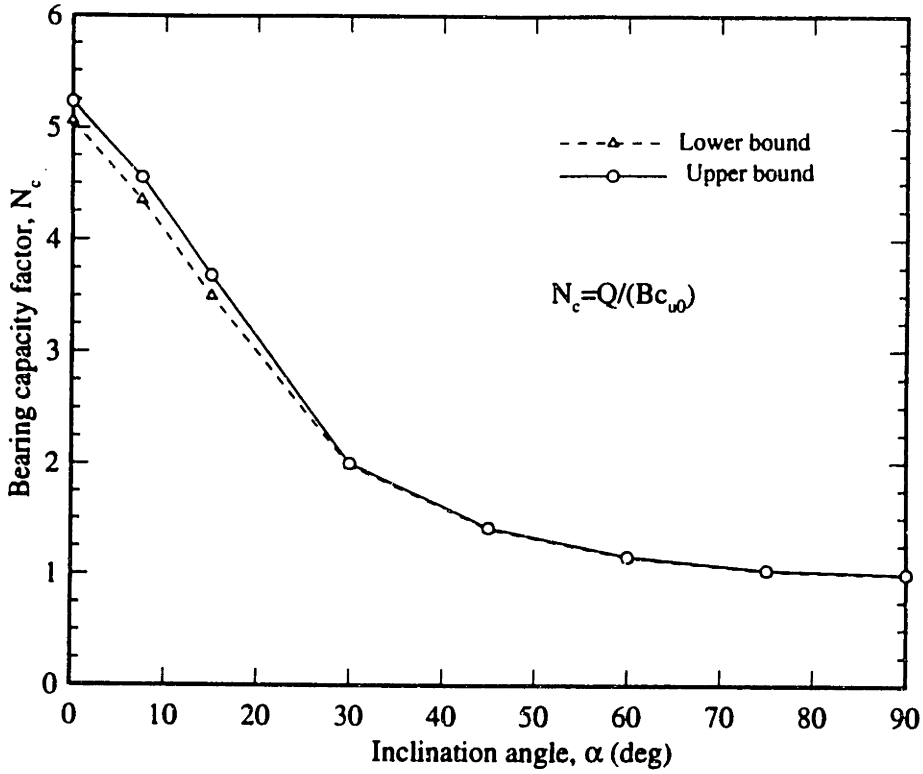

a) Bearing capacity factor versus inclination angle

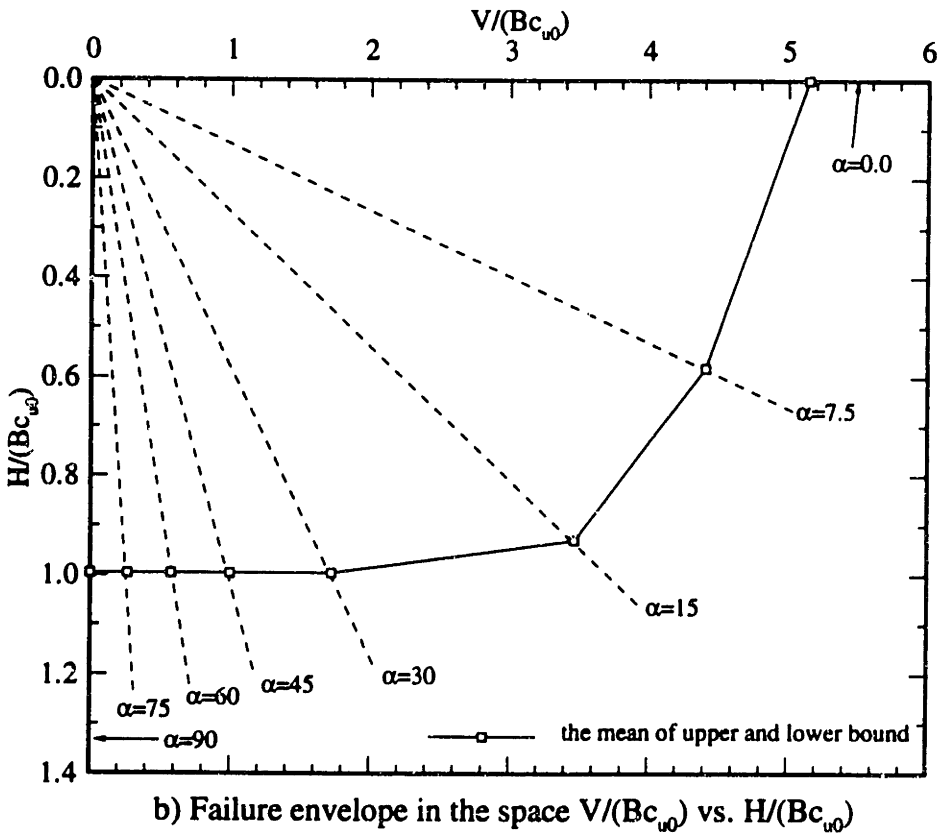

b) Failure envelope in the space $V/(Bc_{u0})$ vs. $H/(Bc_{u0})$

Fig. 5.15 Predictions of collapse for inclined, concentrically loaded footings on homogeneous clay

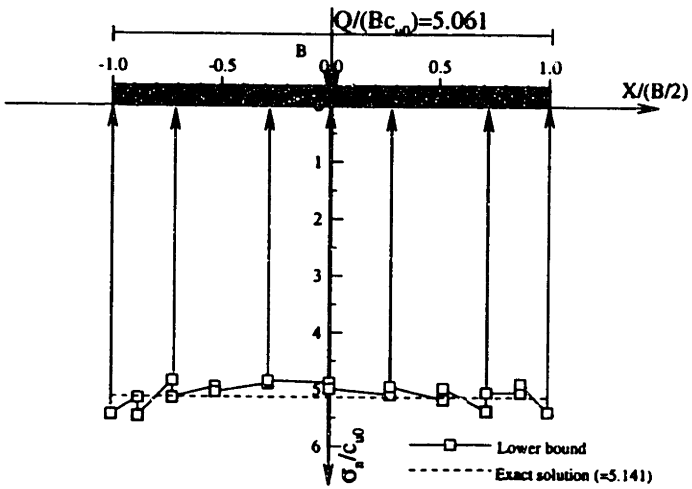

a) α=0, e/B=0.0

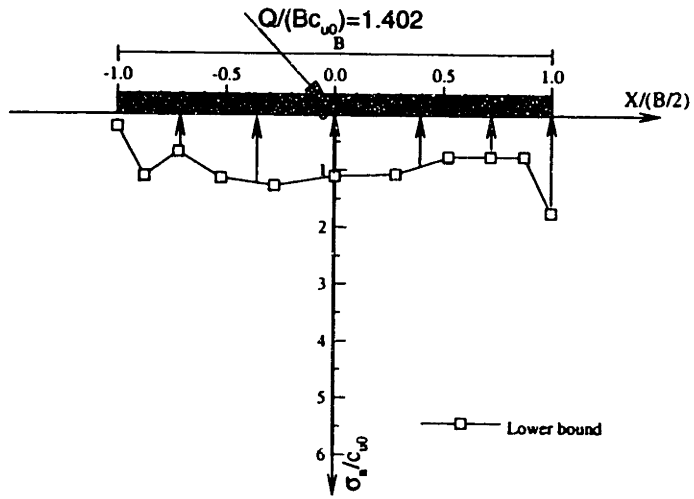

c) α=45 deg., e/B=0.0

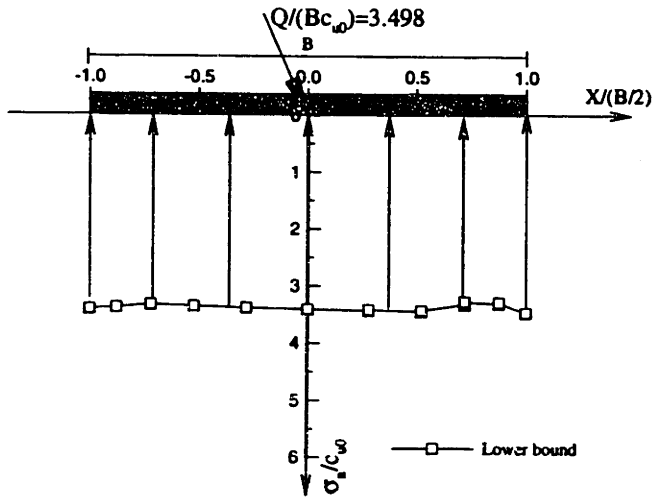

b) α=15 deg., e/B= 0.0

Fig. 5.16 Comparisons of contact normal stress from lower bound analyses of concentrically loaded footings at three inclination angles

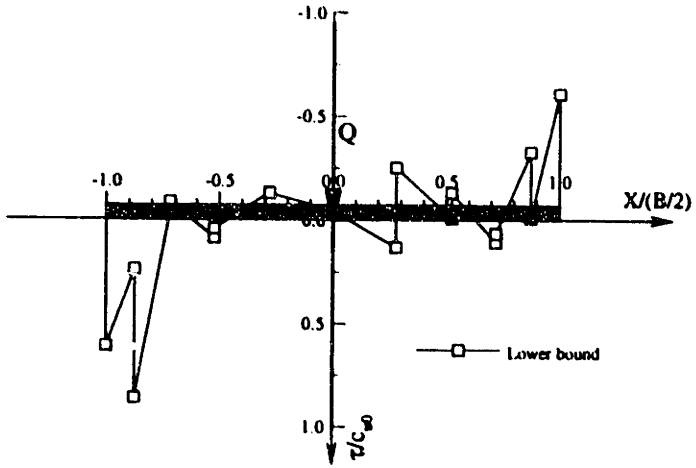

a) α=0, e/B=0.0

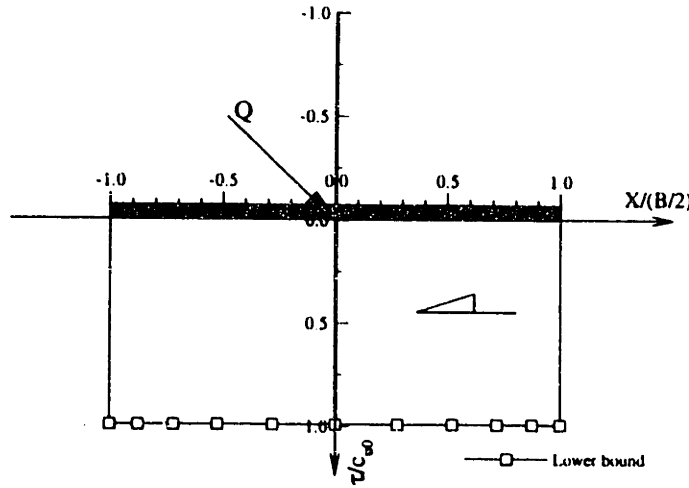

c) α=45 deg., e/B=0.0

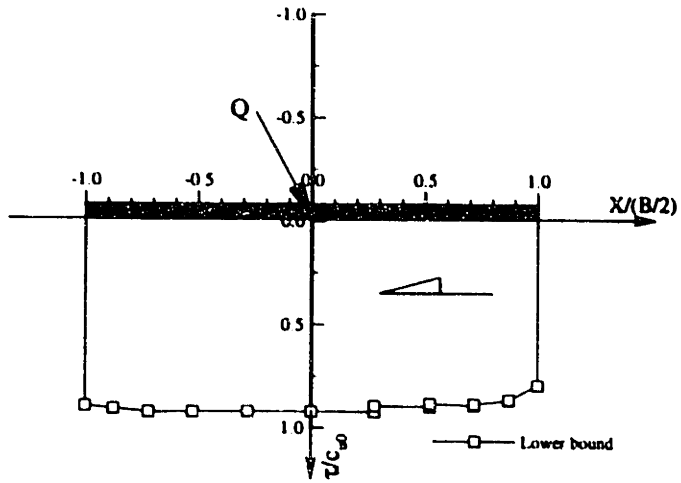

b) α=15 deg., e/B=0.0

Fig. 5.17 Comparisons of contact shear stress from lower bound analyses of concentrically loaded footings at three inclination angles

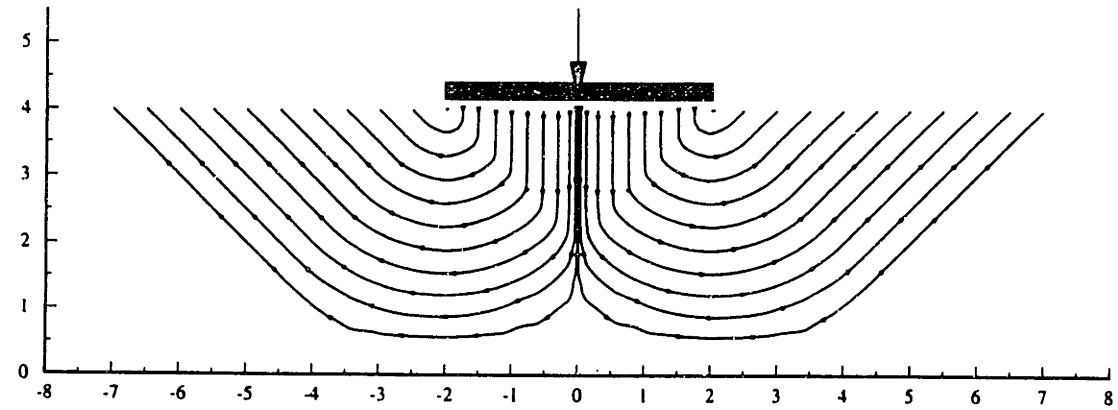

a) α=0, e/B=0.0

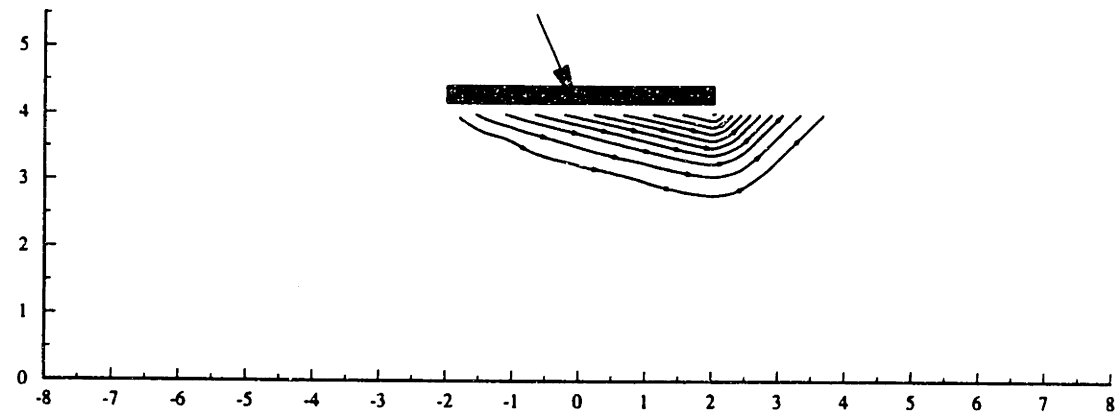

b) α=15 deg., e/B=0.0

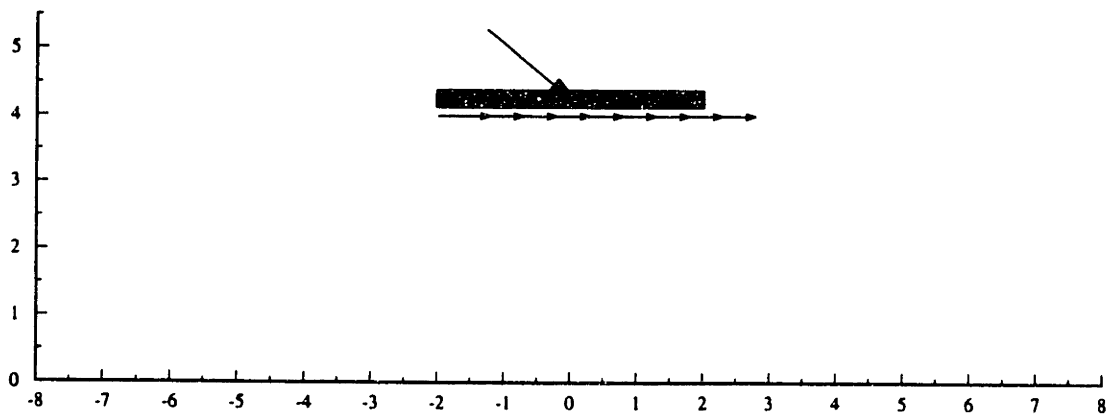

c) α=45 deg., e/B=0.0

Fig. 5.18 Comparisons of velocity characteristics from upper bound analyses of concentrically loaded footings at three different inclination angles

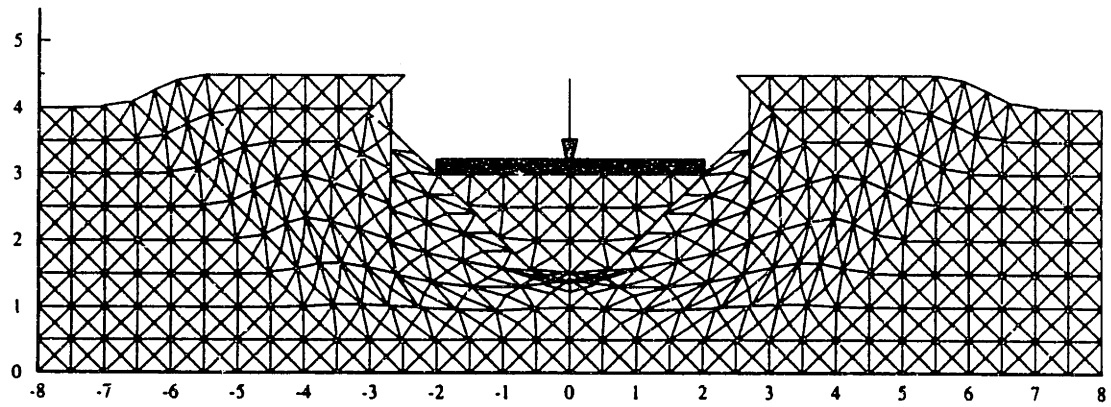

a) α=0, e/B=0.0

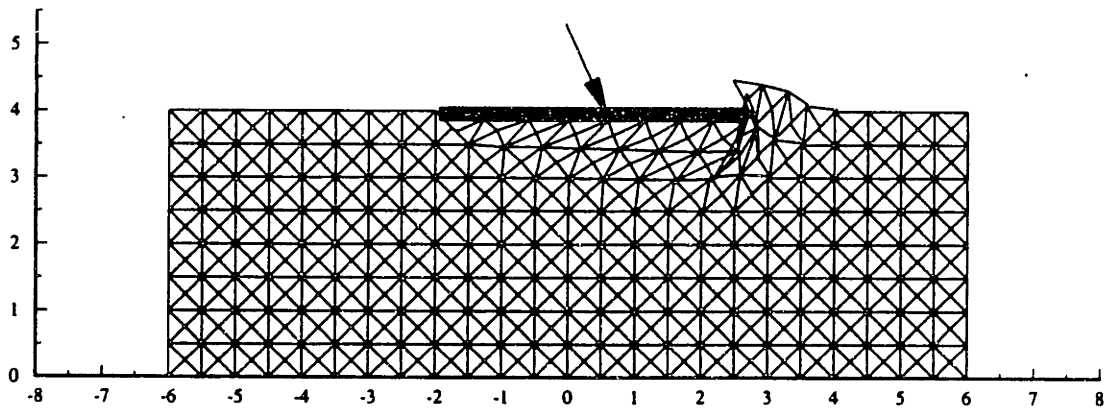

b) α=15 deg., e/B=0.0

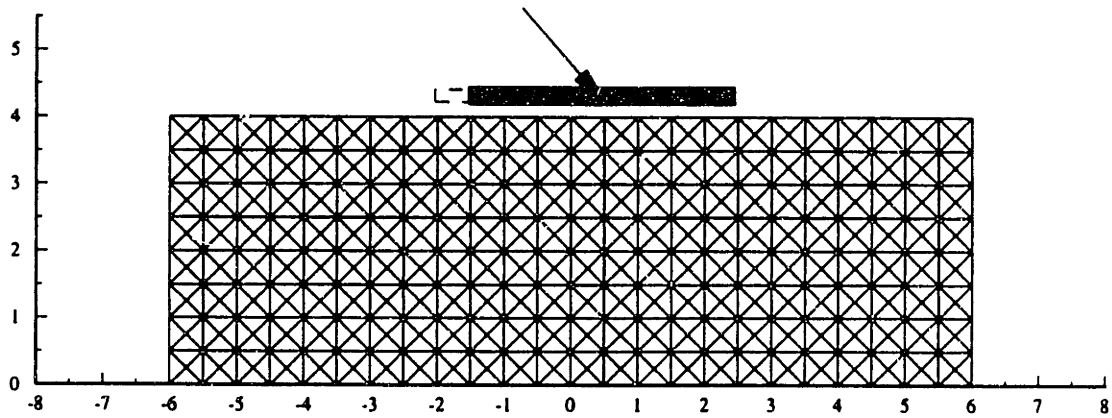

c) α=45 deg., e/B=0.0

Fig. 5.19 Comparisons of deformed mesh from upper bound analyses of concentrically loaded footing at three inclination angles

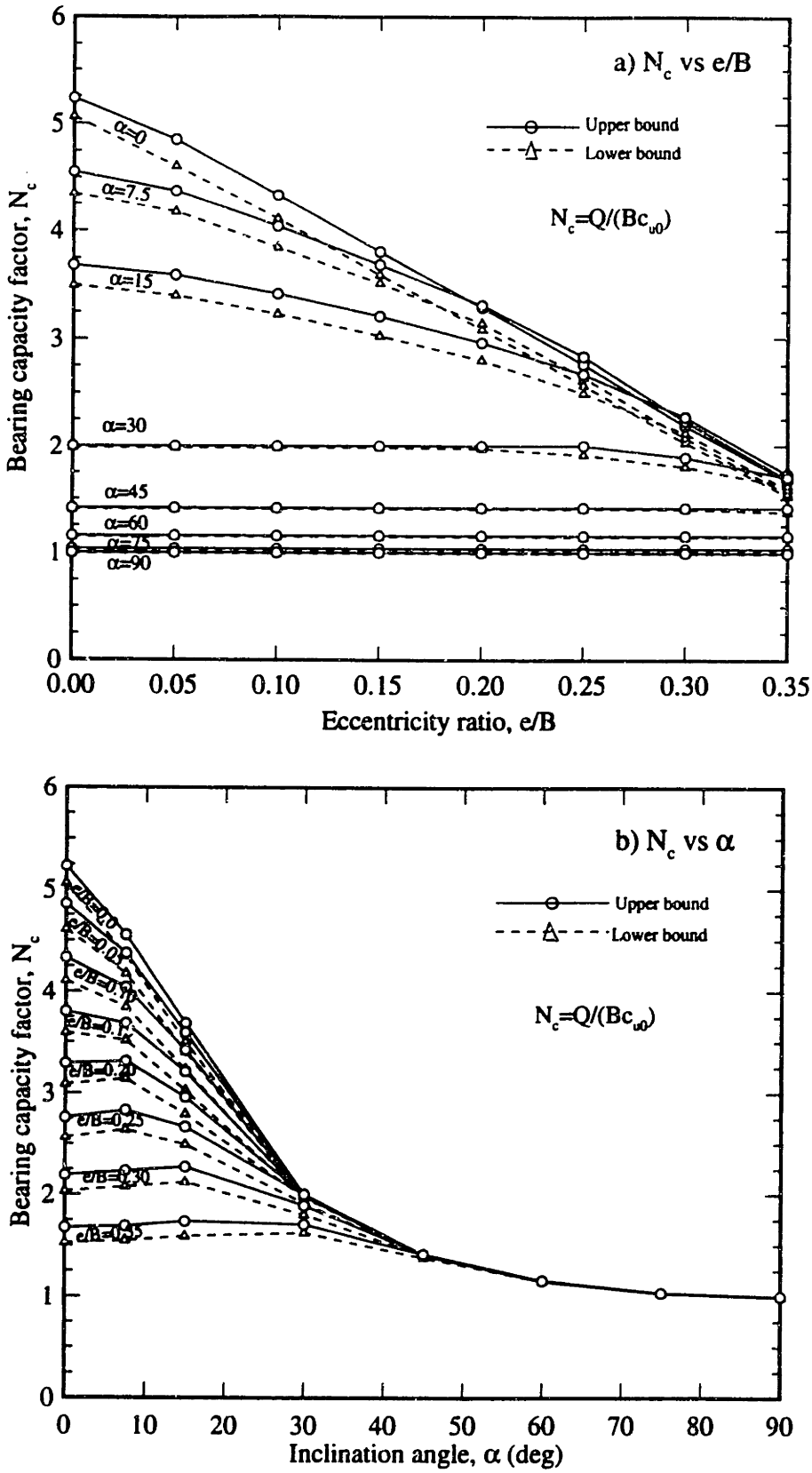

Fig. 5.20 Predictions of bearing capacity factors for Type 1 combined loading of footings on homogenous clay

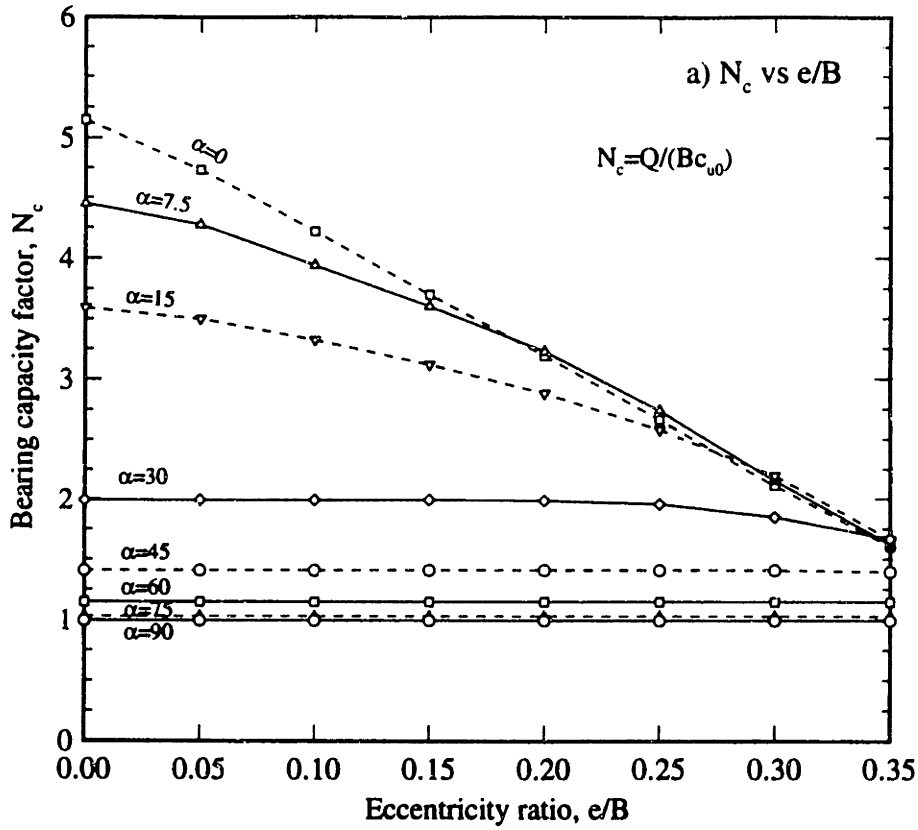

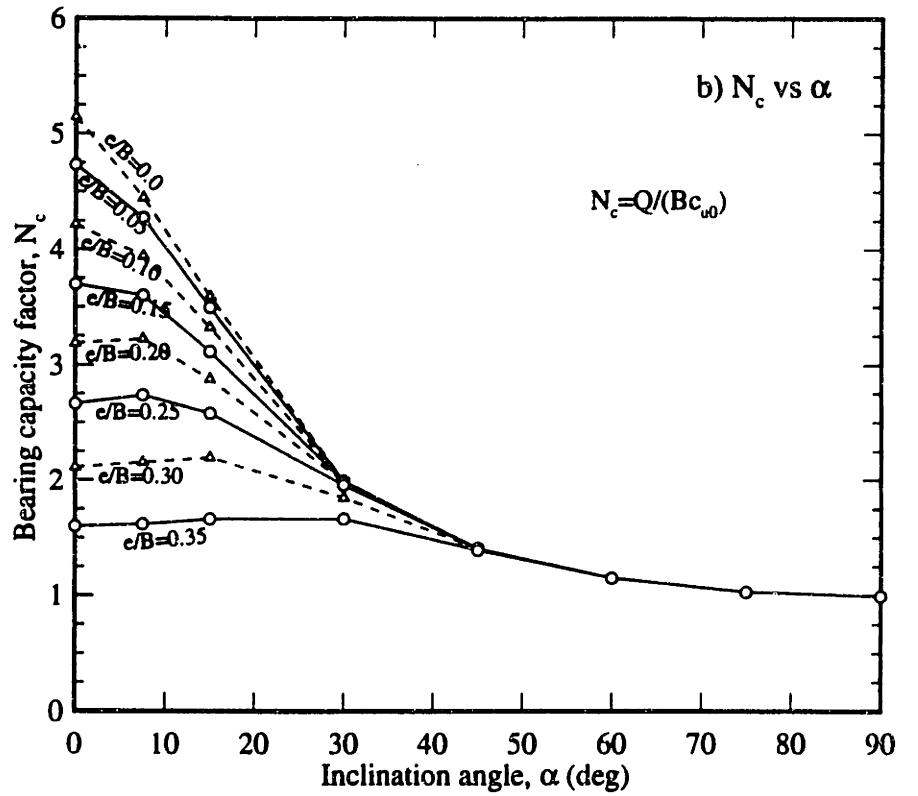

Fig. 5.21 Average bearing capacity factors for Type 1 combined loading of footings on homogeneous clay

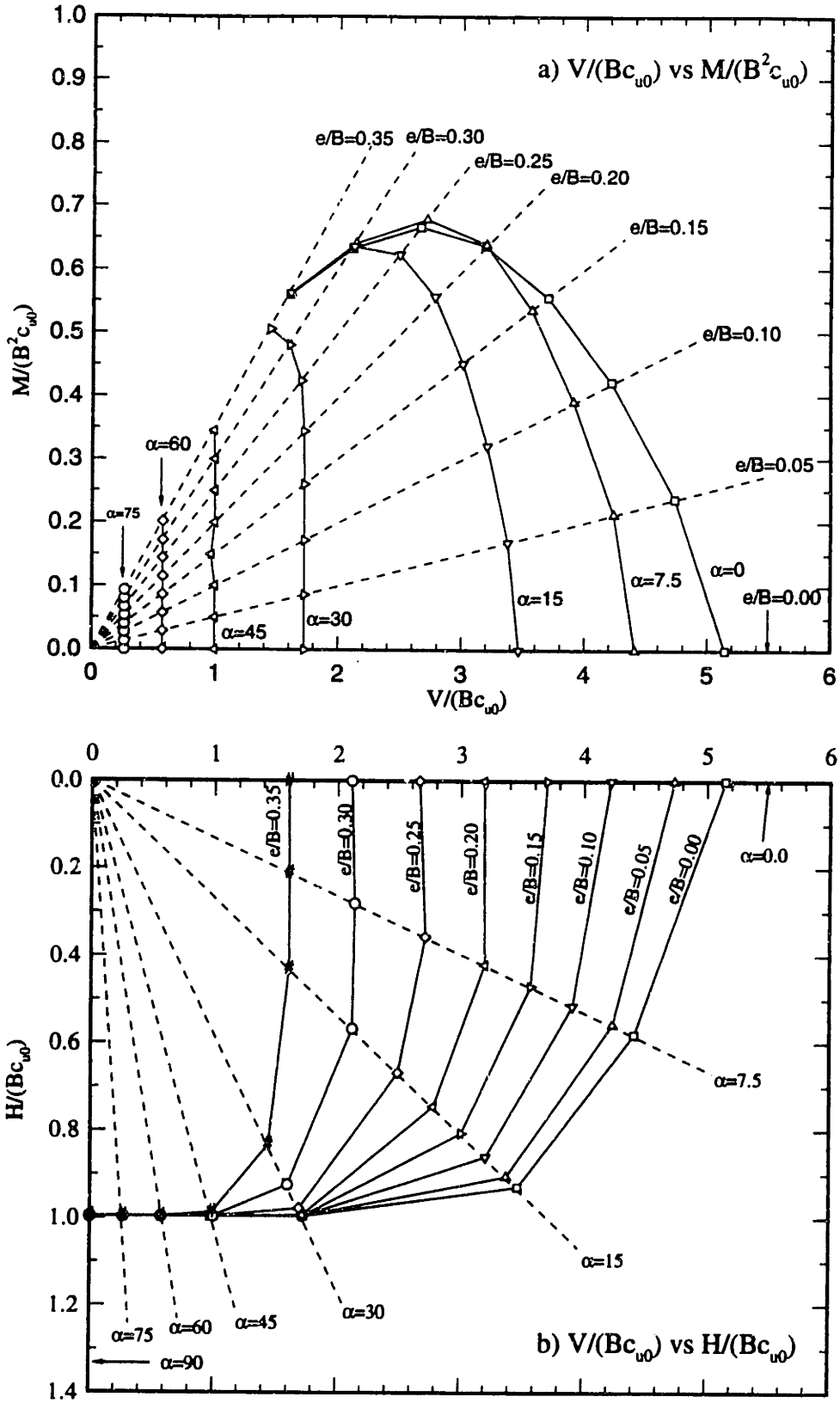

Fig. 5.22 Failure envelope for Type 1 combined loading of footings on homogeneous clay

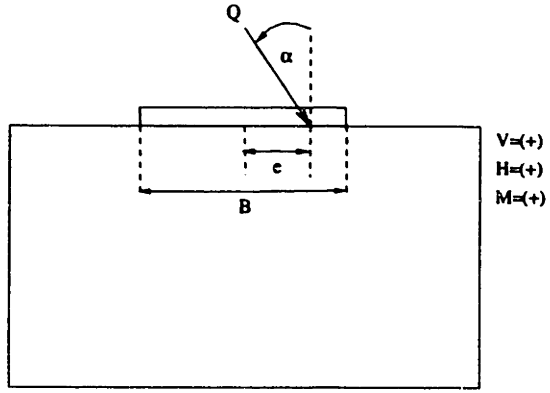

a) Loading Type 1

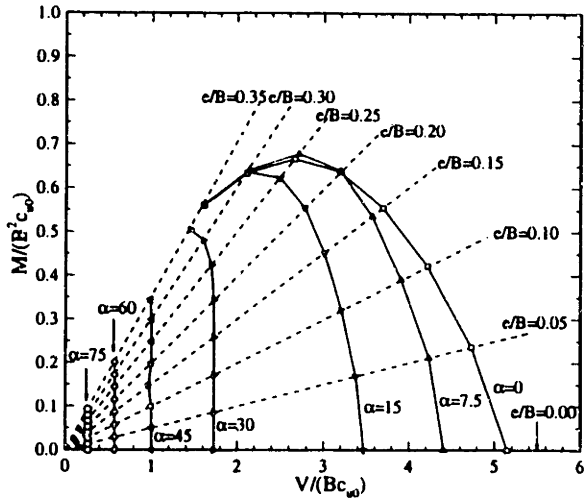

c) Projection in plane $H/(Bc_{u0})=0$

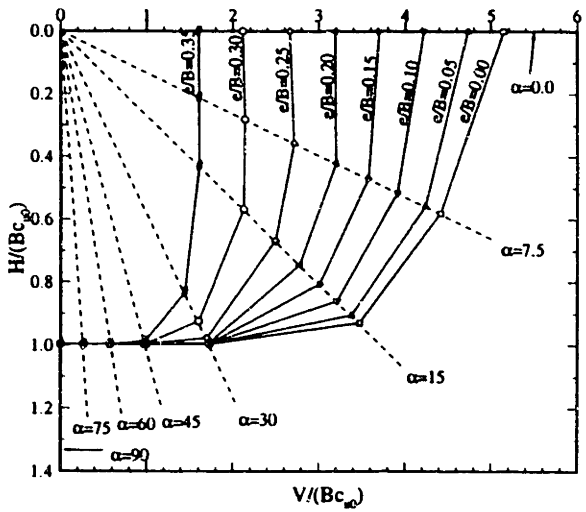

b) Projection in plane $M/(B^2c_{u0})=0$

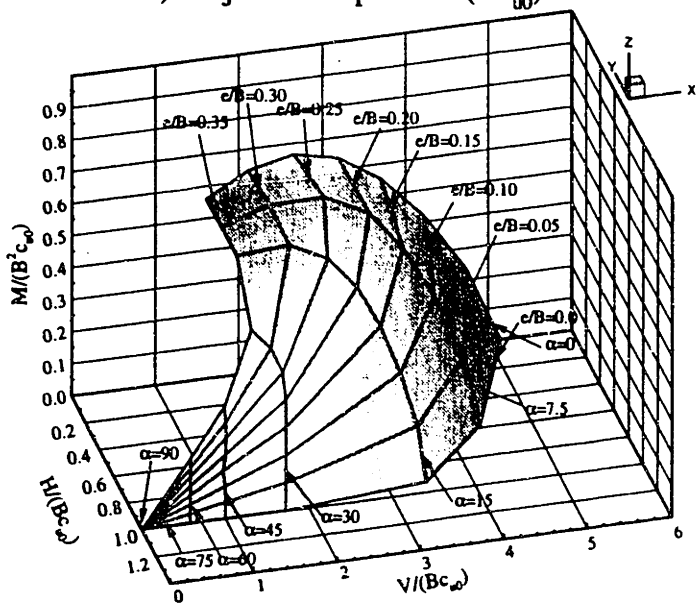

d) Three dimensional perspective view

Fig. 5.23 Three dimensional failure surface for Type 1 combined loading of footings on homogeneous clay

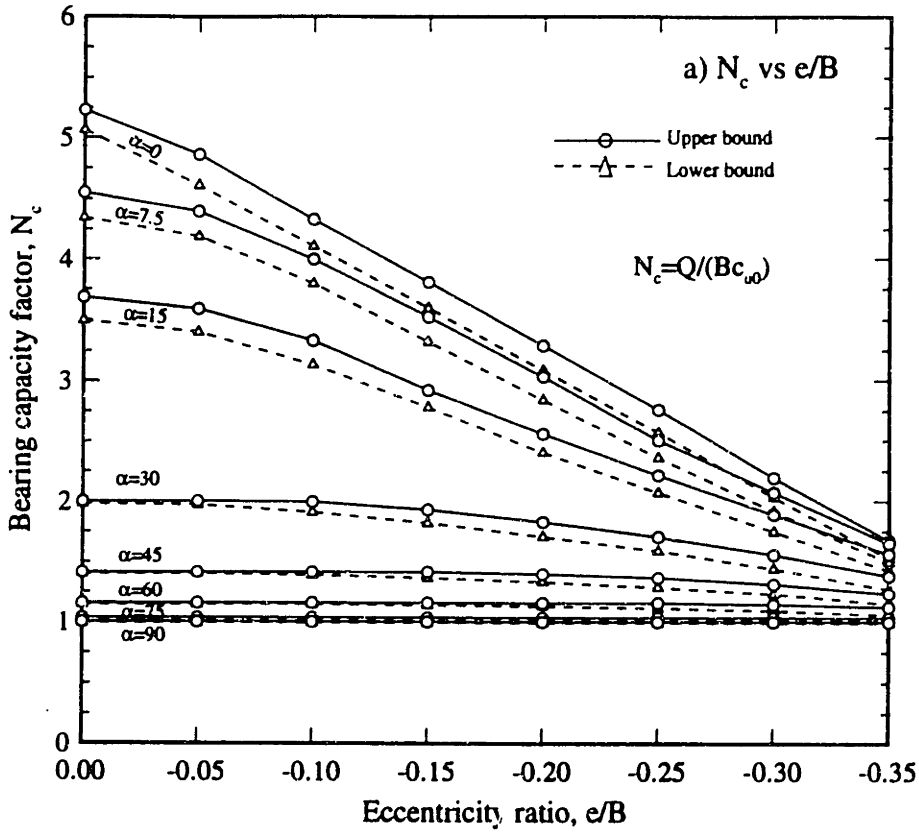

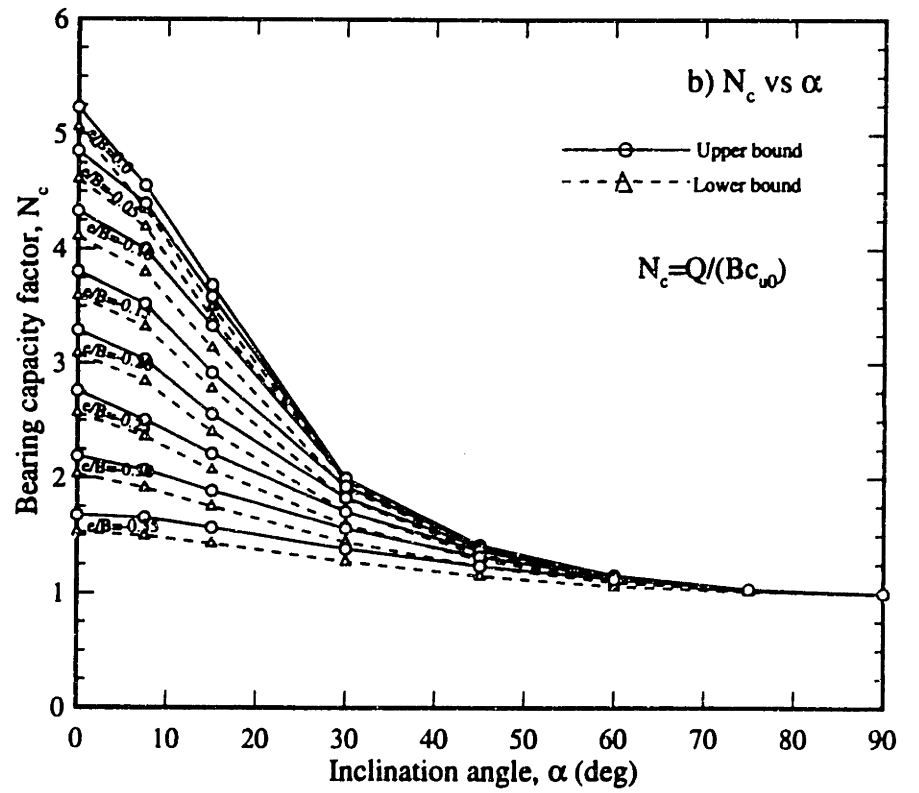

Fig. 5.24 Predictions of bearing capacity factors for Type 2 combined loading of footings on homogeneous clay

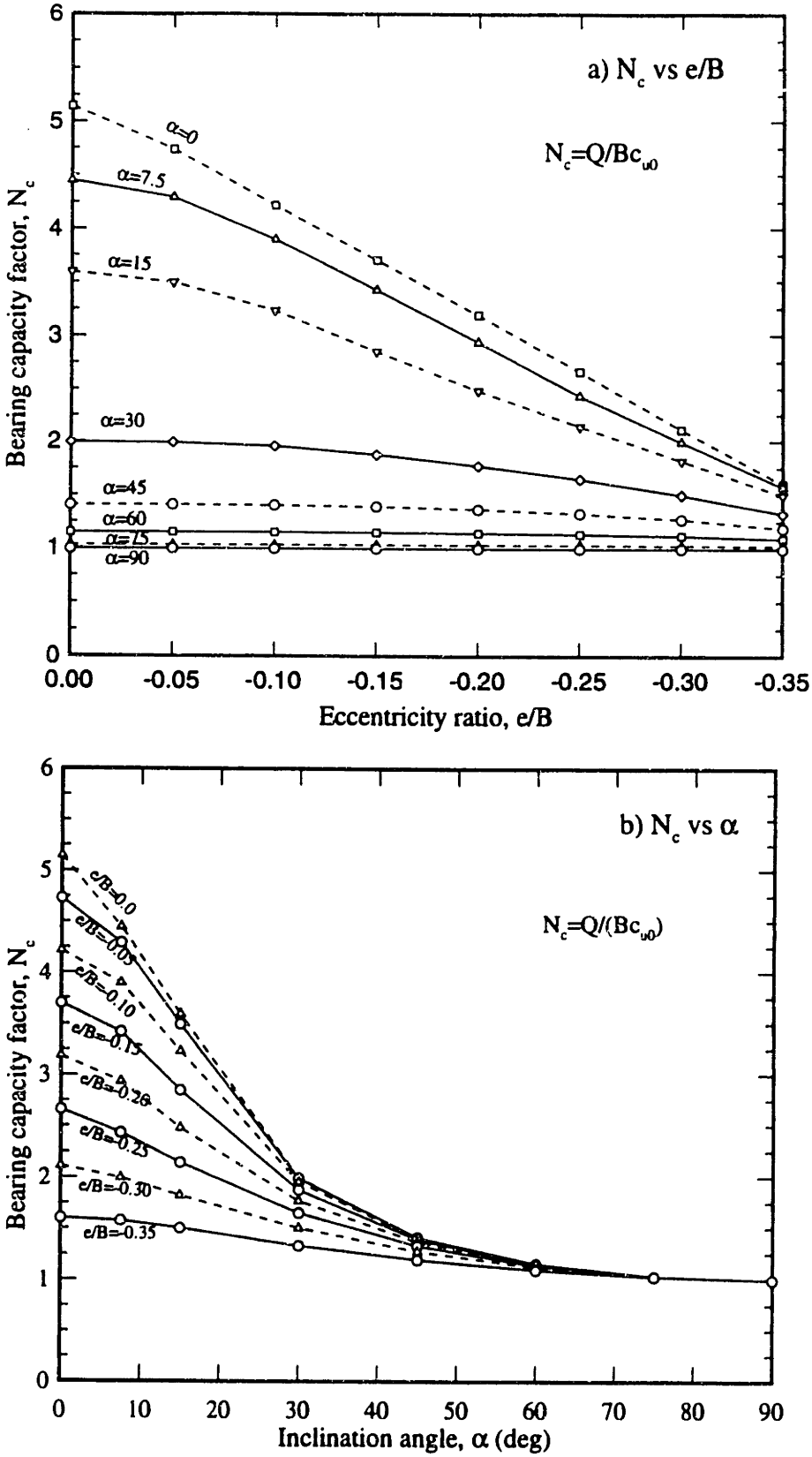

Fig. 5.25 Average bearing capacity factors for Type 2 combined loading of footings on homogeneous clay

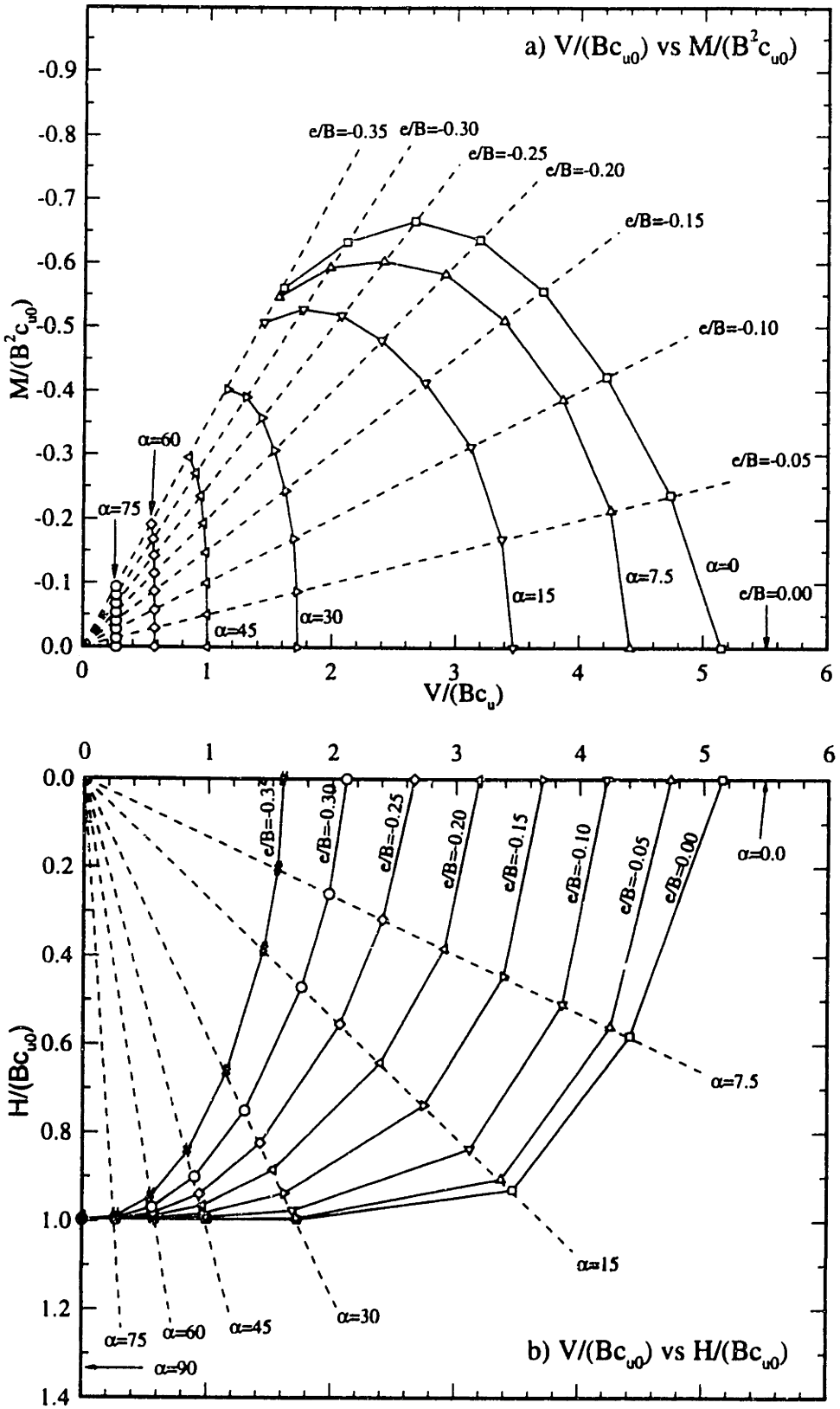

Fig. 5.26 Failure envelope for Type 2 combined loading of footings on homogeneous clay

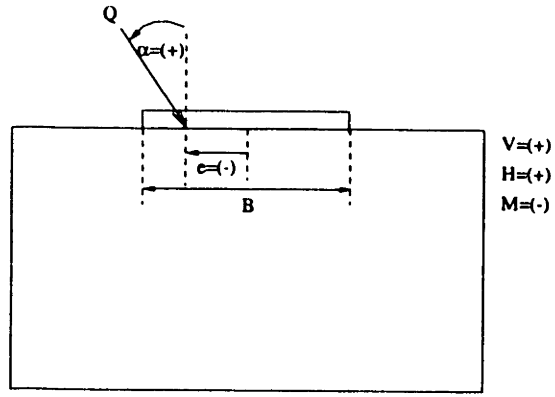

a) Loading Type 2

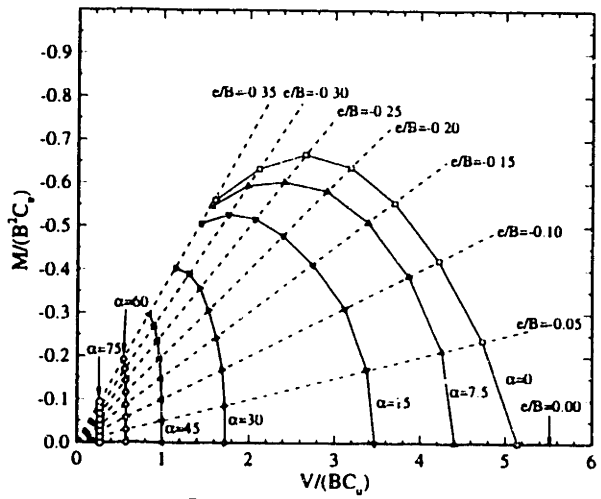

c) Projection in plane $H/(Bc_{u0})=0$

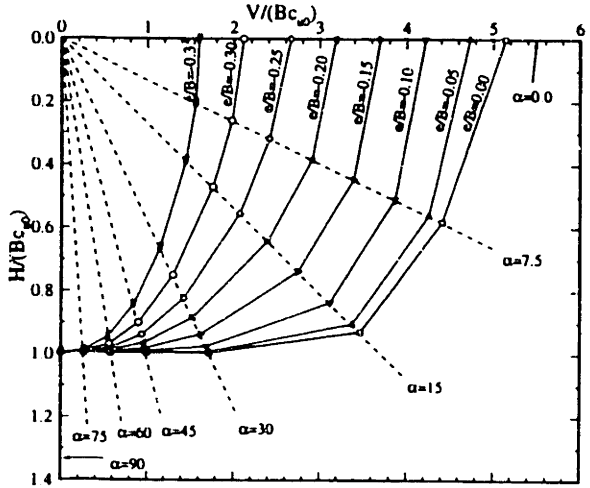

b) Projection in plane $M/(B^2c_{u0})=0$

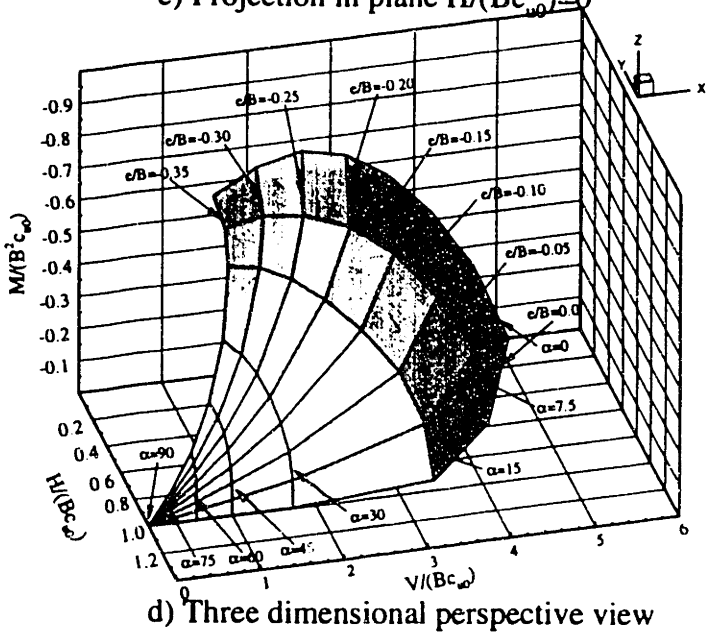

d) Three dimensional perspective view

Fig. 5.27 Three dimensional plot of failure surface for Type 2 combined loading of footings on homogeneous clay

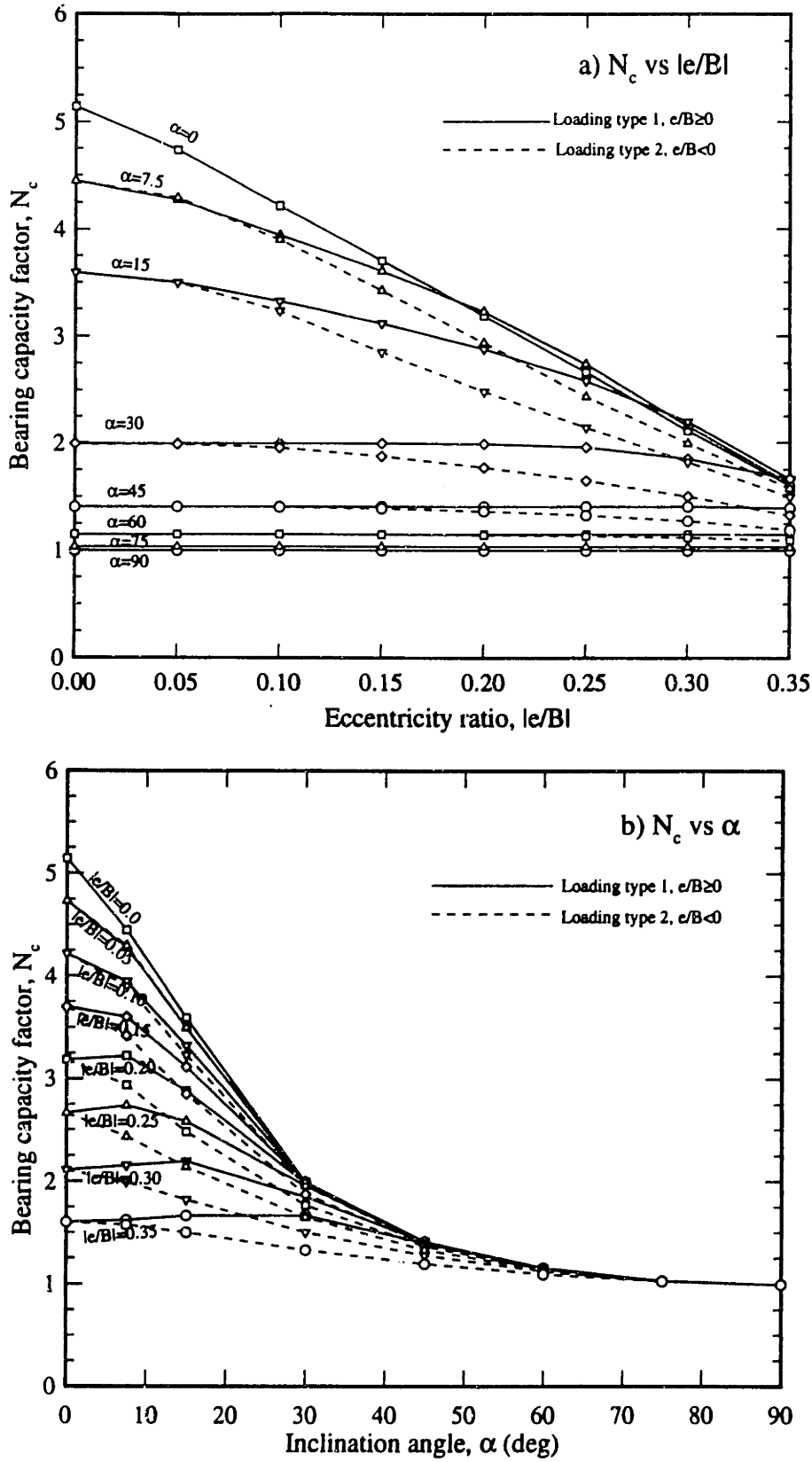

Fig. 5.28 Comparisons of bearing capacity factors for Type 1 and Type 2 combined loading of footings on homogeneous clay

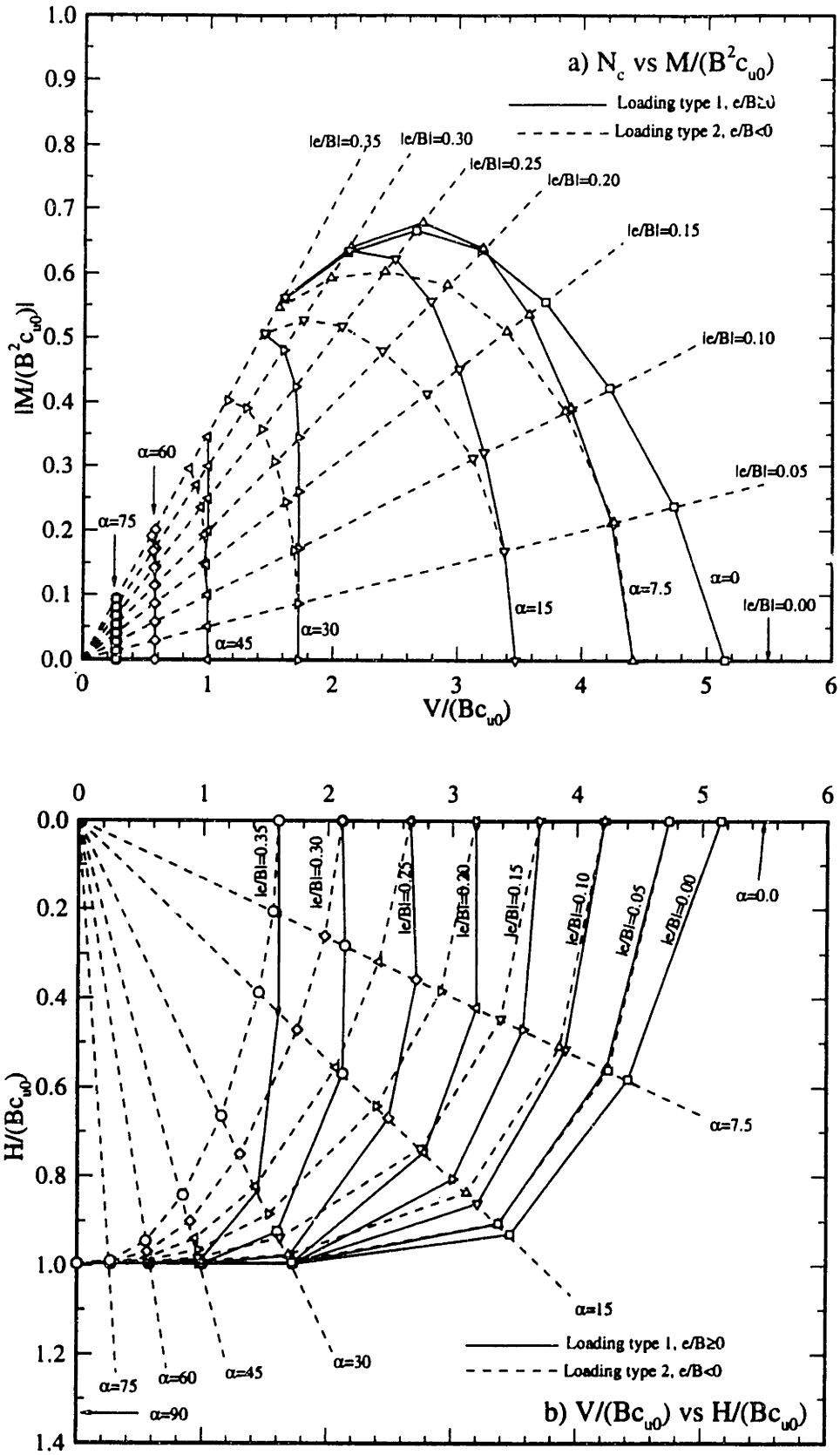

Fig. 5.29 Comparisons of failure envelope for Type 1 and Type 2 combined loading of footings on homogeneous clay

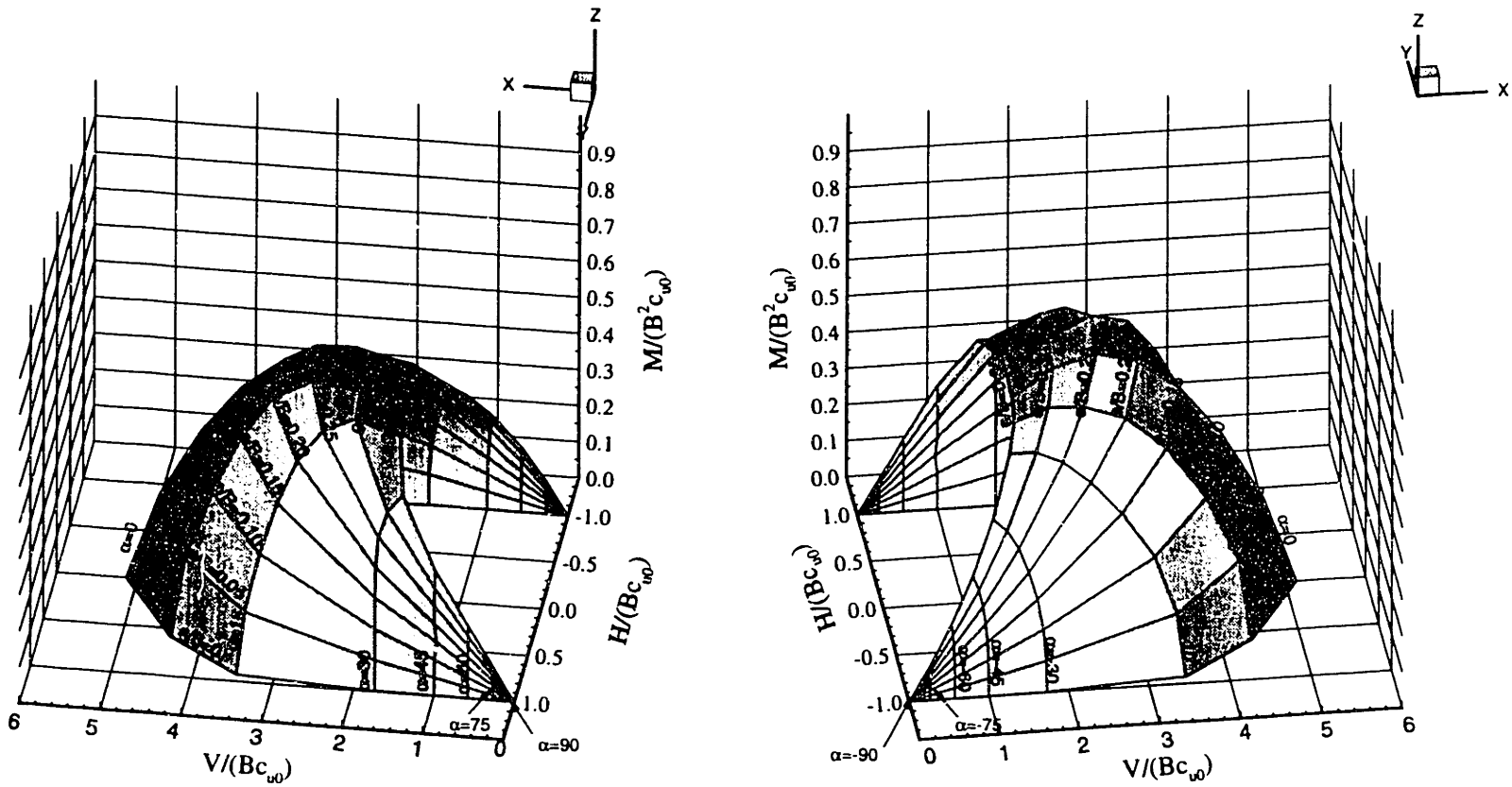

Fig. 5.30 Failure surface for combined loading of footings on homogeneous clay

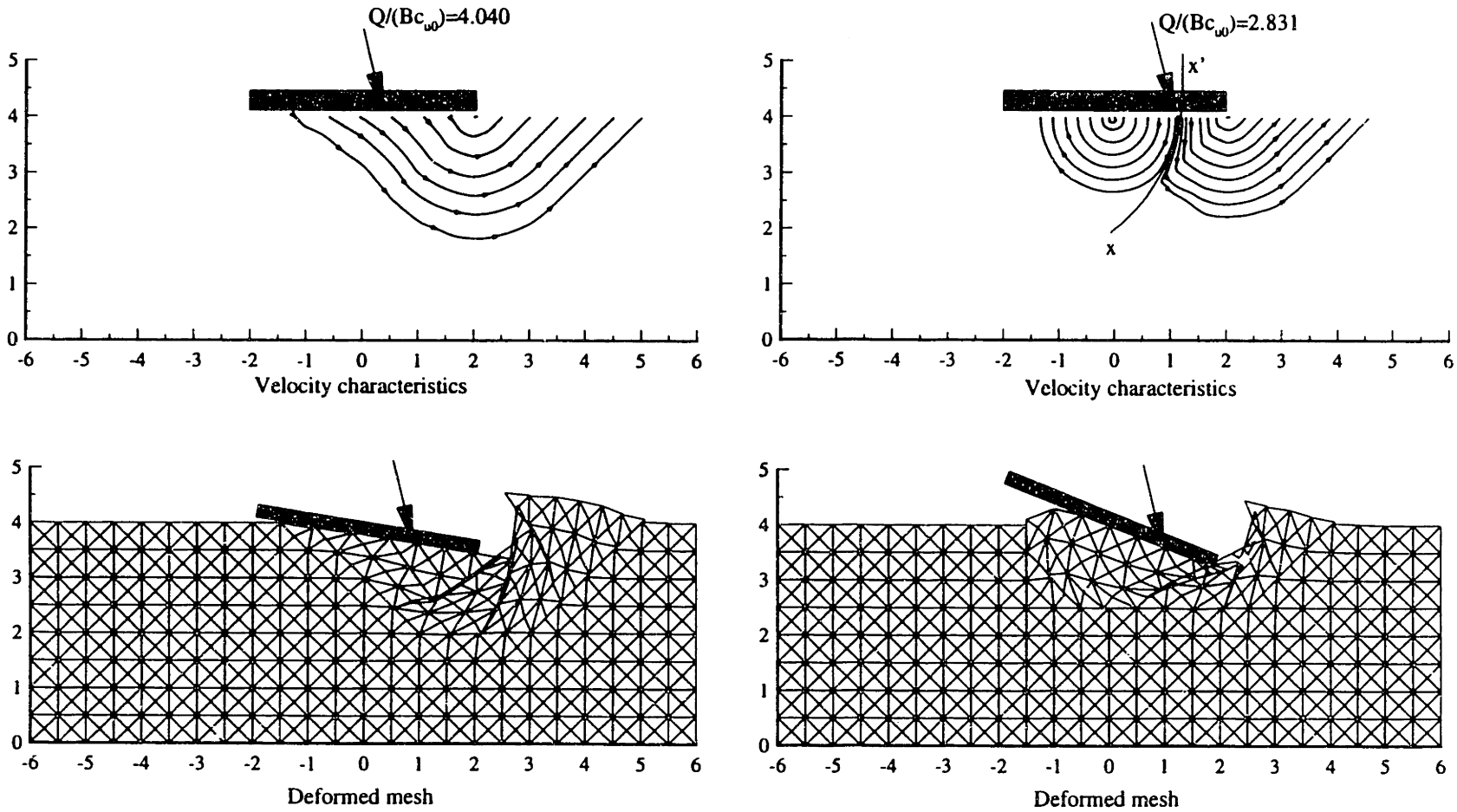

a) α=7.5 deg., e/B=0.10

b) α=7.5 deg., e/B=0.25

Fig. 5.31 Upper bound analyses for Type 1 combined loading of footings on homogeneous clay

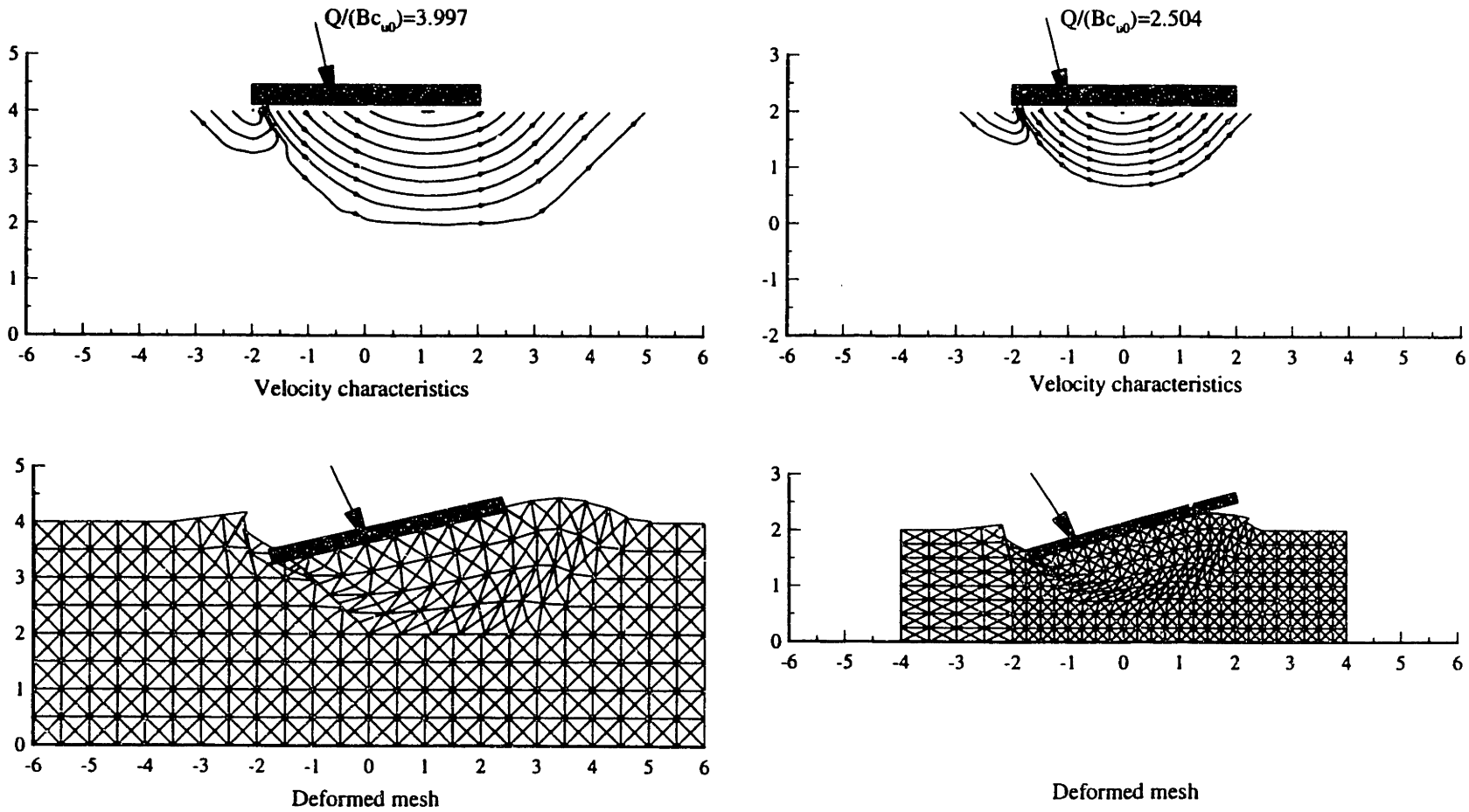

a) α=7.5 deg., e/B=-0.10

b) α=7.5 deg., e/B=-0.25

Fig. 5.32 Upper bound analyses for Type 2 combined loading of footings on homogeneous clay

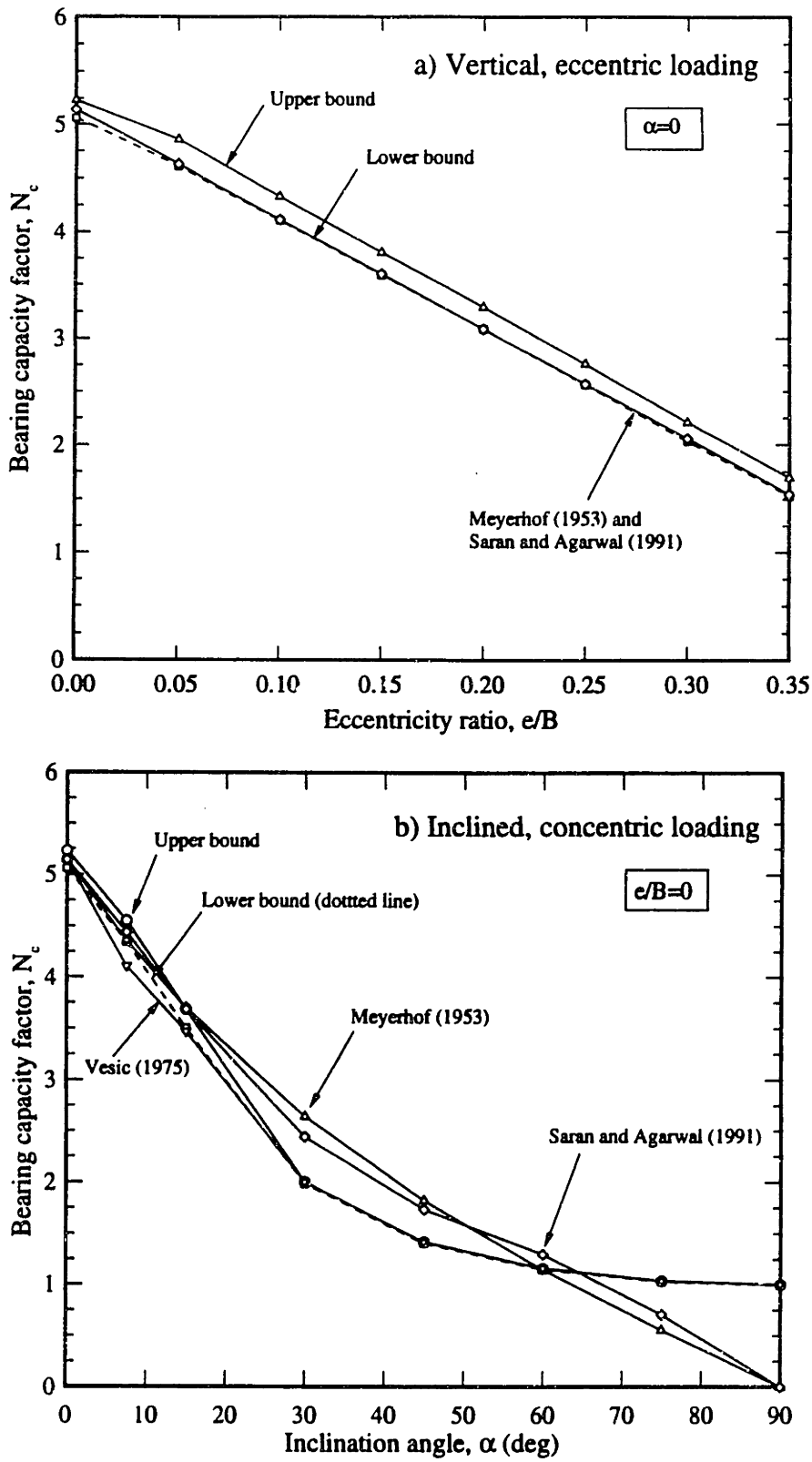

Fig. 5.33 Evaluation of published bearing capacity factors for a) Vertical, eccentric loading; and b) Inclined, concentric loading of footings on homogeneous clay

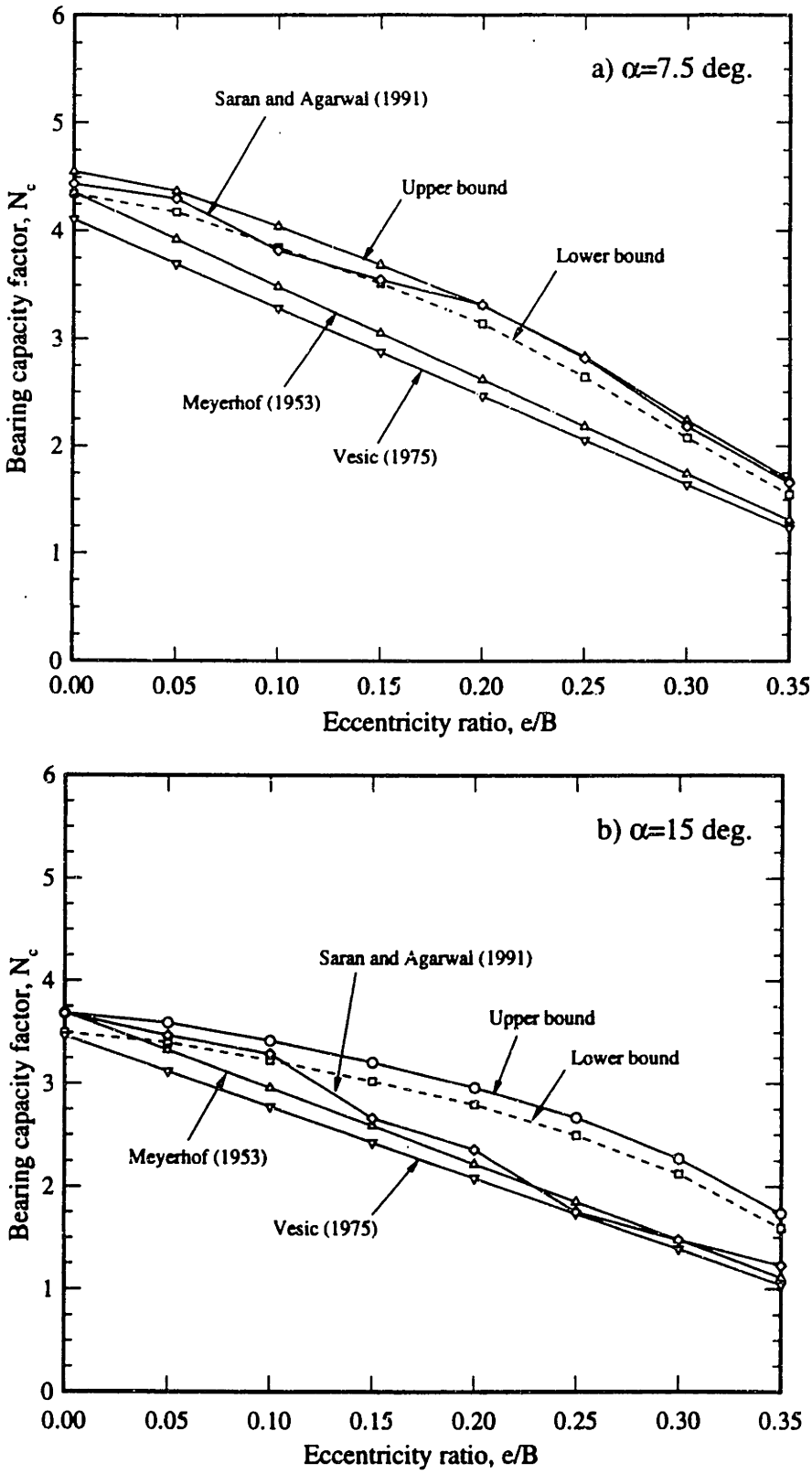

Fig. 5.34 Evaluation of published bearing capacity factors for Type 1 combined loading of footings on homogeneous clay

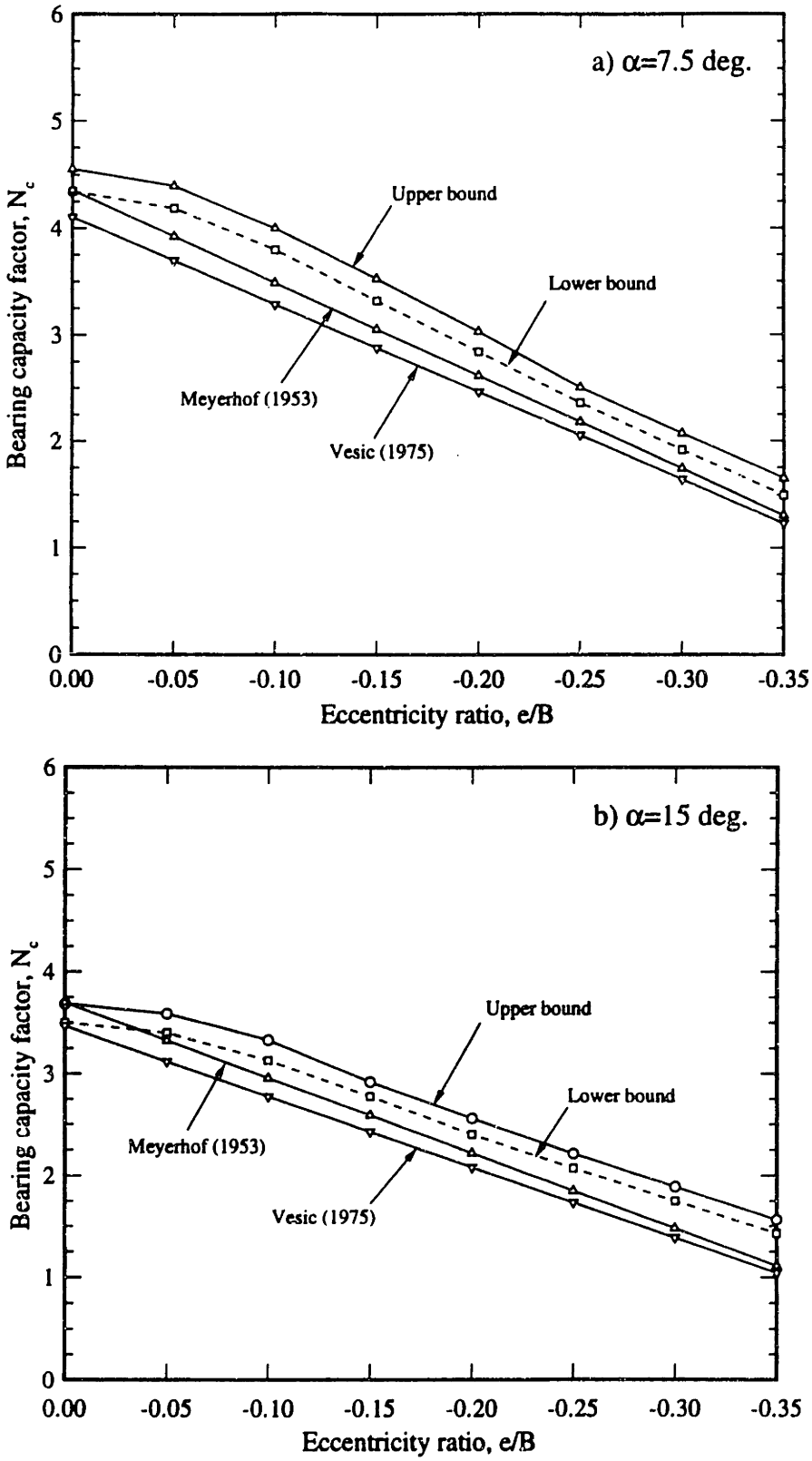

Fig. 5.35 Evaluation of published bearing capacity factors for Type 2 combined loading of footings on homogeneous clay

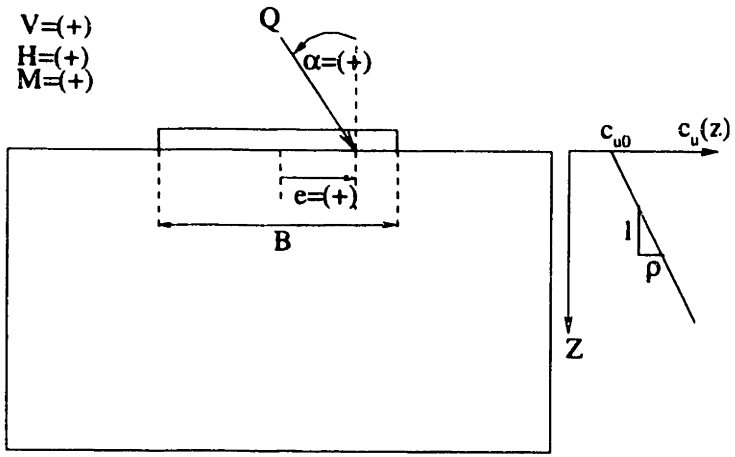

Loading type 1

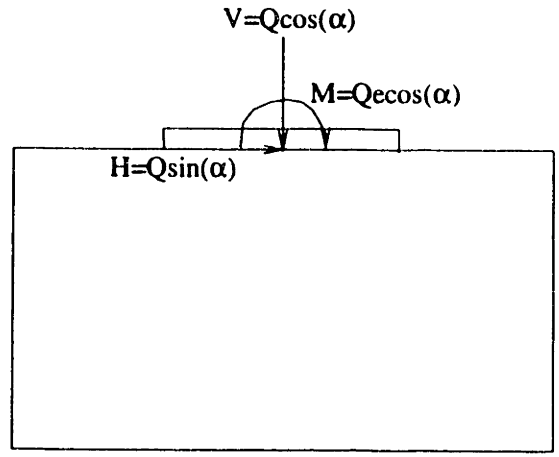

Positive sign convention for equivalent forces V,H and M

Soil Properties

Cohesion at surface, c_{u0}

Change of cohesion with depth, ρ

Range of strength profile parameter, $\rho B/c_{u0}$: 0, 2, 4, 6, 8, 12

Range of e/B and α

Vertical eccentric loading, e/B = 0.0-0.35, increment of 0.05

Inclined concentric loading, α = 0, 2.5, 5, 7.5, 10, 15, 20, 30 deg.

Fig. 5.36 Load geometry and soil parameters for limit analyses of footings on non-homogenous clay

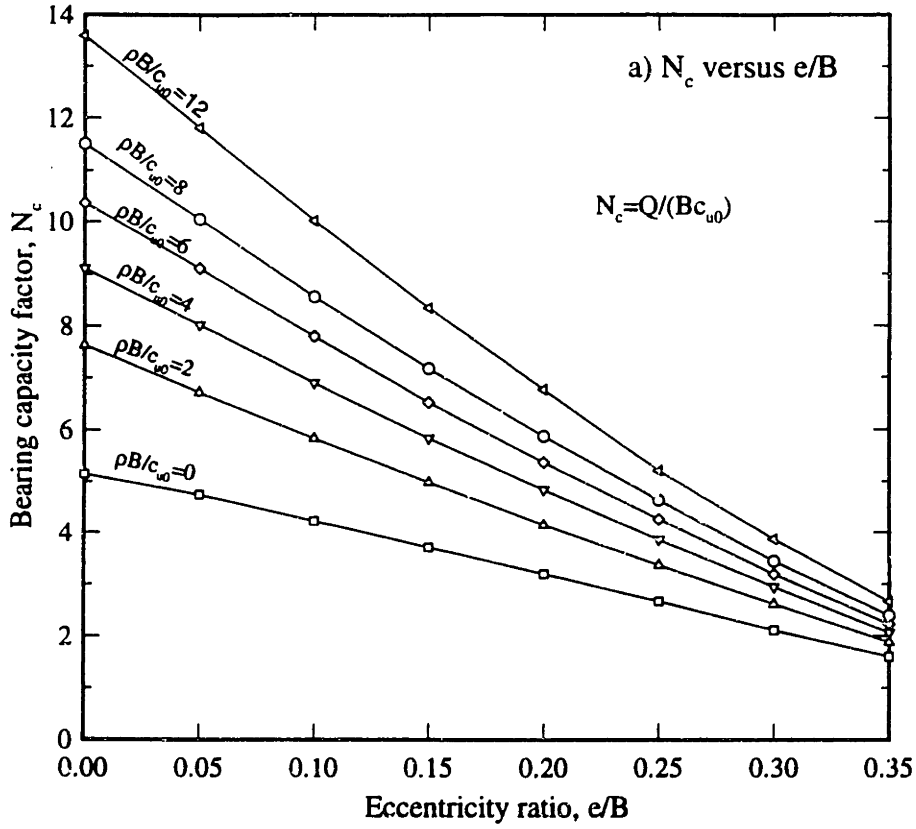

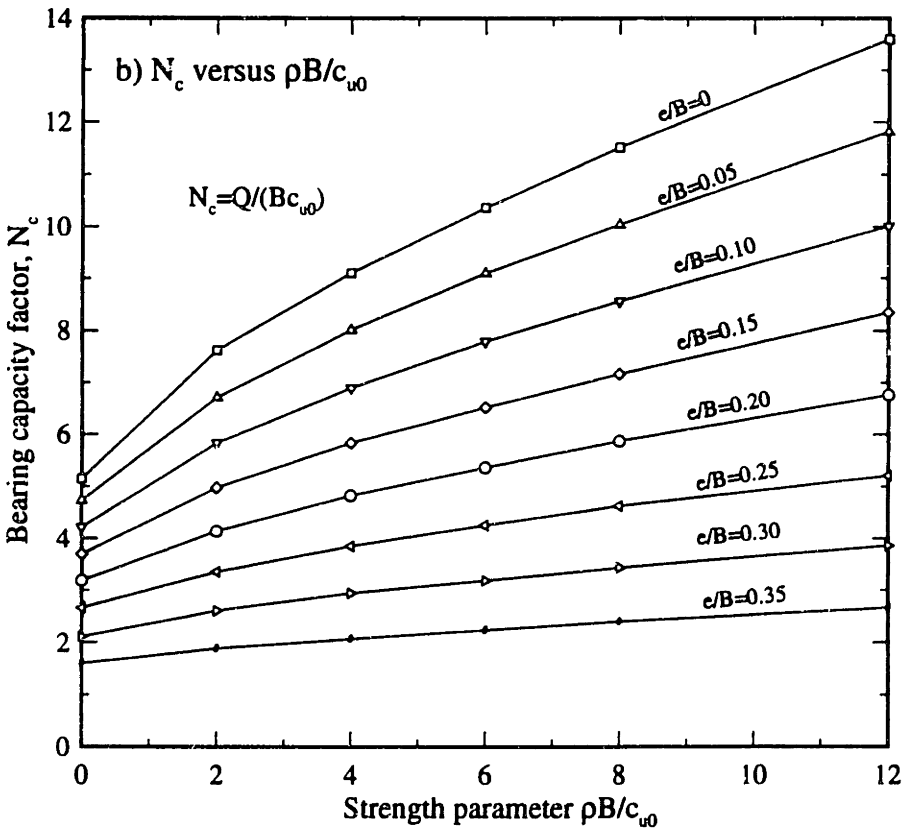

Fig. 5.37 Bearing capacity factors for vertical eccentric loading of footings on non-homogeneous clay

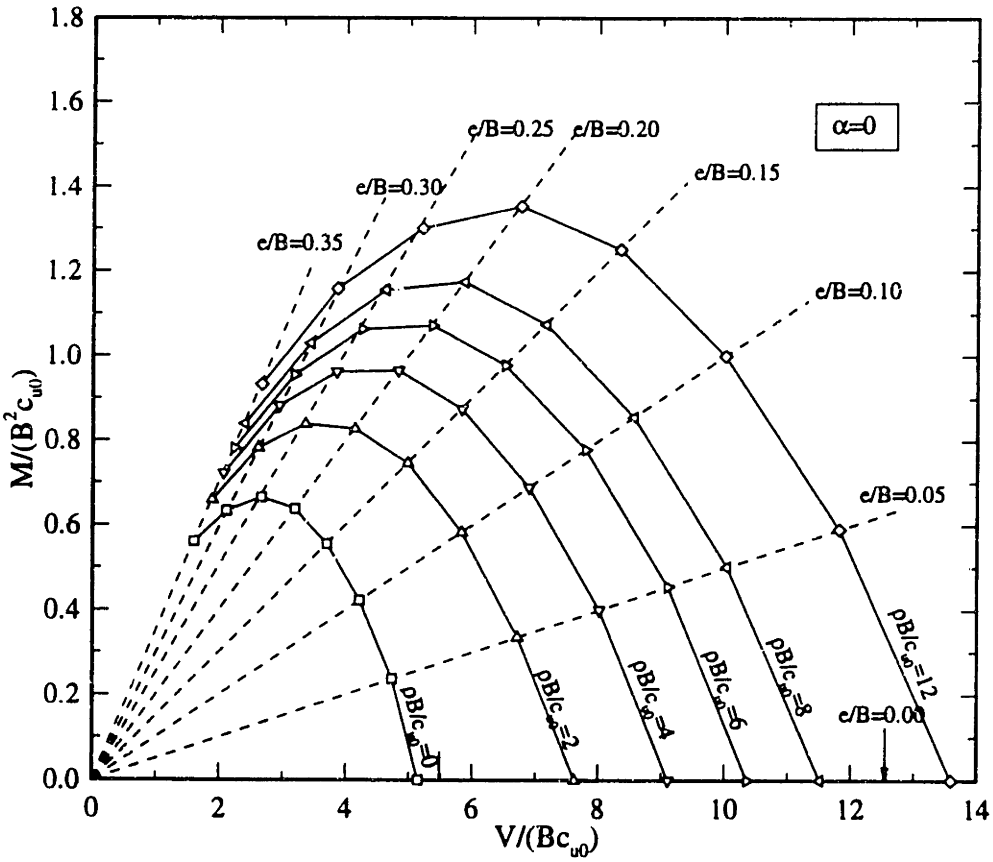

Fig. 5.38 Failure envelope for vertical eccentric loading of footings on non-homogeneous clay

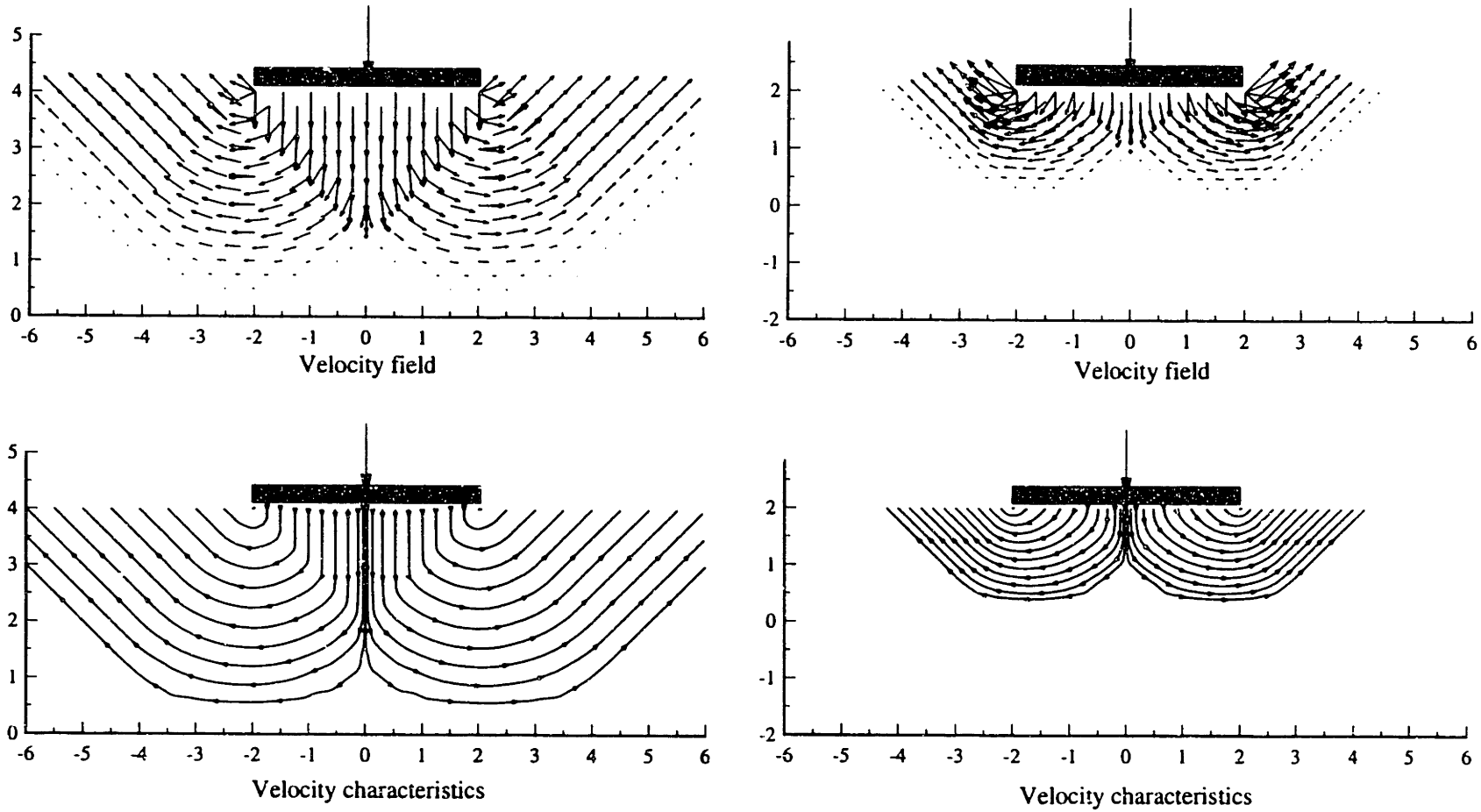

a) $\rho B/c_{u0}=0$, $\alpha=0$, $e/B=0.0$

b) $\rho B/c_{u0}=2.0$, $\alpha=0$, $e/B=0.0$

Fig. 5.39 Effect of strength non-homogeneity on velocity field and velocity characteristics for concentric loading of footings

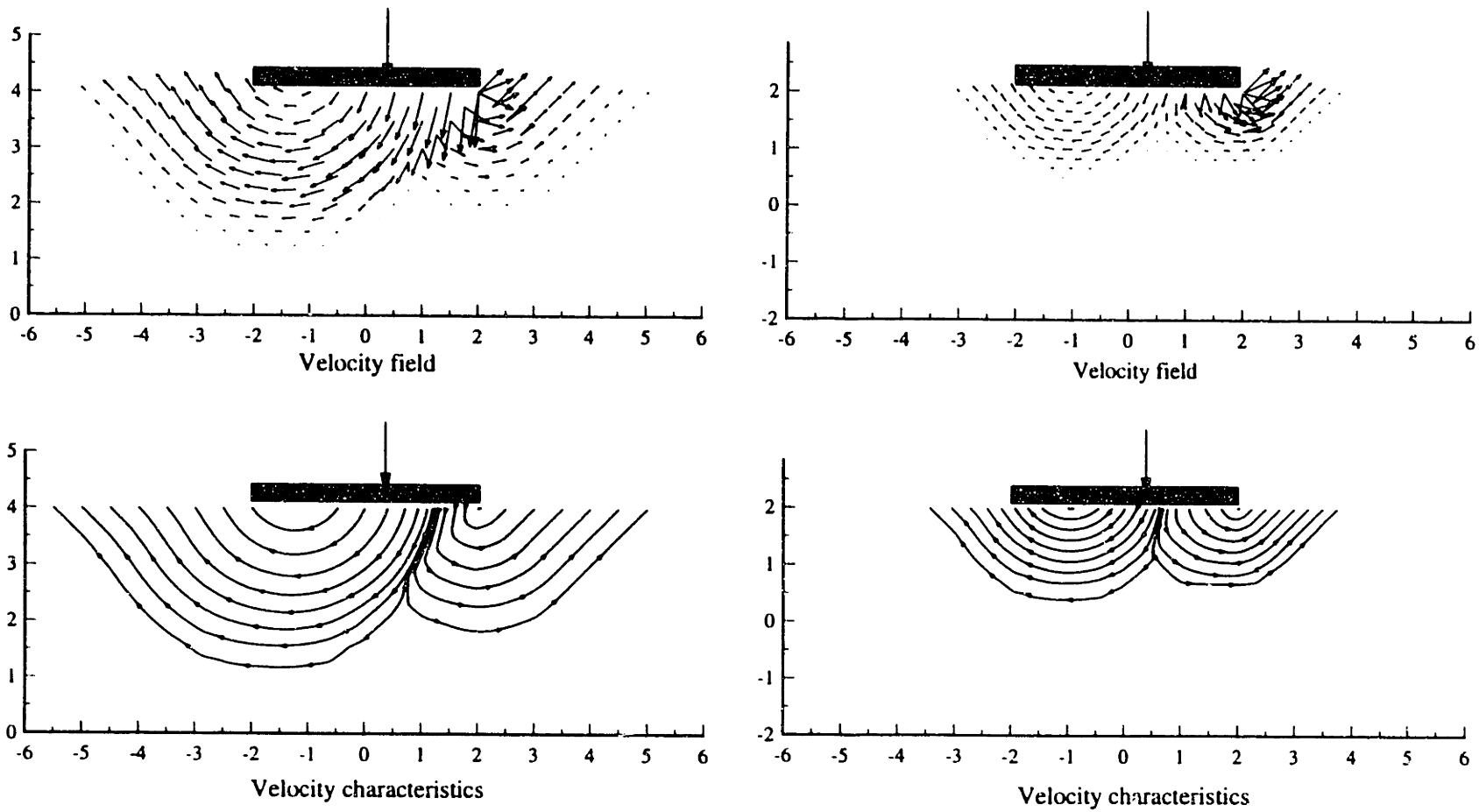

a) $\rho B/c_{u0}=0$, $\alpha=0$, $e/B=0.10$

b) $\rho B/c_{u0}=2.0$, $\alpha=0$, $e/B=0.10$

Fig. 5.40 Effect of strength non-homogeneity on velocity field and velocity characteristics for footings with small load eccentricity

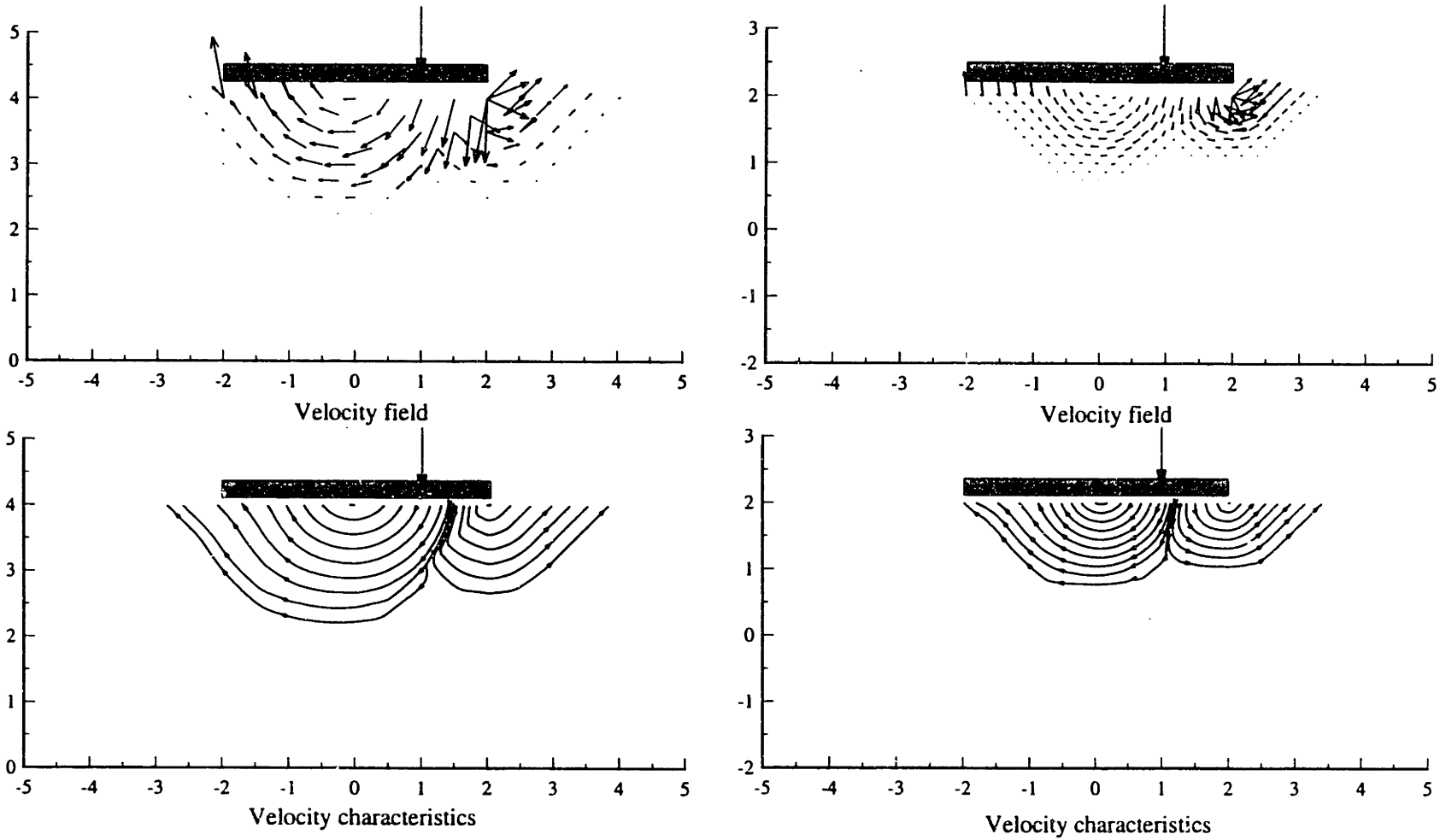

a) $\rho B/c_{u0}=0$, $\alpha=0$, $e/B=0.25$

b) $\rho B/c_{u0}=2.0$, $\alpha=0$, $e/B=0.25$

Fig. 5.41 Effect of strength non-homogeneity on velocity field and velocity characteristics for footings with large load eccentricty

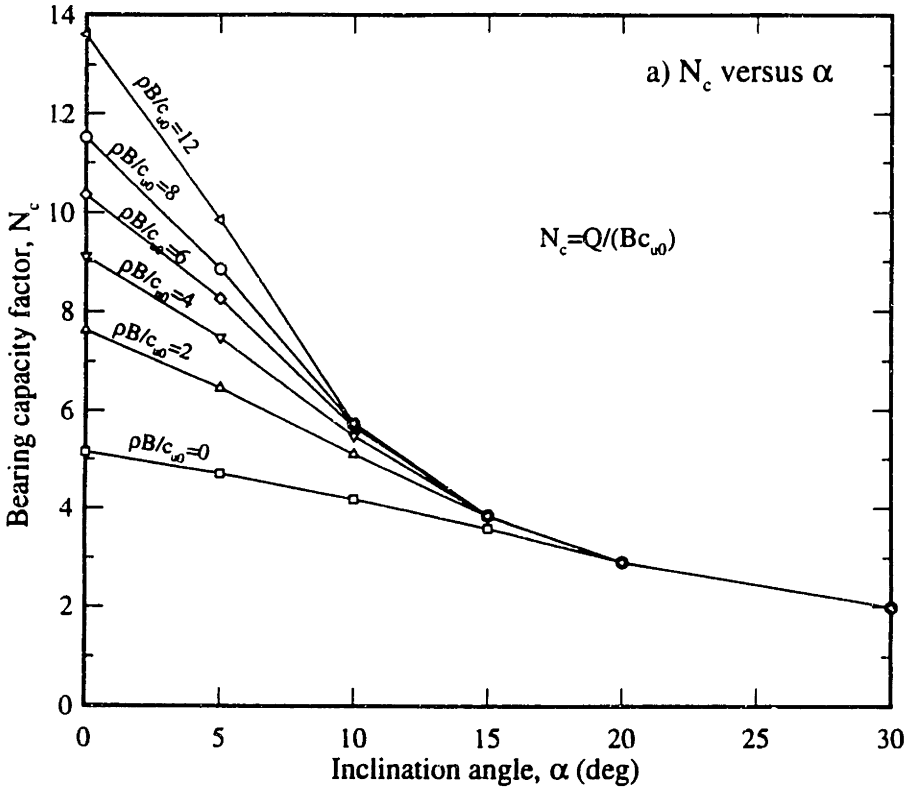

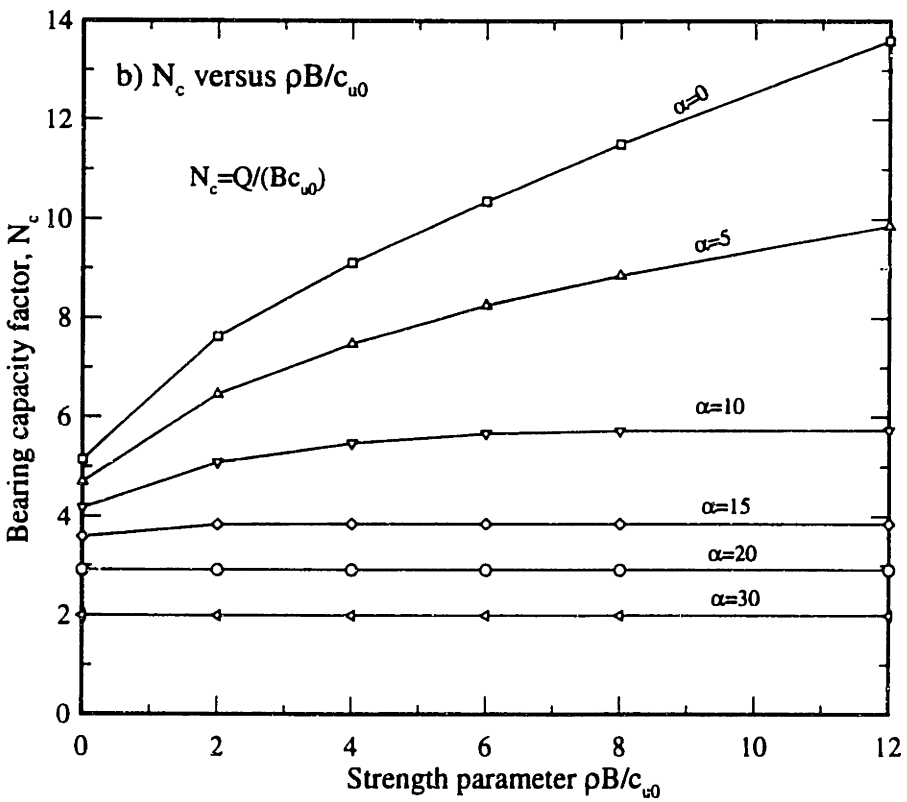

Fig.5.42 Bearing capacity factors for inclined concentric loading of footings on non-homogeneous clay

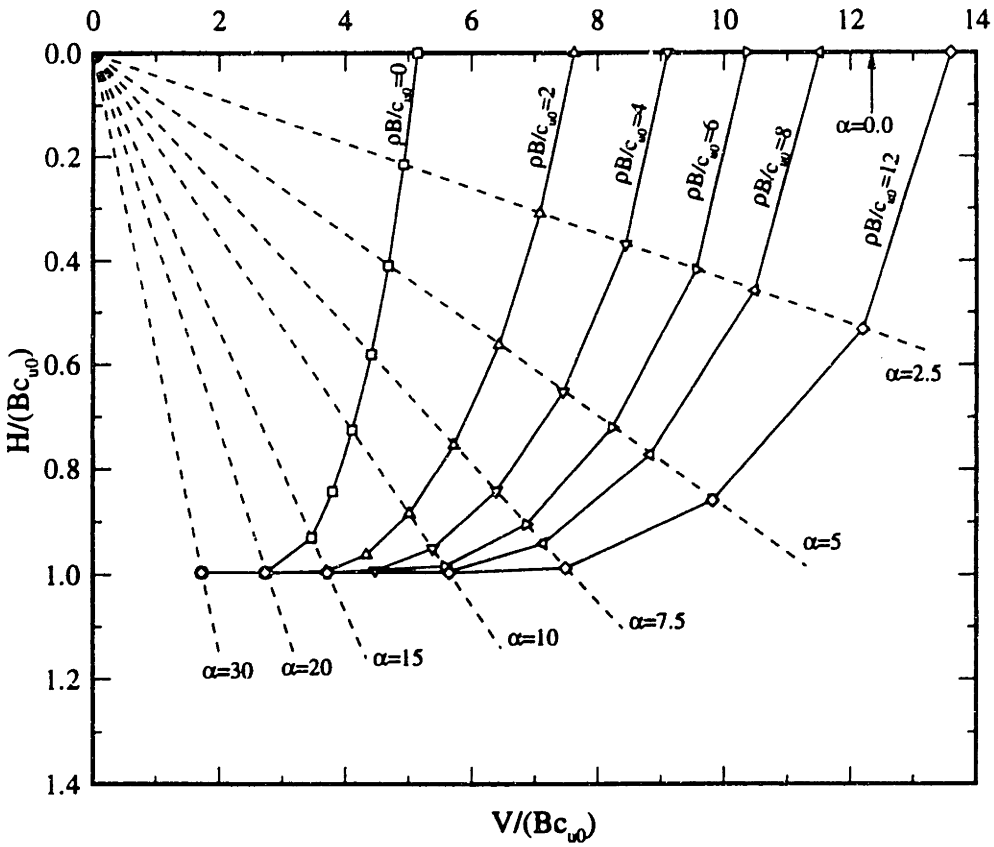

Fig.5.43 Failure envelope for inclined concentric loading of footings on non-homogeneous clay

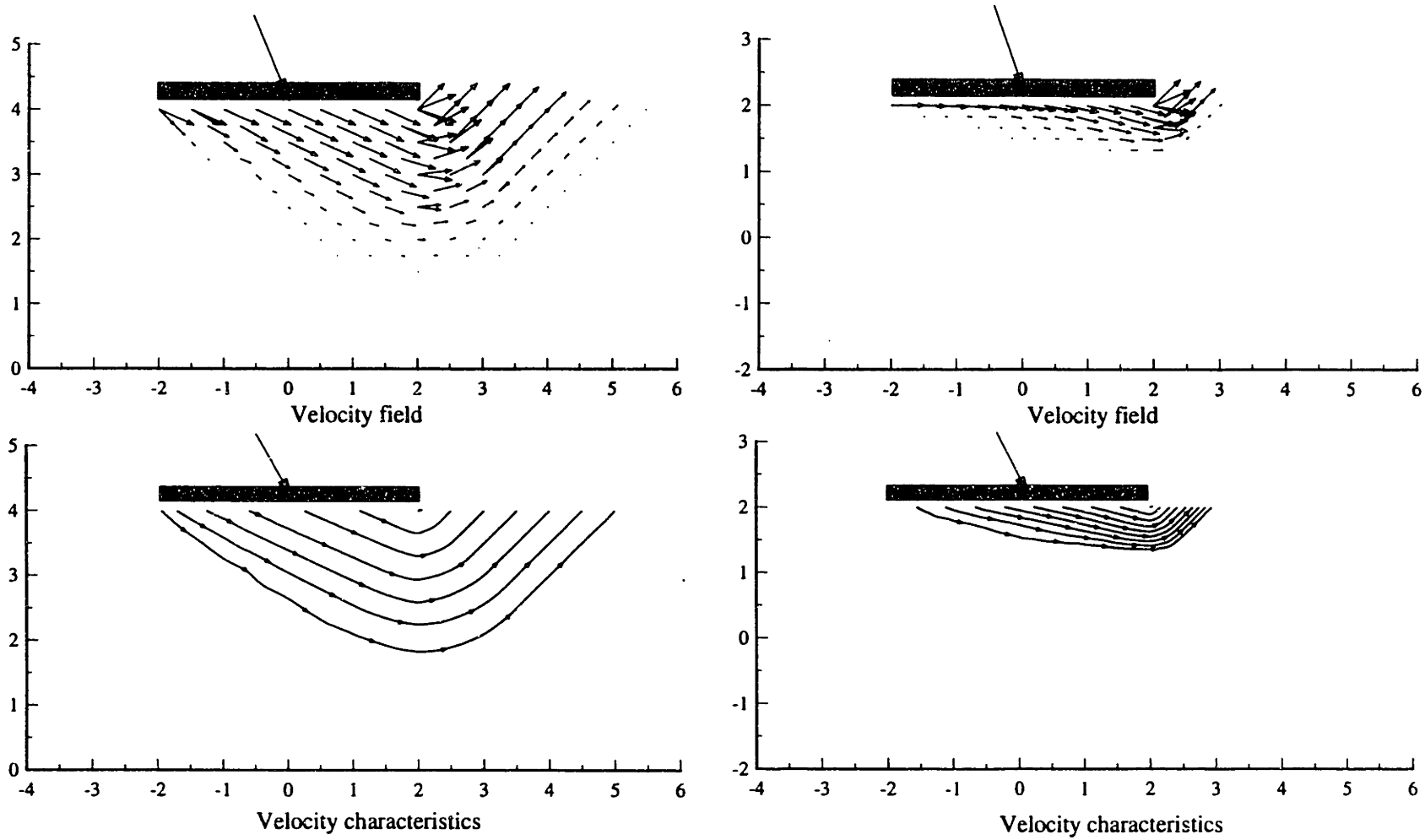

a) $\rho B/c_{u0}=0$, $\alpha=10.0$ deg., e/B=0.0

b) $\rho B/c_{u0}=2$, $\alpha=10.0$ deg., e/B=0.0)

Fig. 5.44 Effect of strength non-homogeneity on velocity field and velocity characteristics for inclined concentric loading of footings

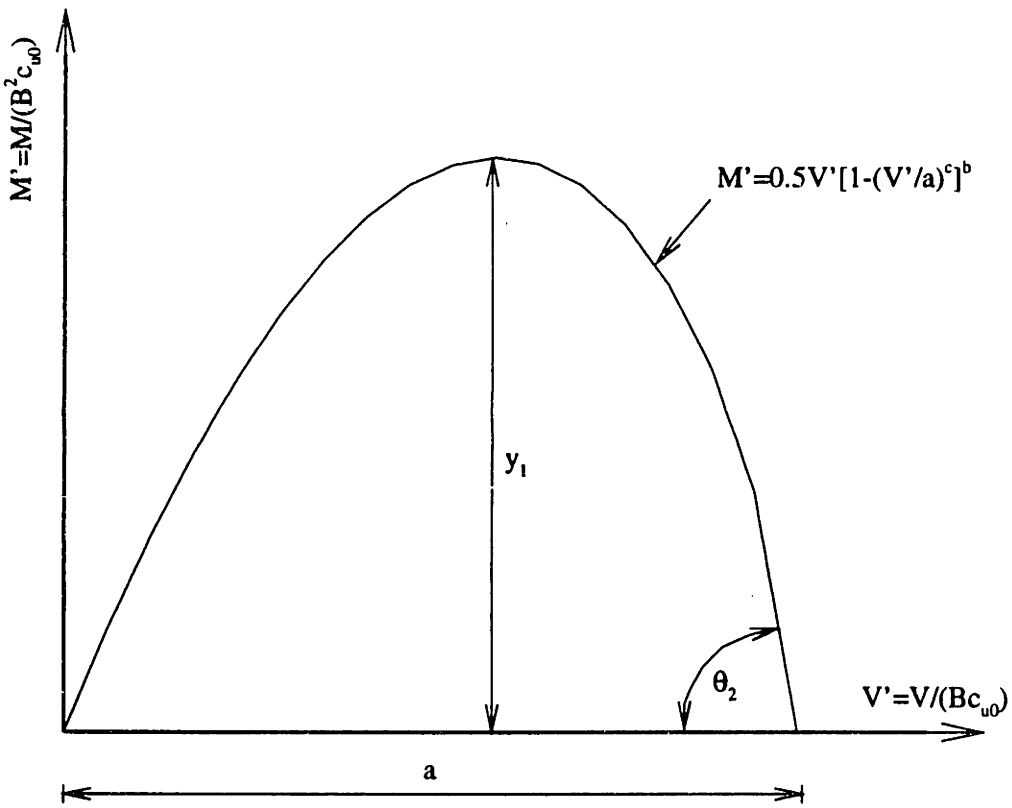

Fig. 4.45 Proposed failure envelope for inclined and eccentric loaded of footins on clay

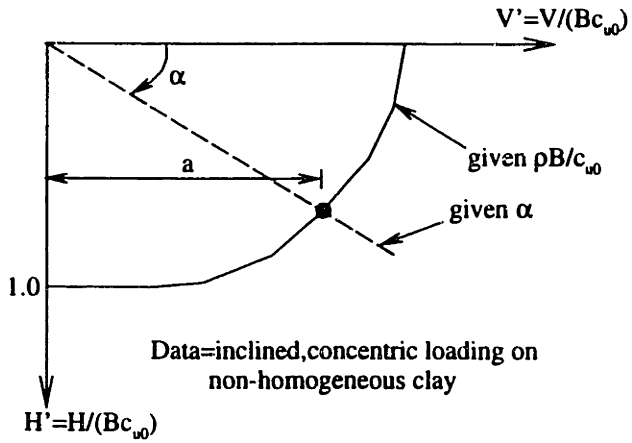

a) Determination of the parameter a

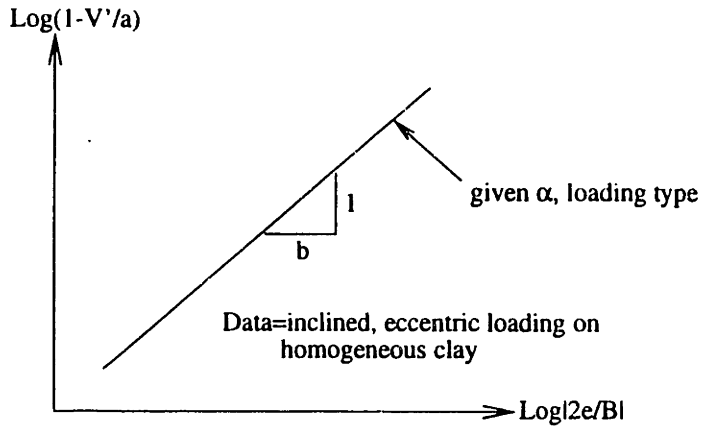

c) Determination of the parameter b

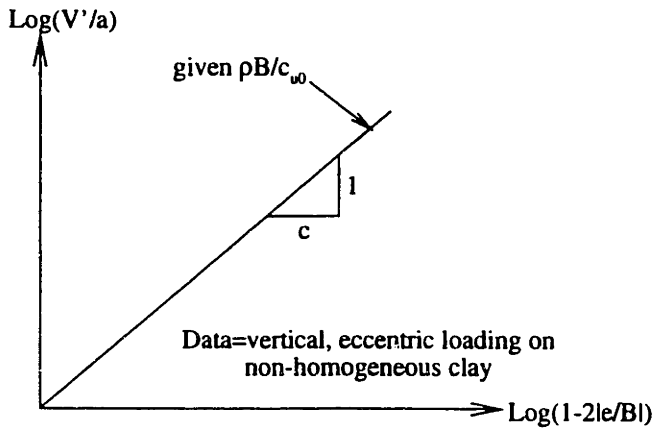

b) Determination of the parameter c

Fig. 5.46 Determiation of three parameters governing failure envelope for inclined and eccentric loadings of footings on clay

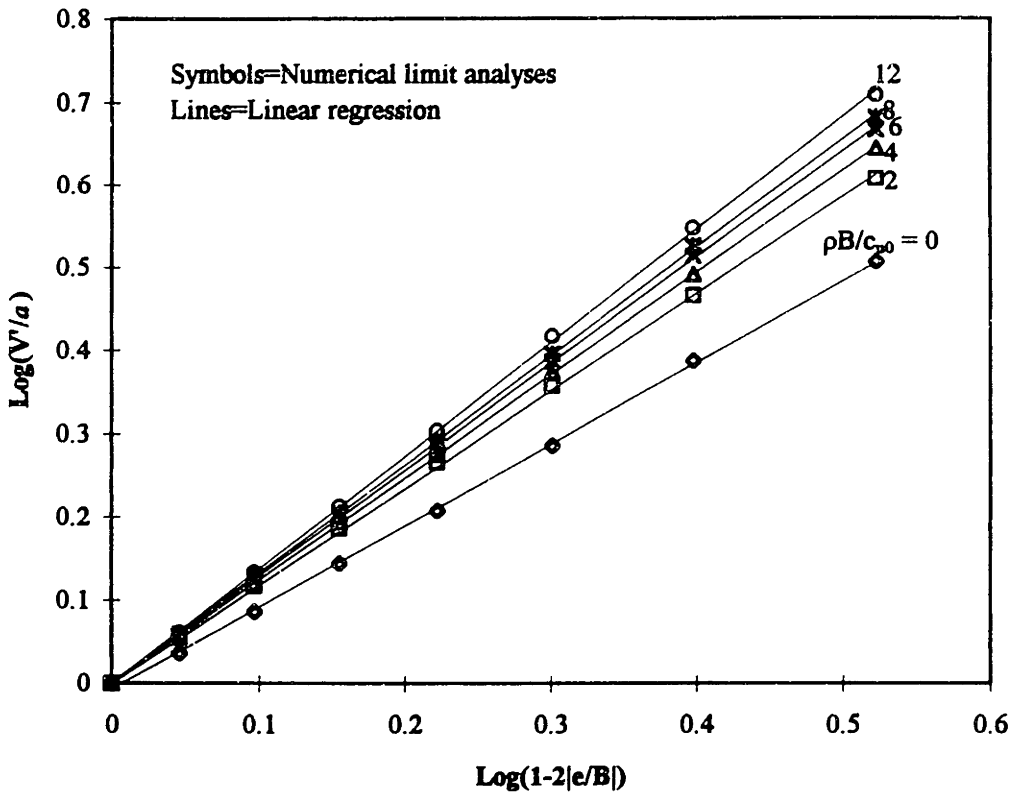

Linear regression results

$\rho B/c_{u0}$	$1/c$	r^2
0	0.9803	0.9996
2	1.1619	0.9998
4	1.2333	1
6	1.2809	0.9999
8	1.3079	0.9999
12	1.3629	0.9998

Figure 5.47 Determination of paramter c from vertical, eccentric loading of of footings on non-homogeneous clay

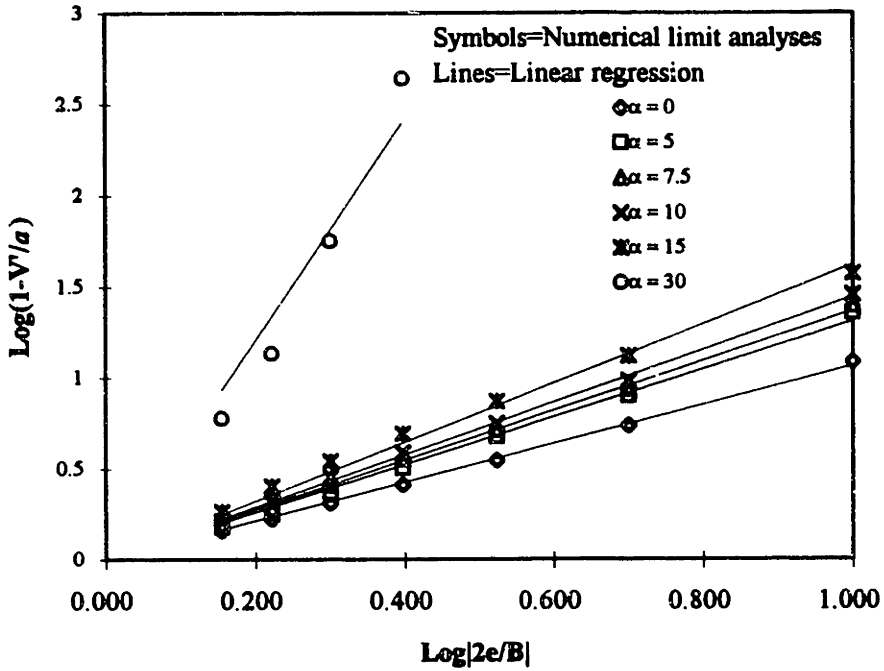

α (deg.)	1/*b*	r^2
0	1.0636	0.9982
5	1.3095	0.9951
7.5	1.3699	0.9980
10	1.4435	0.9985
15	1.6197	0.9911
30	6.0461	0.9361

a) Loading Type 1

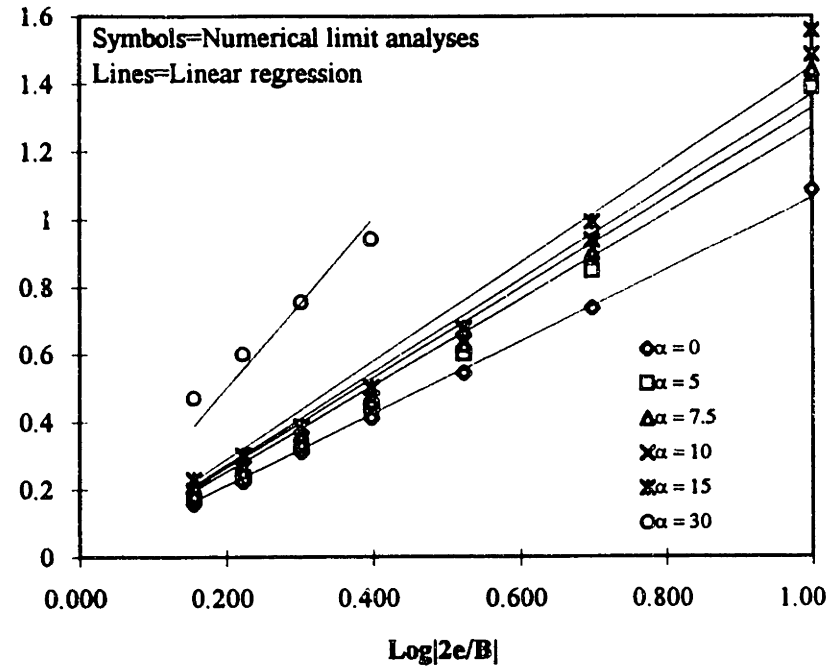

α (deg.)	1/*b*	r^2
0	1.0636	0.9982
5	1.2716	0.9740
7.5	1.327	0.9758
10	1.3696	0.9749
15	1.4501	0.9794
30	2.5066	0.9042

b) Loading Type 2

Figure 5.48 Determination of parameter *b* from combined loading of footings on homogeneous clay

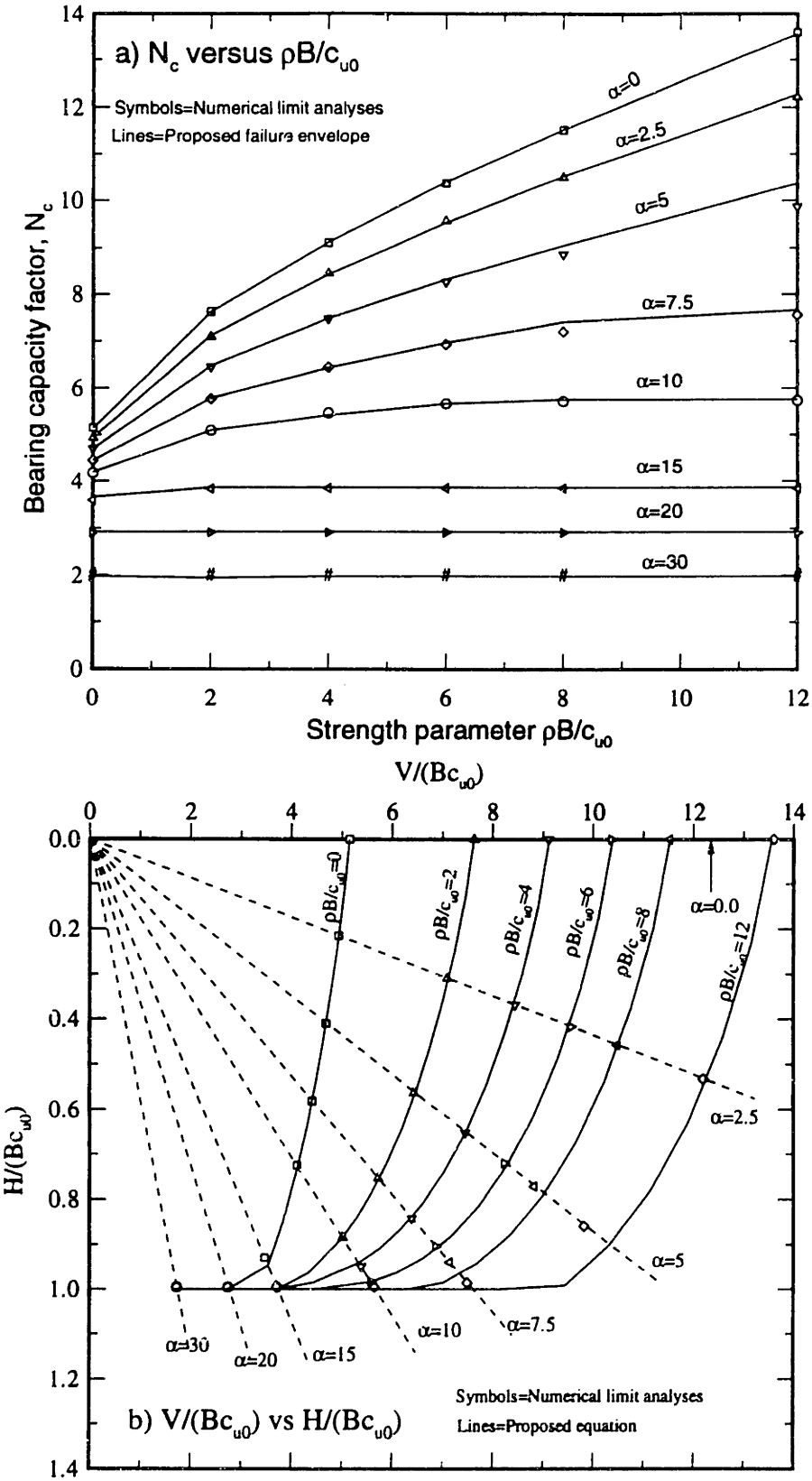

Fig. 5.49 Evaluation of proposed failure envelope for inclined concentric loading of footings on non-homogeneous clay

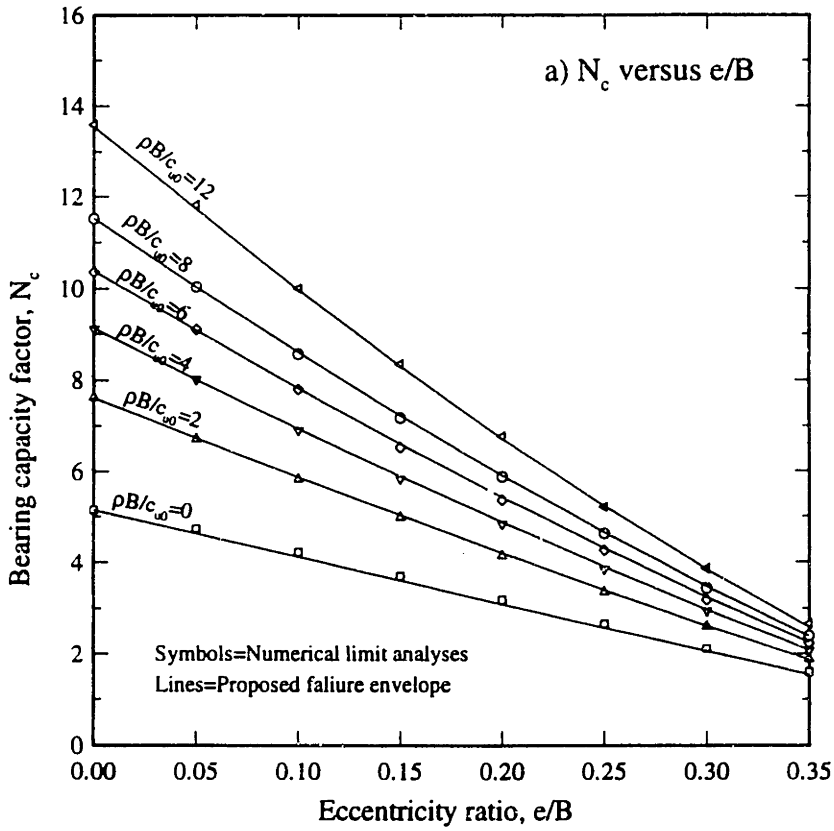

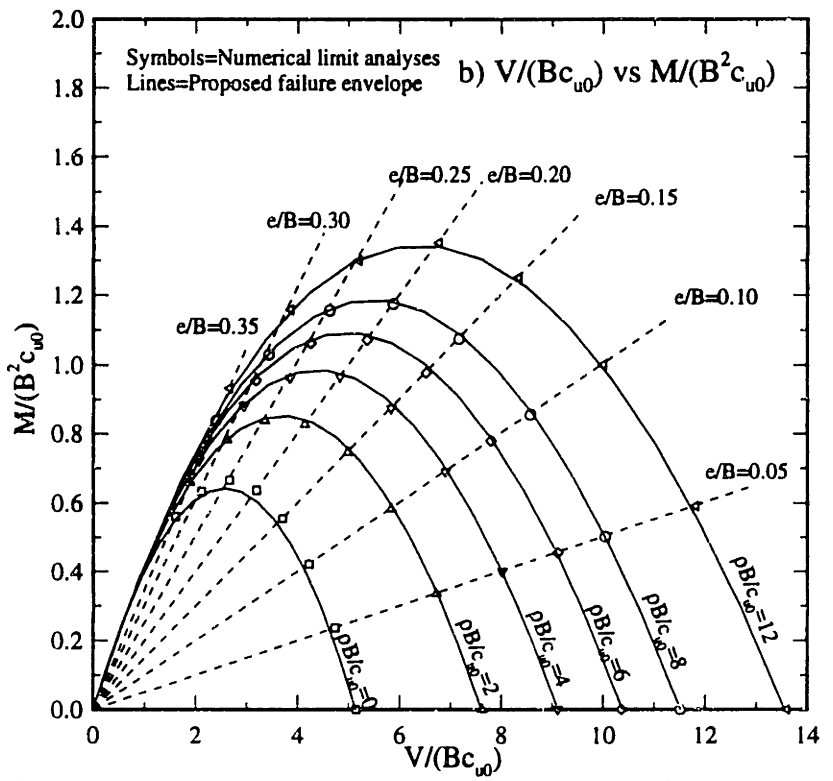

Fig. 5.50 Evaluation of proposed failure envelope for vertical eccentric loading of footings on non-homogeneous clay

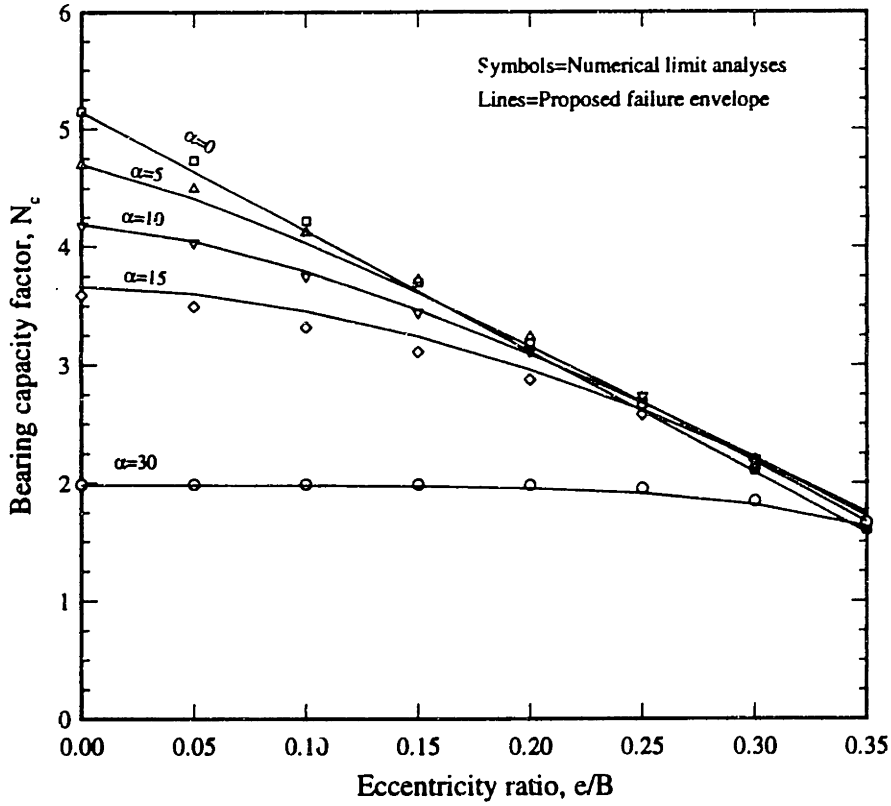

Fig. 5.51 Evaluation of proposed bearing capacity factors for Type 1 combined loading of footings on homogeneous clay

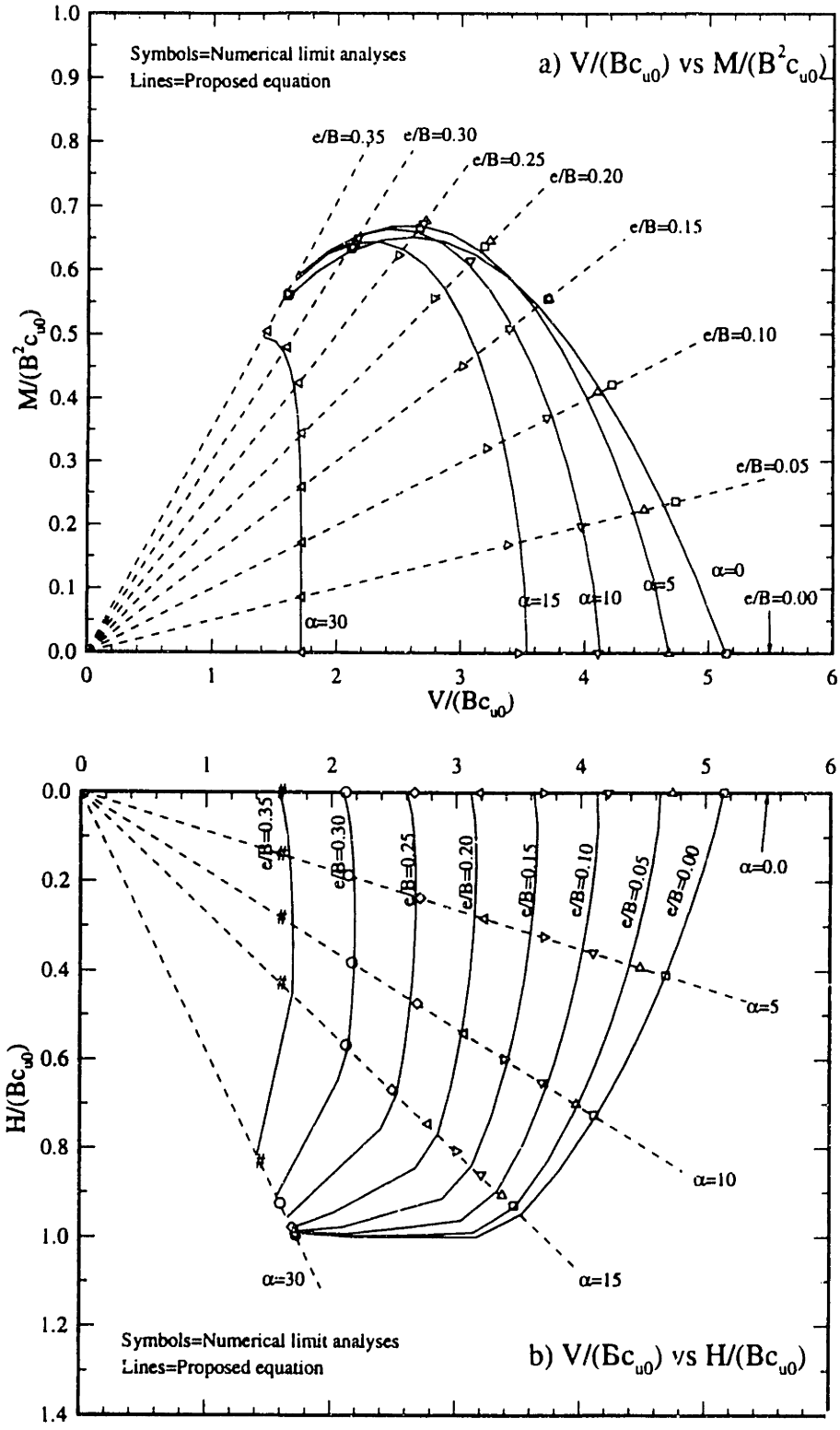

Fig. 5.52 Evaluation of proposed failure envelope for Type 1 combined loading of footings on homogeneous clay

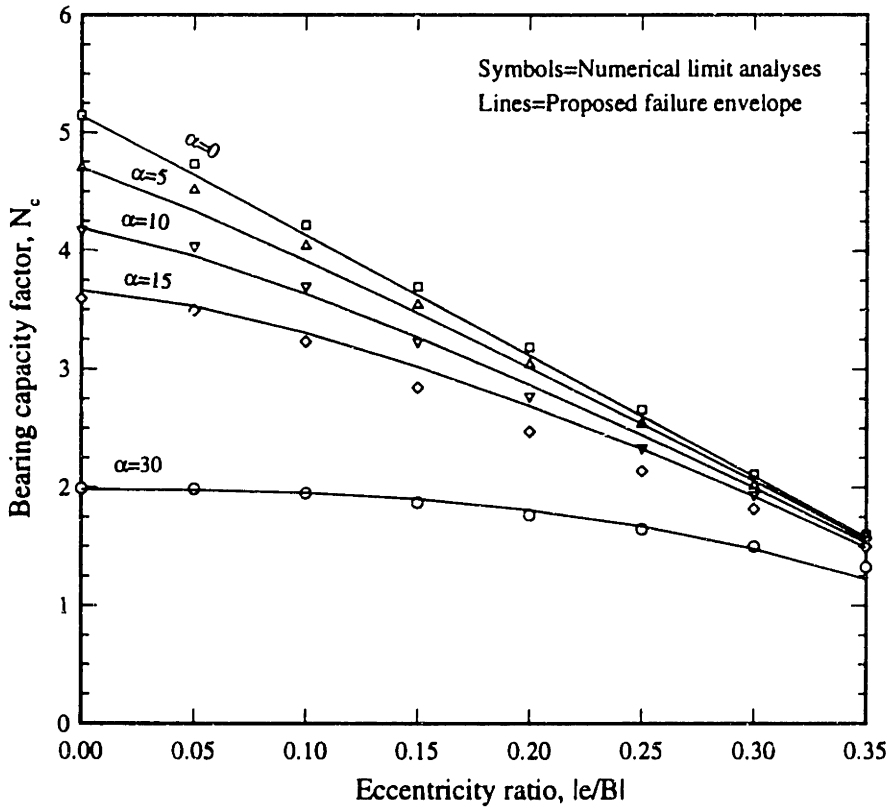

Fig. 5.53 Evaluation of proposed bearing capacity factors for Type 2 combined loading of footings on homogeneous clay

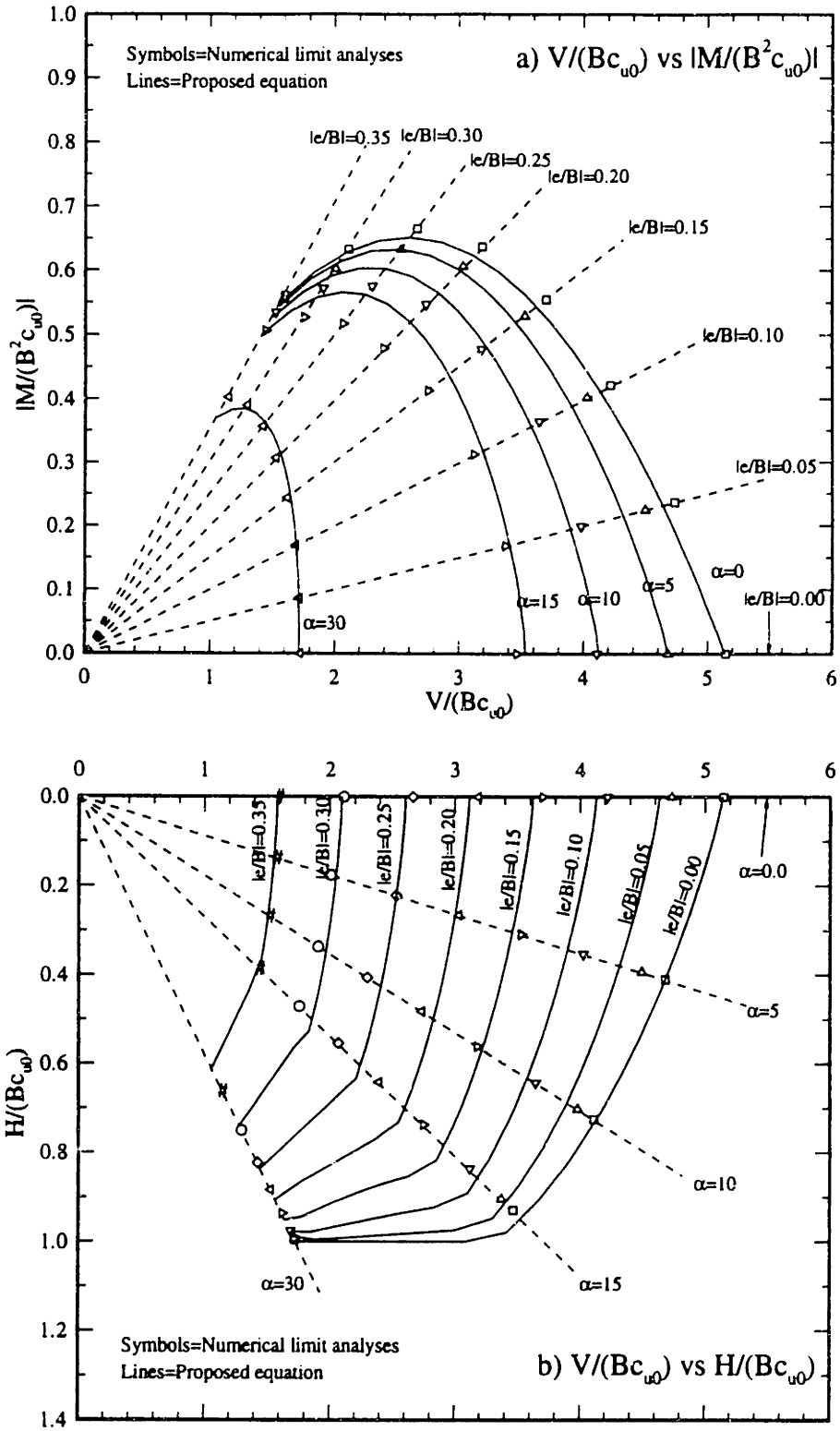

Fig. 5.54 Evaluation of proposed failure envelope for Type 2 combined loading of footings on homogeneous clay

6. Summary, Conclusions and Recommendations

Recent developments of efficient numerical methods of limit analyses (Sloan, 1988a; Sloan and Kleeman, 1994), which satisfy rigorous lower and upper bound theorems, offer a new approach to practical collapse calculations in geotechnical engineering. The thesis has evaluated numerical limit analyses for predicting the undrained bearing capacity of footings on clay. Predictive capabilities of the method have been demonstrated by further applications for inclined and eccentric loading of footings on clay. The research uses software developed and supplied to MIT by Prof. Sloan of the University of Newcastle, Australia.

The following sections (6.1-6.4) summarize the principal findings of this research, while Section 6.5 gives recommendations for further study.

6.1 Methods of Assessing the Collapse

Chapter 2 reviews the methods of assessing the collapse of stability problem in geotechnical engineering. Limit equilibrium methods, slip-line analysis and limit analyses all calculate collapse loads assuming rigid-perfectly plastic material behavior. In contrast, conventional displacement based finite element method simulate the complete load-deformation behavior using constitutive laws which model the stress-strain strength properties of the soil.

Limit equilibrium calculations assume the location of a trial failure surface and solve the factor of safety using static equilibrium equations. When the failure mass is discretized, additional assumptions are required for the interslice forces in order to use these equations. The method searches for the critical failure surface which corresponds to the minimum factor of safety.

The slip-line field analysis uses the bound theorems in order to obtain the exact collapse load. First, the stress field in the vicinity of applied load is constructed to satisfy equilibrium, stress boundary conditions, and the yield criterion. Secondly, the velocity field associated with the stress field is constructed to satisfy velocity boundary conditions and flow rule. Finally, if the stress field can be extended throughout the soil mass in a

statically admissible manner, the load calculated from the complete stress field is said to be a true collapse load.

The limit analysis method uses two separate calculations of lower bound and upper bound collapse loads. In the lower bound calculation, the solution comprises a statically admissible stress field which satisfies equilibrium, stress boundary conditions, and yield criterion, while the upper bound calculation obtains a kinematically admissible velocity field which satisfies compatibility equations, velocity boundary conditions, and associated flow rule.

Conventional limit analyses and slip-line field analysis suffer from the disadvantages that they are very difficult to apply to complicated boundary conditions, non-homogeneous soil properties, etc. In contrast, the limit equilibrium method can be applied to these practical problems, but suffers from inherent uncertainties in the selection of failure mechanisms and search procedures which affect the accuracy of the solution. The difficulty in using the conventional finite element method lies in implementing non-linear finite element analyses which depends on the ability of incremental procedure and constitutive soil models.

6.2 Numerical Lower and Upper Bound Formulations

Chapter 3 describes the proposed numerical lower bound and upper bound formulations for plane strain problems based on papers by Sloan (1988a) and Sloan and Kleeman (1994). The analyses use finite element discretization and interpolation, satisfy the constraints of the lower and upper bound theorems through linear programming formulations which are solved using an active set algorithm (Best and Ritter, 1985). The major advantage of the numerical limit analysis is that it can be applied to complex loadings and non-homogeneous soil profiles.

In the lower bound formulation, the soil mass is discretized into 3-noded triangle elements, with special extension elements to ensure static admissibility of the solutions in a soil half-space. The analyses solve the unknown nodal stress components (σ_x, σ_y, τ_{xy}), which are assumed to vary linearly within each element. Statically admissible stress fields are obtained by satisfying the constraints of static equilibrium, stress boundary conditions,

and Mohr-Coulomb yield with stress discontinuities at the interface between adjacent elements. The non-linear Mohr-Coulomb yield criterion is approximated by a series of linear constraints on the stresses, which ensure that the solutions never exceed the exact yield function. The lower bound load is obtained by maximizing the applied load subject to the constraints of static admissibility.

In the upper bound formulation, the soil mass is also discretized into triangular elements with unknown nodal velocities (u_x, u_y). The analyses assume that the velocities vary linearly within each element. Plastic deformation of each elements are controlled by a specified number of unknown plastic multiplier rates $\dot{\lambda}_i$ [1] (which are constrained to be non-negative). Plastic deformation is allowed to occur within the elements, while velocity discontinuities can occur along all interfaces between adjacent elements triangles. A kinematically admissible velocity field is defined by the constraints of compatibility, velocity boundary conditions, and associated flow. The non-linear yield criterion is linearized by using a polygonal approximation, which circumscribes the original yield surface. The upper bound collapse load is obtained by maximizing the applied load subject to the constraints of kinematic admissibility

6.3 Evaluation of Method: Undrained Loading of Footings on Clay

Chapter 4 evaluates the numerical upper and lower bound limit analyses in predicting the undrained bearing capacity for vertically loaded footings on clay. Numerical experiments have established the effects of mesh refinement and arrangement, and yield surface linearizations on the accuracy of the numerical solutions. Further calculations demonstrate the capabilities of the analyses for non-homogeneous soil profiles, in which the undrained shear strength increases linearly with depth, and compare results for rough and smooth bases as a first step in modeling soil-structure interaction. The results of studies can be summarized as follows:

[1] where i corresponds to the linearization of the yield functions

Both lower bound and upper bound solutions are affected by the yield surface linearization. Reliable solutions for undrained loading are obtained by approximating the Tresca yield criterion with a 24-sided polygon. The lower bound calculations are affected very significantly by the mesh arrangement and refinement while extension elements are necessary to represent the soil half-space. The analyses in section 4.2 show how the accuracy of the lower bound solution can be improved by: i) using the highest density of elements in regions of high stress gradients; ii) extending the size of the discretized domain relative to the footing width; and iii) refining the mesh density.

The upper bound solution is much less sensitive to mesh arrangement and mesh refinement as the formulation allows plastic deformation to occur both within elements and along the velocity discontinuities between elements. Upper bound solutions are not affected by the size of the domain boundary provided that the failure mechanism is fully contained within the discretized domain.

Although the analyses provide bounds on the true collapse load, section 4.2 shows that improvement in solution accuracy requires careful section and refinement of the mesh. In this thesis, mesh refinements have been carried out to ensure that the collapse load is computed to an pre-defined tolerance ±4-5%. In many cases, the actual computations are significantly more accurate, with upper and lower bounds bracketing the true collapse load to within ± 2%.

The computation times required for each analysis typically range from 15-30 mins of CPU using a DEC ALPHA 3000-300X workstation. No direct comparisons of computation time have been made with conventional displacement-base finite element solutions. However, it is clear that the limit analyses are both practical and efficient for plane strain analyses.

Detailed interpretation of the numerical limit analyses show that the stress field and contact normal stress distributions from lower bound analyses are in excellent agreement with the solutions by the method of characteristics. In addition, the velocity fields and failure mechanisms are in excellent agreement with the exact solutions for both the homogeneous (Prandtl, 1920) and non-homogeneous strength profiles (Davis and Booker, 1973).

Limit analyses for rough rigid footings were performed by introducing additional constraints on the shear resistance of the soil-footing interface for footings on non-homogeneous clay. Interface slippage can occur at the edge of the footing and is dependent on the soil strength profile, $\rho B/c_{u0}$. For $\rho B/c_{u0} < 3$, no slippage occurs, while for $\rho B/c_{u0} > 100$, slippage can extend across the full width of the footing.

6.4 Undrained Bearing Capacity for Footings on Clay with Inclined and Eccentric Loads

Chapter 5 presents applications of the numerical limit analysis for computing the capacity of footings on clay with inclined and eccentric loads, a problem with no published analytical solution. Combinations of inclined and eccentric loads are more difficult to analyze as the rigid footing can separate from the underlying soil or can slide along the surface. These difficult failure mechanisms are controlled by the combined effects of inclination angles and eccentricity ratios of the applied load. The original upper and lower bound programs (Sloan, 1988a; Sloan and Kleeman, 1994) were modified to include constraints governing the soil-structure interface for this situation. Results of the (modified) lower bound analyses for vertical, eccentric loads with e/B = 0.25, show that the contact normal stress is zero over a large portion of soil-footing interface, which indicates that the separation will occur within this zone (see Fig. 5.12c). Similarly, (modified) upper bound solutions for the same problem show a physical separation between the base of footing and underlying soil (see Fig. 5.14c). Analyses for concentric loads at large inclination angles, $\alpha > 45°$, generate sliding failure along the surface (see Fig. 5.18c). Hence, the modified programs replicate the full range of failure mechanisms expected under inclined and eccentric loading. In all cases, the true collapse loads are bounded within ± 4-5% (see Tables 5.4, 5.5 and 5.9) with computation times in the range 30-45 mins (see Tables 5.7 and 5.10).

The collapse loads can be represented by a three-dimensional failure envelope in terms of the statically equivalent forces, $V/(Bc_{u0})$ (vertical), (H/Bc_{u0}) (horizontal) and $M/(B^2c_{u0})$ (moment) (see Figs. 5.22 and 5.26). The calculations show that the failure surface is a closed and convex (see Fig. 5.30) and is non-symmetric for different directions

of load application (Type 1 vs Type 2) relative to the centroid of the footing (see Fig. 5.29). Moreover, the results reveal that for all ranges of inclination angle and eccentricity ratio, the capacity for Type 2 loading is always less than that for Type 1 (see Fig. 5.28).

Bearing capacity factors computed from the numerical limit analyses have been compared with existing empirical solutions (Meyerhof, 1953; Vesic, 1975; Saran and Agarwal, 1991). For eccentric, vertical loading, the effective width concept proposed by Meyerhof (1953) is a lower bound solution on the true collapse load (see Fig. 5.33a) while bearing capacity factors proposed for inclined, centric loads do not agree with the theoretical bounds from limit analyses. Published solutions for inclined and eccentric loading generally underestimate the true collapse loads (range from numerical upper and lower bounds) by 20-25% (Figs. 5.33-5.35).

Analyses of non-homogeneous layers were also performed for two cases: 1) vertical, eccentric loadings; and 2) inclined, concentric loadings. The results show that strength non-homogeneity increases the bearing capacity factor (see Figs. 5.37 and 5.42) and reduces the size of the failure zone (see Figs. 5.39-5.41, and 5.44). In addition, it can also increase the range of combined load conditions which cause separating between the underlying soil and sliding along the surface.

Section 5.5 proposes an empirical curve fitting procedure for the computed collapse load (equations 5.25 and 5.29) and describes a simple procedure for estimating the input parameters for the curve fitting functions. Comparisons with the computed collapse loads show the proposed function fits very well with the results of numerical limit analyses with relatively small errors (less than 10%; see Figs. 5.47-5.52).

6.5 Recommendations

Further research on the numerical limit analysis should be pursued in two general area: 1) improvement and development of the predictive capabilities of the original programs, and 2) application of the analyses to investigate other geotechnical problems.

The predictive capabilities of the original program should be improved in the following areas:

1. The original programs permit only homogeneous soils or profiles where the undrained shear strength increases linearly with depth. In practice, however, we usually encounter problems where the soil profiles consist of discrete soil strata, or more irregular strength profiles. Thus, generalized soil profiles should be incorporated into the analyses.
2. The current computer codes assume isotropic yield for the soil. For most real soils, particularly cohesive soils, the shear strength varies with principal stress directions and hence, programs should be modified to include a generalized anisotropic yield criterion.
3. It is well-known that the Mohr-Coulomb yield criterion with associated flow predicts a much larger rate of dilations than that observed in laboratory tests in sands. Thus, the program should also be modified to include a more realistic yield criterion for sands in which the peak friction angle varies with the confining pressure (e.g. Pestana, 1994).
4. The current formulation is limited to plane strain problems. Further development could be carried out to generalized formulation for analyses of axisymmetric or 3-D geometries.
5. Although the objective function is well defined for shallow foundation problems, for other classes of problem such as slope stability, the selection of the objective function is less straightforward. Further research is necessary to generalize classes of objective function for practical geotechnical analyses.

6. The addition of structural elements, such as beam elements, can be incorporated in the program to investigate the problems of soil-structure interaction, which involve failure of both the soil and structure.
7. The factor of safety is an important concept in the limit design approach. For bearing capacity problems, it is easy to define the factor of safety as the ratio of the collapse load to the applied load. However, for other practical problems such as excavation or embankment problems, the determination of the factor of safety is quite complicated. In order to be able to use results of limit analyses in the design, it is necessary to develop more general definitions of the safety level.

There are many possible applications of the numerical limit analyses geotechnical engineering. Some examples include:

1. Base stability of braced excavation is a challenging problem because the failure may occur due to shear distortion in the soil mass and/or bending of the structural wall pile. None of the existing solutions (e.g. Terzaghi, 1943) consider failure of the structural elements.
2. Slope stability problem is perhaps the most common class of stability analyses occurring in geotechnical practice. Numerical limit analyses have several advantages over existing limit equilibrium methods (LEM) in estimating slope stability: i) they provide a well defined range on the true collapse (which avoids approximation of LEM); and ii) they eliminate the search for the critical failure surface. Application of the numerical limit analyses for practical slope stability problems are contingent on the development of procedures to handle non-homogenous ground conditions and generalizations of the objective functions.
3. The numerical limit analyses can also be used to investigate other practical problems in soil structure interaction: i) the bearing capacity of (circular or strip) footings embedded in the soil and subjected to an inclined and eccentric loading; and ii) lateral loaded piles or walls; and iii) load capacity of grouting anchors etc.

References

Abdi, R., de Buhan, P., and Pastor, J. (1994). "Calculation of the critical height of a homogenized reinforced soil wall a numerical approach." Int. J. Numer. Anal. Methods in Geomech., 18, 485-505.

Anderheggen, E., and Knopfel, H. (1972). "Finite element limit analysis using linear programming." Int. J. Solids Struct., 8, 1413-1431.

Assadi, Ali, and Sloan, S. W. (1990). "Undrained stability of shallow square tunnel." J. Geotech. Eng., ASCE., 117(8), 1152-1173.

Atkinson, J. H. (1981). Foundations and Slopes., McGraw-Hill.

Bathe, K. J. (1982). Finite elements procedures in engineering analysis. Prentice-Hall, Englewood Cliffs, NJ.

Bishop, A. W. (1955). "The use of the slip circle in the stability analysis of slopes." Géotechnique, 5, 7-17.

Bishop, A. W., and Morgenstern, N. R. (1960). "Stability coefficients for earth slopes." Géotechnique, 10, 129-50.

Best, M. J., and Ritter, K. (1985). Linear Programming: Active Set Analysis and Computer Programs, Prentice-Hall, New Jersey.

de Buhan, P., Mangiavacchi, R., Nova, R., Pelligrini, G. and Salençon, J. (1989). "Yield design of reinforced earth walls by a homogenization method." Géotechnique, 39, (2), 189-201.

de Buhan, P. and Siad, L. (1989). "Influence of a soil-strip interface failure condition on the yield strength of reinforced earth." Computers and Geotechnics, 7, 3-18.

Bottero, A., Negre, R., Pastor, J., and Turgeman, S. (1980). "Finite element method and limit analysis theory for soil mechanics problems." Comp. Meth. Appl. Mech. Eng., 22 131-149.

Brinch Hansen, J. (1970). "A revised and Extended Formula for bearing capacity." Bulletin No. 28, Danish Geotehcnical Institute, Copenhagen, 5-11.

Caquot, A. and K'erisel, J. (1948). "Tables for the calculation of passive pressure, active pressure and bearing capacity of foundation." Gauthier-Villars, Paris.

Chen, W. F. (1975). Limit Analysis and Soil Plasticity, Elsevier, Amsterdam.

Chen, W. F. (1990). Nonlinear analysis in soil mechanics, Elsevier, Amsterdam.

Chuang P. H. (1992a). "Stability analysis in geomechanics by linear programming. I: Formulation." J. Geotech. Eng., ASCE., 118(11), 1696-1715.

Chuang P. H. (1992b). "Stability analysis in geomechanics by linear programming. II: Application." J. Geotech. Eng., ASCE., 118(11), 1716-1726.

Cox, A.D. (1962). "Axially symmetric plastic deformation in soils II. Indentation of ponderable soils" Int. Jour. Mech. Sci., 4, 371-380.

Cox, A.D., Eason, G. and Hopkins, H.G. (1961). "Axially symmetric plastic deformation of soils" Phil. Trans. Roy. Soc., Series A, 254, 1-45.

Davis, E. H. and Booker, J. R. (1973). "The effect of increasing strength with depth on the bearing capacity of clays." Géotechnique, 23 (4), 551-563.

Davis, E. H. and Christian, J. T. (1971). "Bearing capacity of anisotropic cohesive soil." J. Soil Mech. Found. Div., ASCE., 97(SM5), 753-769.

Debeer, E. E. (1987). "Analysis of shallow foundations." Geotechnical Modeling and Applications, Ed S. M. Sayed, 212-321.

Drucker, D.C., Greenberg, H.J. and Prager, W. (1952). "Extended limit design theorems for continuous media" Q. Appl. Math., 9, 381-389.

Drucker, D.C. and Prager, W. (1952). "Soil mechanics and plastic analysis or limit design." Q. Appl. Math., 10, 157-165.

Eurocode E7 (1993). "Design and construction of foundations, retaining structures and earthworks." European Commission, Bruxelles.

Fellenius, W. (1926). Mechanics of soils. Statika Gruntov, Gosstrollzdat.

Fellenius, W. (1936). "Calculation of stability of earth dams." Trans. 2nd Int. Congr. Large Dams, 4, 445

Fredlund, D. G., and Krahn, J. (1977). "Comparison of slope stability methods of analysis." Can. Geot. J., 14, 429-439.

Garber, M. and Baker, R. (1977). "Bearing capacity by variational method." J. Geotech. Engrg. Div., ASCE, 103 (GT11), 1209-1225.

Hansen, J. Brinch. (1961) "A general formula for bearing capacity." Danish Geotechnical Institute, Bulletin No. 11.

Heyman, J. (1973). "The stability of a vertical cut." Int. J. Mech. Sci., 15, 845-854.

Hill, R. (1950). The mathematical theory of plasticity. Clarendon Press, Oxford.

Houlsby, G.T. and Wroth, C.P. (1982). "Direct solution of plasticity problems in soils by the method of characteristics." Proceedings of the 4th International Conference on Numerical Methods in Geomechanics, Edmonton, 3, 1059-1071.

Janbu, N. (1954). "Stability analysis of slopes with dimensionless parameters." Harvard Soil Mechanics Series, No. 46, 81lp.

Kötter, F. (1903). Die Bestimmung des Druckes an Gekrummten Gleitflachen, eine Aufgabe aus der Lehre vom Erddruck. Monatsber. Akad. Wiss. Berlin, 229-233.

Ladd, C. C., and Foot, R. (1974). "New design procedure for stability of soft clays." J. Geotech. Engrg. Div., ASCE, 100 (7), 763-786

Lee, I.K. (1975). "Application of plasticity theory to the prediction of earth pressures." Soil Mechanics, Recent Development, Unisearch, Kensington, 27-81.

Lysmer, J. (1970). "Limit analysis of plane problems in soil mechanics." J. Soil Mech. Found. Div., ASCE., 96(SM4), 1311-1334.

Mesri, G., and Choi, Y. K. (1985). "Settlement analysis of embankments on soft clays." J. Geotech. Engrg. Div., ASCE, 111(4), 441-464.

Meyerhof, G. G. (1953). "The bearing capacity of foundation under eccentric and inclined loads." Proceedings, Third International Conference on Soil Mechanics and Foundation Engineering, Zurich, 1, 440-445.

Morgenstern, N. R., and Price, V. E. (1965). " The analysis of the stability of generalized slip surfaces." Géotechnique, 15, 79-93.

Nagtegaal, J. C., Parks, D. M., and Rice, J. R. (1974). "On numerically accurate finite element solutions in the fully plastic range", Comp. Meth. Appl. Mech. Eng., 4, 153-177.

Nayak, G. C. and Zienkiewicz, O.C. (1972). "Elasto-plastic stress analysis". A generalization for various constitutive relations including strain softening. Int. J. Numer. Methods Eng., 17, 14-41.

Pastor, J. (1976). "Application de l'analyse Limit'e a l'etude de la Stabiliti'e des Pentes et des Talus.", Thesis, Institute de M'echanique, Grenoble.

Pastor, J. (1978). "Limit analysis: Numerical determination of complete statical solutions-Application to the vertical cut." Journal de M'echanique Appliqu'ee, 2(2), 167-196.

Pestana-Nascimento, J. M. (1994). "A unified constitutive model for clays and sands." ScD thesis, Dept. of Civil and Environmental Eng., Massachusetts Institute of Technology, Cambridge, MA.

Poulos, H.G,. and Davis, E.H. (1974). Elastic solutions for soil and rock mechanics. Wiley and Sons.

Prandtl, L. (1920). Über die Harte plastischer Körper. Nachr. K. Ges. Wiss. Gott., Math-Phys. Kl., 74-85.

Saran, S. and Agarwal R. K. (1991). "Bearing capacity of eccentrically obliquely loaded footing." J. of Geotech. Eng., ASCE., 117, 11, 1669-1690.

Sawicki, A. (1983). "Plastic limit behavior of reinforced earth." J. of Geotech. Eng., ASCE., 109, 1000-1005.

Sawicki, A. (1988). "Plastic behavior of reinforced earth.", Chapter 3 in Civil Engineering Practice Vol. 3 - Geotechnical Ocean Engineering (Ed: P.N. Cheremisinoff, N.P. Cheremisinoff and S.L. Cheng), 45-64.

Scott, R.F. (1965). Principles of Soil Mechanics. Addison-Wesley.

Shield, R. T. (1955). "The plastic indentation of a layer by a flat punch." Q. Appl. Mathe., 8, 1, 27-46.

Sloan S. W. (1988a). "Lower bound limit analysis using finite elements and linear programming." Int. J. Numer. Anal. Methods in Geomech., 12(1), 61-77.

Sloan S. W. (1988b). "A steepest edge active set algorithm for solving sparse linear programming problems." Int. J. Numer. Anal. Methods in Geomech., 26(12), 2671-2685.

Sloan S. W. (1989). "Upper bound limit analysis using finite elements and linear programming." Int. J. Numer. Anal. Methods in Geomech., 13, 263-282.

Sloan S. W., Assadi, A., and Purushothaman, N. (1990). "Undrained stability of a trap door" Géotechnique, 40(1), 45-65.

Sloan S. W., and Assadi, A. (1993). "Stability of shallow tunnels in soft ground." Predictive Soil Mechanics, Thomas Telford, London.

Sloan S. W., and Kleeman (1994). "Upper bound limit analysis using discontinuous velocity fields." Research Report 096.05.1994, The University of Newcastle, Australia.

Sloan S. W., and Randolph M. F. (1982). "Numerical prediction of collapse loads using finite element methods.", Int. J. Num. Analy. Meth. Geomech., 6, 47-76.

Sokolovskii, V. V. (1965). Statics of Granular Media, Pergamon Press, New York, N.Y.

Spencer, E. (1967). "A method of analysis of the stability of embankments assuming parallel interslice forces." Géotechnique, 17, 11-26.

Taylor, D. W. (1948). Fundamentals of Soil Mechanics. Wiley and Sons.

Terzaghi, K. (1943). Theoretical Soil Mechanics. Wiley and Sons.

Toh, C. T., and Sloan, S. W. (1980). "Finite element analyses of isotropic and anisotropic cohesive soils with a view to correctly predicting impending collapse." Int. J. Num. Analy. Meth. Geomech., 4, 1-23.

Vesic, A. S. (1975). "Bearing capacity of shallow foundations." Foundation Engineering Handbook, H. F. Winterkorn and H. Y. Fang (Ed.) Van Nostrand Reinhold Company, 121-145.

Whittle, A. J. (1987). "A constitutive model for over-consolidated clays with application to the cyclic loading of friction piles." ScD thesis, Dept. of Civil and Environmental Eng., Massachusetts Institute of Technology, Cambridge, MA.

Yu., H. S. and Sloan, S. W. (1993). "Rigorous plasticity solutions for the bearing capacity of a cohesionless-ponderable soil." Research Report, The University of Newcastle, Australia.

Yu., H. S. and Sloan, S. W. (1994a). "Upper-bound limit analysis of a rigid-plastic body with frictional interfaces." Int. J. Mech. Sci., 36(3), 219-229.

Yu., H. S. and Sloan, S. W. (1994b). "Limit analysis of reinforced soils using finite elements." Research Report 092.03.1994, The University of Newcastle, Australia.

Yu. H. S. and Sloan, S. W. (1994c). "Limit analysis of anisotropic soils using finite elements and linear programming.", Mech. Research Commun., 21(6), 545-554.

Yu., H. S., Sloan, S. W., and Kleeman, P. W. (1994). "A quadratic element for upper bound limit analysis." Engineering Computations, 11, 195-212.

Appendix A. Proof of the Upper Bound Theorem

The proofs of the upper and lower bound theorems given below are taken from Chen (1975).

Before we begin to prove the bound theorems, it is necessary to prove the property of convex yield surface with the associated flow rule, as they will be used later. Suppose that the state of stress σ_{ij}^{P} is a point on a yield surface and $\dot{\varepsilon}_{ij}^{P}$ is a corresponding plastic strain rate, while σ_{ij}^{E} is any other point inside the yield surface. The convexity property of the yield surface together with the associated flow rule requires that:

$$\sigma_{ij}^{P}.\dot{\varepsilon}_{ij}^{P} > \sigma_{ij}^{E}.\dot{\varepsilon}_{ij}^{P} \qquad \text{(A1)}$$

Proof: Let $F(\sigma_{ij})$ is a yield function. Thus, the plastic strain rate $\dot{\varepsilon}_{ij}^{P}$ is defined by the flow rule as:

$$\text{For } F(\sigma_{ij}) = 0 \qquad \dot{\varepsilon}_{ij}^{P} = \dot{\lambda}\frac{\partial F}{\partial \sigma_{ij}} \qquad \text{(A2)}$$

where $\dot{\lambda}$ = a non-negative plastic multiplier rate

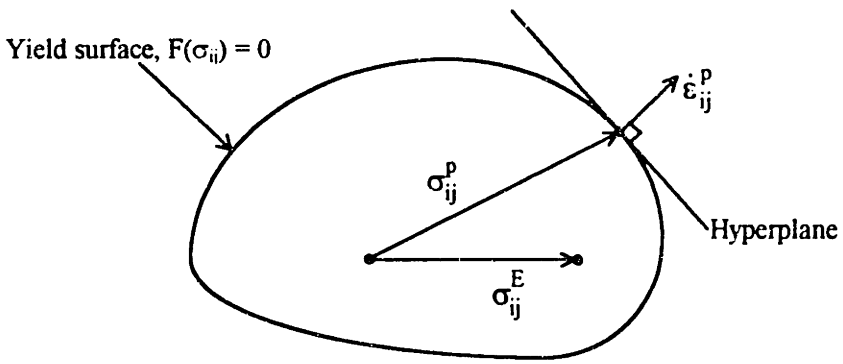

Fig. A2.1 Proof of the convexity property of the yield surface with flow rule

This expression means that $\dot{\varepsilon}_{ij}^{P}$ is a vector which is outward normal to the yield surface at σ_{ij}^{P}, shown in Figure A2.1. The tangential hyperplane in the figure is expressed as:

$$\sigma_{ij}^{p}.\dot{\varepsilon}_{ij}^{p} = b \qquad \text{(A3)}$$

where b is the dot product value between σ_{ij}^{p} and $\dot{\varepsilon}_{ij}^{p}$.

Because the yield surface is convex, the entire yield surface must lie on one side of any tangential hyperplane. Hence, that side [$F(\sigma_{ij}) < 0$; the left side of the hyperplane] corresponds to the negative direction of the normal vectorσ_{ij}^{E}, and is given by:

For $F(\sigma_{ij}) < 0$: $\qquad \sigma_{ij}.\dot{\varepsilon}_{ij}^{p} < b \qquad \text{(A4)}$

Since σ_{ij}^{E} lies inside the yield surface, it must satisfy $F(\sigma_{ij}^{E}) < 0$ and hence, equation A4 holds for σ_{ij}^{E} :

$$\sigma_{ij}^{E}.\dot{\varepsilon}_{ij}^{p} < b \qquad \text{(A5)}$$

Combining equations A3 and A5, we have:

$$\sigma_{ij}^{p}.\dot{\varepsilon}_{ij}^{p} > \sigma_{ij}^{E}.\dot{\varepsilon}_{ij}^{p} \qquad \square$$

Now, we will start to prove the upper bound theorem. The theorem states that if a kinematically admissible velocity field is found, the external applied load will be an upper bound solution on the true collapse load. To prove the theorem, assume it false. Then, we show that this leads to a contradiction.

The false statement is that we find the kinematically admissible velocity field u_i^{p*}, but the collapse does not occur due to the surface traction T_i, and the body force F_i. That means that an equilibrium distribution of stress σ_{ij}^{E} which satisfies $F(\sigma_{ij}^{E}) < 0$ must therefore exist. The system of the body are:

Equilibrium set: T_i, F_i, and σ_{ij}^{E} are in equilibrium.

Compatibility set: u_i^{p*} and σ_{ij}^{E} are compatible.

Applying the virtual work given in equation 2.10 to these two system yields:

$$\int_A T_i u_i^{p*} dA + \int_V F_i u_i^{p*} dV = \int_V \sigma_{ij}^{E} \dot{\varepsilon}_{ij}^{p*} dV \qquad \text{(A6)}$$

The left hand side in the equation, which is the rate of external forces do work, can be equated to the rate of internal dissipation $\int_V \sigma_{ij}^P \dot{\varepsilon}_{ij}^{p^*} dV$:

$$\int_V \sigma_{ij}^p \dot{\varepsilon}_{ij}^{p^*} = \int_V \sigma_{ij}^E \dot{\varepsilon}_{ij}^{p^*} dV \qquad \text{(A7)}$$

where σ_{ij}^p is the plastic stress state corresponding to σ_{ij}^E

However, the convexity and flow rule as discussed earlier require that $\sigma_{ij}^p . \dot{\varepsilon}_{ij}^{p^*} > \sigma_{ij}^E . \dot{\varepsilon}_{ij}^{p^*}$, for $F(\sigma_{ij}^E) < 0$. This leads to a contradiction and thus proves the upper bound theorem. □

Appendix B. Proof of the Lower Bound Theorem

The lower bound theorem states that if a statically admissible stress field is found, the external applied load will be a lower bound solution on the true collapse load, and collapse will not take place. Again, to prove the theorem, assume it false. We show that this leads to a contradiction.

The false statement is that we obtain the statically admissible stress, σ_{ij}^{E}, but the collapse takes place. If the body collapses due to the surface traction T_i^c, and the body force F_i^c, a collapse pattern associated with the actual stresses, strain rates, and velocities, $\sigma_{ij}^{c}, \dot{\varepsilon}_{ij}^{c}$ and u_i^c exists. The collapse stress σ_{ij}^{c} is also in equilibrium with the loads T_i^c and F_i^c, while the collapse strain rate $\dot{\varepsilon}_{ij}^{c}$ is compatible with the collapse velocity u_i^c. Notice that we have two equilibrium systems:

System 1: σ_{ij}^{E}, T_i^c, F_i^c

System 2: σ_{ij}^{c}, T_i^c, F_i^c

Applying the virtual work shown in equation 2.10 to these two systems gives rise to:

$$\text{System1:} \quad \int_A T_i^c u_i^c dA + \int_V F_i^c u_i^c dV = \int_V \sigma_{ij}^{E} \dot{\varepsilon}_{ij}^{c} dV \qquad \text{(B1)}$$

$$\text{System 2:} \quad \int_A T_i^c u_i^c dA + \int_V F_i^c u_i^c dV = \int_V \sigma_{ij}^{c} \dot{\varepsilon}_{ij}^{c} dV \qquad \text{(B2)}$$

Hence:

$$\int_V \sigma_{ij}^{c} \dot{\varepsilon}_{ij}^{c} = \int_V \sigma_{ij}^{E} \dot{\varepsilon}_{ij}^{c} dV \qquad \text{(B3)}$$

Since at collapse, all deformation is plastic, it follows that $\dot{\varepsilon}_{ij}^{c} = \dot{\varepsilon}_{ij}^{pc}$ and equation B3 becomes:

$$\int_V \sigma_{ij}^{c} \dot{\varepsilon}_{ij}^{pc} = \int_V \sigma_{ij}^{E} \dot{\varepsilon}_{ij}^{pc} dV \qquad \text{(B4)}$$

However, the convexity and flow rule as discussed in the preceding appendix require that $\sigma_{ij}^{c}.\dot{\varepsilon}_{ij}^{pc} > \sigma_{ij}^{E}.\dot{\varepsilon}_{ij}^{pc}$, for $F(\sigma_{ij}^{E}) < 0$. This leads to a contradiction and thus proves the lower bound theorem. □

Appendix C. Derivation of Constraints for 3-Noded Triangular Extension Element (Equations 3.5p and 3.5q)

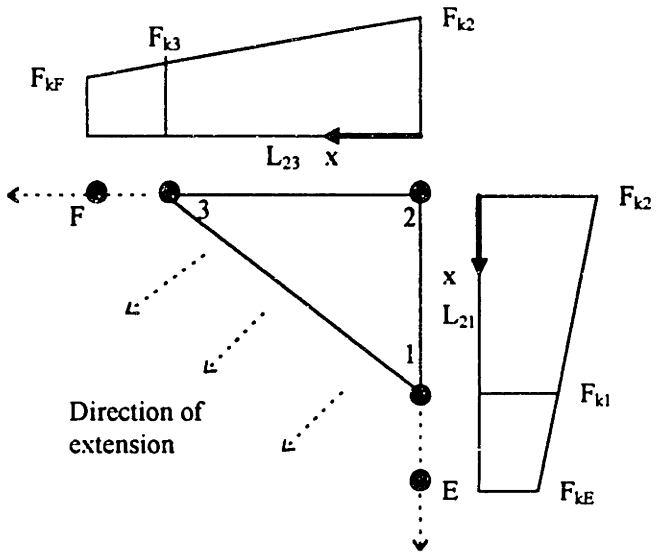

Fig. C1 3-noded Triangular Extension Element

Figure C1 shows the 3-noded triangular extension element with nodes 1, 2, and 3. Points E and F are located along the edge 2-1 and 2-3 respectively in directions of the extension zone. Referring to equation 3.5k, the value of k^{th} side of the linearized Mohr-Coulomb yield criterion is given by:

$$F_k = N_1 F_{k1} + N_2 F_{k2} + N_3 F_{k3} = \sum_{i=1}^{3} N_i F_{ki} \le 0 \qquad \text{(C1)}$$

where $F_{ki} = A_k \sigma_{xi} + B_k \sigma_{yi} + C_k \tau_{xyi} - D_i$; k = 1, 2,..., p ; i = 1, 2, 3

N_i = the linear shape functions given by equation 3.1b

It is from equation C1 that F_k varies linearly within the element. Consider the edge along nodes 2-1-E. The value of F_k at point E can be written as a linear function of the values at nodes 2 and 1 as:

$$F_{kE} = F_{k2}\{1 - \frac{x}{L_{21}}\} + F_{k1}\frac{x}{L_{21}} \qquad \text{(C2)}$$

i.e.,

$$F_{kE} = F_{k2} + \frac{x}{L_{21}}\{F_{k1} - F_{k2}\} \qquad (C3)$$

The value of the k^{th} linearized yield function at point E, F_{kE} must satisfy the yield condition, i.e. $F_{kE} \leq 0$. Since the value of x/L_{21} is non-negative, this condition is satisfied by enforcing the following constraints:

$$F_{k2} \leq 0; \text{ and } (F_{k1} - F_{k2}) \leq 0 \qquad (C4)$$

Similarly, along the edge 2-3-F, the value of F_k at point F is given by:

$$F_{kF} = F_{k2}\{1 - \frac{x}{L_{23}}\} + F_{k3}\frac{x}{L_{23}} \qquad (C5)$$

which can be rearranged:

$$F_{kF} = F_{k2} + \frac{x}{L_{23}}(F_{k3} - F_{k2}) \qquad (C6)$$

The value of the k^{th} linearized yield function at point F, F_{kF} must also satisfy the yield condition, $F_{kF} \leq 0$. Since the value of x/L_{23} is non-negative, this condition is satisfied by enforcing the constraints:

$$F_{k2} \leq 0 \text{ and } (F_{k3} - F_{k2}) \leq 0 \qquad (C7)$$

By combining equations C4 and C7, the constraints of the linearized yield criterion for a 3-noded triangular extension element are obtained as:

$$F_{k2} \leq 0, (F_{k1} - F_{k2}) \leq 0 \text{ and } (F_{k3} - F_{k2}) \leq 0 \qquad (C8)$$

It must be proven that these conditions are also valid for the stresses throughout the zone of the extension element (i.e, at all points between points F and E).

Using the shape-function identity $(N_1 + N_2 + N_3) = 1$ to substitute for F_k in equation C1, gives:

$$F_k = N_1(F_{k1} - F_{k2}) + F_{k2} + N_3(F_{k3} - F_{k2}) \qquad (C9)$$

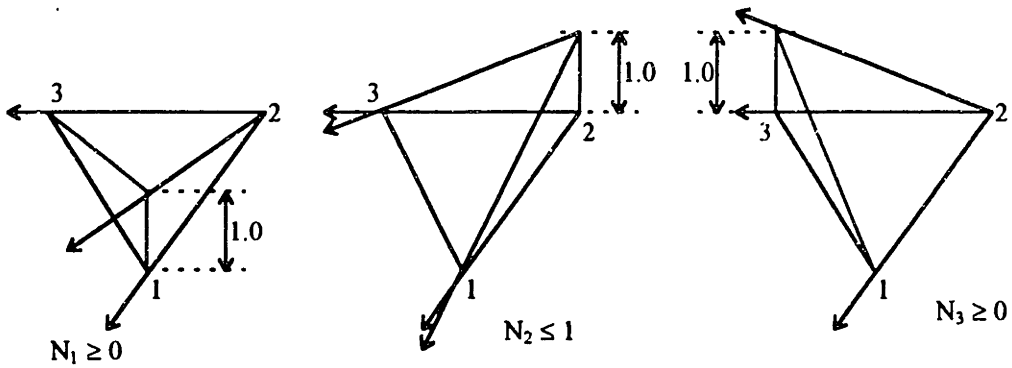

Fig. C2 Range of N_i

Figure C2 illustrates the geometric representation of the range of N_i for the 3-noded triangular extension element. The range of each shape function is given by:

$$N_1 \geq 0,\ N_2 \leq 1.0,\ N_3 \geq 0 \qquad \text{(C10)}$$

Substituting equations C10 and C8 into equation C9, the sign of F_k is guaranteed to be non-positive, thus satisfying the yield condition. This establishes that by enforcing the constraints of equation C7, the stresses throughout the zone of extension element do not violate the yield criterion. □

Appendix D. Derivation of Constraints for 4-Noded Rectangular Extension Element (Equations 3.2c, 3.5s, and 3.5t)

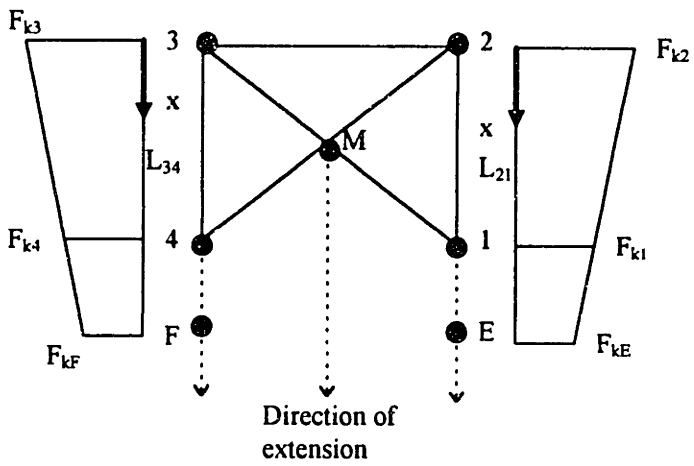

Fig. D1 4-noded Rectangular Extension Element

Equality constraints which must be enforced at the 4th node of a rectangular extension element (equation 3.2c; Figure D1) can be obtained as follows. The stresses vary linearly within the element, and hence the stresses at the midpoint of edge 1-3 (point M) are simply calculated from the average of the stresses at nodes 1 and 3:

$$\sigma_{xM} = (\sigma_{x1} + \sigma_{x3})/2 \qquad \text{(D1)}$$

$$\sigma_{yM} = (\sigma_{y1} + \sigma_{y3})/2$$

$$\tau_{xM} = (\tau_{x1} + \tau_{x3})/2$$

Similarly, the stresses at the node 4 follow the same linear variation as the first three nodes. Thus, the stresses at midpoint of edge 2-4 (point M) are given by:

$$\sigma_{xM} = (\sigma_{x2} + \sigma_{x4})/2 \qquad \text{(D2)}$$

$$\sigma_{yM} = (\sigma_{y2} + \sigma_{y4})/2$$

$$\tau_{xM} = (\tau_{x2} + \tau_{x4})/2$$

Equating equations D1 to D2 gives expression for the stresses at node 4 (equation 3.2c):

$$\sigma_{x4} = \sigma_{x1} - \sigma_{x2} + \sigma_{x3} \qquad \text{(D3)}$$

$$\sigma_{y4} = \sigma_{y1} - \sigma_{y2} + \sigma_{y3}$$

$$\tau_{xy4} = \tau_{xy1} - \tau_{xy2} + \sigma_{xy3}$$

□

The constraints for the linearized yield criterion of a 4-noded rectangular extension element can be proved as follows.

Since the stresses vary linearly within element and F_k is linear function of the stresses (equation C1), it follows from equation D3 that the value of the linearized yield surface for node 4 has the same expression as this equation:

$$F_{k4} = F_{k1} - F_{k2} + F_{k3} \qquad \text{(D4)}$$

Consider the edge defined by nodes 2-1-E (Figure D1). The value of F_k at point E can be obtained by linearly extrapolating from nodes 2 and 1:

$$F_{kE} = F_{k2}\{1 - \frac{x}{L_{21}}\} + F_{k1}\frac{x}{L_{21}} \qquad \text{(D5)}$$

This equation can be rewritten as:

$$F_{kE} = F_{k2} + \frac{x}{L_{21}}\{F_{k1} - F_{k2}\} \qquad \text{(D6)}$$

To be statically admissible stress, F_{kE} must satisfy the yield condition, that is $F_{kE} \leq 0$. Since the value of x/L_{21} is non-negative, this condition is satisfied if enforcing the constraints:

$$F_{k2} \leq 0; \text{ and } (F_{k1} - F_{k2}) \leq 0 \qquad \text{(D7)}$$

Similarly, for the edge 3-4-F, gives the value of F_k at point F:

$$F_{kF} = F_{k3}\{1 - \frac{x}{L_{23}}\} + F_{k4}\frac{x}{L_{23}} \qquad \text{(D8)}$$

Substituting equation D3 and rearranging the terms, equation D8 changes to:

$$F_{kF} = F_{k3} + \frac{x}{L_{34}}\{F_{k1} - F_{k2}\} \qquad \text{(D9)}$$

F_{kF} must also satisfy the yield condition according to the lower bound theorem ($F_{kF} \leq 0$). Since the value of x/L_{34} is non-negative, this condition is satisfied if:

$$F_{k3} \leq 0 \text{ and } F_{k1} - F_{k2} \leq 0 \qquad \text{(D10)}$$

Combining equations D7 and D10 yields the constraints for the linearized yield criterion of 4-noded rectangular extension element.

$$F_{k2} \leq 0, (F_{k1} - F_{k2}) \leq 0 \text{ and } (F_{k3} - F_{k2}) \leq 0 \qquad \text{(D11)}$$

The final step of this proof is to show that these constraints do not violate the yield criterion throughout the zone of the extension element. This can be shown as follows.

Using the shape-function identity $N_1 + N_2 + N_3 = 1$ to substitute for F_k in equation C1, gives:

$$F_k = N_1(F_{k1} - F_{k2}) + F_{k2}(1 - N_3) + N_3F_{k3} \qquad \text{(D12)}$$

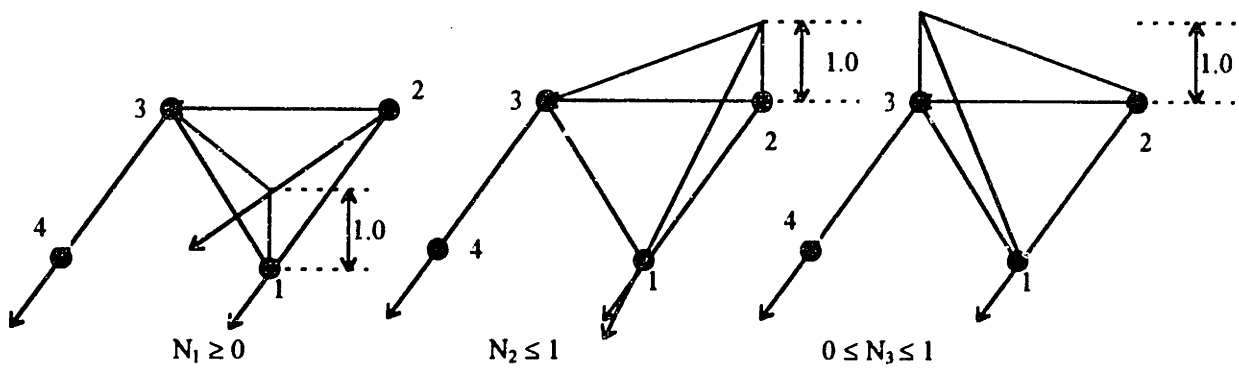

Fig. D2 Perspective view of range of N_i

Figure D2 illustrates the geometric representation of the range of N_i for the 4-noded triangular extension element. The range of each shape function is:

$$N_1 \geq 0, \; N_2 \leq 1 \, , \, 0 \leq N_3 \leq 1 \qquad \text{(D13)}$$

Substituting equations D11 and D13 into equation 12, the sign of F_k is always be non-positive, thus satisfying the yield condition. Therefore, by enforcing the constraints of equation D11, the stresses throughout the zone of extension element do not violate the yield criterion. □

Appendix E. Proof of Velocity Jump Decomposition

The goal of this appendix is to show that by assuming $|\Delta U| = U^+ + U^-$ and $\Delta U = U^+ - U^-$, subject to the constraints, U^+ and $U^- \geq 0$, at least one of the two variables, U^+ or U^- are zero:

Let $|\Delta U| = U^+ + U^-$ (E1)

$\Delta U = U^+ - U^-$ (E2)

$U^+ \geq 0$ (E3)

$U^- \geq 0$ (E4)

Let us draw the feasible sets of constraints E1-E4 in two dimensional spaces of U^+ vs. U^-. Three cases are considered.

Case 1: $\Delta U = 0$.

$0 = U^+ + U^-$ (E5)

$0 = U^+ - U^-$ (E6)

$U^+ \geq 0$ (E7)

$U^- \geq 0$ (E8)

So, both U^+ and $U^- = 0$

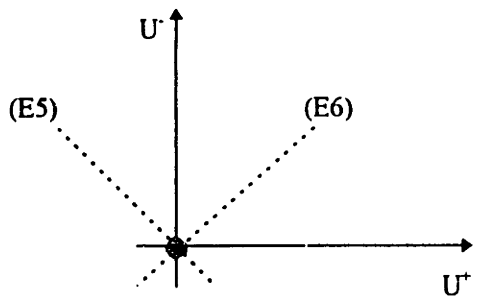

Fig. E1

Case 2: ΔU is positive. Let, $\Delta U = a$, $a > 0$

$a = U^+ + U^-$ (E9)

$a = U^+ - U^-$ (E10)

$U^+ \geq 0$ (E11)

$U^- \geq 0$ (E12)

So, $U^+ = a$ and $U^- = 0$

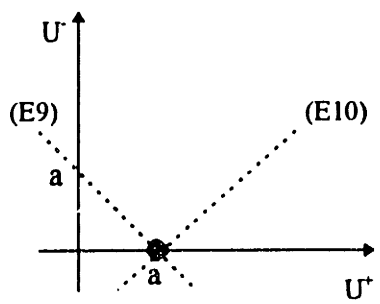

Fig. E2

Case 3: ΔU is negative. Let, $\Delta U = -a$, $a > 0$

$$a = U^+ + U^- \qquad \text{(E13)}$$

$$-a = U^+ - U^- \qquad \text{(E14)}$$

$$U^+ \geq 0 \qquad \text{(E15)}$$

$$U^- \geq 0 \qquad \text{(E16)}$$

So, $U^+ = 0$ and $U^- = a$

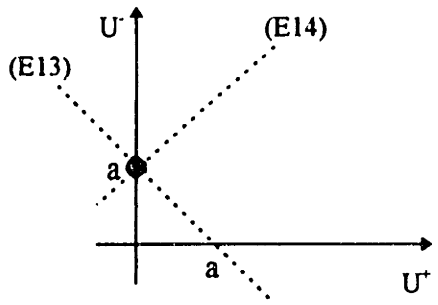

Fig. E3

According to the results of three cases, it can be concluded that by substituting $|\Delta U|$ with $U^+ + U^-$ and ΔU with $U^+ - U^-$, with subject to the constraints, U^+ and $U^- \geq 0$, at least one of the two variables, U^+ or U^- are zero. □